Active vibration control using the centrifugal forces of eccentrically rotating masses

Vom Promotionsausschuss der
Technischen Universität Hamburg-Harburg
zur Erlangung des akademischen Grades
Doktor-Ingenieur (Dr.-Ing.)

genehmigte Dissertation

von
Richard Bäumer

aus
Gerolzhofen

2017

Gutachter:	Prof. Dr.-Ing. Uwe Starossek
	Prof. Dr. Herbert Werner
Vorsitzender des Prüfungsausschusses:	Prof. Dr.-Ing. Gerhard Bauch
Tag der mündlichen Prüfung:	16. Oktober 2017

Meinen Eltern

*

Vorwort

Die vorliegende Dissertation entstand im Rahmen meiner Tätigkeit als Wissenschaftlicher Mitarbeiter an der Technischen Universität Hamburg-Harburg. Über die fünf Jahre der Entstehung dieser Arbeit haben mich viele Menschen begleitet und unterstützt, denen ich an dieser Stelle danken möchte.

Prof. Dr.-Ing. Uwe Starossek war mein Doktorvater. Als Mitarbeiter seines Lehrstuhls konnte ich fachlich und persönlich viel von ihm lernen. Mit seiner federführenden, klaren und zugleich zuvorkommenden Art war er mir stets ein Vorbild. Prof. Dr. Herbert Werner danke ich für die Unterstützung im Bereich der Regelungstechnik.

Besonderer Dank gilt den Mitarbeitern des Insituts für Baustatik und Stahlbau. Frau Inge Spahn, Herrn Dr.-Ing. Jürgen Priebe, Herrn Dipl.-Ing. Axel Seils und Herrn Olaf Wittleben möchte ich für die herzliche und solide Unterstützung danken. Hervorzuheben ist die Arbeit von Herrn Axel Seils. Seine Fachkenntnisse im Bereich Versuch ermöglichten die Durchführung von zahlreichen Erprobungen.

Danken möchte ich auch Herrn M.Sc. Richard Terrill für das Gegenlesen der Arbeit und die inhaltlichen Anmerkungen, welche viel in meine Arbeit einflossen. Redaktionelle Eingriffe in meine Arbeit übernahm Frau Sandra Büldt. Ihr gilt außerdem mein Dank für die vielen hochwertigen Zeichnungen.

Meine Geschwister Johanna, Maria und Jonas und natürlich meine lieben Eltern Barbara und Christoph haben mich auf meinem Lebensweg uneingeschränkt unterstützt. Ihnen gilt mein besonderer Dank.

Hamburg, November 2017

Richard Bäumer

*

Summary

In this PhD thesis, active vibration control using eccentrically rotating masses is investigated. The basic layout of the so-called twin rotor damper (TRD) consists of two eccentric control masses rotating about two parallel axes. In a preferred mode of operation, the continuous rotation mode, both control masses rotate in opposite direction with a constant angular velocity. Under further operational constraints, the generated centrifugal forces superimpose to a harmonic control force in a single direction.

The thesis begins with the presentation of control algorithms to ensure the continuous motion of the control masses and anti-phasing between the control force and the velocity of a single degree of freedom (SDOF) oscillator performing mono-frequent vibrations; thus, the TRD provides the desired damping action. An analytic steady-state response solution of a SDOF oscillator under harmonic excitation with and without the action of the TRD is derived and validated experimentally. The inability of the TRD to damp small vibrations in the continuous rotation mode becomes apparent and is discussed.

Subsequently, stochastically forced vibrations are studied. To ensure the anti-phasing between the velocity of the SDOF oscillator and the control force of the TRD, the TRD must deviate from the continuous rotation mode by varying the angular velocity of the rotors. If the required variation of the angular velocity is too high, it is no longer beneficial to operate the TRD in the continuous rotation mode. It is shown that below a specific vibration-amplitude threshold, an operation in the continuous rotation mode is no longer beneficial. To additionally control vibrations below the specified vibration-amplitude threshold, the TRD is required to operate in an alternative mode of operation, the so-called swinging mode. Although a greater damping performance is achieved with the continuous rotation mode, the swinging mode is required for the damping of small vibrations. Based on numerical simulations and experiments, the effectiveness of the proposed control-loop and tuning procedure for the damping of stochastically forced vibrations is validated.

Finally, the layout of the TRD is modified allowing for the vibration control of an oscillator with two translational degrees of freedom. The two degree of freedom oscillator performs planar motion and has an elliptic motion path when a free vibration is considered. The control masses now rotate about a single axis. By imposing small variations in the angular velocity, the direction of the control force can be changed in the plane of motion of the two degree of freedom (TDOF) oscillator. This allows for the vibration control of the TDOF oscillator in the continuous rotation mode with small variations in the angular velocities. The control algorithm works as follows. The direction of the major axis of the elliptic motion path is detected. To achieve maximum damping action, the directed harmonic control force is set such that it is in anti-phase with the velocity of the TDOF oscillator along the major axis. The algorithm was validated experimentally for free vibrations and numerically for stochastically forced vibrations. For a TDOF oscillator with small inherent damping, it is shown that the power demand and the energy consumption of the adapted TRD are smaller than those of a conventional active mass damper.

*

Contents

*

Nomenclature

Within the following list, abbreviations, symbols, operators and subscripts are given. The list contains recurring symbols of major importance. Symbols with minor importance, which only occur intermittently, are not listed.

Abbreviations

CAMD	conventional active mass damper
DOMA	direction of major axis
LE	limiting error
PLL	phase-locked loop
RDP	ramp-down process
RUP	ramp-up process
SDOF	single degree of freedom
TAP	target angular position
TAV	target angular velocity
TDOF	two degree of freedom
TMD	tuned mass damper
TRD	twin rotor damper

Greek Symbols

α	phase difference
Δ	deviation/offset/error
η	frequency ratio
θ	angular position for swinging mode
ϑ	direction of major axis
μ	mass ratio
ξ	damping ratio (to critical)
φ	angular position
ϕ	phase the displacement lags behind the excitation force in steady-state
$\varphi_{t,f}$	filtered target angular position
φ_t	target angular position
ψ	vibration phase
ω	(angular) frequency
ω_e	(angular) excitation frequency
ω_f	(circular) filter frequency
ω_n	natural (circular) frequency

Operators

$\hat{(..)}$	estimate
$..(t)$	indication of time-dependency
$\dot{(..)}$	time derivative
$(..)^{\mathrm{T}}$	transpose of a matrix

Roman Symbols

a, b	coefficients describing rotor dynamics
a_n	coefficients describing ramp-up/ramp-down trajectory
A_{off}	vibration amplitude below which the TRD turns off or switches in the swinging mode
A_{on}	vibration amplitude above which the TRD it turned on or switches in the continuous rotation mode
A_t	approximated tangential force component

$A_{\dot{\varphi}}$ ..... approximated variations of filtered target angular velocity
A ..... vibration amplitude
c ..... damping coefficient
ce ..... control error limited to values between $-\pi$ and π
$\boldsymbol{C}(s)$ ..... transfer function/matrix of controller
c_{φ} ..... control effort of PLL filter
$c_{x/y}$ ..... mean standard deviation of controlled displacement responses
D ..... dynamic amplification/indication of damping direction
d_m ..... displacement along major axis
d ..... relative displacement between control/excitation mass and main mass
E ..... energy
e ..... error
E_t ..... expected tangential force component
f_d ..... inherent damping force
F ..... force normalized by mass
f ..... force
f_i ..... total inertial force
f_s ..... restoring spring force
G_P ..... transfer function describing the dynamics of the single degree of freedom oscillator
G_{S2} ..... transfer function describing dynamics of linear actuator with control effort as input and displacement as output
G_S ..... transfer function describing dynamics of linear actuator with control effort as input and velocity as output
H ..... transfer function ensuring a smooth ramp up/down process
$\boldsymbol{I}$ ..... identity matrix
J ..... rotational inertia of a single rotor
K_P, K_{φ} ..... proportional feedback gain
k ..... stiffness
l ..... number of vibration periods
M_a ..... transfer function with control effort u_a as input and angular position φ as output
m ..... mass
M ..... moment created by one actuator
m_s ..... total mass of SDOF oscillator
M_v ..... transfer function with control effort u_a as input and angular velocity $\dot{\varphi}$ as output
n ..... rank of polynomial/number of considered vibration periods
P_a ..... power of an actuator
P_c ..... mean standard deviation of required powers of actuators
P_i ..... power of displacement due to initial conditions
P ..... mechanical power/power of a signal
$P_{rms,rot}$ ..... power required for the continuous rotation mode
$P_{rms,sw}$ ..... power required for the swinging mode
P_r^* ..... continuously computed power ratio
P_e ..... power of displacement due to excitation
P_T ..... power of one TRD unit
P_r ..... power ratio
P_t ..... total power of displacement

P_x ..... continuously derived power of displacement
r ..... rod length/radius
$s/s(t)$ ..... Laplace variable/time-varying signal
T_n ..... natural period length
T ..... period length/length of time interval
T_r ..... re-synchronization time
T_s ..... sampling time
t ..... time
u ..... control effort
$u_{x/y}$ ..... standard deviation of uncontrolled displacement responses
$V_{\dot{\varphi}}$ ..... expected variations of filtered target angular velocity
W ..... work
w ..... weight function
x ..... displacement of single degree of freedom oscillator/displacement coordinate of two degree of freedom osicllator
y ..... displacement coordinate of two degree of freedom osicllator
Y ..... logic signal indicating the mode of operation
$\boldsymbol{z}$ ..... state vector

Subscripts

0 ..... initial/amplitude
a ..... actuator/actual/adjusted/approximated
b ..... border
c ..... control/controlled/constant
cl ..... closed-loop
d ..... damped
e ..... excitation/exact/estimated
f ..... filtered
m ..... measured
n ..... natural
ol ..... open-loop
opt ..... optimal
p ..... peak
rd ..... ramp down
rms ..... root mean square
r ..... radial
ru ..... ramp up
std ..... standard deviation
tr ..... transient
t ..... tangential/target
T ..... twin rotor damper
u ..... uncontrolled

$*$

1

Introduction

Vibrations are frequently a subject for engineers. They can be wanted or unwanted [1]. In the first case, e.g. electromechanically induced vibrations of cones, vibrations are intentionally generated to produce sound waves [1]. In the second case, vibrations can negatively affect such things as material lifetime and human comfort. They can even lead to failure, for instance, of long-span bridges under strong wind action [2]. Earthquakes can produce seismic waves capable of threatening the integrity of structures and the lives of the inhabitants. In automobiles, engine vibrations and car vibrations induced by bad road conditions can make the driver uncomfortable [1]. To suppress or isolate such vibrations from other machinery parts or humans, damping devices can be utilized. There are three classifications of damping devices: passive, adaptive and active [3].

The implementation of passive damping devices in structures, e.g. bridges, is quite common. In [4], a tuned mass damper is used to mitigate pedestrian-induced vibrations. Tuned mass dampers have been researched extensively and are frequently used to reduce wind induced building vibrations, suppress vibrations of power transmission lines and wind turbine tower vibrations [5, 6]. Next to the tuned mass damper, there are other passive devices, like base isolation systems to isolate structures from the earthquake motion, friction dampers (e.g. fluid dampers), and other mechanical dampers (e.g. pendulum-type absorbers), see [7, 8, 9]. Passive devices are tuned to a single particular frequency. Therefore, they are only effective over a narrowband of frequencies. If the environmental or operating conditions of the system to be damped change, passive devices may become untuned and lose their effectiveness [3].

In such cases, adaptive devices can be more effective. By adjusting specific parameters, their behavior can be varied during operation. Advances concerning this have led to a variety of adaptive tuned mass dampers and associated control strategies, see [3, 10, 11, 12, 13, 14, 15]. However, reliability and maintainability concerns may be one of the reasons that have prevented the wide use of such devices [3].

Reliability and maintainability concerns are also often associated with active devices. Active devices consist, among other things, of an active element. This active element can, for instance, produce a force or a moment on a reaction mass. Advantages of active devices over passive and adaptive devices include a broader band of effective frequencies and higher control authority [3, 16, 17]. Active devices have also been implemented, e.g. for structural control, see [18, 19]. Further active devices and corresponding control algorithms are presented in [20, 21, 22]. Active devices are, however, more complex and require an external power supply, resulting frequently in higher costs in terms of design and operation.

Most active mass dampers generate their damping action by continuously accelerating and decelerating control masses. The resulting inertial forces are set such that they oppose the velocity of the system to be damped [17]. The velocity of the system can be used as feedback, which makes the design of the control-loop simple. In this work, such active mass dampers will be referred to as conventional active mass dampers.

In [23], an active mass damper implementing the centrifugal forces of eccentrically rotating masses was presented. The basic layout, referred to as the twin rotor damper (TRD), consists of two eccentric control masses which rotate with equal and constant angular velocity about two parallel axes. In a preferred mode of operation, the continuous rotation mode, both control masses rotate in opposite directions. The resulting centrifugal forces are used for the vibration control of a single degree of freedom oscillator. The nearly constant angular velocity results in a power advantage in comparison to conventional active mass dampers.

In this thesis, the research done in [23] is further developed and augmented for the control of stochastically forced vibrations. Furthermore, the TRD setup and control algorithms are adapted and developed for the control of an oscillator with two translational degrees of freedom.

This work is structured a follows. In the following chapter, the layout of the TRD is presented along with the manner in which the control force is generated in the continuous rotation mode. A continuous feedback control for the TRD is then derived, allowing for the vibration control of a single degree of freedom (SDOF) oscillator performing monofrequent vibrations. The TRD operated in the continuous rotation mode is then compared to a conventional active mass damper regarding power efficiency. For reaching and leaving the continuous rotation mode, ramp-up and ramp-down trajectories are developed. Thereafter, a complete closed-loop control damping cycle for the TRD is presented, validated experimentally and discussed. An analytic solution describing the steady-state response of a SDOF oscillator subjected simultaneously to a harmonic excitation force and the action of the TRD (operated in the continuous rotation mode) is derived, analyzed and validated experimentally. The steady-state damping performance of the TRD is then compared analytically with a passive device. The inability of the TRD to control small vibrations in the continuous rotation mode is discussed at the end of this chapter along with two further methods previously assumed to solve this problem.

In chapter 3, the use of the TRD for stochastically forced vibrations is studied. It is determined that using the TRD below a certain vibration threshold is ineffective in the continuous rotation mode. Therefore, an alternative mode of operation, the swinging mode, is investigated for the control of small vibrations. In a design example, the SDOF oscillator is exposed to a stochastic excitation force and the action of the TRD. A corresponding tuning procedure is proposed for automatically switching the TRD between the two modes of operation. Numerical simulations and experiments are performed.

In chapter 4, the layout of the TRD is adapted. The adapted layout allows for a control force which can change direction in a plane, thus to control the vibrations of an oscillator with two translational degrees of freedom. The free vibrations of this oscillator are analyzed first. A corresponding control algorithm is suggested and verified with a test setup for the damping of free vibrations. The use of the adapted TRD for stochastically forced vibrations is studied using numerical simulations.

2

Twin rotor damper

2.1 Layout and preferred mode of operation

As shown in figure 2.1 and [23], the twin rotor damper (TRD) consists of two control masses $m_c/2$. These masses are hinged by two mass-less rods with the length r to two parallel axes. The angular position $\varphi(t)$ clearly defines the motion of both rotors (control mass with mass-less rod), where (t) indicates the time dependency.

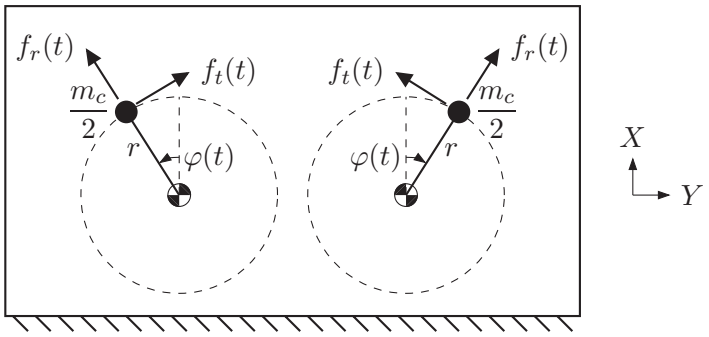

Figure 2.1: Twin rotor damper [24]

If the rotors are in motion ($\dot{\varphi}(t) \neq 0$), radial forces $f_r(t)$ (centrifugal forces) drawing away from the center of the axis are created, see figure 2.1. Such a radial force $f_r(t)$ is given by:

$$f_r(t) = \frac{1}{2} m_c r \dot{\varphi}(t)^2 \tag{2.1}$$

The dot operator indicates the derivative with respect to time.

If the rotors are additionally accelerated ($\ddot{\varphi}(t) \neq 0$), in addition to the radial forces, tangential forces, $f_t(t)$, are created, see figure 2.1. Such a tangential force is given by:

$$f_t(t) = \frac{1}{2} m_c r \ddot{\varphi}(t) \tag{2.2}$$

If, as indicated in figure 2.1, the angular positions of both rotors are equal, the force components of $f_r(t)$ and $f_t(t)$ in Y-direction cancel each other out, whereas the force components in X-direction superimpose to the force, $f_T(t)$, created by the TRD:

$$f_T(t) = m_c r \left[\dot{\varphi}(t)^2 \cos\varphi(t) + \ddot{\varphi}(t) \sin\varphi(t)\right] \tag{2.3}$$

If the rotors are driven with a constant angular velocity, the TRD operates in the so called continuous rotation mode. Consequently, the second term in the square bracket of (2.3) cancels out and a harmonic control force

$$f_c(t) = m_c r \dot{\varphi}^2 \cos\varphi(t) \tag{2.4}$$

with the constant amplitude $m_c r\dot{\varphi}^2$ is generated. Due to the constant angular velocity, the angular position changes proportionally to time. This is shown in the following equation

$$\varphi(t) = \dot{\varphi}t + \varphi_0 \tag{2.5}$$

in which φ_0 is the initial angular position.

If the angular positions of both rotors are unequal, a moment or a combination of a moment and a force is created. However, these cases will not be handled in this work. Further information regarding this can be found in [23, p. 8-13].

Note that in the continuous rotation mode, the preferred mode of operation, the tangential forces (second term in the square bracket on the right-hand side of (2.3)) are to be kept as small as possible. In another mode of operation, the so called swinging mode, primarily these tangential forces are used for damping. In contrast to the continuous rotation mode, the rotors must be accelerated and decelerated continuously to generate the desired damping action. Therefore, in the swinging mode, the TRD acts as a conventional active mass damper which generates its control action by continuously accelerating and decelerating control masses. Control algorithms for the swinging mode are presented in section 3.5.

2.2 Single degree of freedom oscillator

2.2.1 Governing differential equations

Within this section, open-loop studies of the single degree of freedom (SDOF) oscillator of figure 2.2 including the action of the TRD are carried out.

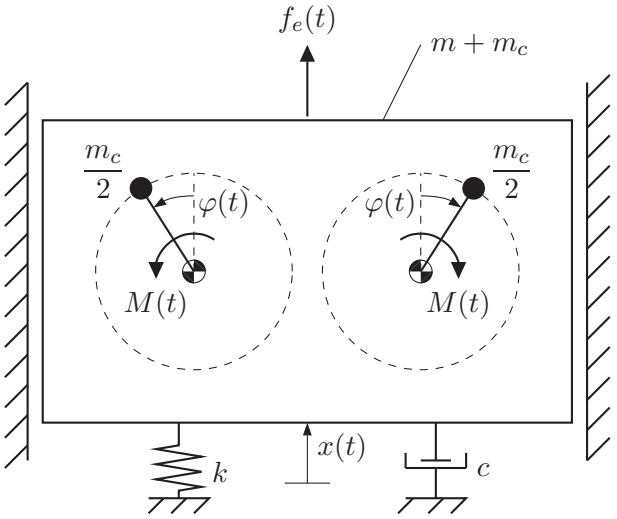

Figure 2.2: Twin rotor damper for SDOF oscillator [24]

The motion of the SDOF oscillator is defined by the displacement coordinate $x(t)$. Assuming a free vibration in which the rotors are not in motion ($\dot{\varphi} = 0$), the motion of the SDOF oscillator is governed by the homogeneous differential equation:

$$(m + m_c)\ddot{x}(t) + c\dot{x}(t) + kx(t) = 0 \tag{2.6}$$

in which $m + m_c$ is the total mass, c the damping coefficient and k the stiffness of the oscillator [1, 25]. In (2.6), the first term represents the total inertial force $f_i(t)$, the second

the inherent damping force $f_d(t)$ and the third the restoring spring force $f_s(t)$ [25]. In the following, the forces on the left-hand side of (2.6) will be referred to as system forces. Dividing (2.6) by $m + m_c$ gives

$$\ddot{x}(t) + 2\xi\omega_n\dot{x}(t) + \omega_n^2 x(t) = 0 \tag{2.7}$$

in which the natural (circular) frequency ω_n and the damping ratio ξ are defined in the following equations [25, 1].

$$\omega_n = \sqrt{\frac{k}{m + m_c}} \tag{2.8}$$

$$2\xi\omega_n = \frac{c}{m + m_c} \tag{2.9}$$

Taking the action of the TRD and an excitation force $f_e(t)$ into consideration, the motion of the SDOF oscillator is described by

$$(m + m_c)\ddot{x}(t) + c\dot{x}(t) + kx(t) = m_c r\left[\dot{\varphi}(t)^2\cos\varphi(t) + \ddot{\varphi}(t)\sin\varphi(t)\right] + f_e(t) \tag{2.10}$$

in which the first term on the right-hand side is $f_T(t)$. Dividing (2.10) by the total mass $m + m_c$ yields

$$\ddot{x}(t) + 2\xi\omega_n\dot{x}(t) + \omega_n^2 x(t) = \mu_c r\left[\dot{\varphi}(t)^2\cos\varphi(t) + \ddot{\varphi}(t)\sin\varphi(t)\right] + F_e(t) \tag{2.11}$$

in which μ_c is the control mass ratio and $F_e(t)$ the excitation force (normalized by the mass $m + m_c$) defined in (2.12) and (2.13), respectively.

$$\mu_c = \frac{m_c}{m + m_c} \tag{2.12}$$

$$F_e(t) = \frac{f_e(t)}{m + m_c} \tag{2.13}$$

In this work, lower-case f-variables refer to forces, whereas upper-case F-variables refer to forces normalized by mass.

The free body diagram of a single rotor including all forces creating a moment about the axis is shown in figure 2.3.

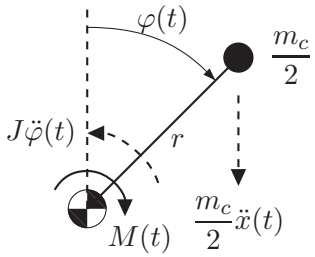

Figure 2.3: Free body diagram of a single rotor [24]

Establishing the dynamic equilibrium yields

$$M(t) - \frac{1}{2}m_c r^2\ddot{\varphi}(t) + \frac{1}{2}m_c r\ddot{x}(t)\sin\varphi(t) = 0 \tag{2.14}$$

in which $M(t)$ is the moment created by one actuator to drive the rotor. The second term on the left-hand side of (2.14) is the moment induced by the rotational inertia of a rotor and the third one the moment induced by an acceleration of the SDOF oscillator. By treating the control masses as lumped masses, the rotational inertia J of one rotor is $m_c r^2/2$. For practical applications, the rotational inertia induced by the shaft, the rod, etc. must be considered.

2.2.2 Optimal initial angular position for particular initial conditions

In [23], research was carried out to optimize the initial angular position of the rotors, $\varphi_0 = \varphi(t = 0)$. This was done by assuming initial conditions, e.g. $x_0 = x(t = 0)$ and $\dot{x}_0 = \dot{x}(t = 0)$, for the SDOF oscillator and minimizing the work done by the control force under the constraint of (2.15) [23].

$$\dot{\varphi} = \omega_n \tag{2.15}$$

With the constraint of (2.15) and (2.5), the control force of (2.4) becomes:

$$f_c(t) = m_c r \omega_n^2 \cos(\omega_n t + \varphi_0) \tag{2.16}$$

The optimization of the initial angular position is briefly repeated here [23]. Recalling (2.6), assuming that inherent damping is not present ($\xi = 0$), taking the control force of (2.16) into consideration and dividing, as before, by $m + m_c$ gives:

$$\ddot{x}(t) + \omega_n^2 x(t) = \mu_c r \omega_n^2 \cos(\omega_n t + \varphi_0) \tag{2.17}$$

Solving (2.17) for $x(t)$ gives (2.18) [23].

$$x(t) = x_0 \cos(\omega_n t) + \frac{\dot{x}_0}{\omega_n} \sin(\omega_n t) + \frac{1}{2}\mu_c r \left[\omega_n t \sin(\omega_n t + \varphi_0) - \sin(\varphi_0) \sin(\omega_n t)\right] \tag{2.18}$$

Deriving (2.18) with respect to time yields [23]:

$$\begin{aligned} \dot{x}(t) = &- x_0 \omega_n \sin(\omega_n t) + \dot{x}_0 \cos(\omega_n t) + ... \\ &\frac{1}{2}\mu_c r_c \left[\omega_n^2 t \cos(\omega_n t + \varphi_0) + \omega_n \cos\varphi_0 \sin(\omega_n t)\right] \end{aligned} \tag{2.19}$$

The work W_c (normalized by the total mass $m + m_c$) done by the control force on the SDOF oscillator over l vibration cycles is as given by

$$W_c = \mu_c r \omega_n^2 \int_0^{\frac{2\pi}{w_n} l} \dot{x}(t) \cos(\omega_n t + \varphi_0) \mathrm{d}t \tag{2.20}$$

where l is a positive integer number [23]. Deriving W_c with respect to φ_0, setting this equal to zero and doing some rearrangements gives [23, p. 62]:

$$x_0 \cos\varphi_0 - \frac{\dot{x}_0}{w_n} \sin\varphi_0 = 0 \tag{2.21}$$

As can be seen in [23], (2.21) does not depend on the number of vibration cycles l. Solving (2.21) for φ_0, the non-trivial solution

$$\varphi_0 = \operatorname{atan}\left(\frac{x_0 \omega_n}{\dot{x}_0}\right) \tag{2.22}$$

is found [23]. The tan-function is periodic in π. To check whether φ_0 corresponds to a positive or negative peak (work done by the control force on the SDOF oscillator becomes minimal or maximal), the second derivative of (2.20) with respect to φ_0 is calculated:

$$\frac{\mathrm{d}^2 W_c}{\mathrm{d}\varphi_0^2} = -x_0 \sin\varphi_0 - \frac{\dot{x}_0}{\omega_n} \cos\varphi_0 \tag{2.23}$$

Table 2.1 shows the ranges of various optimal initial angular positions, $\varphi_{0,opt}$, see last column, for different initial condition ranges described by constraints for x_0 and $\dot{x}_0$, see first column.

Table 2.1: Calculation of ranges of optimal initial angular positions for different initial condition ranges described by constraints for x_0 and $\dot{x}_0$

x_0 and $\dot{x}_0$	φ_0 according to (2.22)	$\varphi_{0,opt}$
$x_0 > 0 \wedge \dot{x}_0 > 0$	$]0; \frac{1}{2}\pi[\ \vee \ ]\pi; \frac{3}{2}\pi[$	$]\pi; \frac{3}{2}\pi[$
$x_0 > 0 \wedge \dot{x}_0 < 0$	$]\frac{1}{2}\pi; \pi[\ \vee \ ]\frac{3}{2}\pi; 2\pi[$	$]\frac{3}{2}\pi; 2\pi[$
$x_0 < 0 \wedge \dot{x}_0 < 0$	$]0; \frac{1}{2}\pi[\ \vee \ ]\pi; \frac{3}{2}\pi[$	$]0; \frac{1}{2}\pi[$
$x_0 < 0 \wedge \dot{x}_0 > 0$	$]\frac{1}{2}\pi; \pi[\ \vee \ ]\frac{3}{2}\pi; 2\pi[$	$]\frac{1}{2}\pi; \pi[$
$x_0 > 0 \wedge \dot{x}_0 = 0$	$\frac{1}{2}\pi \ \vee \ \frac{3}{2}\pi$	$\frac{3}{2}\pi$
$x_0 < 0 \wedge \dot{x}_0 = 0$	$\frac{1}{2}\pi \ \vee \ \frac{3}{2}\pi$	$\frac{1}{2}\pi$
$x_0 = 0 \wedge \dot{x}_0 > 0$	$0 \ \vee \ \pi$	π
$x_0 = 0 \wedge \dot{x}_0 < 0$	$0 \ \vee \ \pi$	0
$x_0 = 0 \wedge \dot{x}_0 = 0$	undefined	undefined

The values in the second column give the value ranges for φ_0 according to (2.22). These value ranges for φ_0 are restricted to values from zero to 2π (one revolution). Taking, for instance, the first row ($x_0 > 0 \wedge \dot{x}_0 > 0$), the solution for φ_0 lies, according to (2.22), in one of the following value ranges: $]0; \frac{1}{2}\pi[$ or $]\pi; \frac{3}{2}\pi[$. Evaluating both value ranges with help of (2.23) and under the constraints of the first column, the second derivative of (2.23) is smaller than zero for the first value range ($]0; \frac{1}{2}\pi[$) and greater than zero for the second value range ($]\pi; \frac{3}{2}\pi[$). Therefore, the desired minimum of the work done by the control force is obtained with the second value range, $]\pi; \frac{3}{2}\pi[$, see last column of table 2.1. The same procedure can be performed for the other initial condition ranges.

The results of table 2.1 can be summarized by introducing the atan2-function, which is defined and illustrated in figure 2.4.

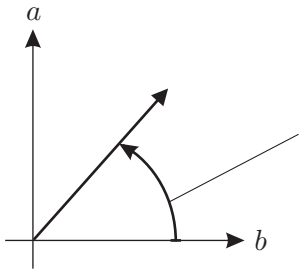

$$\operatorname{atan2}(a,b) = \begin{cases} \operatorname{atan}\left(\frac{a}{b}\right) & \text{if } b > 0 \\ \operatorname{atan}\left(\frac{a}{b}\right) + \pi & \text{if } b < 0 \text{ and } a \geq 0 \\ \operatorname{atan}\left(\frac{a}{b}\right) - \pi & \text{if } b < 0 \text{ and } a < 0 \\ \frac{\pi}{2} & \text{if } b = 0 \text{ and } a > 0 \\ -\frac{\pi}{2} & \text{if } b = 0 \text{ and } a < 0 \\ \text{undefined} & \text{if } b = 0 \text{ and } a = 0 \end{cases}$$

Figure 2.4: atan2-function [26, 27]

The atan2-function is frequently used in the field of electrical engineering and is often referred to as four-quadrant inverse tangent, see e.g. [26, 27]. The output of the atan2-function has a value range from $-\pi$ to π. Thus, it provides a unique solution for $\varphi_{0,opt}$ within one revolution. With this atan2-function, the optimal initial angular position $\varphi_{0,opt}$ can be expressed as shown in the following equation:

$$\varphi_{0,opt} = \operatorname{atan2}(x_0\omega_n; \dot{x}_0) + \pi \qquad \text{for} \qquad \xi = 0 \tag{2.24}$$

If inherent damping is present, the angular velocity $\dot{\varphi}$ of the rotors is to be set equal to the damped natural circular frequency ω_d given in (2.25) [1, 23, 25].

$$\omega_d = \omega_n\sqrt{1-\xi^2} \tag{2.25}$$

Inherent damping is considered by inserting the inherent damping force into (2.17) and replacing ω_n by ω_d. This yields:

$$\ddot{x}(t) + 2\xi\omega_n\dot{x}(t) + \omega_n^2 x(t) = \mu_c r\omega_d^2 \cos(\omega_d t + \varphi_0) \tag{2.26}$$

The solution of (2.26) and its time derivative are given by

$$\begin{aligned} x(t) =& \mathrm{e}^{-\xi\omega_n t}\left[A_0\cos(\omega_d t) + B_0\sin(\omega_d t)\right] + \ldots \\ & \mu_c r\chi_1\left[2\chi_2\sin(\omega_d t + \varphi_0) + \cos(\omega_d t + \varphi_0)\right] \end{aligned} \tag{2.27}$$

$$\begin{aligned} \dot{x}(t) =& \mathrm{e}^{-\xi\omega_n t}\left[(-\xi\omega_n A_0 + \omega_d B_0)\cos(\omega_d t) - (\omega_d A_0 + \xi\omega_n B_0)\sin(\omega_d t)\right] + \ldots \\ & \mu_c r\omega_d\chi_1\left[2\chi_2\cos(\omega_d t + \varphi_0) - \sin(\omega_d t + \varphi_0)\right] \end{aligned} \tag{2.28}$$

whereas A_0, B_0, χ_1 and χ_2 are defined as:

$$A_0 = x_0 - \mu_c r\chi_1\left(2\chi_2\sin\varphi_0 + \cos\varphi_0\right) \tag{2.29}$$

$$B_0 = \frac{1}{\chi_2}\left(\frac{\dot{x}_0}{\xi\omega_n} + x_0\right) - \mu_c r\chi_1\left(\sin\varphi_0 + \frac{2-\xi^2}{\xi^2\chi_2}\cos\varphi_0\right) \tag{2.30}$$

$$\chi_1 = \frac{1-\xi^2}{4-3\xi^2} \qquad \chi_2 = \frac{\sqrt{1-\xi^2}}{\xi} \tag{2.31}$$

In [23, p. 65-77], the optimal initial angular position for $0 < \xi < 1$ was derived by minimizing the sum of the work done by the control force and the inherent damping force on the SDOF oscillator. This approach fails to produce a closed-form solution. However, for the particular initial conditions, $x_0 > 0$ and $\dot{x}_0 = 0$, a clearly defined optimal initial angular position was found [23, p. 69-70]. By using the atan2-function and performing the same procedure as done for the oscillator without inherent damping, the optimal initial angular position $\varphi_{0,opt}$ for oscillators with inherent damping can be written in a more compact form:

$$\varphi_{0,opt} = \operatorname{atan2}\left(-2\sqrt{1-\xi^2}, -\xi\right) \qquad \text{for} \qquad 0 < \xi < 1, x_0 > 0 \text{ and } \dot{x}_0 = 0 \tag{2.32}$$

In [23], the optimal initial angular position was derived by minimizing the sum of the work done by the control force and the inherent damping force. Here, an estimate for the optimal initial angular position is derived by minimizing solely the work done by the control force. This can be done by assuming that the effect of the control force on the motion of the SDOF oscillator is much larger than that of the inherent damping force. Furthermore, it is assumed that the control force is small enough such that it does not dictate the motion of the oscillator. With these assumptions, the velocity response of the SDOF oscillator of (2.28) becomes

$$\dot{x}_f(t) = \mathrm{e}^{-\xi\omega_n t}\left[(-\xi\omega_n A_0 + \omega_d B_0)\cos(\omega_d t) - (\omega_d A_0 + \xi\omega_n B_0)\sin(\omega_d t)\right] \tag{2.33}$$

and can be used to calculate the normalized work done by the control force on the oscillator. Forming the integral, as done before, gives (2.34)

$$\begin{aligned} W_c &= \mu_c r\omega_d^2 \int_0^{\frac{2\pi}{w_d}l} \dot{x}_f(t)\cos(\omega_d t + \varphi_0)\mathrm{d}t \\ &= \mu_c r\omega_n\xi\chi_1\left(\Xi_1\cos\varphi_0 + \Xi_2\sin\varphi_0\right)\left(1 - \mathrm{e}^{-2l\frac{\pi}{\chi_2}}\right) \end{aligned} \tag{2.34}$$

whereas Ξ_1 and Ξ_2 are given by

$$\Xi_1 = -\frac{\omega_n x_0}{\xi} + 2\dot{x}_0\chi_2^2 \qquad (2.35)$$
$$\Xi_2 = \frac{2\omega_n x_0 \chi_2}{\xi} + \dot{x}_0\chi_2$$

W_c of (2.34) can be seen as a fictitious work done by the control force on the SDOF oscillator.

Taking the derivative of (2.34) with respect to φ_0, setting this equal to zero and solving for the φ_0 gives (2.36).

$$\varphi_0 = \operatorname{atan}\left(\frac{\Xi_2}{\Xi_1}\right) \qquad (2.36)$$

This equation gives a closed-form solution for φ_0 as a function of the initial conditions of the SDOF oscillator and the damping ratio. As before, the solution for φ_0 repeats in π. To make the solution repeat in 2π, thus providing a unique solution within zero to 2π, the atan2-function is used. The solutions are shown in the following equation:

$$\varphi_{0,1} = \operatorname{atan2}\left(\Xi_2, \Xi_1\right) \qquad \varphi_{0,2} = \operatorname{atan2}\left(-\Xi_2, -\Xi_1\right) \qquad (2.37)$$

To check if the work done by the control force has a positive or negative peak, the second derivative of (2.34) with respect to φ_0 is formed, see (2.38).

$$\frac{\mathrm{d}^2 W_c}{\mathrm{d}\varphi_0^2} = \mu_c r \omega_n \xi \chi_1 \left(\Xi_1 \cos\varphi_0 + \Xi_2 \sin\varphi_0\right)\left(\mathrm{e}^{-2l\frac{\pi}{\chi_2}} - 1\right) \qquad (2.38)$$

By replacing φ_0 by $\varphi_{0,1}$ in (2.38) and by varying the initial conditions (x_0 and $\dot{x}_0$) and the damping ratio ($0 < \xi < 1$), it can be proven numerically that the second derivative of W_c is smaller than zero. Therefore, the work done by the control force is a maximum. The same procedure can performed using $\varphi_{0,2}$. However, in this case, the desired minimum is obtained. Using the assumptions made above, the estimated optimal initial angular position $\varphi_{0,opt,e}$ for SDOF oscillators with inherent damping equals $\varphi_{0,2}$. $\varphi_{0,2}$ of (2.37) can be rewritten, see the following equation:

$$\varphi_{0,opt,e} = \operatorname{atan2}\left(-\xi\dot{x}_0 - 2\omega_n x_0; \frac{\omega_n x_0}{\chi_2} - 2\xi\chi_2\dot{x}_0\right) \qquad (2.39)$$

The limit value of the optimal initial angular position for SDOF oscillators with inherent damping can be calculated for $\xi \to 0$ (SDOF oscillator without inherent damping) by:

$$\lim_{\xi\to 0}\varphi_{0,opt,e} = \operatorname{atan2}\left[\underbrace{-\xi\dot{x}_0}_{\to 0} - 2\omega_n x_0; \underbrace{\frac{\omega_n x_0 \xi}{\sqrt{1-\xi^2}}}_{\to 0} - 2\underbrace{\sqrt{1-\xi^2}}_{\to 1}\dot{x}_0\right] = \operatorname{atan2}\left(-\omega_n x_0; -\dot{x}_0\right) \qquad (2.40)$$

The limit value coincides with the value of (2.24). This is a possible indicator that $\varphi_{0,opt,e}$ provides a general solution for the optimal initial angular position for the SDOF oscillator with inherent damping under the influence of the TRD. However, as shown in the following paragraph, this is not true.

To compare the optimal initial angular position of (2.32), which was derived in [23] (within this derivation, the work done by the control force and the inherent damping force is minimized), with the estimate of (2.39), both functions were evaluated with respect to ξ for the particular initial conditions $x_0 > 0$ and $\dot{x}_0 = 0$, see figure 2.5/A.

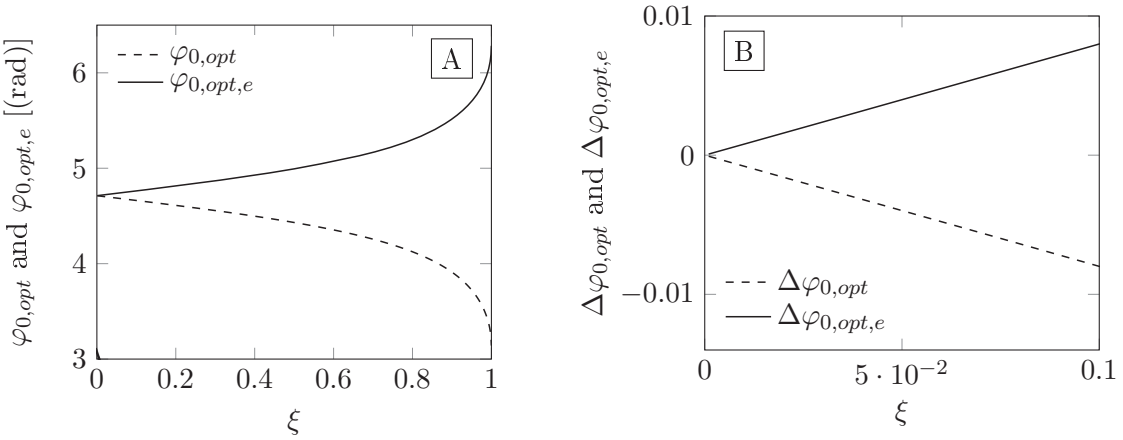

Figure 2.5: Optimal initial angular positions $\varphi_{0,opt}$ and its estimate $\varphi_{0,opt,e}$ with respect to the damping ratio ξ for the particular initial conditions $x_0 > 0$ and $\dot{x}_0 = 0$ and deviations from $3/2\pi$ according to (2.41)

For $\xi = 0$, $x_0 > 0$ and $\dot{x}_0 = 0$, $\varphi_{0,opt}$ of (2.32) and $\varphi_{0,opt,e}$ of (2.39) are equal to $3/2\pi$, see also (2.40). The curves differ as soon as $\xi > 0$ and the deviations increase with the damping ratio. Interestingly, the deviations from the value $3/2\pi$ are equal, but have different signs. An explanation for this was not found. However, by evaluating the controlled free vibration response, it can be checked numerically that with $\varphi_{0,opt,e}$ of (2.39), the work done by the control force becomes minimal whereas with $\varphi_{0,opt}$ of (2.32), the total work done by the control force and the inherent damping force becomes minimal. This validates the derivations of (2.32) and (2.39).

In figure 2.5/B, the deviations of the optimal initial angular position and its estimate from the value $3/2\pi$ normalized by 2π, see (2.41), are shown.

$$\Delta\varphi_{0,opt} = \frac{\varphi_{0,opt} - \frac{3}{2}\pi}{2\pi} \qquad \Delta\varphi_{0,opt,e} = \frac{\varphi_{0,opt,e} - \frac{3}{2}\pi}{2\pi} \tag{2.41}$$

For oscillators with small damping ratios ($\xi < 0.1$), see figure 2.5/B, the deviation $\Delta\varphi_{0,opt,e}$ from the value $3/2\pi$ is less than 1 %. Therefore, for SDOF oscillators with small inherent damping ratios ($0 < \xi < 0.1$), the influence of inherent damping on the optimal initial angular position is small for $x_0 > 0$ and $\dot{x}_0 = 0$. Consequently, (2.24) (optimal initial angular position for oscillators without inherent damping) also provides a good and better estimate than (2.39) for oscillators with small inherent damping ratios.

Furthermore, is seems that the assumption of taking only the free vibration response into consideration and minimizing the virtual work done by the control force seems to be an acceptable simplification. Note that doing this for the SDOF oscillator without inherent damping yields an optimal initial angular position equal to (2.24).

2.3 Derivation of target angular position

2.3.1 Single degree of freedom oscillator under particular initial conditions and the control force of the twin rotor damper

Figure 2.6/A shows the displacement $x(t)$ of the SDOF oscillator without inherent damping normalized by the initial displacement x_0 with $x_0 > 0$ and $\dot{x}_0 = 0$, see (2.18).

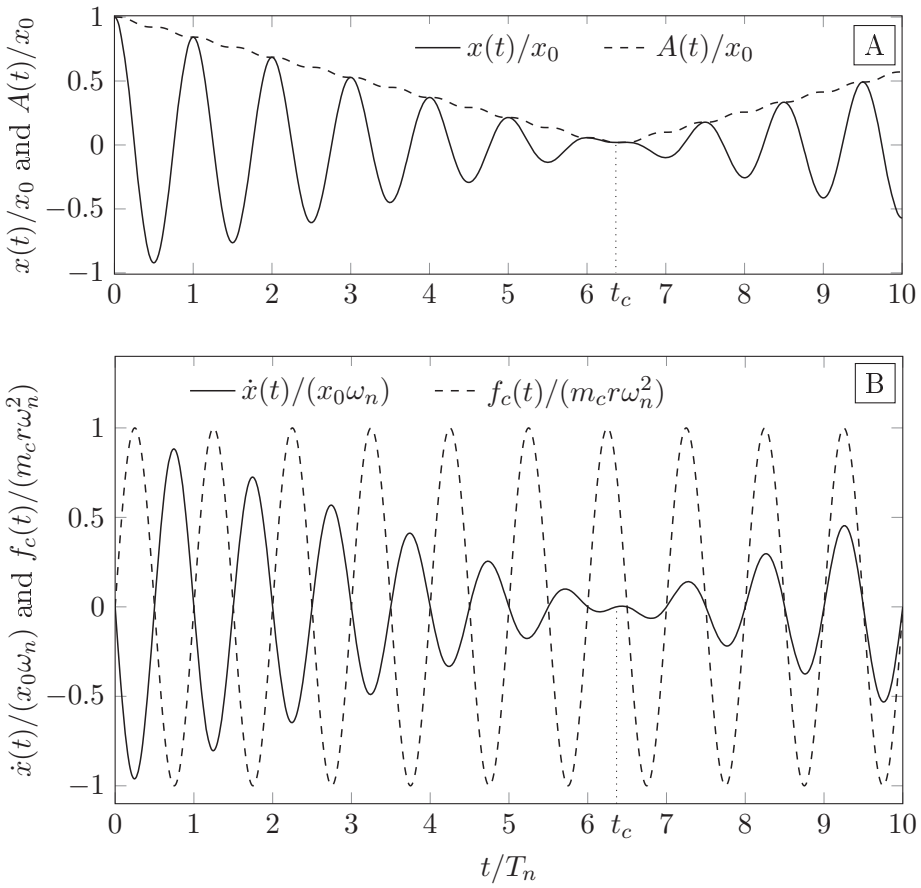

Figure 2.6: A: Normalized displacement $x(t)/x_0$ with normalized vibration amplitude $A(t)/x_0$, B: Normalized velocity $\dot{x}(t)/(\omega_n x_0)$ with normalized control force $f_c(t)/\left(m_c r\omega_n^2\right)$, both subfigures for $\mu_c r/x_0 = 0.05$, $x_0 > 0$, $\dot{x}_0 = 0$, $\varphi_0 = 3/2\pi$

The SDOF oscillator is only under the action of the control force of (2.16) with the optimal initial angular position according to (2.24). The time axis is normalized by the natural period length given by:

$$T_n = \frac{2\pi}{\omega_n} \tag{2.42}$$

As can be seen in figure 2.6, the vibration amplitude

$$A(t) = \sqrt{x(t)^2 + \left(\frac{\dot{x}(t)}{\omega_n}\right)^2} \tag{2.43}$$

decreases until t_c. After t_c, the vibration amplitude increases. t_c is given by

$$t_c = \frac{x_0}{\mu_c r\pi} \tag{2.44}$$

see [23, p. 49]. Note t_c is dimensionless.

Figure 2.6/B shows the corresponding velocity $\dot{x}(t)$ normalized by $(x_0\omega_n)$, see (2.19), and the corresponding control force. Up to t_c, the velocity and the control force have different sign. After t_c, they have the same sign. Therefore, the SDOF oscillator is damped until t_c, after which it is re-excited.

To prevent the re-excitation after t_c, the TRD must depart from the continuous rotation mode. This can be done, for instance, by turning the TRD off once the vibration amplitude falls below a lower vibration-amplitude threshold and back on once the vibration amplitude exceeds a higher vibration-amplitude threshold. This method and two further methods to prevent re-excitation are studied in section 2.5 and 2.9, respectively.

As needed later, an estimate envelope line connecting the positive peaks for $t < t_c$ can be calculated according to (2.45), which can be derived from (2.18), see also [23, p. 50]

$$x_p(t) = \sqrt{x_0^2 + \left(\frac{\dot{x}_0}{\omega_n}\right)^2} - \frac{1}{2}\mu_c r \omega_n t \tag{2.45}$$

It was assumed that the optimal initial angular position according to (2.24) is used. The line of (2.45) provides the exact line for the particular initial conditions $x_0 > 0$ and $\dot{x}_0 = 0$, whereas it is an approximation for all other cases.

Figure 2.7/A shows the displacement of the SDOF oscillator including inherent damping calculated according to (2.27) with the vibration amplitude according to (2.46) and with $x(t)$ and $\dot{x}(t)$ of (2.27) and (2.28).

$$A(t) = \sqrt{x(t)^2 + \left(\frac{\dot{x}(t)}{\omega_d}\right)^2} \tag{2.46}$$

The time axis is normalized by the damped period length, T_d, given in (2.47).

$$T_d = \frac{2\pi}{\omega_d} \tag{2.47}$$

As before, the particular initial conditions, $x_0 > 0$ and $\dot{x}_0 = 0$, are assumed. Furthermore, the SDOF oscillator is only under the action of the control force (right-hand side of (2.26)) with the optimal initial angular position of according to (2.32). Figure 2.7/B shows the velocity according to (2.28) and the control force. As for the SDOF oscillator without inherent damping, up to a certain time-point, the vibration amplitude given in (2.46) decays. The decay is due to the inherent damping and the control force of the TRD. After this time-point, the motion is re-excited by the TRD. The time-point at which the vibrations nearly come to rest can also be calculated for SDOF oscillators with inherent damping. However, the calculation is quite complex and not needed for further derivations, therefore, not presented.

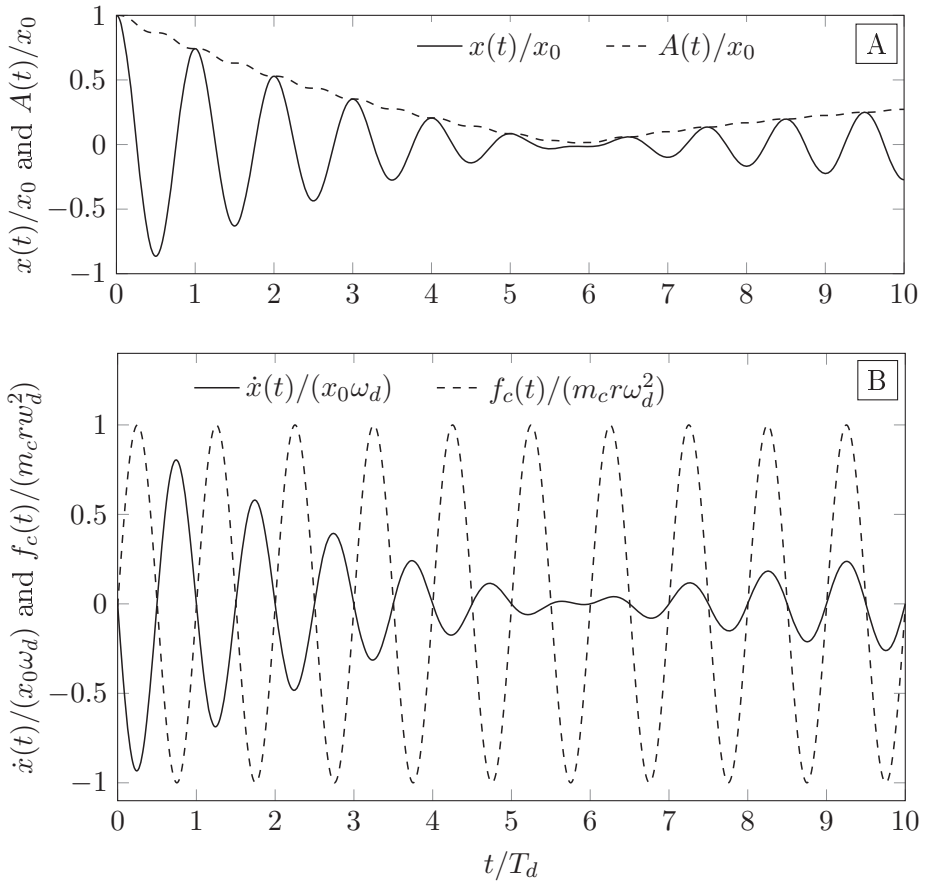

Figure 2.7: A: Normalized displacement $x(t)/x_0$ with normalized vibration amplitude $A(t)/x_0$ according to (2.46), B: Normalized velocity $\dot{x}(t)/(x_0\omega_d)$ with control force $f_c(t)/\left(m_c r\omega_d^2\right)$, both subfigures for $\mu_c r/x_0 = 0.03$, $\xi = 0.03$, $x_0 > 0$, $\dot{x}_0 = 0$, φ_0 according to (2.32)

2.3.2 Difference between angular rotor position and vibration phase

To describe the vibration progression within a single period, two additional states

$$\psi(t) = \operatorname{atan2}\left(x(t); \frac{\dot{x}(t)}{\omega_n}\right) \tag{2.48}$$

$$\psi^*(t) = \operatorname{atan2}\left(\dot{x}(t); \frac{\ddot{x}(t)}{\omega_n}\right) \tag{2.49}$$

are introduced. These states describe the vibration process as indicated in figure 2.8 [28].

The atan2-function allows for the description of a full vibration period. The values of $\psi(t)$ and $\psi^*(t)$ are restricted to values between zero and 2π. Henceforth, $\psi(t)$ and $\psi^*(t)$ will be referred to as vibration phase. The lengths of the vectors, $A(t)$ and $A^*(t)$, are used to indicate the vibration amplitude. $A(t)$ is measured in m and was introduced in (2.43). For $\xi = 0$, $A^*(t)$ is given by

$$A^*(t) = \sqrt{\dot{x}(t)^2 + \left(\frac{\ddot{x}(t)}{\omega_n}\right)^2} \tag{2.50}$$

and is measured in m/s.

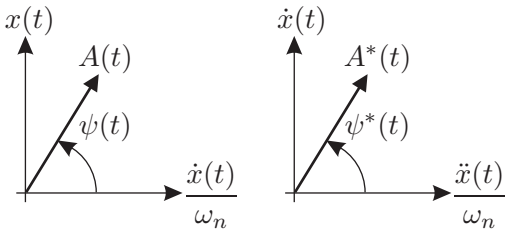

Figure 2.8: Vibration phases and vibration amplitudes

Considering free vibrations without inherent damping, the vectors of figure 2.8 would rotate counterclockwise with the natural circular frequency of the SDOF oscillator and a constant length. If inherent damping is present, the vibration amplitude would decay exponentially in time.

Assuming the control force of the TRD and the motion of the SDOF oscillator is as shown in figure 2.6, the vectors $A(t)$ and $A^*(t)$ decrease in length until the time-point t_c. Once t_c is reached, the vectors will increase in length. Additionally, the vectors will not rotate with an angular velocity equal to the natural circular frequency ω_n. This is due to the effect that the control force has on the motion of the SDOF oscillator. The variation of the angular velocity, $\dot{\psi}(t)$ and $\dot{\psi}^*(t)$, from the natural circular frequency is larger, the smaller the vibration amplitudes become. The amplitude of the control force is constant in the continuous rotation mode, whereas the system forces decrease with the vibration amplitudes. This leads to the increased influence of the control force on vibrations with small amplitudes.

Taking inherent damping into consideration, ω_n is replaced by ω_d. Doing this gives the vibration amplitudes, $A(t)$ and $A^*(t)$, for SDOF oscillators with inherent damping, see (2.51).

$$A(t) = \sqrt{x(t)^2 + \left(\frac{\dot{x}(t)}{\omega_d}\right)^2} \qquad A^*(t) = \sqrt{\dot{x}(t)^2 + \left(\frac{\ddot{x}(t)}{\omega_d}\right)^2} \tag{2.51}$$

The vibration phases, $\psi(t)$ and $\psi^*(t)$, are calculated analogously, see (2.52).

$$\psi(t) = \operatorname{atan2}\left(x(t); \frac{\dot{x}(t)}{\omega_d}\right) \qquad \psi^*(t) = \operatorname{atan2}\left(\dot{x}(t); \frac{\ddot{x}(t)}{\omega_d}\right) \tag{2.52}$$

To build up a relation between the motion of the SDOF oscillator and the angular position of the rotors, two new state variables, the phase differences, $\alpha(t)$ and $\alpha^*(t)$, are introduced:

$$\alpha(t) = \varphi(t) - \psi(t) \qquad \alpha^*(t) = \varphi(t) - \psi^*(t) \tag{2.53}$$

These variables represent the phase differences between the angular positions of the rotors and the vibration phases.

As the angular position of the rotors and the vibration phases of the SDOF oscillator both have a value range from zero to 2π, the phase differences inherit a range from -2π to 2π. This can be derived from (2.53). Adding or subtracting integer multiples of 2π will neither have an impact on the vibration phases nor on the angular position of the rotors. This is due to the properties of rotational motion allowing for the use of the same mathematical operations for the phase difference. Therefore, the phase difference $\alpha(t)$ and $\alpha^*(t)$ are restricted to values between zero and 2π.

Figure 2.9 shows the phase differences belonging to figure 2.6 [28].

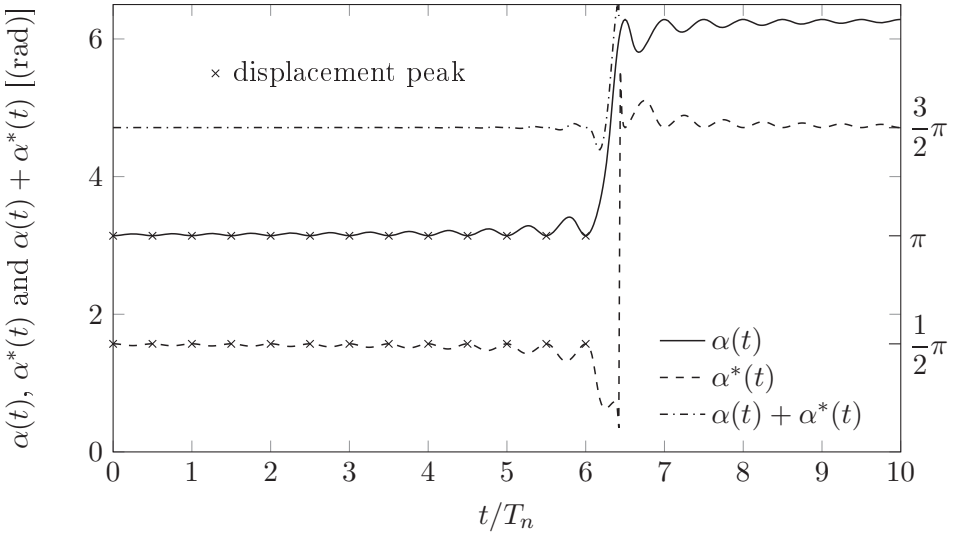

Figure 2.9: Phase differences according to (2.53) and sum of phase differences belonging to figure 2.6

Figure 2.9 shows the phase differences to achieve optimal performance (according to the minimization of the work done by the control force, see subsection 2.2.2). For $t < t_c$, these phase differences can be approximated by the constant values of $\alpha(t) \approx \pi$ and $\alpha^*(t) \approx \pi/2$. As can be seen in figure 2.9, at the time-point t_c, the phase differences, $\alpha(t)$ and $\alpha^*(t)$, jump to approximately $3/2\pi$ and 2π. At this instant, the TRD switches from positive active damping to negative active damping (excitation).

Assuming $\alpha(t)$ and $\alpha^*(t)$ are the constant values, π and $\pi/2$, the deviation from the values needed to achieve optimal damping performance is relatively small. This justifies the assumption that the values are considered as constants until t_c. From figure 2.9, it becomes evident that the phase differences coincide with the constant values each time a (negative or positive) displacement peak occurs. However, the deviations from the assumed constant values are the larger, the smaller the vibration amplitudes are. This is due to the increased influence of the control force on the motion of the SDOF oscillator for smaller vibration amplitudes. Additionally, the differences between the approximated constant values for $\alpha(t)$ and $\alpha^*(t)$ and their actual values are approximately equal to each other; however, they have different signs. Therefore, the sum of the phase differences $\alpha(t)+\alpha^*(t)$ is also computed and shown in figure 2.9. For the computation of the sum, $\alpha(t) + \alpha^*(t)$, a value range from zero to 4π must be considered. This must be done as both $\alpha(t)$ and $\alpha^*(t)$ inherit a value range from zero to 2π. The values oscillate close to the constant value $3/2\pi$ for $t < t_c$ and jump to $2\pi + 3/2\pi$ at $t = t_c$. This is not shown in figure 2.9 due to the scaling of the vertical axis. It can be seen clearly that the deviations of the sum of the phase differences from the constant value $3/2\pi$ for $t < t_c$ are significantly smaller than the deviations of the individual phase differences from their constant values.

Considering inherent damping, the phase differences are calculated analogously; however, the phases of (2.52) are used. These phase differences are shown in figure 2.10 belonging to figure 2.7 [28].

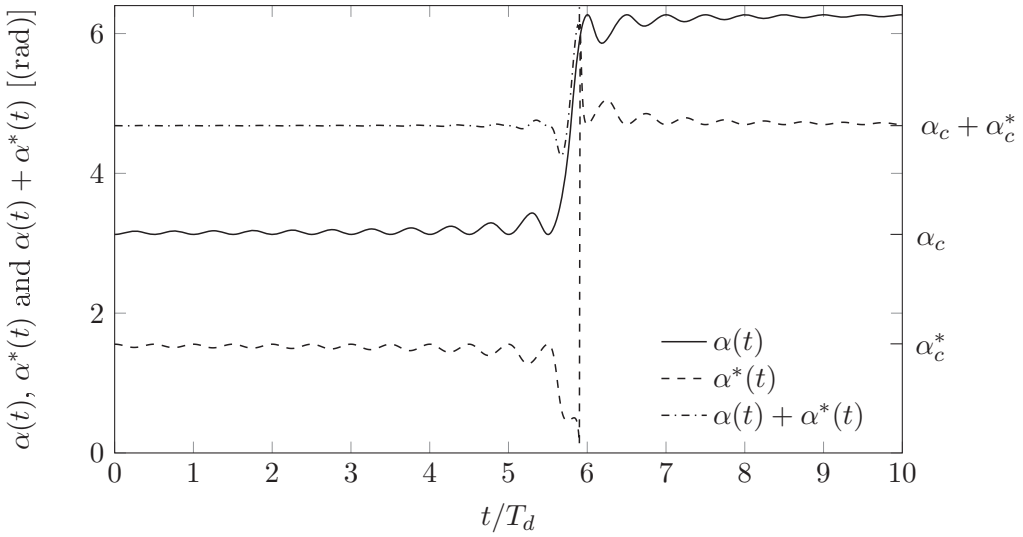

Figure 2.10: Phase differences according to (2.53) and sum of phase differences belonging to figure 2.7

It can be seen from figure 2.10 that the phase differences $\alpha(t)$ and $\alpha^*(t)$ also jump at t_c by approximately π. Similar to SDOF oscillators without inherent damping, at this instant, the control force switches from positive active damping to negative active damping, see figure 2.7. It is assumed again that $\alpha(t)$ and $\alpha^*(t)$ are constant values for $t < t_c$. These constant values can be computed by calculating the phase differences for $t = 0$. Considering the initial conditions $x_0 > 0$ and $\dot{x}_0 = 0$ and (2.32), the constant values, $\alpha_c(\xi)$ and $\alpha_c^*(\xi)$ are given in the following equation.

$$\alpha_c(\xi) = \operatorname{atan2}\left(-2\sqrt{1-\xi^2}, -\xi\right) - \frac{\pi}{2} \qquad \alpha_c^*(\xi) = \operatorname{atan2}\left(-2\sqrt{1-\xi^2}, -\xi\right) - \pi \quad (2.54)$$

The equations of (2.54) are also valid for SDOF oscillators without inherent damping, see figure 2.9. This can be shown by evaluating (2.54) for $\xi = 0$.

Considering the sum of the phase differences, $\alpha(t) + \alpha^*(t)$, in figure 2.10, it jumps from the approximated value $\alpha_c + \alpha_c^*$ to approximately $\alpha_c + \alpha_c^* + 2\pi$, which is not shown due to the scaling of the vertical axis.

In figure 2.11 and 2.12, the phase differences are shown for two vibration periods under positive active damping ($t < t_c$) with different damping ratios [28].

The vertical axes are scaled differently than in the previous figures.

It becomes evident that the phase differences coincide with the constant values of (2.54) each time a displacement peak occurs. The deviation from the constant values α_c and α_c^* is larger, the higher the damping ratio ξ. Moreover, the deviations increase with smaller vibration amplitudes, which can be explained, as before, by the higher influence of the control force on the motion. It also becomes apparent that the absolute value of the deviation of $\alpha(t)$ and $\alpha^*(t)$ from the constant values of α_c and α_c^* are approximately equal with opposite signs, see figure 2.11 and 2.12.

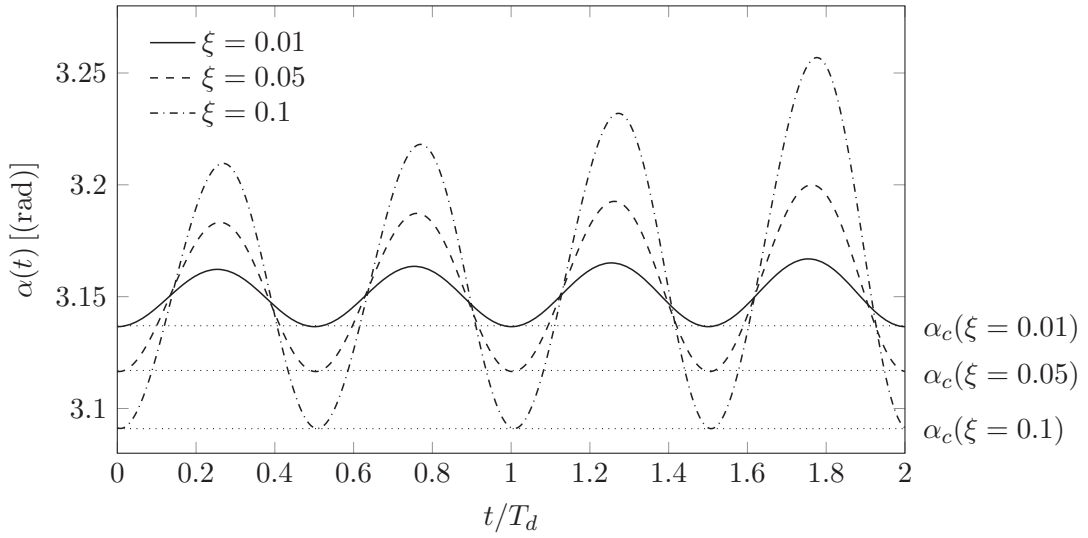

Figure 2.11: Phase difference $\alpha(t)$ for several damping ratios ξ, φ_0 according to (2.32) with $\mu_c r/x_0 = 0.03$, $x_0 > 0$ and $\dot{x}_0 = 0$

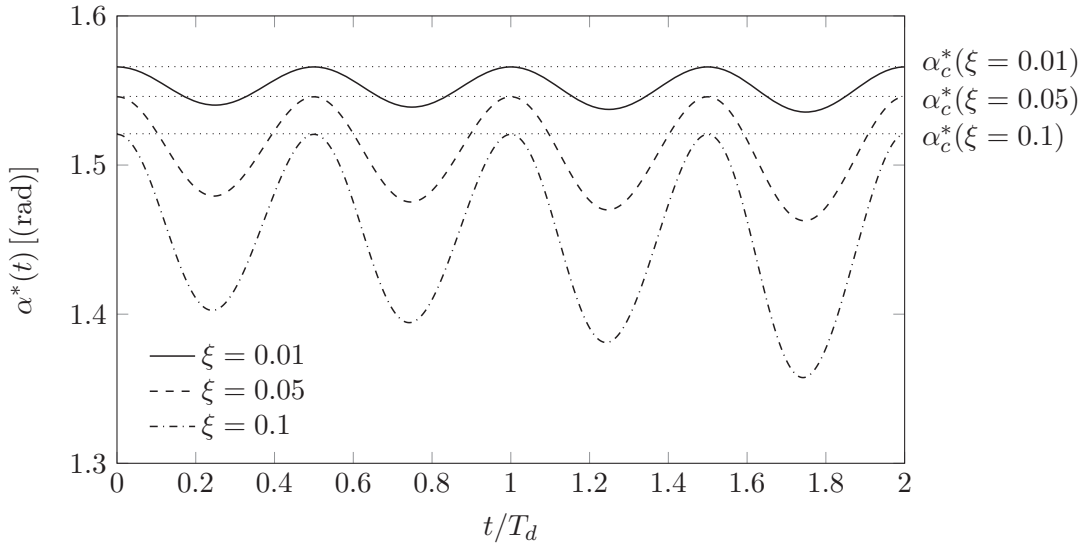

Figure 2.12: Phase difference $\alpha(t)$ for several damping ratios ξ, φ_0 according to (2.32) with $\mu_c r/x_0 = 0.03$, $x_0 > 0$ and $\dot{x}_0 = 0$

2.3.3 Target angular position and state space representation

To derive the target angular position, it is illustrative to use a state space representation. This will be done with the help of the phase difference $\alpha(t)$ without inherent damping. $\psi(t)$ is seen once in the left subfigure of figure 2.8 and twice in figure 2.13.

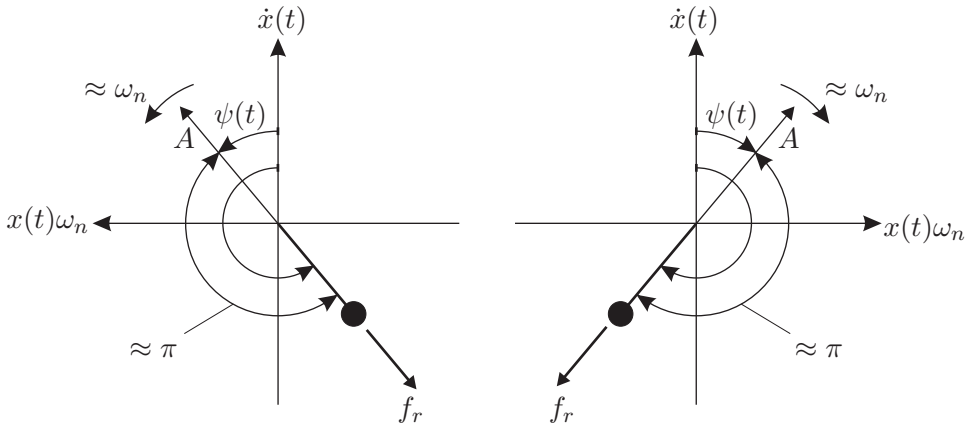

Figure 2.13: Analysis in a state space [24]

In figure 2.13, it needs to be taken into consideration that the direction of the horizontal axis in the left and right subfigure differ. Therefore, the vibration phase $\psi(t)$ rotates clockwise in the right subfigure, whereas in the left subfigure counterclockwise. In subsection 2.3.2, it was shown that for optimal damping performance, the difference between the angular position of the rotors $\varphi(t)$ and the vibration phase $\psi(t)$ is approximately constant. With this information, it is now possible to calculate a target angular position, $\varphi_t(t)$, for the rotors at each time-point. This can be done by adding the approximately constant phase difference to the vibration phase, see (2.55) in which $\psi(t)$ is substituted by (2.48).

$$\varphi_t(t) = \operatorname{atan2}\left(x(t); \frac{\dot{x}(t)}{\omega_n}\right) + \pi \tag{2.55}$$

The vibration phase $\psi(t)$ can be obtained by measuring the displacement and the velocity continuously. Alternatively, observers can be used. Further comments are given in subsection 2.6.2.

Under the assumption that the angular position $\varphi(t)$ equals the target angular position $\varphi_t(t)$ (this can be realized by a controller which 'perfectly' tracks the target angular position) the target angular position defines the direction of the radial forces f_r. Now taking both subfigures in figure 2.13 into consideration, it can be seen that the force components in $\dot{x}(t)$-direction superimpose such that the resultant always is in anti-phase to the velocity $\dot{x}(t)$ of the SDOF oscillator.

Due to the influence of the radial forces on the motion of the SDOF oscillator, the first time derivative of the phase of vibration $\dot{\psi}(t)$ is no longer constant, but only approximately the natural frequency ω_n. The more influence the control force has on the motion, the larger the deviation of $\dot{\psi}(t)$ from ω_n will become. A target angular position can be computed analogously with the vibration phase $\psi^*(t)$, see (2.56).

$$\varphi_t^*(t) = \psi^*(t) + \frac{1}{2}\pi \tag{2.56}$$

For SDOF oscillators with inherent damping, the target angular position can be derived analogously, see (2.57) with $\alpha_c(\xi)$ and $\alpha_c^*(\xi)$ given in (2.54).

$$\varphi_t(t) = \psi(t) + \alpha_c(\xi) \qquad \varphi_t^*(t) = \psi^*(t) + \alpha_c^*(\xi) \tag{2.57}$$

As can be seen from figure 2.9, the deviations of $\alpha(t)$ and $\alpha^*(t)$ from their constant values are equal with opposite signs. To produce a more durable, constant value, the phase differences are added together and the target angular position $\varphi_{t,s}$ is calculated, see (2.58); here durable is meant to indicate that the deviations from the constant values are smaller.

$$\varphi_{t,s}(t) = \frac{1}{2}\left(\psi(t) + \psi^*(t) + \frac{3}{2}\pi\right) \tag{2.58}$$

Doing the same for the SDOF oscillator with inherent damping yields (2.59).

$$\varphi_{t,s}(t) = \frac{1}{2}\left(\psi(t) + \psi^*(t) + \alpha_c + \alpha_c^*\right) \tag{2.59}$$

Note that when the target angular position is computed with (2.58) or (2.59), it must be considered that there are two possible target angular positions in the range from zero to 2π. This is because two vibration phases, each with a slope of approximately ω_n, are added together, producing a saw-tooth shaped curve with a slope of approximately $2\omega_n$, see (2.58). The factor 0.5 in (2.58) divides the slope in half so that the superimposed target angular velocity has the desired slope of approximately ω_n. This explains why two possible target angular positions in the range from zero to 2π are possible. One corresponds to damping, the other to excitation. To identify the target angular position corresponding to damping, the deviation from the target angular position according to (2.55) can be computed. If this deviation lies within the value range from $-\pi$ to π, it is the target angular position corresponding to damping; otherwise, it is the one corresponding to excitation, consequently π must be added.

Comparing (2.24) (optimal initial angular position for SDOF oscillators without inherent damping) with (2.55), it can be seen that (2.55) can also be obtained by replacing the initial conditions x_0 and $\dot{x}_0$ by continuous states $x(t)$ and $\dot{x}(t)$. This cannot be done for SDOF oscillators with inherent damping as a closed-form expression for the optimal initial angular position for $\xi > 0$ has not been found. However, it could be done using the approximate optimal angular position, see (2.39), which was obtained using a simplified derivation, see section 2.2.2. Doing the same substitutions ($x_0 \to x(t)$ and $\dot{x}_0 \to \dot{x}(t)$) gives an approximated target angular position $\varphi_{t,a}$, see (2.60).

$$\varphi_{t,a} = \operatorname{atan2}\left(-\chi_2\xi\dot{x}(t) - 2\chi_2\omega_n x(t); \omega_n x(t) - 2\chi_2^2\xi\dot{x}(t)\right) \tag{2.60}$$

2.3.4 Resulting target angular velocities

For the control algorithm of the continuous rotation mode, it is of particular interest to calculate the target angular velocity resulting from the target angular positions. The more constant the angular velocity of the rotors is, the lower the power demand on the actuators for accelerating and decelerating the rotors.

The target angular velocity is derived for figure 2.6 in the following. As it was assumed $\dot{\varphi} = \text{constant}$, the TRD was simulated to be in the continuous rotation mode. With help of (2.55), (2.56) and (2.58), the saw-tooth shaped target angular positions are calculated. Taking the time derivatives which is done numerically for brevity gives the target angular velocities $\dot{\varphi}_t(t)$, $\dot{\varphi}_t^*(t)$ and $\dot{\varphi}_{t,s}(t)$. These target angular velocities are shown in figure 2.14.

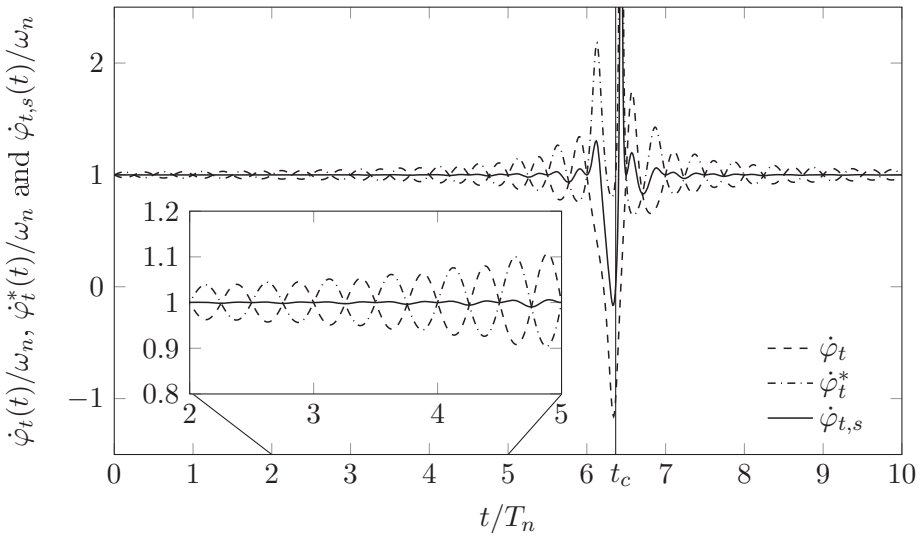

Figure 2.14: Target angular velocities $\dot{\varphi}_t(t)$, $\dot{\varphi}_t^*(t)$ and $\dot{\varphi}_{t,s}(t)$ computed according to (2.55), (2.56) and (2.58) belonging to figure 2.6

It becomes evident that the target angular velocities $\dot{\varphi}_t(t)$ and $\dot{\varphi}_t^*(t)$ oscillate in anti-phase with a frequency of approximately $2\omega_n$ and with approximately the same magnitude about the natural frequency ω_n. Furthermore, the magnitude of the oscillations increases with lower vibration amplitudes, see figure 2.14. When the vibration amplitude goes to infinity, the oscillations vanish. Conversely, when the vibration amplitude becomes small, the oscillations become unacceptably large. For $t/T_n > t_c$, the TRD excites the motion of the SDOF oscillator, therefore this time period is not of interest. Inspecting the detail showing the time interval in which the SDOF oscillator is under positive active damping of the TRD in figure 2.14, it can be seen that the oscillations of the target angular velocity are significantly smaller with the target angular position $\dot{\varphi}_{t,s}$ given by (2.58). The oscillations of the target angular velocities are a result of the deviation of the phase differences from their constant values.

The target angular velocities were computed analogously for figure 2.7, see figure 2.15. A very similar tendency can be seen; except, the oscillations are larger when inherent damping is present. Note that the approximated target angular position $\varphi_{t,a}(t)$ according to (2.60) nearly coincides with φ_t (first equation of (2.57)). For conciseness, these saw-tooth shaped curves are not plotted. Consequently, the resulting target angular velocities nearly coincide. This verifies the assumptions used for the derivation of the approximated optimal initial angular position at the end of subsection 2.2.2. Therefore, the corresponding target angular velocities nearly coincide, see legend of figure 2.15.

2.3.5 Computation of target angular position using the exact phase difference

Within this subsection, a computation method is proposed using the exact phase difference. This method is not used for the rest of this thesis, but it may be of interest for future theoretical works, see subsection 2.3.6. It was shown that the oscillations of the target angular velocity are due to the deviations of the phase difference from their constant values. To compensate for this, the exact phase difference is considered. This is done for the phase difference $\alpha(t)$ for SDOF oscillators without inherent damping.

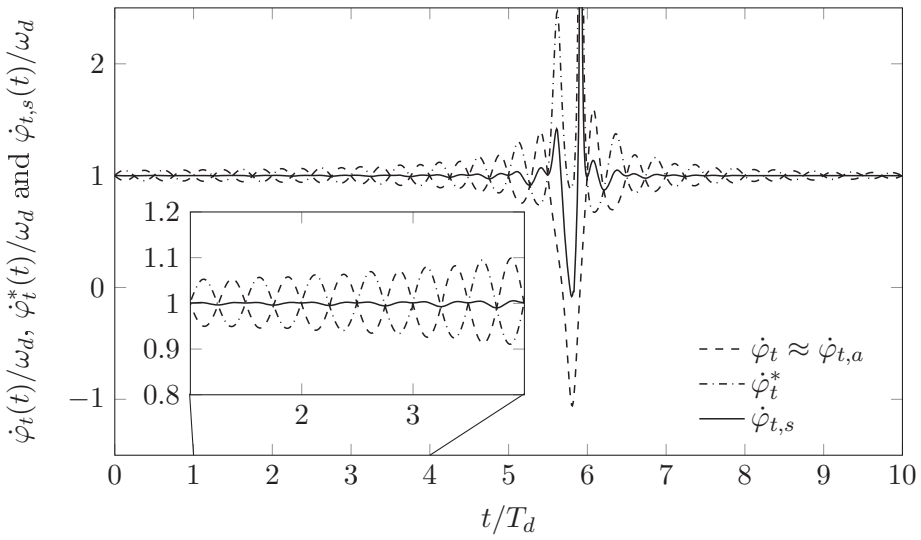

Figure 2.15: Target angular velocities $\dot{\varphi}_t(t)$, $\dot{\varphi}_t^*(t)$ and $\dot{\varphi}_{t,s}(t)$ computed according to (2.57) and (2.59) belonging to figure 2.7

Recalling $\alpha(t)$ and inserting (2.48) yields (2.61) with $\varphi_{0,opt}$ of (2.24).

$$\alpha(t) = \varphi(t) - \psi(t) = \varphi_{0,opt} + \omega_n t - \text{atan2}\left(x(t); \frac{\dot{x}(t)}{\omega_n}\right) \tag{2.61}$$

Solving this for $\varphi(t)$ and substituting $\varphi(t)$ by the exact target angular position, $\varphi_{t,e}(t)$, gives (2.62).

$$\varphi_{t,e}(t_r) = \underbrace{\varphi_{0,opt} + \omega_n t_r - \text{atan2}\left(x(t_r); \frac{\dot{x}(t_r)}{\omega_n}\right)}_{\text{consideration of exact phase difference}} + \psi(t) \tag{2.62}$$

in which t was replaced, in the terms considering the exact phase difference, by a reference time t_r.

The first three terms of (2.62) describe the exact phase difference with respect to the reference time. This was approximated before with π. The fourth term of (2.62) is calculated continuously. The phase difference $\alpha(t)$ coincides with the constant value π each time a displacement peak occurs, see figure 2.9. At these points in time, a computation of the exact phase difference can be started with respect to t_r. It provides the exact phase difference until $t_r = 0.5T_n$ at which the next displacement peak is expected. This procedure can be seen as a prediction for the exact phase difference. The following procedure may be used for a corresponding control algorithm.

The initial value of the exact phase difference is π, which is the approximated constant value for $\alpha(t)$. Once a displacement peak is detected, the following values needed for the computation of the exact phase difference are reset:

$$t_r = 0 \qquad x_0 = x(t) \qquad \dot{x}_0 = 0 \qquad \varphi_{0,opt} = \frac{3}{2}\pi \tag{2.63}$$

$\mu_c r$ and ω_n are assumed as known constants. The target angular position $\varphi_{t,e}(t)$ can then be computed with help of (2.18), (2.19) and (2.62) as a function of the running time variable t_r and with $\psi(t)$.

Due to an excitation force or model uncertainties (e.g. in m_c or m), the actual period length can be shortened or elongated. In these cases, the next displacement peak occurs before or after the time-point $t = 0.5T_n$. Due to the proposed control algorithm, the exact phase difference would jump from its current value to π as t_r is set to zero when a displacement peak occurs. If the period length is shortened, the phase difference jumps to the value π, see dotted arrow in figure 2.16 indicated with ①.

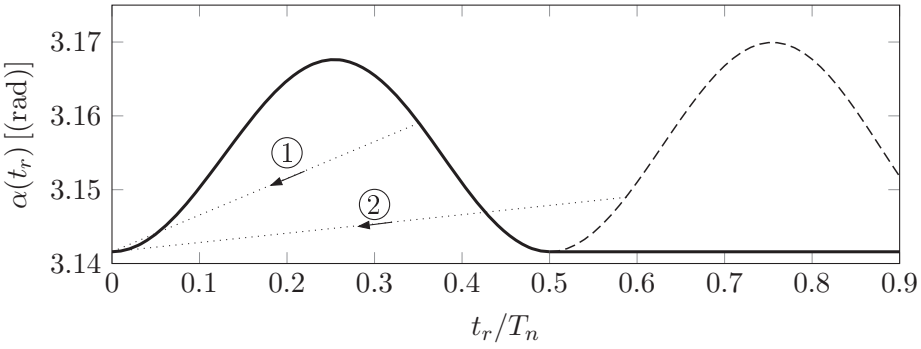

Figure 2.16: Discontinuities in target angular position

These discontinuities can be avoided if the displacement peak occurs at $t_r > 0.5T_n$ by approximating the phase difference with π for $t_r > 0.5T_n$. Then, the target angular position is computed as given by

$$\varphi_{t,e}(t) = \left[\varphi_{0,opt} + \omega_n t_r - \text{atan2}\left(x(t_r); \frac{\dot{x}(t_r)}{\omega_n}\right)\right] \text{rect}\left(\frac{2\,(t_r - 0.25T_n)}{T_n}\right) + ... \qquad (2.64)$$
$$\pi\epsilon(t_r - \frac{T_n}{2}) + \psi(t)$$

in which rect is the rectangular function operator and ϵ the step function operator. The rectangular function outputs the value one for $t_r < 0.5T_n$ and the value zero for $t_r \geq 0.5T_n$ in (2.64). The step function outputs the value zero for $t_r < 0.5T_n$ and one for $t_r \geq 0.5T_n$. Thus, the target angular position of (2.64) considers the exact phase difference for $t_r < 0.5T_n$ and the approximated phase difference for time values $t_r > 0.5T_n$. By doing this, discontinuities in the trajectory of the target angular position are avoided if the period length is elongated at the expense of variations in the target angular velocity. Discontinuities are not avoided if the period length is shortened.

Alternatively, the discontinuities can be avoided by building up a relation between the running time variable t_r and the vibration phase ψ. As t_r starts off at zero when a displacement peak occurs, whereas ψ starts off at the value $\pi/2$ (a fourth of a period) when a displacement peak occurs, the relation between t_r and ψ is as given in (2.65).

$$\frac{t_r(t)}{T_n} = \frac{\psi(t)}{2\pi} - \frac{1}{4} \qquad (2.65)$$

Doing so, t_r is not a time variable; instead, it is a function of ψ, which is continuously updated with help of (2.48) in which $x(t)$ and $\dot{x}(t)$ are also continuously updated. t_r still refers to the time passed since the last positive displacement peak occurred. Therefore, t_r is restricted to values between zero and T_n.

The control algorithm is discussed in the following with help of the block diagram of figure 2.17.

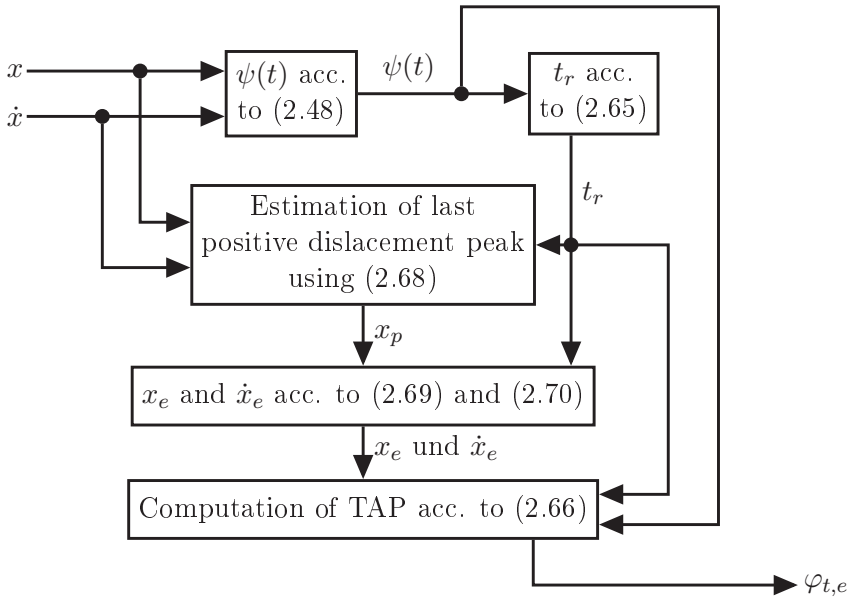

Figure 2.17: Control algorithm considering the exact phase difference

If the actual frequency of the SDOF oscillator changes, for instance due to an excitation force, the vibration phase changes accordingly and therefore t_r. To continuously consider the exact phase difference, (2.62) is recalled, see (2.66)

$$\varphi_{t,e}(t) = \frac{3}{2}\pi + \omega_n t_r - \operatorname{atan2}\left[x_e(t_r), \dot{x}_e(t_r)/\omega_n\right] + \psi(t) \tag{2.66}$$

in which the substitution

$$\varphi_{0,opt} \rightarrow \frac{3}{2}\pi \tag{2.67}$$

was performed and in which $x_e(t_r)$ and $\dot{x}_e(t_r)$ refer to the estimated displacement and velocity response for considering the exact phase difference. $x_e(t_r)$ and $\dot{x}_e(t_r)$ are derived in the following.

To estimate the magnitude of the last positive displacement peak continuously, (2.45) is reconsidered. To look backwards in time, t is replaced by $-t$ and the initial states are replaced by the continuous states ($x_0 \rightarrow x(t)$ and $\dot{x}_0 \rightarrow \dot{x}(t)$). Furthermore, as t_r refers to the time passed since the last positive displacement peak occurred, t is replaced by t_r, see (2.68).

$$x_p(t) = \sqrt{x(t)^2 + \left(\frac{\dot{x}(t)}{\omega_n}\right)^2} + \frac{1}{2}\mu_c r \omega_n t_r \tag{2.68}$$

(2.68) provides an estimate of the magnitude of the last positive displacement peak as a function of the actual states $x(t)$, $\dot{x}(t)$ and $\psi(t)$. To now calculate $x_e(t_r)$ and $\dot{x}_e(t_r)$, (2.18) and (2.19) are recalled, see (2.69) and (2.70)

$$x_e(t) = x_p(t)\cos\left(\omega_n t_r\right) + \frac{1}{2}\mu_c r\left[-\omega_n t_r \cos\left(\omega_n t_r\right) + \sin\left(\omega_n t_r\right)\right] \tag{2.69}$$

$$\dot{x}_e(t) = -x_p(t)\omega_n \sin\left(\omega_n t_r\right) + \frac{1}{2}\mu_c r \omega_n^2 t_r \sin\left(\omega_n t_r\right) \tag{2.70}$$

in which the substitutions of (2.71) were performed.

$$\varphi_0 \to \frac{3}{2}\pi \qquad x_0 \to x_p(t) \qquad \dot{x}_0 \to 0 \qquad t \to t_r \tag{2.71}$$

Figure 2.18 shows the target angular velocity $\dot{\varphi}_{t,e}$ corresponding to the target angular position of (2.66) belonging to figure 2.6. For comparison purposes, $\dot{\varphi}_t(t)$ from (2.55) is also shown.

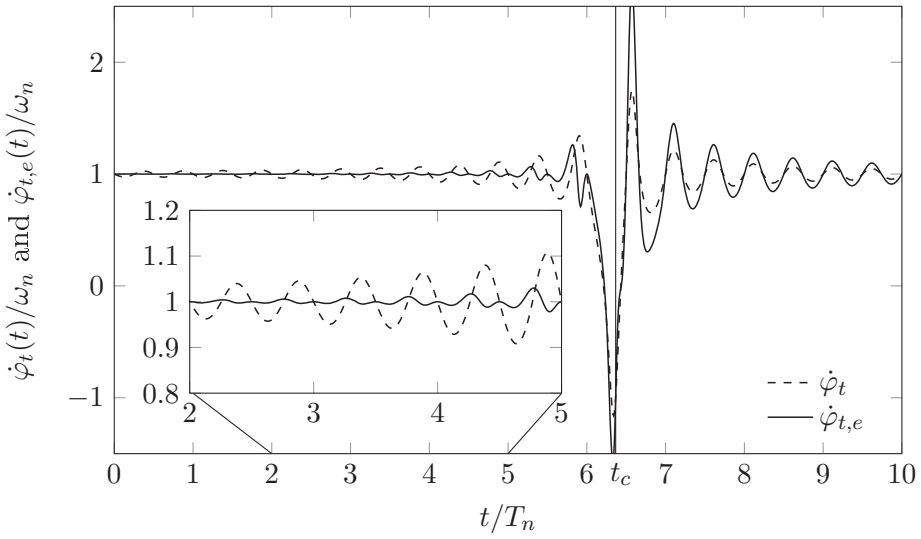

Figure 2.18: Target angular velocities $\dot{\varphi}_t(t)$ and $\dot{\varphi}_{t,e}(t)$ computed according to (2.55) and (2.66) belonging to figure 2.6

It becomes evident that the variations in the target angular velocity are reduced drastically by using the exact phase difference, see the detail of figure 2.18. The remaining oscillations in $\dot{\varphi}_{t,e}(t)$ are due to the approximation of the last displacement peak, see (2.68). To eliminate this negative effect, one can (temporarily) back-calculate (2.18) and (2.19) to determine the exact magnitude of the last positive displacement peak instead of back-calculating the approximation of (2.68). However, as this makes the computation even more elaborative and due to other reasons mentioned in the following discussion, these considerations are not further pursued. However, the principal approach presented here might be useful for further studies, see subsection 2.3.6.

2.3.6 Discussion

Summary

In subsection 2.3.3, target angular positions were derived by assuming particular initial conditions for the SDOF oscillator. Using the target angular positions, the control force of the TRD operates in the continuous rotation mode damping the motion of the SDOF oscillator. It was found that in order to achieve the desired damping action of the TRD, the phase difference between the angular position of the rotors and the vibration phase must be held constant. This holds for the case that the influence of the control force of the TRD is negligible. However, once the control force of the TRD influences the motion of the SDOF oscillator, the phase difference is not perfectly constant. It deviates slightly from a constant value. This results in variations in the target angular velocity which increase with the control force to system forces ratio and with the damping ratio of the SDOF oscillator. To cope with this negative effect, two methods were derived. One superimposes

the two phase differences; the other one uses the exact phase difference. For the first one, the acceleration is additionally required as an input. As the acceleration signal would become noisy when the SDOF oscillator is subjected to a stochastic excitation force, this method is not further pursued. The second method using the exact phase difference is computationally laborious, but might be an interesting approach if the rotors are affected by gravitational accelerations, requiring variations in the target angular velocities.

Performed numerical simulations
In [28], a study was performed in which the oscillator was subjected solely to particular initial conditions. Simulations were performed in which a closed-loop angular position control ensuring the tracking of the target angular position was applied. It was shown that with all target angular positions mentioned in the previous paragraph, the damping performance, which was measured with help of the decay rate in the displacement peaks, was nearly the same. However, using the target angular position derived using superposition, see (2.58) and (2.59), caused the smallest oscillations of the angular velocities. Note that within these simulations, the tangential forces were also considered, whereas for the comparison of figure 2.14, the tangential forces were neglected by simulating the TRD in an open-loop configuration with constant angular velocity.

Former theoretical work
The variations in the angular velocity of the rotors inspected in this section were previously investigated within [23, p. 301]. The control algorithm derived in [23] produces a target (angular) acceleration for the rotors. As, according to the author's knowledge, it is not possible to control rotor accelerations, this procedure was not further pursued. Furthermore, it is felt by the author of this work that an angular position control is required, resulting from the fact that the angular positions of the rotors determine the direction of the radial forces and therefore the phase of the control force. This enables the control force to be set in anti-phase to the velocity of the SDOF oscillator, see subsection 2.3.3.

Reducing variations in angular velocities using appropriate control strategies
The variations in the target angular velocity described in the first paragraph of this discussion can also be reduced by using appropriate control strategies which will be presented in subsection 2.5.3. Therefore, the superposition method and the one using the exact phase difference are not considered any further in this work.

Appropriate assumptions
From subsection 2.2.2, adequate results for the target angular positions of the rotors were obtained by assuming a free vibration response of the SDOF oscillator and minimizing the work the control force would perform on the motion; see subsection 2.2.2. From figure 2.10, it becomes evident that the deviations from the constant values $\alpha_c(t)$ and $\alpha_c^*(t)$ are relatively small when referring them to one revolution, 2π. The same applies to SDOF oscillators with small inherent damping ($0 < \xi < 0.1$), see figures 2.11 and 2.12. This shows that for the derivation of the target angular position, the effects of small inherent damping ($0 < \xi < 0.1$) can be neglected.

Therefore, the author felt that it is needed to emphasize two assumptions: First, small inherent damping can be neglected. Second, by assuming a free vibration response and minimizing the work that the control force would perform on the motion of the SDOF oscillator, adequate results for the target angular position are derived.

2.4 Comparison with conventional active mass damper

In this section, the TRD—operated in the continuous rotation mode—is compared to a conventional active mass damper (CAMD), see figure 2.19. The CAMD produces its control action by continuously accelerating and decelerating a control mass.

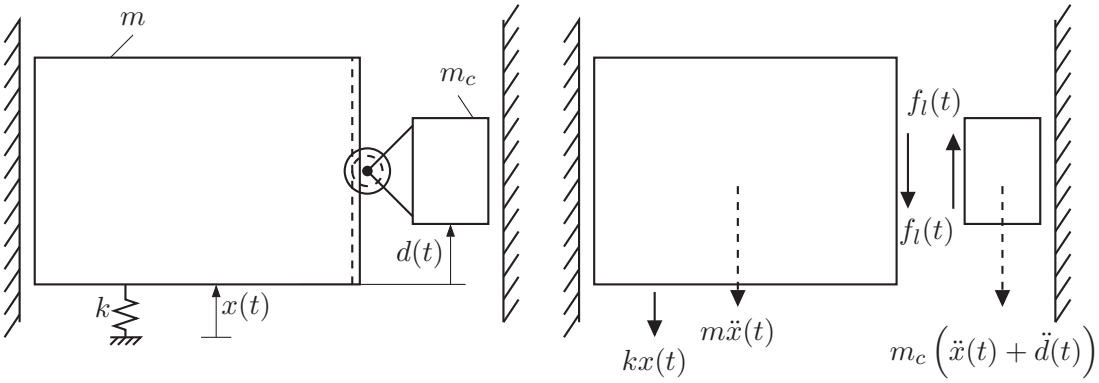

Figure 2.19: Active mass damper (left) and corresponding free body diagram (right) [24]

For such an active mass damper, the inertial forces generated by accelerating and decelerating the control mass are used for damping. These inertial forces can be set such that they oppose the velocity of the system to be damped [17]. The velocity of the system can be used as feedback, which makes the design of the control-loop simple in comparison to the design of the control-loop for the TRD. The assessment criteria used for the comparison done here are energy consumption and power demand. The term energy consumption refers to the electrical energy required by the actuators and will be defined for the TRD and the CAMD in the following.

A single vibration period is considered, inherent damping is neglected and the TRD is considered first. Note that for oscillators with inherent damping, identical derivations can be performed. However, such derivations are more complex and do not provide additional insight. With these assumptions, (2.6) is recalled and the control force of (2.16):

$$(m+m_c)\ddot{x}(t)+kx(t)=m_c r\omega_n^2\cos\left(\omega_n t+\varphi_0\right) \tag{2.72}$$

It is now assumed that the vibration amplitude remains constant. This is done by assuming that a fictive excitation force, which is not indicated in (2.72), neutralizes the control force of the TRD. Consequently, with the initial conditions

$$x_0>0 \qquad\qquad \dot{x}_0=0 \tag{2.73}$$

the displacement response is as given by:

$$x(t)=x_0\cos\left(\omega_n t\right) \tag{2.74}$$

The following derivations are also valid for different initial conditions. Taking the time derivative of (2.74) yields

$$\dot{x}(t)=-x_0\omega_n\sin\left(\omega_n t\right) \tag{2.75}$$

To achieve optimal damping performance, the optimal initial angular position φ_0 from (2.72) is set according to (2.24) for the initial conditions of (2.73). Consequently, the control force is:

$$f_c(t)=m_c r\omega_n^2\cos\left(\omega_n t-\frac{\pi}{2}\right)=m_c r\omega_n^2\sin\left(\omega_n t\right) \tag{2.76}$$

Inspecting (2.75) and (2.76), it can be seen from the sign that the control force, $f_c(t)$, is in anti-phase with the velocity of the SDOF oscillator. The power of a single rotor of the TRD is the product of the angular velocity of the rotors $\dot{\varphi}(t)$ and the moment $M(t)$, see figure 2.2. Considering that there are two rotors, the power $P_T(t)$ of one TRD-unit is:

$$P_T(t) = 2M(t)\dot{\varphi}(t) \tag{2.77}$$

An expression for $M(t)$ can be found by solving (2.14) for $M(t)$ and inserting (2.5) with the optimal initial angular position of (2.24) and the time derivative of (2.75). This yields:

$$M(t) = -0.5 m_c r x_0 r \omega_n^2 \left[\cos\left(\omega_n t\right)\right]^2 \tag{2.78}$$

Inserting (2.78) into (2.77) while considering that $\dot{\varphi}(t) = \omega_n$, gives the power of one TRD unit:

$$P_T(t) = -m_c r x_0 \omega_n^3 \left[\cos\left(\omega_n t\right)\right]^2 \tag{2.79}$$

This power is zero or negative for all t. Integrating $P_T(t)$, from t_l to t_u, gives the work done by the actuators of the TRD for an arbitrary time interval, see (2.80).

$$E_T = \int_{t=t_l}^{t=t_u} P_T(t)\mathrm{d}t \tag{2.80}$$

Before further discussing the power and work done by the TRD, the CAMD is considered. The CAMD is designed as in figure 2.19. For comparability, the control mass m_c is the same as for the TRD. As illustrated in figure 2.19, it is attached to the SDOF oscillator via a gear rack mechanism. The coordinate $x(t)$ defines the motion of the SDOF oscillator as before and the coordinate, $d(t)$, the relative motion between the SDOF oscillator and the control mass. The force $f_l(t)$ must be provided by an actuator to impose the desired relative motion $d(t)$, see free body diagram in figure 2.19.

Establishing the dynamic equilibrium of the SDOF oscillator and of the control mass, as indicated in the free body diagram in figure 2.19, gives the following equations:

$$m\ddot{x}(t) + kx(t) + f_l(t) = 0 \tag{2.81}$$

$$f_l(t) = m_c \left(\ddot{x}(t) + \ddot{d}(t)\right) \tag{2.82}$$

Inserting (2.82) into (2.81) and doing some rearrangements yields

$$\left(m + m_c\right)\ddot{x}(t) + kx(t) = f_{c,A}(t) \tag{2.83}$$

in which the term $f_{c,A}(t)$ is equal to $-m_c\ddot{d}(t)$ and represents the control force of the CAMD. As for the TRD, it is assumed that the control force of the CAMD is neutralized by a fictive excitation force, which is not indicated in figure 2.19. Therefore, the solution of (2.83) is as given in (2.74) and (2.75).

The velocity of the SDOF oscillator is used as feedback.

In the following, a stability check is performed. Taking the Laplace transform of (2.83) yields

$$\left(m + m_c\right)X(s)s^2 + kX(s) = F_{c,A}(s) \tag{2.84}$$

in which s is the Laplace variable. Note the initial conditions of (2.83) are neglected as they have no influence on the stability check. Using (2.8) and doing some rearrangements gives the transfer function $G_P(s)$ with $f_{c,A}(t)$ as input and $x(t)$ as output.

$$G_P(s) = \frac{X(s)}{F_{c,A}(s)} = \frac{1}{m + m_c} \frac{1}{s^2 + \omega_n^2} \tag{2.85}$$

Using the velocity $\dot{x}(t)$ as feedback and inspecting the closed-loop of figure 2.20 gives the controller

$$C(s) = K_P s \tag{2.86}$$

in which K_P is the constant feedback gain. The unit of K_P is Ns/m, which is dropped in the following. To bring the oscillator to rest, the reference input x_r is set to zero.

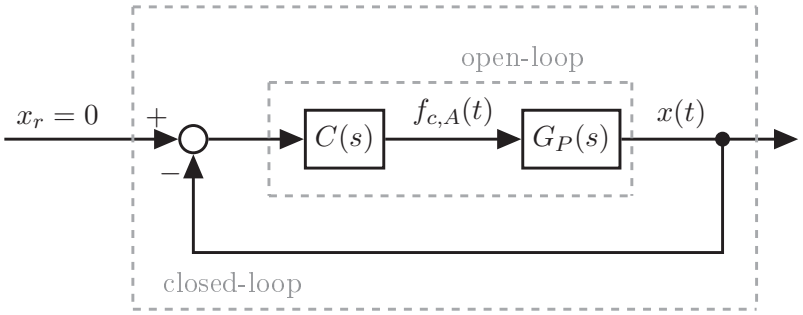

Figure 2.20: Closed-loop of CAMD

The controller produces the control force $f_{c,A}(t)$. By doing this, the dynamics of the actuator are neglected. The stability of the closed-loop in figure 2.20 is checked using a Root Locus plot. It suffices to show that the poles of the open-loop transfer function $C(s)G_P(s)$ lie in the left half plane. The Root Locus plot of $C(s)G_P(s)$ is shown in figure 2.21.

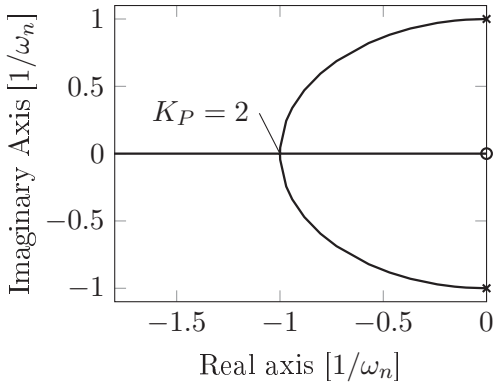

Figure 2.21: Root Locus of open-loop $C(s)G_P(s)$

In figure 2.21, the conjugate pole pair is indicated by crosses and the zero of the controller by a circle for $K_P = 0$. The zero does not change position if K_P is increased; it only changes the location of the poles, which determine the dynamics of the closed-loop.

If K_P is increased, the complex conjugate pole pair moves on a circular path towards the real axis. For $K_P = 2$, the poles meet on the real axis meaning that the oscillator is critically damped. Increasing K_P further, one pole will move towards the origin and the other towards minus infinity. Therefore, it is shown that the poles lie in the left half plane for all positive K_P, meaning that the closed-loop in stable.

Continuing to consider the closed-loop of the CAMD, which uses the velocity as feedback, the control force of the CAMD can also be written as follows

$$f_{c,A}(t) = -K_P \dot{x}(t) \tag{2.87}$$

in which the minus is due to the negative feedback, see figure 2.20. Inserting the velocity of (2.75) gives

$$f_{c,A}(t) = K_P x_0 \omega_n \sin(\omega_n t) \tag{2.88}$$

The control forces of the CAMD and the TRD are both sin-functions, see (2.76) and (2.88). To achieve equal damping performance, the control force amplitudes must coincide. This is done by setting:

$$K_P = \frac{m_c r \omega_n}{x_0} \tag{2.89}$$

Inserting (2.89) into (2.88) gives (2.90).

$$f_{c,A}(t) = m_c r \omega_n^2 \sin(\omega_n t) \tag{2.90}$$

This control force $f_{c,A}(t)$ is generated by imposing a relative acceleration $\ddot{d}(t)$, see right-hand side of (2.83) and the subsequent paragraph. Setting these equations equal, solving for $\ddot{d}(t)$ and integrating twice with respect to time gives the relative displacement imposed by the actuator of the CAMD to achieve equal damping performance, see (2.91).

$$d(t) = r \sin(\omega_n t) \tag{2.91}$$

Note that it was assumed that the control mass of the CAMD oscillates about its midpoint. Therefore, the integration constants are zero. Furthermore, from (2.91), it can be seen that the radius r of the TRD corresponds to half of the stroke of the CAMD; thus, comparability regarding size is guaranteed. Inserting the appropriate derivatives of (2.91) and (2.75) into (2.82) gives (2.92), which is the force provided by the actuator of the CAMD.

$$f_l(t) = -m_c \omega_n^2 \left[x_0 \cos(\omega_n t) + r \sin(\omega_n t) \right] \tag{2.92}$$

The power of the CAMD is given by

$$P_l(t) = f_l(t) \dot{d}(t) \tag{2.93}$$

Inserting the derivative of (2.91) and (2.92) into (2.93) gives (2.94).

$$P_l(t) = -m_c r \omega_n^3 \left\{ x_0 \left[\cos(\omega_n t) \right]^2 + \frac{1}{2} r \sin(2\omega_n t) \right\} \tag{2.94}$$

Integrating this over an arbitrary time interval

$$E_l = \int_{t=t_l}^{t=t_u} P_l(t) \mathrm{d}t \tag{2.95}$$

gives the work done by the actuator of the CAMD.

The work done by the actuators of the TRD and the actuator of the CAMD are shown in table 2.2 for certain time intervals. Considering the complete damping period ($t_l = 0$, $t_u = T_n$), it becomes evident that the work is equal. This proves that both damping devices achieve the same damping performance. It can also be seen that the TRD has a constant work rate within all considered time intervals, see table 2.2. This is in contrast to the CAMD, which has additional work terms. The sign of these terms is not constant, see second term in the square brackets of table 2.2. The additional work terms result in a larger power demand on the actuator of the CAMD and are for accelerating and decelerating the control mass. This can also be seen in figure 2.22 which shows the normalized required power of the TRD and the CAMD.

Table 2.2: Work done by the damping devices considering different time intervals [24]

t_l/T_n	t_u/T_n	$E_l/(m_c x_0 r \omega_n^2 \pi)$	$E_T/(m_c x_0 r \omega_n^2 \pi)$
0	0.25	$-[0.25 + 0.5x_0/(\pi r)]$	-0.25
0.25	0.50	$-[0.25 - 0.5x_0/(\pi r)]$	-0.25
0.50	0.75	$-[0.25 + 0.5x_0/(\pi r)]$	-0.25
0.75	1.00	$-[0.25 - 0.5x_0/(\pi r)]$	-0.25
0	1.00	-1.00	-1.00

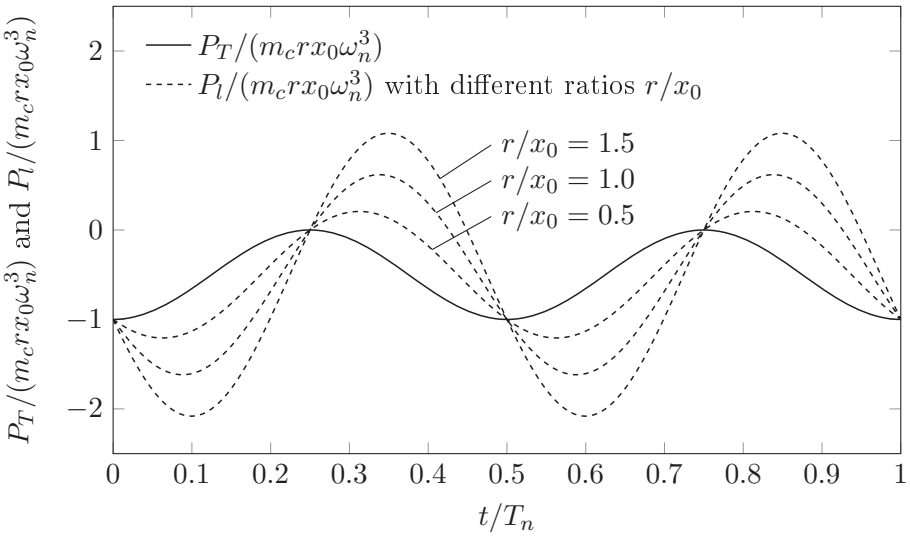

Figure 2.22: Comparison regarding power demand considering one vibration cycle, see (2.79) and (2.94) [24]

Note that both power demands are normalized equally. The required power for the TRD is negative for all t and independent from the ratio r/x_0. This is in contrast to the CAMD. The power demand of the CAMD depends on the ratio between its stroke $2r$ and the vibration amplitude, indicated by x_0. This dependency is illustrated in figure 2.22 for different ratios, r/x_0. If this ratio approaches zero, meaning that the stroke is large in comparison to x_0, the normalized power curves of the TRD and the CAMD coincide. However, the damping effect vanishes. The larger the ratio r/x_0, the higher the power demand of the CAMD becomes in comparison to the TRD.

To evaluate the magnitude of the power demands of both devices over one period, the root mean square value is calculated. The root mean square value of a signal $s(t)$ is calculated

by

$$\mathrm{rms}(s(t)) = \sqrt{\frac{1}{t_u - t_l}\int_{t_l}^{t_u} s(t)^2 \mathrm{d}t} \tag{2.96}$$

in which the integral from t_l to t_u is formed. The term 'signal' refers to a physical quantity (e.g. force, velocity, displacement) which varies in time.

Note that the powers derived above, see (2.79), (2.94) and figure 2.22, change in time, whereas the power demands derived in the following with (2.96) are scalar quantities describing the magnitude of the powers. As the powers of both devices, see (2.79) and (2.94), are periodic, it suffices to evaluate the power over one vibration period from $t_l = 0$ to $t_u = T_n$. Calculating the root mean square values of $P_T(t)$ and $P_l(t)$ and normalizing those equally by $m_c r \omega_n^3 x_0$ gives the following expressions:

$$\frac{\mathrm{rms}(P_T)}{m_c r \omega_n^3 x_0} = \frac{1}{4}\sqrt{6} \tag{2.97}$$

$$\frac{\mathrm{rms}(P_l)}{m_c r \omega_n^3 x_0} = \frac{1}{4}\sqrt{2}\sqrt{3 + \left(\frac{r}{x_0}\right)^2} \tag{2.98}$$

As can be seen from (2.98), the power of the CAMD does not only depend on m_c, r, ω_n and x_0; it additionally depends on the ratio r/x_0. The higher this ratio, the larger the power demand on the conventional active mass damper in comparison to the power demand of the TRD, which is constant, see (2.97). For $r/x_0 = 0$, the power demands of (2.97) and (2.98) are equal. The power demand benefit of the TRD over the CAMD increases the larger the ratio r/x_0 becomes.

Discussion

- Assuming that half the stroke of the CAMD equals x_0, meaning that $r/x_0 = 1$, the power demand of the CAMD is $\sqrt{2}/2 \approx 0.707$ according to (2.98). This is approximately 15.5 % more than that of the TRD ($(0.707 - 0.612)/0.612 \approx 0.155$).

- Using the CAMD, the control mass must be stopped and re-accelerated frequently. In contrast to this, the control masses of the TRD rotate with a nearly constant angular velocity. This type of motion leads to less mechanical wear. Therefore, another great advantage of the TRD is possibly the lower mechanical wear on its components in comparison to the mechanical wear of the CAMD. Furthermore, a rotational motion (required for the TRD) can usually be created more economically than a linear motion, which is another advantage of the TRD.

- Within the comparison of this section, it was assumed that the TRD operates in the continuous rotation mode. It must be mentioned that this mode of operation must somehow be reached and left. This requires additional power, which was not considered in this section. To reach and leave the continuous rotation mode, ramp-up and ramp-down trajectories are developed in subsection 2.5.2.

- A mono-frequent vibration was assumed. When the TRD is used for stochastically forced vibrations, additional angular accelerations are required to ensure the anti-phasing between the velocity of the SDOF oscillator and the control force of the TRD. Stochastically forced vibrations are treated in chapter 3.

2.5 On-off method

2.5.1 Introduction

In section 2.3, it was discussed that the SDOF oscillator is re-excited after the time-point t_c is reached, see figure 2.6. In [23], several methods were proposed to prevent the re-excitation. Using the on-off method, the TRD is turned off when the vibration amplitude falls below a lower vibration-amplitude threshold and it is turned back on again when another higher chosen vibration-amplitude threshold is exceeded. Therefore, to reach and leave the continuous rotation mode in an energy- and power efficient manner, ramp-up and ramp-down trajectories are developed in this section. Furthermore, a closed-loop angular position control is proposed and validated experimentally in this section.

A second possibility to prevent re-excitation was suggested in [23]. To achieve optimal damping performance, the control force of the TRD is set in anti-phase to the velocity of the SDOF oscillator. This can be achieved using a closed-loop angular position control ensuring that the rotors track the target angular position derived in section 2.3. By detuning the anti-phasing for smaller vibration amplitudes, the damping effect can be regulated. A control algorithm ensuring this is presented in subsection 2.9.2.

A third possibility to cope with the issue of re-excitation is the use of a second identical TRD unit [23]. When the vibration amplitudes are large, both TRD units jointly damp the motion. For small vibration amplitudes, the control forces of the TRD units are set in anti-phase such that the resultant force effect vanishes; thus, the SDOF is not re-excited. A control algorithm corresponding to this method is presented in subsection 2.9.3.

2.5.2 On-off method for the continuous rotation mode

Ramp-up process

The ramp-up process (RUP) starts when the rotors are set in motion from a certain starting angular position and ends when the rotors have firstly reached the desired angular velocity of the continuous rotation mode and secondly have the desired target angular position. For the derivation of the ramp-up trajectory design, inherent damping is not considered as it does not contribute to the understanding of the design principle. In order to describe the time during the RUP, an additional running time variable, t_1, is introduced. It is set to zero at the start of the RUP.

To derive an energy-efficient and power-efficient RUP, it is beneficial to introduce some energy parameters. The rotational energy stored in both rotors is described by

$$E_r(t) = 2\left(\frac{1}{2}J\dot{\varphi}(t)^2\right) \tag{2.99}$$

in which J is the rotational inertia of a single rotor. The factor of two in (2.99) comes from the fact that one TRD units entails two rotors. This energy is zero at the time-point $t_1 = 0$ as the rotors are at rest.

The RUP has a duration of T_{ru}. T_{ru} is a design variable for the ramp-up trajectory. During the RUP, rotational energy is transferred to the rotors. The energy needed for both rotors to reach the continuous rotation mode is $E_r(t_1 = T_{ru}) = J\omega_n^2$. This rotational energy can come either from the actuators driving the rotors or from the vibration energy of the

SDOF oscillator. The vibration energy, $E_v(t)$, stored in the SDOF oscillator is given by:

$$E_v(t) = \frac{1}{2}\left(m + m_c\right)\dot{x}(t)^2 + \frac{1}{2}kx(t)^2 \tag{2.100}$$

The vibration energy that is transferred into rotational energy for the rotors during the RUP is named $E_s(t_1 = T_{ru})$; likewise, the rotational energy that comes from the actuators is referred to as $E_a(t_1 = T_{ru})$. The energy values $E_s(t_1)$ and $E_a(t_1)$ are zero at the start of the RUP ($t_1 = 0$). (2.101) holds when the RUP is completed.

$$E_s(t_1 = T_{ru}) + E_a(t_1 = T_{ru}) = E_r(t_1 = T_{ru}) \tag{2.101}$$

To reduce the energy provided by the actuators during the RUP ($E_a(t_1 = T_{ru})$), the rotational energy coming from the SDOF oscillator ($E_s(t_1 = T_{ru})$) is maximized. To penalize the work done by the actuators, the cost function of (2.102) is applied

$$E_a(t_1) = 2\int_{t_1=0}^{t_1=T_{ru}} P_a(t_1)\mathrm{d}t_1 \tag{2.102}$$

in which $P_a(t)$ is the power of one actuator. In (2.102), positive as well as negative energy values are taken into account meaning that energy used for decelerating (braking) the rotors can be regained. However, this cannot be guaranteed in practice. For this reason, trajectories will also be developed with the assumption that all braking energy is lost. This results in a second cost function

$$E_a^+(t_1) = 2\int_{t_1=0}^{t_1=T_{ru}} P_a^+(t_1)\mathrm{d}t_1 \tag{2.103}$$

in which the plus sign indicates that only positive power values are taken into account.

To derive the RUP trajectory, it is illustrative to reconsider the motor equation, see (2.104) and figure 2.23. This figure shows all forces generating moments about the center of a single axis.

$$M(t) - \frac{1}{2}m_c r^2\ddot{\varphi}(t) + \frac{1}{2}m_c r\ddot{x}(t)\sin\varphi(t) = 0 \tag{2.104}$$

In figure 2.23, the moment generated by the rotational inertia $J\ddot{\varphi}(t)$ is replaced in (2.104) by $m_c r^2/2\ddot{\varphi}(t)$ by assuming the control masses as point masses ($J = m_c r^2/2$).

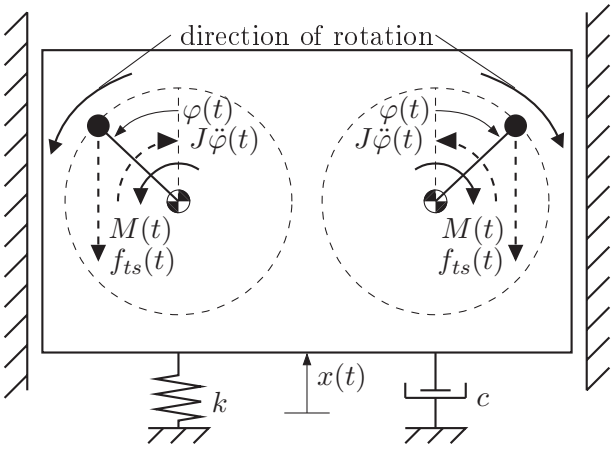

Figure 2.23: Forces generating moments about the center of axis

To make the RUP energy-efficient, the inertial forces induced by the translational acceleration of the SDOF oscillator

$$f_{ts}(t) = \frac{1}{2} m_c \ddot{x}(t) \tag{2.105}$$

are used in such a way that they aid the rotational motion of the rotors in the desired direction.

It is assumed that the SDOF oscillator exhibits large vibration amplitudes. This implies that the system forces dictate the motion of the SDOF oscillator during the RUP. This can be assumed because the TRD is turned on when the vibration amplitudes are large. Furthermore, to start with, it is assumed that the RUP begins once the acceleration of the SDOF oscillator $\ddot{x}(t)$ switches sign from minus to plus. Assuming additionally that $T_{ru} = 0.5T_n$ leads to an acceleration of the SDOF oscillator during the RUP of a half sine wave:

$$\ddot{x}(t_1) = x_{on}\omega_n^2 \sin(\omega_n t_1) \tag{2.106}$$

in which x_{on} is the amplitude of the displacement that corresponds to the vibration-amplitude threshold, A_{on}, at which the TRD is turned on. With the assumptions made above, it is guaranteed that the acceleration of the SDOF oscillator is positive for the duration of the RUP. Therefore, the moments induced by the forces $f_{ts}(t_1)$ are positive during the RUP and support the rotational motion of the rotors, see figure 2.23.

The initial conditions of the RUP are

$$\varphi(t_1 = 0) = \varphi_s \qquad \dot{\varphi}(t_1 = 0) = 0 \qquad \ddot{\varphi}(t_1 = 0) = 0 \tag{2.107}$$

in which φ_s is a free parameter referred to as the starting angular position.

The rotors are at rest at the start of the RUP. To reduce mechanical wear, any strong jerking motion of the rotors should be avoided. This can be done by setting the angular acceleration $\ddot{\varphi}(t)$ to zero at the beginning and end of the RUP. At the end of the RUP, the angular velocity of the rotors $\dot{\varphi}(t)$ is wanted to be equal to the natural frequency of the SDOF oscillator ω_n. Additionally, the angular position of the rotors is wanted to be equal to the target angular position for the continuous rotation mode; this position is obtained by inserting the conditions of the SDOF oscillator at the end of the RUP, $x(t_1 = T_{ru}) = 0$ and $\dot{x}(t_1 = T_{ru}) > 0$, resulting from (2.106), into (2.55). Therefore, the final conditions of the RUP are as shown in (2.108).

$$\varphi(t_1 = T_{ru}) = \pi \qquad \dot{\varphi}(t_1 = T_{ru}) = \omega_n \qquad \ddot{\varphi}(t_1 = T_{ru}) = 0 \tag{2.108}$$

Ramp-up trajectories, $\varphi_{ru}(t_1)$, are, to start with, generated using a five degree polynomial

$$\varphi_{ru}(t_1) = a_5 t_1^5 + a_4 t_1^4 + a_3 t_1^3 + a_2 t_1^2 + a_1 t_1 + a_0 \tag{2.109}$$

where a_i are the polynomial coefficients. The degree of the polynomial must be larger than or equal to five as there are six boundary conditions to be fulfilled. Taking the time derivatives of (2.109) with respect to t_1 gives the following equations:

$$\dot{\varphi}_{ru}(t_1) = 5a_5 t_1^4 + 4a_4 t_1^3 + 3a_3 t_1^2 + 2a_2 t_1 + a_1 \tag{2.110}$$

$$\ddot{\varphi}_{ru}(t_1) = 20a_5 t_1^3 + 12a_4 t_1^2 + 6a_3 t_1 + 2a_2 \tag{2.111}$$

Inserting the boundary conditions of (2.107) and (2.108) into the respective derivatives, see (2.109) to (2.111), it follows directly that $\varphi_s = a_0$, $a_1 = 0$ and $a_2 = 0$. The remaining system of equation is shown in the following equation:

$$\begin{pmatrix} T_{ru}^5 & T_{ru}^4 & T_{ru}^3 \\ 5T_{ru}^4 & 4T_{ru}^3 & 3T_{ru}^2 \\ 20T_{ru}^3 & 12T_{ru}^2 & 6T_{ru} \end{pmatrix} \begin{pmatrix} a_5 \\ a_4 \\ a_3 \end{pmatrix} = \begin{pmatrix} \pi - \varphi_s \\ \omega_n \\ 0 \end{pmatrix} \tag{2.112}$$

Ramp-up trajectories were generated while varying the starting angular position φ_s. Before discussing figure 2.24 and 2.25, it is useful to introduce additional energy parameters. The total work done on both rotors during the RUP can be obtained by subtracting the rotational energy stored in both rotors at the beginning and end of the RUP. This is done by inserting the second boundary conditions of (2.107) and (2.108), respectively, into (2.99) and establishing the difference, see the following equation:

$$E_r(t_1 = T_{ru}) = J\dot{\varphi}(t_1 = T_n)^2 - \dot{\varphi}(t_1 = 0)^2 = J\omega_n^2 \tag{2.113}$$

The work done by the SDOF oscillator on both rotors during the RUP is obtained by calculating the integral from $t_1 = 0$ to $t_1 = T_{ru}$ over the product of the moment induced by the inertial forces f_{ts} and the velocity of the rotors, see figure 2.23 and the following equation:

$$E_s(t_1 = T_{ru}) = \int_{t_1=0}^{t_1=T_{ru}} 2f_{ts}(t)r\left[\sin\varphi(t_1)\right]\dot{\varphi}(t_1)\mathrm{d}t_1 \tag{2.114}$$

Inserting (2.105) and (2.106) into (2.114) yields:

$$E_s(t_1 = T_{ru}) = m_c r x_{on}\omega_n^2 \int_{t_1=0}^{t_1=T_{ru}} \sin\left(\omega_n t_1\right)\sin\varphi(t_1)\dot{\varphi}(t_1)\mathrm{d}t_1 \tag{2.115}$$

The work done by the actuators on the rotors is established by forming the difference between $E_r(t_1 = T_{ru})$ and $E_s(t_1 = T_{ru})$, see (2.116).

$$E_a(t_1 = T_{ru}) = E_r(t_1 = T_{ru}) - E_s(t_1 = T_{ru}) \tag{2.116}$$

See also (2.101) and corresponding discussion.

Figure 2.24 shows the work done by the SDOF oscillator on the rotors $E_s(t_1 = T_{ru})$ due to the forces $f_{ts}(t)$ normalized by the total work required by the rotors $E_r(t_1 = T_{ru})$ during the RUP. This ratio is plotted against the starting angular position φ_s for different values of $J/(m_c r x_{on})$.

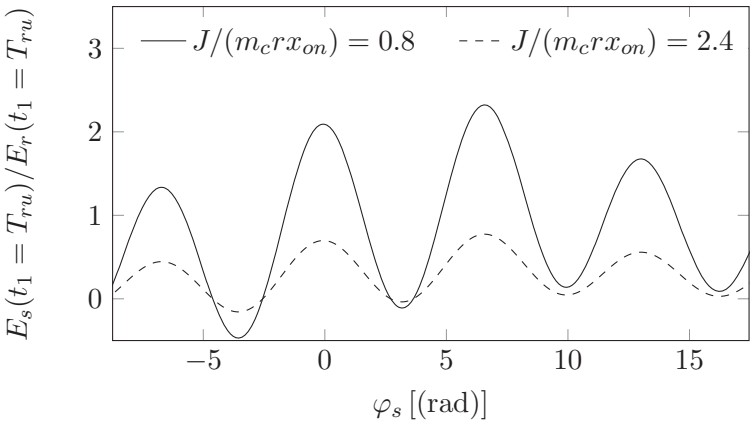

Figure 2.24: Work done by the SDOF oscillator over total work done on the rotors during the RUP for $T_{ru} = 0.5T_n$ [24]

The fraction $J/(m_c r x_{on})$ is dimensionless and its influence on the RUP will be discussed later. Maximizing the ratio of the work done by the SDOF oscillator on the rotors normalized by the total work required to be done on the rotors is equivalent to minimizing the cost function of (2.102). As can be seen in figure 2.24, there are several positive peaks. There is a global positive peak at the starting angular position $\varphi_s \approx 6.6\,(\text{rad})$. It indicates the optimal starting angular position due to the cost function of (2.102). However, when using the ramp-up trajectory corresponding to this optimal starting angular position, the rotors would start off accelerating in the wanted direction, thereupon decelerated and stopped, then finally accelerated in the wanted direction. For practical purposes, this is not meaningful and only becomes optimal due to the cost function of (2.102) which assumes that braking energy can be regained. However, from figure 2.24, some general conclusions about the RUP can be drawn. The curves are identical in shape and, by varying the fraction $J/(m_c r x_{on})$, they can be scaled. The higher the ratio $E_s(t_1 = T_{ru})/E_r(t_1 = T_{ru})$, the more energy comes from the SDOF oscillator during the RUP, consequently the actuators have to do less work. By considering this work ratio, it is possible to derive the following statements. The less energy is consumed by the actuators,

1. the lower the rotational inertia J (1),
2. the higher the mass-radius control product $m_c r$ (2) and
3. the higher the displacement amplitude x_{on} at which the TRD is turned on (3) become.

Statement (1) is apparent when inspecting (2.113). The total energy needed for the RUP of the TRD increases linearly with the rotational inertia J, however, J has no direct impact on the work done by the SDOF oscillator on the rotors, see (2.115). Therefore, the more work has to be done by the actuators, the higher J becomes. For the RUP, the rotors should be designed such that J is as small as possible, to be more precise, the rotational inertias of parts to be set into rotational motion are to be minimized.

Note that statements (1) and (2) somehow struggle with each other. For the design of a TRD unit, the mass-radius control product is usually set first such that the desired damping action in the continuous rotation mode is achieved. The geometry of the control

masses should then be chosen such that the mass-radius control product is maximized while minimizing the rotational inertia determined by their geometry.

Statements (2) and (3) can be reasoned with (2.115). The energy transferred from the SDOF oscillator increases linearly with the mass-radius-control product $m_c r$ and the displacement amplitude x_{on} at which the RUP starts. The mass-radius control product is the property which also determines the damping effect of the TRD. This property is usually set before the ramp-up trajectory is designed. The displacement amplitude x_{on} at which the TRD is turned on at should be set as high as possible to design an energy-efficient ramp-up process. However, the TRD is only active if x_{on} is exceeded. In order to keep the vibration-amplitude range in which the TRD is not active as small as possible, x_{on} should be set to a small value. Therefore, the choice of x_{on} is a trade-off between an energy-efficient RUP and a wide vibration-amplitude range in which the TRD is active. Because of this, the parameters J, $m_c r$ and x_{on} should be chosen carefully by the designer.

Note that the natural frequency ω_n does not have an effect on the curves of figure 2.24 as ω_n contributes quadratically to both energy values, see (2.113) and (2.115).

Having established these relationships, the more practical cost function, (2.103), is now considered. Minimizing the ratio of the positive work to be done by the actuators on the rotors over the total work needed to be done on the rotors is equivalent to minimizing the cost function of (2.103). For the plotted curves, the negative peaks can be found in the vicinity of a starting angular position of about $\varphi_s \approx 1.3\,(\text{rad})$, see figure 2.25, which is then optimal according to the cost function of (2.103).

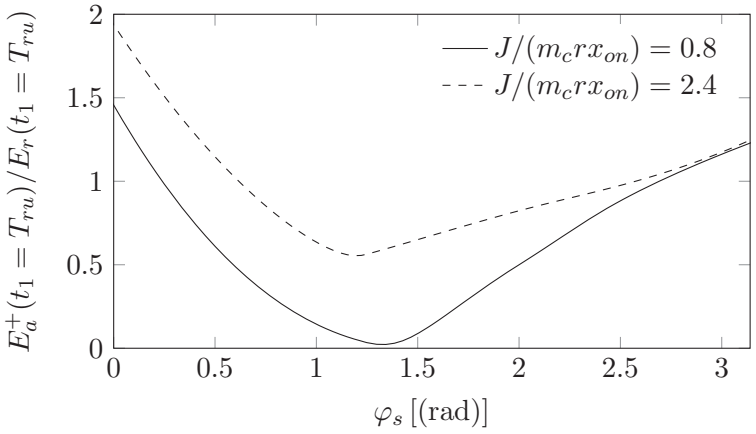

Figure 2.25: Positive work done by the actuators over total work done on the rotors during the RUP for $T_{ru} = 0.5 T_n$ [24]

Considering the curve with $J/(m_c r x_{on}) = 2.4$ with the corresponding optimal angular starting position, $\varphi_s = 1.2\,(\text{rad})$, only 55 % of the rotational energy for the rotors must be provided by the actuators, the rest comes from the SDOF oscillator. For $J/(m_c r x_{on}) = 0.8$, nearly the entire energy for the rotors comes from the SDOF oscillator. Furthermore, the optimal starting angular position φ_s varies with the ratio $J/(m_c r x_{on})$.

It has been found that the energy consumption for the RUP can be further improved by increasing the ramp-up duration T_{ru}. When T_{ru} is increased, the inertial forces $f_{ts}(t)$ have more time to transform vibration energy into rotational energy of the rotors. Note that

when the ramp-up duration is increased, the initial conditions of (2.107) remain, whereas one final condition $\varphi(t_1 = T_{ru})$ of the ramp-up process (see (2.108)) changes due to (2.55).

It also needs to be mentioned that during the RUP, the SDOF oscillator is already being actively damped by the TRD as vibration energy stored in the SDOF oscillator is transferred into rotational energy for the rotors. However, when the ramp-up duration is increased, it takes more time until the TRD provides the damping action generated in the continuous rotation mode.

The optimization is now repeated with a cost function which penalizes the standard deviation according to (2.96) of the power demand on the actuators. For this purpose, the power $P_s(t_1)$ of the SDOF oscillator on the rotors during the RUP is obtained by deriving (2.115) with respect to time, see (2.117).

$$P_s(t_1) = m_c r x_{on} \omega_n^2 \sin(\omega_n t_1) \sin\varphi(t_1) \dot{\varphi}(t_1) \tag{2.117}$$

The rotational power performed on both rotors is given by

$$P_t(t_1) = 2J\ddot{\varphi}(t_1)\dot{\varphi}(t_1) \tag{2.118}$$

The difference between (2.118) and (2.117) is the power to be provided by both actuators, see the following equation:

$$P_a(t_1) = P_t(t_1) - P_s(t_1) \tag{2.119}$$

Subsequently, the magnitude of the power demand on the actuators is calculated with help of the root mean square value given in (2.96):

$$\mathrm{rms}(P_a(t_1)) = \sqrt{\frac{1}{T_{ru}} \int_{t_1=0}^{t_1=T_{ru}} P_a(t_1)^2 \mathrm{d}t_1} \tag{2.120}$$

Figure 2.26 shows the magnitude of the power demand on the actuators of the TRD during the RUP plotted against the starting angular position φ_s.

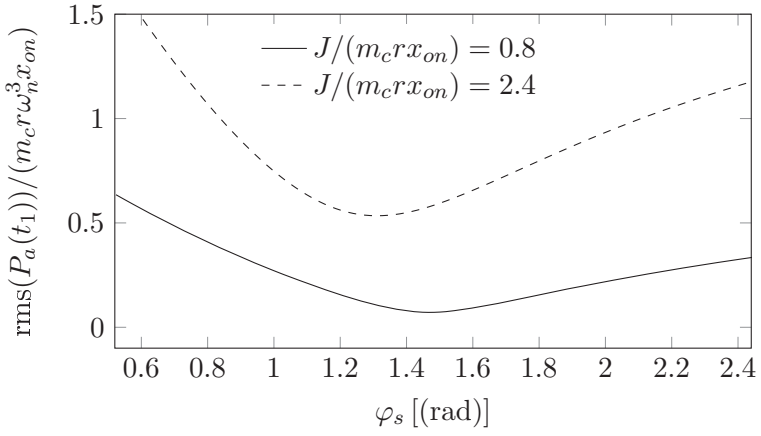

Figure 2.26: Magnitude of power demand on actuators plotted against starting angular position φ_s for $T_{ru} = 0.5T_n$

The negative peaks of both plotted curves can be found in the vicinity of $\varphi_s \approx 1.4\,(\mathrm{rad})$, close to the negative peaks of figure 2.25.

Ramp-up process considering inherent damping

For the derivation of the ramp-up trajectory, it was assumed that inherent damping is not present. For $\xi > 0$, several aspects must be considered. This is discussed in the following for SDOF oscillators with small inherent damping ($0 < \xi < 0.1$). ω_n is replaced by ω_d. If $\xi > 0$, the envelope of the half sine wave of (2.106) is not constant. Instead, the harmonic sinusoidal acceleration response will decay exponentially. However, for $\xi < 0.1$, this decay is small assuming that $T_{ru} = 0.5T_d$. The acceleration response during the RUP is assumed to have the form of a positive half sine wave, see (2.106). Consequently, for the velocity and the displacement at the end of the RUP holds:

$$x(t_1 = T_{ru}) = 0 \qquad \dot{x}(t_1 = T_{ru}) > 0 \tag{2.121}$$

With (2.121) and (2.52), $\psi(t_1 = T_{ru}) = 0$, which is the vibration phase at the end of the RUP. Consequently, according to (2.57) with α_c according to (2.54), the target angular position at the end of the RUP becomes

$$\varphi_t(t_1 = T_{ru}) = \alpha_c\,(\xi) \tag{2.122}$$

This target angular position is then substituted into the final conditions, see (2.108). The same optimization as done for figure 2.25 is now performed considering small inherent damping ratios, see figure 2.27.

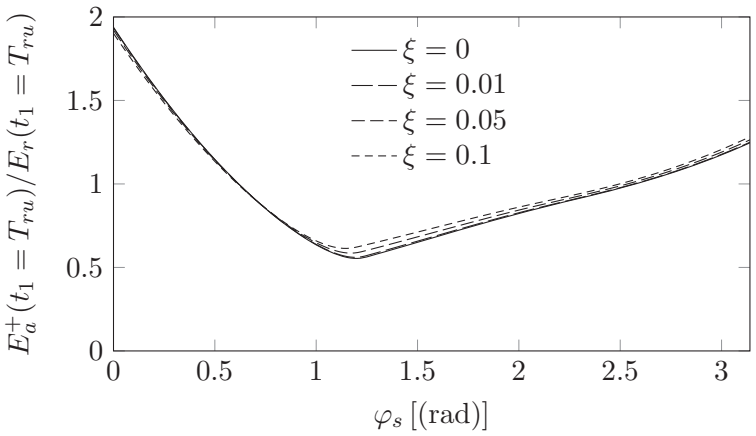

Figure 2.27: Positive work done by the actuators over total work done on the rotors for several inherent damping ratios during the RUP for $T_{ru} = 0.5T_d$ and $J/(m_c r A) = 2.4$

From this figure, it can be seen that for the considered case, $J/(m_c r x_{on}) = 2.4$, the influence of small inherent damping on the optimal starting angular position is small. Furthermore, the positive work to be performed by the actuators increases slightly with the damping ratio. It is, for the considered case, 55 % for $\xi = 0$ and 61 % for $\xi = 0.1$. Therefore, small inherent damping has little influence on the ramp-up trajectory design. This was checked for several values of $J/(m_c r x_{on})$, arriving at the same conclusion.

Ramp-up process using the singular value decomposition

It is possible to improve the ramp-up trajectory by increasing the degree of the trajectory polynomial, see (2.109)

$$\varphi_{ru}(t_1) = \sum_{i=0}^{i=n} a_i t_1^i \tag{2.123}$$

in which n is a positive integer equal to or larger than five. By inserting the six boundary conditions of (2.107) and (2.108), an under-determined system is formed

$$\boldsymbol{A}^{6\text{x}(n+1)}\boldsymbol{a}^{(n+1)\text{x}1} = \boldsymbol{b}^{6\text{x}1} \tag{2.124}$$

in which the upper indexes denote the size of the matrices.

The system of equations in (2.124) can be solved using the singular value decomposition [29]. The unknown coefficients of (2.123) are a_0, a_1, a_2,...,a_n forming the vector $\boldsymbol{a}$.

Using the singular value decomposition, the matrix $\boldsymbol{A}^{6\text{x}(n+1)}$ can be factorized as shown in the following:

$$\boldsymbol{A}^{6\text{x}(n+1)} = \boldsymbol{U}^{6\text{x}6}\boldsymbol{\Sigma}^{6\text{x}(n+1)}\left(\boldsymbol{V}^{(n+1)\text{x}(n+1)}\right)^{\text{T}} \tag{2.125}$$

in which $\boldsymbol{U}^{6\text{x}6}$ and $\boldsymbol{V}^{(n+1)\text{x}(n+1)}$ are unitary and orthogonal matrices [29]. T indicates the transpose version of a matrix. The matrix $\boldsymbol{\Sigma}^{6\text{x}(n+1)}$ has only diagonal entries, $\sigma_1 \geq \sigma_2 \geq ... \geq \sigma_6 \geq 0$, which are called the singular values of $\boldsymbol{A}^{6\text{x}(n+1)}$. The columns of $\boldsymbol{U}^{6\text{x}6}$ are the left singular vectors of $\boldsymbol{A}^{6\text{x}(n+1)}$, $\boldsymbol{u}_1$, $\boldsymbol{u}_2$,...,$\boldsymbol{u}_6$ and the columns of $\boldsymbol{V}^{(n+1)\text{x}(n+1)}$ are the right singular vectors of $\boldsymbol{A}^{6\text{x}(n+1)}$, $\boldsymbol{v}_1$, $\boldsymbol{v}_2$,...,$\boldsymbol{v}_{n+1}$. Taking (2.125) and doing some rearrangements yields the following equation

$$\boldsymbol{A}^{6\text{x}(n+1)} = [\boldsymbol{u}_1\sigma_1, \boldsymbol{u}_2\sigma_2, ..., \boldsymbol{u}_6\sigma_6, \boldsymbol{0}, ..., \boldsymbol{0}]\,[\boldsymbol{v}_1, \boldsymbol{v}_2, ..., \boldsymbol{v}_{n+1}]^{\text{T}} \tag{2.126}$$

in which $\boldsymbol{0}$ is a zero matrix of appropriate dimensions. The purpose of using singular value decomposition becomes evident when it is considered that the vectors, $\boldsymbol{v}_7$, $\boldsymbol{v}_8$,...,$\boldsymbol{v}_{n+1}$ all lie in the null space of $\boldsymbol{A}^{6x(n+1)}$ [29]. From (2.126), the so called pseudo-inverse of $\boldsymbol{A}$, which is $[\boldsymbol{u}_1\sigma_1, \boldsymbol{u}_2\sigma_2, ..., \boldsymbol{u}_6\sigma_6, \boldsymbol{0}, ..., \boldsymbol{0}]\,[\boldsymbol{v}_1, \boldsymbol{v}_2, ..., \boldsymbol{v}_6]^{\text{T}}$, can be calculated.

With this information, (2.126) can be solved as seen in (2.127) in which $\boldsymbol{c}^{(n-5)x1}$ is a vector scaling the vectors lying in the null space of $\boldsymbol{A}^{6xn}$.

$$\begin{aligned}\boldsymbol{a}^{(n+1)x1} = &[\boldsymbol{v}_1, \boldsymbol{v}_2, ..., \boldsymbol{v}_6]^{(n+1)x6}\begin{bmatrix}\sigma_1 & 0 & \dots & 0\\ 0 & \sigma_2 & \dots & 0\\ \vdots & 0 & \ddots & \vdots\\ 0 & \dots & 0 & \sigma_6\end{bmatrix}^{-1}[\boldsymbol{u}_1, \boldsymbol{u}_2, ..., \boldsymbol{u}_6]^{6x6^{\text{T}}}\boldsymbol{b}^{6x1} + ...\\ &[\boldsymbol{v}_7, \boldsymbol{v}_8, ..., \boldsymbol{v}_{n+1}]^{(n+1)x(n-5)}\,\boldsymbol{c}^{(n-5)x1}\end{aligned} \tag{2.127}$$

The scaling vector, $\boldsymbol{c}^{(n-5)x1}$, can be chosen arbitrarily and is to be varied to optimize the ramp-up trajectory, for instance, based on the cost functions of (2.102) or (2.103). Ramp-up trajectories using the singular value decomposition are developed for the test setup in section 2.6.

Initially, it was assumed that the RUP starts when the acceleration response of the SDOF oscillator changes sign from minus to plus. This assumption is removed when considering

a trajectory polynomial with a degree increasing to infinity as it allows the trajectory to start with a held angular position.

Ramp-down process

After the TRD is ramped-up, it works in the continuous rotation mode until the vibration amplitude falls below a certain turn-off vibration threshold, A_{off}. The rotors must then be ramped-down and brought to their starting angular position. For this ramp-down process (RDP) with a time duration T_{rd}, a ramp-down trajectory $\varphi_{rd}(t_2)$ is designed in the following. For $\varphi_{rd}(t_2)$, an additional running time variable, t_2, is introduced in order to describe the time during the RDP. t_2 is set to zero when the RDP is initiated. At $t_2 = 0$, the rotors rotate approximately with the natural frequency of the SDOF oscillator and are at a certain angular position, φ_d, which is referred to as ramp-down angular position. When the RDP ends, it is required that the angular position of the rotors equals the starting angular position φ_s—the angular position of the next RUP—and are at rest. As before to reduce mechanical wear, the RDP is required to start and end without jerking. Therefore, the initial and final conditions for the RDP are:

$$\begin{aligned} \varphi_{rd}(t_2 = 0) &= \varphi_d & \varphi_{rd}(t_2 = T_{rd}) &= \varphi_s \\ \dot{\varphi}_{rd}(t_2 = 0) &= \omega_n & \dot{\varphi}_{rd}(t_2 = T_{rd}) &= 0 \\ \ddot{\varphi}_{rd}(t_2 = 0) &= 0 & \ddot{\varphi}_{rd}(t_2 = T_{rd}) &= 0 \end{aligned} \tag{2.128}$$

The ramp-down angular position φ_d and the ramp-down duration T_{rd} are to be chosen by the designer. These parameters are to be set such that the power demand on the actuators is not governed by the RDP. As before, a polynomial as shown in the following equation can then be assumed:

$$\varphi_{rd}(t_2) = \sum_{i=0}^{i=5} a_i t_2^i. \tag{2.129}$$

By inserting the conditions of (2.128), a system of equations is obtained again. It can be solved for the coefficients a_0, a_1, ..., a_n determining the ramp-down trajectory.

2.5.3 Complete damping sequence and closed-loop angular position control

With the target angular position for the continuous rotation mode including trajectories to ramp the TRD up and down, a procedure for a complete damping sequence is now proposed. Figure 2.28 shows the target angular position, $\varphi_t(t)$, for one damping sequence.

The rotors are initially at rest and positioned at the starting angular position. As soon as the SDOF oscillator exceeds the vibration-amplitude threshold A_{on} and the acceleration response of the SDOF oscillator changes sign from minus to plus, the time variable t_1 is set to zero and the computed ramp-up trajectory is used as the target angular position (TAP), see figure 2.28. The ramp-up trajectory is used as the TAP for the ramp-up duration minus the duration of the transition $T_{ru} - T_{tr}$.

The transition is implemented to avoid discontinuities (which would result in a jerking motion) in the target angular position when switching over from the ramp-up trajectory to the target angular position given by the algorithm from the continuous rotation mode. Such discontinuities occur when the actual frequency of the SDOF oscillator changes, for instance, due to an excitation force or model inaccuracies (TRD or SDOF oscillator).

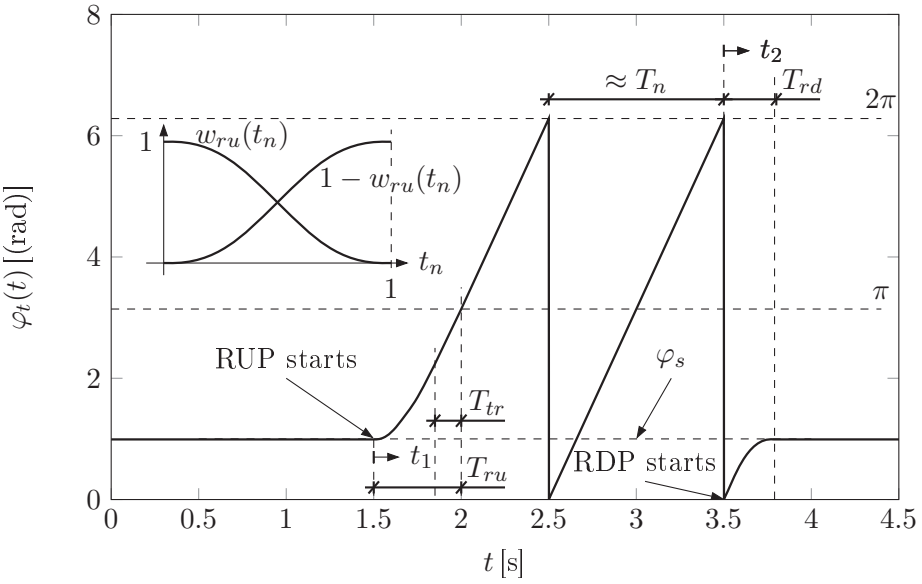

Figure 2.28: Complete damping sequence [24]

For the duration of the transition, from $t_1 = T_{ru} - T_{tr}$ to $t_1 = T_{ru}$, the target angular position is a combination of the angular position given by the ramp-up trajectory and the target angular position given by the algorithm of the continuous rotation mode. Both positions are weighted with respect to the time variable, $t_n = (t_1 - T_{ru} + T_{tr})/T_{tr}$, see the subfigure in figure 2.28. $w_{ru}(t_n)$ is used to weight the target angular position of the ramp-up trajectory and $1 - w_{ru}(t_n)$ the target angular position for the continuous rotation mode. The weight function $w_{ru}(t_n)$ is computed by assuming a polynomial with a degree of five which meets the following boundary conditions: $w_{ru}(t_n = 0) = 1$, $\dot{w}_{ru}(t_n = 0) = 0$, $\ddot{w}_{ru}(t_n = 0) = 0$, $w_{ru}(t_n = 1) = 0$, $\dot{w}_{ru}(t_n = 1) = 0$ and $\ddot{w}_{ru}(t_n = 1) = 0$. The transition time T_{tr} is to be chosen by the designer.

When the RUP is completed, the TRD operates in the continuous rotation mode until firstly the vibration amplitude falls below the turn-off vibration amplitude and secondly the target angular position of the continuous rotation mode passes the ramp-down angular position. At this instant, the time variable t_2 is set to zero and the computed ramp-down trajectory is used as the TAP. At $t_2 = T_{rd}$, the RDP terminates with the TAP equal to the starting angular position. The rotors are then held at this angular position until the next damping sequence starts.

A complete damping sequence with the output of a TAP, $\varphi_t(t)$, for each point in time was presented. This TAP is then compared to the (actual) angular position of the rotors $\varphi(t)$. As indicated in figure 2.29, it follows that the error $e(t)$ is as described in (2.130).

$$e(t) = \varphi_t(t) - \varphi(t) \tag{2.130}$$

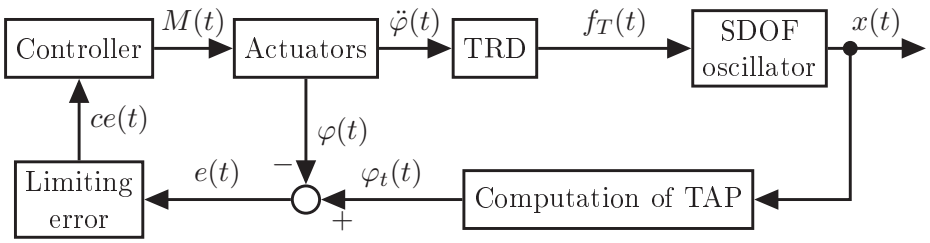

Figure 2.29: Closed-loop angular position control [24]

Before the error is fed into the controller, it is restricted to values between $-\pi$ and π, see block 'Limiting error' (LE) in figure 2.29. As it is possible to add or subtract arbitrary multiples of 2π to $\varphi(t)$ without loss of information, it is also possible to perform the same mathematical operation on the error. The control error can then be interpreted as follows: If the control error $ce(t)$ is positive ($0 < ce(t) < \pi$), the TAP precedes $\varphi(t)$. If the control error is negative ($-\pi < ce(t) < 0$), the TAP lags behind the $\varphi(t)$. The controller outputs a control action, e.g. a moment $M(t)$ acting on the rotors. The controller generates such a moment that the angular position tracks the TAP. Tracking problems are extensively researched, see e.g. [30]. The control action of the actuators results in an angular acceleration of the rotors, $\ddot{\varphi}(t)$, which is the input of the TRD. The TRD then exerts the force $f_T(t)$ which acts on the SDOF oscillator. The SDOF oscillator outputs the state variables which are then used to compute the TAP for the next time step.

2.6 Experimental verification

2.6.1 Test setup

The vibration control of a SDOF oscillator using the TRD was validated on a test setup at Hamburg University of Technology. The test setup consists of a rigid supporting structure from which a table is suspended via three leaf springs, see figure 2.30. The table is equipped with two TRD units and a linear actuator, see right subfigure. The leaf springs are arranged in a configuration such that the motion of the table is only possible in a single, horizontal direction. Therefore, the motion of the table can be idealized as a SDOF oscillator as shown in figure 2.2. With the help of the linear actuator, an excitation mass can be accelerated relative to the table in the single, horizontal direction. This produces an excitation force on the table.

The mass m_L of the leaf springs is 12.7 kg. The total modal mass m_s of the SDOF oscillator is computed as

$$m_s = m_t + \frac{156}{420} m_L = 29.9\,\text{kg} + \frac{156}{420} 12.7\,\text{kg} = 34.6\,\text{kg} \tag{2.131}$$

in which m_t refers to the mass of the table. The table mass m_t includes the mass of both TRD units and the mass of the linear actuator with an excitation mass of $m_e = 2.0\,\text{kg}$. The mass of the leaf springs contributes to the mass of the SDOF oscillator with a factor of 156/420, see [25, p. 187]. It is one entry of the consistent-mass matrix of a straight beam segment; it is the first entry in [25, p. 187].

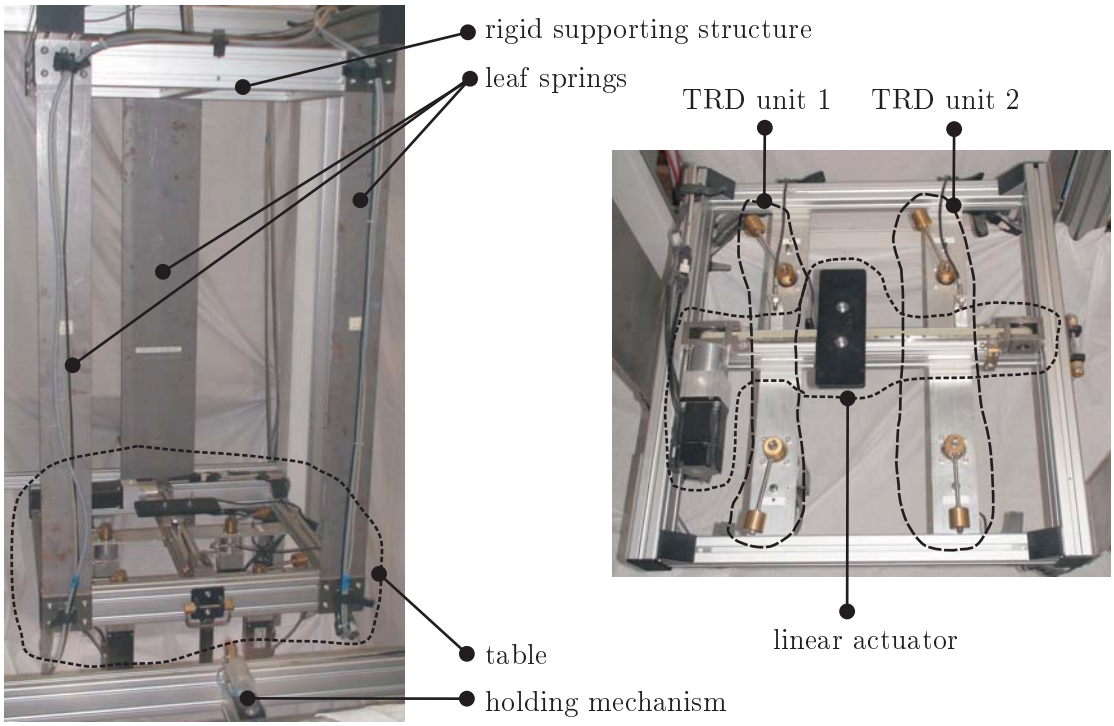

Figure 2.30: Test setup of SDOF oscillator (side view and top view)

With the help of free vibration tests, the damped natural frequency ω_d of the SDOF oscillator and the logarithmic decrement

$$\delta = \frac{1}{l} \ln \frac{x_p(t)}{x_p(t + nT_d)} \tag{2.132}$$

was measured; $x_p(t)$ refers to the peak value of a positive displacement peak and $x_p(t+nT_d)$ to a positive peak value l vibration periods thereafter [25]. Figure 2.31 refers to a free vibration motion of the test setup. Up to $t = 2.60\,\mathrm{s}$, the table is held with help of the holding mechanism at $x = 0.10\,\mathrm{m}$, see figure 2.30. At $t = 2.60\,\mathrm{s}$, the table is released from this position and oscillates freely. After $t = 100\,\mathrm{s}$, the free vibration test is stopped.

To better characterize the properties of the SDOF oscillator, three free vibration tests were performed. The data points of positive displacement peaks in the vicinity of $x = 0.10\,\mathrm{m}$, $0.08\,\mathrm{m}$, ..., $0.02\,\mathrm{m}$ and the number l of completed vibration cycles were read off, see table 2.3. With this information, the properties of the SDOF oscillator for different vibration-amplitude ranges, see first column of table 2.4, are calculated.

For all considered vibration-amplitude ranges, the (measured) damped natural period T_d was computed. In a next step, the logarithmic decrement was calculated, which is not shown in table 2.4. Using the logarithmic decrement, the damping ratio is calculated according to (2.133) [25].

$$\delta = \frac{2\pi\xi}{\sqrt{1 - \xi^2}} \tag{2.133}$$

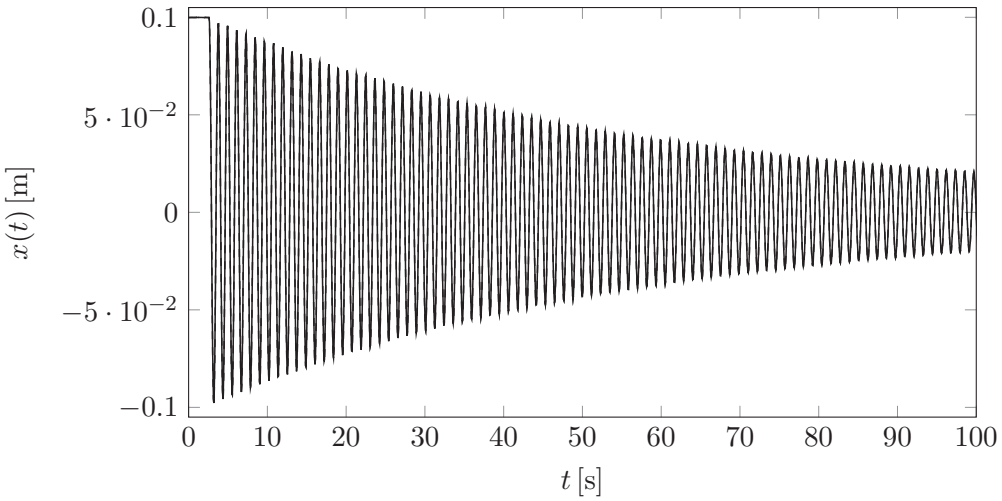

Figure 2.31: Free vibration test with $x_0 = 0.10\,\text{m}$ and $\dot{x}_0 = 0$

Table 2.3: Displacement peak data including number l of passed vibration cycles of three different free vibration tests

Test 1			Test 2			Test 3		
t [s]	x_p [m]	l	t [s]	x_p [m]	l	t [s]	x_p [m]	l
2.61	0.100	0	2.37	0.100	0	2.13	0.100	0
14.29	0.0813	10	15.22	0.0792	11	15.00	0.0791	11
30.67	0.0606	24	30.42	0.0602	24	30.20	0.0600	24
55.24	0.0402	45	54.99	0.0397	45	54.70	0.0396	45
100.90	0.0203	84	100.60	0.0199	84	99.22	0.0202	83

From table 2.4, it becomes evident that the damped natural period T_d is constant, whereas the damping ratio increases slightly with the vibration amplitude. This can be observed for all free vibration tests. To consider the change in the damping ratio, nonlinear behavior of the SDOF oscillator would have to be considered. This can be done by formulating the damping ratio as a function of the vibration amplitude [31]. However, as the change in the damping ratio is small, a linear model is assumed for the SDOF oscillator henceforth. Considering the vibration-amplitude range from $x = 0.10\,\text{m}$ to $0.02\,\text{m}$, the mean damping ratio of the three free vibration tests is $0.305\,\%$ and the mean natural frequency ω_n is $5.37\,(\text{rad})/\text{s}$. These properties will be used in the following investigations and are summarized in table 2.5.

Table 2.4: Characterization of SDOF oscillator properties for different vibration-amplitude ranges

Vibration-amplitude range	Test 1			Test 2			Test 3		
	l	$T_d\,[s]$	$\xi\,[\%]$	l	$T_d\,[s]$	$\xi\,[\%]$	l	$T_d\,[s]$	$\xi\,[\%]$
$x = 0.10\,\text{m}$ to $0.08\,\text{m}$	10	1.17	0.330	11	1.17	0.337	11	1.17	0.339
$x = 0.08\,\text{m}$ to $0.06\,\text{m}$	14	1.17	0.334	13	1.17	0.336	13	1.17	0.338
$x = 0.06\,\text{m}$ to $0.04\,\text{m}$	21	1.17	0.311	21	1.17	0.316	21	1.17	0.315
$x = 0.04\,\text{m}$ to $0.02\,\text{m}$	39	1.17	0.279	39	1.17	0.282	38	1.17	0.282
$x = 0.10\,\text{m}$ to $0.02\,\text{m}$	84	1.17	0.302	84	1.17	0.306	83	1.17	0.307

Table 2.5: System properties of SDOF oscillator and TRD unit 1

m_s [kg]	34.6	m_c [kg]	0.389
ω_n [(rad)/s]	5.37	r [m]	0.110
ξ [%]	0.305	J [kgm^2]	$2.35 \cdot 10^{-3}$

Two TRD units are attached to the table. The properties of TRD unit 1 (introduced in figure 2.30) are also shown in table 2.5. All components (transmissions, rods, control mass, etc.) set in motion by the actuators produce rotational inertial moments. However, for the computation of the rotational inertia J, the rotational moments of inertia of all components other than the control masses are neglected. Therefore, the rotational inertia J of a single rotor is computed by $0.5 m_c r^2$.

2.6.2 Measured and observed states of SDOF oscillator

The displacement $x(t)$ of the table is measured using a laser transducer. This signal is then fed into an electronic monitoring system. For the control algorithm of subsection 2.5.3, the velocity $\dot{x}(t)$ is also required. To make the velocity $\dot{x}(t)$ available, an observer is used [30]. Recalling (2.11), rearranging with (2.3) and solving for $\ddot{x}(t)$ gives

$$\ddot{x}(t) = F_e(t) + F_T(t) - 2\xi\omega_n\dot{x}(t) - \omega_n^2 x(t) \tag{2.134}$$

with the normalized forces

$$F_T(t) = \frac{f_T(t)}{m_s} \qquad F_e(t) = \frac{f_e(t)}{m_s} \tag{2.135}$$

As seen frequently in the field of control engineering, a block diagram is used to represent (2.134), see figure 2.32, in which s is the Laplace variable.

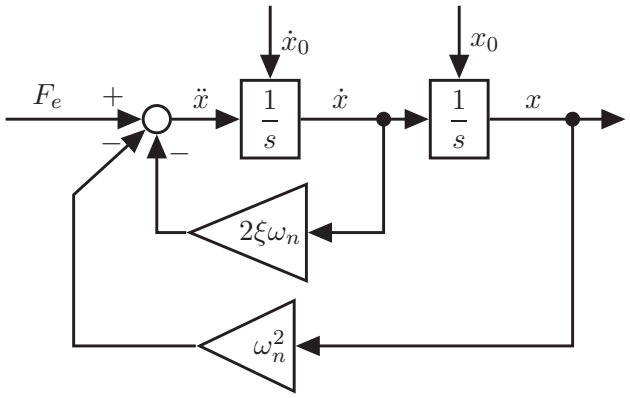

Figure 2.32: Block diagram representing (2.134)

In this work, time-dependencies are not indicated in block diagrams.

The equation of motion governing the dynamics of the SDOF oscillator can be written in an alternative way. By introducing the state vector $\boldsymbol{x}_s(t) = [x(t), \dot{x}(t)]^{\mathrm{T}}$, in which T indicates the transpose, (2.134) can be rearranged as given by

$$\dot{\boldsymbol{x}}_s(t) = \boldsymbol{A}\boldsymbol{x}_s(t) + \boldsymbol{B}\left[F_e(t) + F_T(t)\right] \qquad x(t) = \boldsymbol{C}\boldsymbol{x}_s(t) \tag{2.136}$$

with the state matrix $\boldsymbol{A}$, the input vector $\boldsymbol{B}$ and the output vector $\boldsymbol{C}$ given in (2.137).

$$\boldsymbol{A} = \begin{bmatrix} 0 & 1 \\ -\omega_n^2 & -2\xi\omega_n \end{bmatrix} \qquad \boldsymbol{B} = \begin{bmatrix} 0 \\ 1 \end{bmatrix} \qquad \boldsymbol{C} = \begin{bmatrix} 1 & 0 \end{bmatrix} \tag{2.137}$$

The first equation of (2.136) is the state equation. It consists of a two first order differential equations. The second equation of (2.136) is the output equation. The initial value of the state vector is $\boldsymbol{x}_{s,0} = [x_0, \dot{x}_0]^{\mathrm{T}}$. A block diagram of (2.136) is shown in figure 2.33 in which the bold arrows indicate vector signals. The inputs of the state space model are $F_e(t)$ and $F_T(t)$. Output is the displacement $x(t)$.

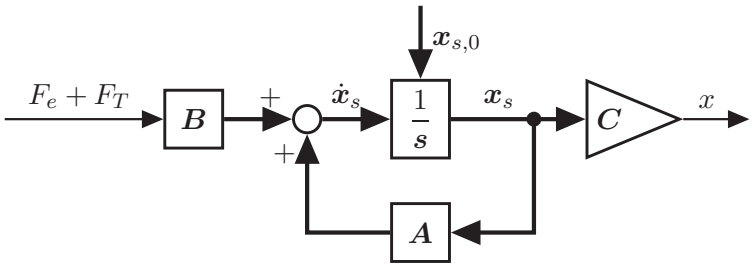

Figure 2.33: Block diagram representing the state-space model of (2.136)

An estimate, $\hat{\boldsymbol{x}}(t)$, for the state vector $\boldsymbol{x}_s(t)$ is now introduced. A method for estimating $\boldsymbol{x}_s(t)$ is to use a model of the SDOF oscillator—estimated model, see (2.138).

$$\dot{\hat{\boldsymbol{x}}}(t) = \boldsymbol{A}\hat{\boldsymbol{x}}(t) + \boldsymbol{B}\left[F_e(t) + F_T(t)\right] \tag{2.138}$$

The error of the displacement is defined as [30]:

$$x(t) - \hat{x}(t) = \boldsymbol{C}\left[\boldsymbol{x}_s(t) - \hat{\boldsymbol{x}}(t)\right] \tag{2.139}$$

By using the error, $x(t) - \hat{x}(t)$, see (2.139) of the displacement as feedback, the estimated model of (2.138) can be corrected continuously, see the following equation

$$\dot{\hat{\boldsymbol{x}}}(t) = \boldsymbol{A}\hat{\boldsymbol{x}}(t) + \boldsymbol{B}\left[F_e(t) + F_T(t)\right] + \boldsymbol{L}\boldsymbol{C}\left[\boldsymbol{x}_s(t) - \hat{\boldsymbol{x}}(t)\right] \tag{2.140}$$

in which $\boldsymbol{L}$ is a proportional feedback gain, see (2.141) [30].

$$\boldsymbol{L} = [l_1, l_2]^{\mathrm{T}} \tag{2.141}$$

Subtracting $\dot{\hat{\boldsymbol{x}}}(t)$ of (2.140) from $\dot{\boldsymbol{x}}_s(t)$ of (2.136) and introducing $\dot{\tilde{\boldsymbol{x}}}(t) = \boldsymbol{x}_s(t) - \hat{\boldsymbol{x}}(t)$ gives

$$\dot{\tilde{\boldsymbol{x}}}(t) = (\boldsymbol{A} - \boldsymbol{L}\boldsymbol{C})\,\tilde{\boldsymbol{x}}(t) \tag{2.142}$$

where the error dynamics $\dot{\tilde{\boldsymbol{x}}}(t)$ are described by the characteristic equation

$$\det\left[s\boldsymbol{I} - (\boldsymbol{A} - \boldsymbol{L}\boldsymbol{C})\right] = 0 \tag{2.143}$$

With help of the proportional feedback gain $\boldsymbol{L}$, the poles can be placed arbitrarily. These poles are to be set such that they are stable, have a suitable damping ratio and are reasonably 'fast' [30]. To ensure that measurement noise in $x(t)$ is suppressed, the damping ratio is usually set to values between 0.80 and 0.95. The poles are reasonably fast if the eigenvalues of the closed-loop are set such that they are two to five times faster than the eigenvalues of the SDOF oscillator [30]. A block diagram with the input and outputs of the observer is shown in figure 2.34.

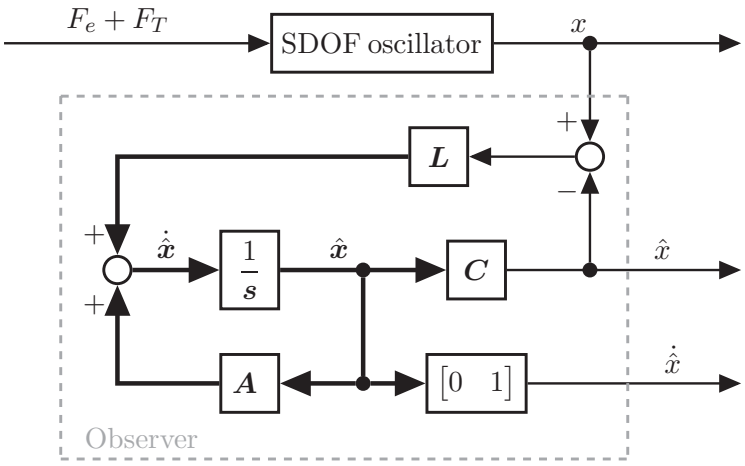

Figure 2.34: Observer of SDOF oscillator

The force $F_T(t)$ produced by the TRD can be constructed with help of the states of the motor. Doing so, only $F_e(t)$ is considered as disturbance. However, when considering $F_T(t)$ and $F_e(t)$ as disturbance and tuning the observer as described in the previous paragraph, the estimate $\hat{\boldsymbol{x}}(t)$ also tracks the state vector $\dot{\boldsymbol{x}}_s(t)$ adequately accurately.

The poles of the error dynamics in the complex plane can be given in polar coordinates; they are then given by the damping ratio ξ_e and the natural frequency $\omega_{n,e}$, see figure 2.35.

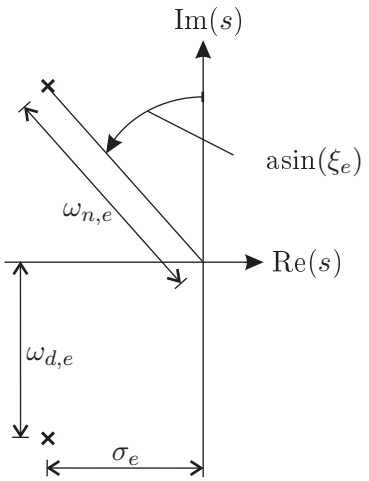

Figure 2.35: s-plane plot for complex pole pair describing the error dynamics [30]

Alternatively, the poles can be given in rectangular coordinates, $s = -\sigma_e \pm j\omega_{d,e}$. (The index e indicates that the properties correspond to the poles determining the dynamics of the error in the estimate.) This relation is shown in (2.144), see also figure 2.35 [30].

$$\sigma_e = \xi_e \omega_{n,e} \qquad \omega_{d,e} = \omega_{n,e}\sqrt{1-\xi_e^2} \tag{2.144}$$

An observer for the test setup is now designed. It is required that $\omega_{n,e}$ is five times larger than the natural frequency ω_n of the SDOF oscillator, see table 2.5. It follows: $\omega_{n,e} = 5{\cdot}5.37\,(\text{rad})/\text{s} = 26.85\,(\text{rad})/\text{s}$. Furthermore, a damping ratio ξ_e of 0.9 is required. It follows according to (2.144) that $\omega_{d,e} = 26.85\,(\text{rad})/\text{s}{\cdot}\sqrt{(1-0.9^2)} \approx 11.70\,(\text{rad})/\text{s}$ and $\sigma_e \approx$

24.17 (rad)/s. Thus, the desired location of the complex pole pair is $s = -24.17\,(\text{rad})/\text{s} \pm j11.70\,(\text{rad})/\text{s}$. The placement of the pole pair is done in MATLAB using the `place` command. The result is a proportional gain $\boldsymbol{L} = [48.31, 690.66]^{\mathrm{T}}$ (units of $\boldsymbol{L}$ are dropped).

With the estimate of the state vector $\hat{\boldsymbol{x}}(t)$, an estimate of the displacement $\hat{x}$ and the velocity $\dot{\hat{x}}$ of the SDOF oscillator is derived, see the following equation:

$$\hat{x} = \begin{bmatrix} 1 & 0 \end{bmatrix} \hat{\boldsymbol{x}} \qquad\qquad \dot{\hat{x}} = \begin{bmatrix} 0 & 1 \end{bmatrix} \hat{\boldsymbol{x}} \tag{2.145}$$

The outputs of the observer of (2.145) are then used for the control algorithm of subsection 2.5.3.

2.6.3 System identification of the actuators

The dynamics of the actuators were identified using the MATLAB System Identification Toolbox [32, 33]. An actuator belonging to one TRD unit defines a system which has the control effort, $u_a(t)$ ($U_a(s)$ in Laplace domain), as input and the corresponding angular position $\varphi(t)$ ($\varphi(s)$ in Laplace domain) as output. Thus, when performing a system identification of an actuator, the dynamics of the transmission, the motor shaft, the adapters etc. are included. The transfer function $M_a(s)$ describing the dynamics of the four individual actuators is shown in (2.146).

$$M_a(s) = \frac{\varphi(s)}{U_a(s)} = \frac{b}{as^2 + s} \tag{2.146}$$

The unit of $u_a(t)$ is voltage and the unit of $\varphi(t)$ is radians. The coefficients b and a were determined for each actuator and are shown in table 2.6.

Table 2.6: Coefficients b and a of the transfer function $M_a(s)$ describing the dynamics of the actuators

	b	a
$M_{a,1}(s)$	3.14	$1.50 \cdot 10^{-3}$
$M_{a,2}(s)$	3.05	$1.08 \cdot 10^{-3}$
$M_{a,3}(s)$	3.18	$2.00 \cdot 10^{-3}$
$M_{a,4}(s)$	3.12	$1.75 \cdot 10^{-3}$

Multiplying with s in frequency domain is equivalent to deriving with respect to time in time domain. Therefore, the transfer function $M_v(s)$ is derived:

$$M_v(s) = \frac{b}{as + 1} \tag{2.147}$$

This transfer function has $u_a(t)$ as input and the angular velocity $\dot{\varphi}(t)$ in radians per second as output.

2.6.4 Ramp-up and ramp-down trajectories for the test setup

For the free vibration tests of this section, ramp-up trajectories are developed for two different initial displacements, $x_0 = 0.05\,\text{m}$ and $x_0 = 0.1\,\text{m}$. The initial velocity is $\dot{x}_0 = 0$. As the inherent damping ξ of the SDOF oscillator is small, see table 2.5, the damped natural frequency can be set equal to the natural frequency. Ramp-up and ramp-down trajectories are developed using the approach described in subsection 2.5.2.

By starting the motion with the initial conditions $x_0 > 0$ and $\dot{x}_0 = 0$, the acceleration response of the SDOF oscillator changes from negative into positive after approximately a quarter of vibration period. At this instant, the TRD is designed to start the RUP. The corresponding acceleration amplitude of the SDOF oscillator can be approximated by $x_0\omega_n^2$. This can be done by neglecting the effect of inherent damping on the motion. With the approximated acceleration amplitude and the data of table 2.5, ramp-up trajectories have been developed according to the cost function of (2.103) for a ramp-up duration T_{ru} of $0.5T_n$ and for polynomials of different order n. For $n > 5$ singular value decomposition was applied; the scaling vector $\boldsymbol{c}^{(n-5)\mathrm{x}1}$ of (2.127) was varied and optimized minimizing the cost function of (2.103).

Figure 2.36 shows the positive work needed to be done by the actuators over the required rotational energy of the rotors at the end of the RUP for two initial displacements $x_0 = 0.05\,\mathrm{m}$ (subfigure A) and $x_0 = 0.1\,\mathrm{m}$ (subfigure B) both for polynomials of different order n.

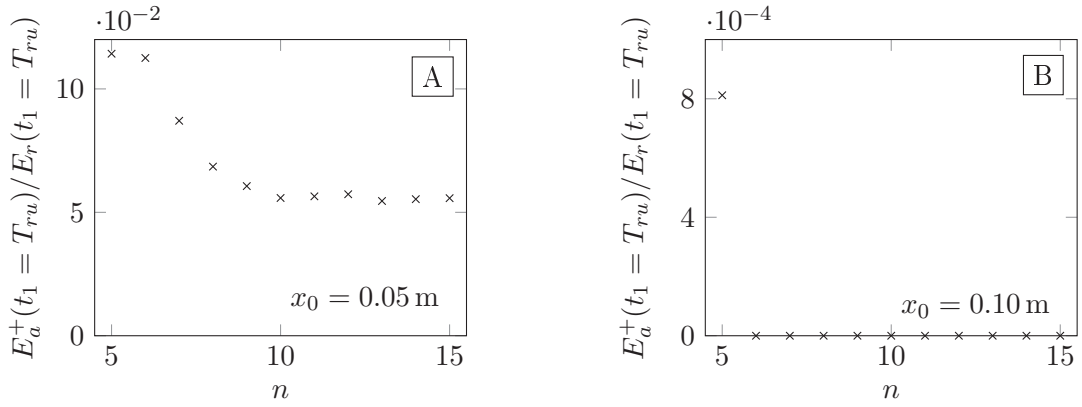

Figure 2.36: Positive work required to be done by the actuators on the rotors over required rotational energy of the rotors at the end of the RUP for polynomials with different order n [24]

Note that the vertical axes are scaled differently. For $x_0 = 0.1\,\mathrm{m}$ and $n = 5$, 0.08 % of $E_r(t_1 = T_{ru})$ is provided by the actuators of the TRD and 99.92 % comes from the vibration energy of the SDOF oscillator. Nearly 100 % comes from vibration energy if n is increased to six. Therefore, a further increase of the order of the polynomial is not necessary for $x_0 = 0.10\,\mathrm{m}$. For a smaller initial displacement of $x_0 = 0.05\,\mathrm{m}$ and $n = 5$, 11.4 % of $E_r(t_1 = T_{ru})$ is provided by the actuators of the TRD and 88.6 % comes from vibration energy. By increasing the order to $n = 10$, only 5.6 % of $E_r(t_1 = T_{ru})$ comes from the actuators of the TRD and 94.4 % from vibration energy. A further increase of the order n does not lead to a further reduction of the positive work to be done by the actuators during the RUP, see figure 2.36/A. Therefore, for $x_0 = 0.05\,\mathrm{m}$, a polynomial with an order of $n = 10$ is chosen. Corresponding coefficients and ramp-up trajectories are shown in figure 2.37 and table 2.7a.

For the following tests, a ramp-up trajectory with $n = 10$ and the coefficients of table 2.7a is used. However, as shown in figure 2.36, the influence of the initial displacement on the energy to be provided by the actuators is crucial.

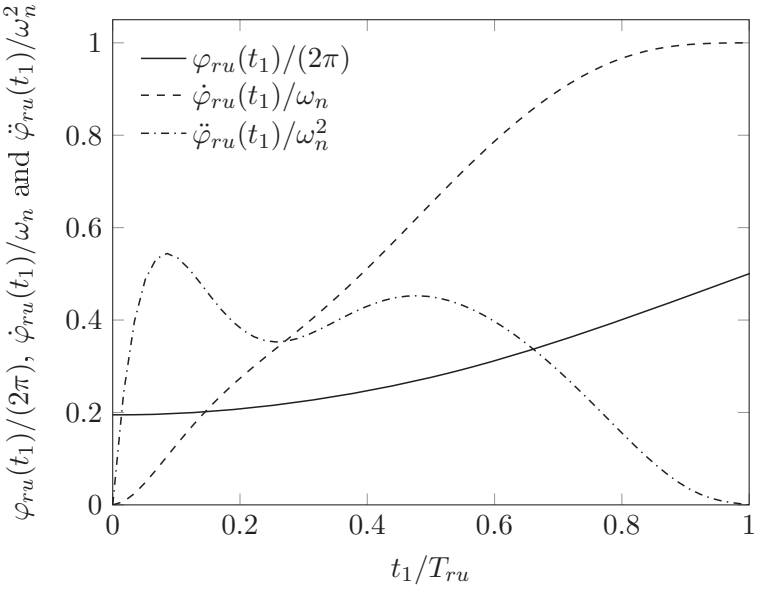

Figure 2.37: Ramp-up trajectory and corresponding time derivatives for $x_0 = 0.05\,\mathrm{m}$ and $n = 10$ [24]

Table 2.7: Coefficients of chosen trajectories

(a) Ramp-up trajectory

a_{10}	a_9	a_8	a_7	a_6	a_5
$-9.574 \cdot 10^3$	$3.300 \cdot 10^4$	$-4.923 \cdot 10^4$	$4.148 \cdot 10^4$	$-2.151 \cdot 10^4$	$6.956 \cdot 10^3$

a_4	a_3	a_2	a_1	a_0
$-1.349 \cdot 10^3$	$1.410 \cdot 10^2$	0	0	1.225

(b) Ramp-down trajectory

a_5	a_4	a_3	a_2	a_1	a_0
0.663	1.03	−4.27	0	5.37	4.71

Ramp-down trajectories were then developed according to subsection 2.5.2. The ramp-down angular position φ_d was set to 1.5π, the ramp-down duration to 1.00 s and the vibration-amplitude A_{off} to 0.01 m. Both parameters were varied such that the rotors are smoothly ramped-down. Inserting the conditions of (2.128) (φ_s is the a_0 value of table 2.7a) into (2.129) gives a system of equations. Solving this yields the coefficients of table 2.7b. Ramp-down trajectories and the corresponding time derivatives are shown in figure 2.38.

2.6.5 Closed-loop angular position and open-loop velocity control

In subsection 2.5.3, a closed-loop angular position control for the rotors was proposed. As the rotors are required to follow a ramp input in the continuous rotation mode, a steady-state error would occur if a controller with only a proportional feedback gain is used. A controller with integral and proportional action (PI controller) is therefore required.

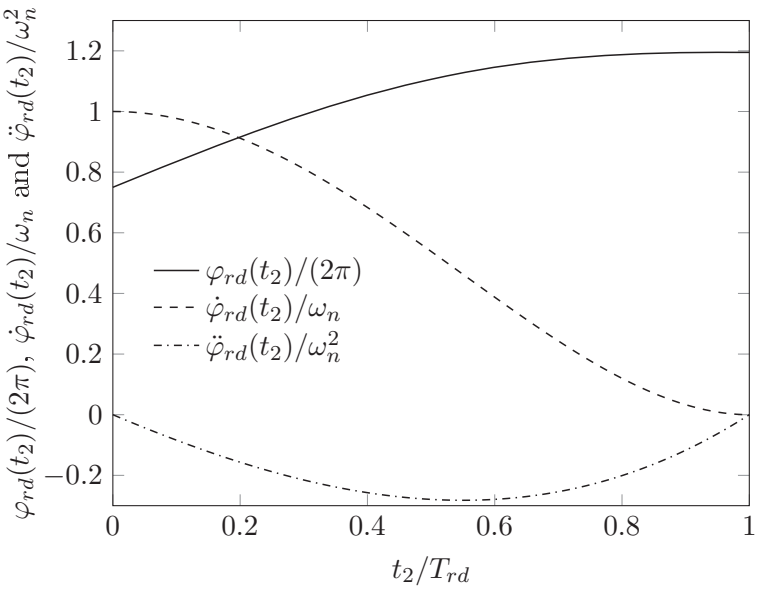

Figure 2.38: Ramp-down trajectory and corresponding time derivatives [24]

Instead of using a PI controller, open-loop angular velocity control can be applied in addition to the closed-loop angular position control. A target angular velocity (TAV) can be computed in addition to the TAP. For the RUP and the RDP, the TAVs are $\dot{\varphi}_{ru}(t_1)$ and $\dot{\varphi}_{rd}(t_2)$ (derivations of (2.123) and (2.129) with respect to time). Furthermore, for the continuous rotation mode, the TAV is the natural frequency of the SDOF oscillator. For the closed-loop angular position controller, a proportional feedback gain is then sufficient. Additionally, to suppress measurement noise in $\varphi(t)$, a pole is added. This control scheme is shown in figure 2.39 for the first actuator.

The control effort $u_{a,1}(t)$ of figure 2.39 is computed by

$$u_{a,1}(t) = \frac{1}{b_1}\dot{\varphi}_t(t) + C(s)ce_1(t) \tag{2.148}$$

in which the first term is the control effort due to the open-loop velocity control and the second term is the control effort due to the closed-loop angular position control. The same control scheme and controller is used for the other actuator.

Stability of the control scheme of figure 2.39 is now discussed. The observer of the SDOF-oscillator uses the measured displacement to produce an estimate of the displacement and the velocity. Due to the pole placement of subsection 2.6.2, the poles lie in the left half-plane (see figure 2.35); thus, this subsystem is stable.

The observed displacement and the observed velocity are then fed to the next block 'Computation of TAP and TAV.' For the RUP and the RDP, the TAPs are as shown in figure 2.37 and 2.38. During the continuous rotation mode, the TAP is computed according to (2.55) (TAP of the continuous rotation mode) and the TAV is set equal to the natural frequency ω_n. Therefore, the block 'Computation of TAP and TAV' computes values for the TAP and the TAV within a limited value range. Furthermore, as there are no feedback loops in this block, the question of stability does not arise.

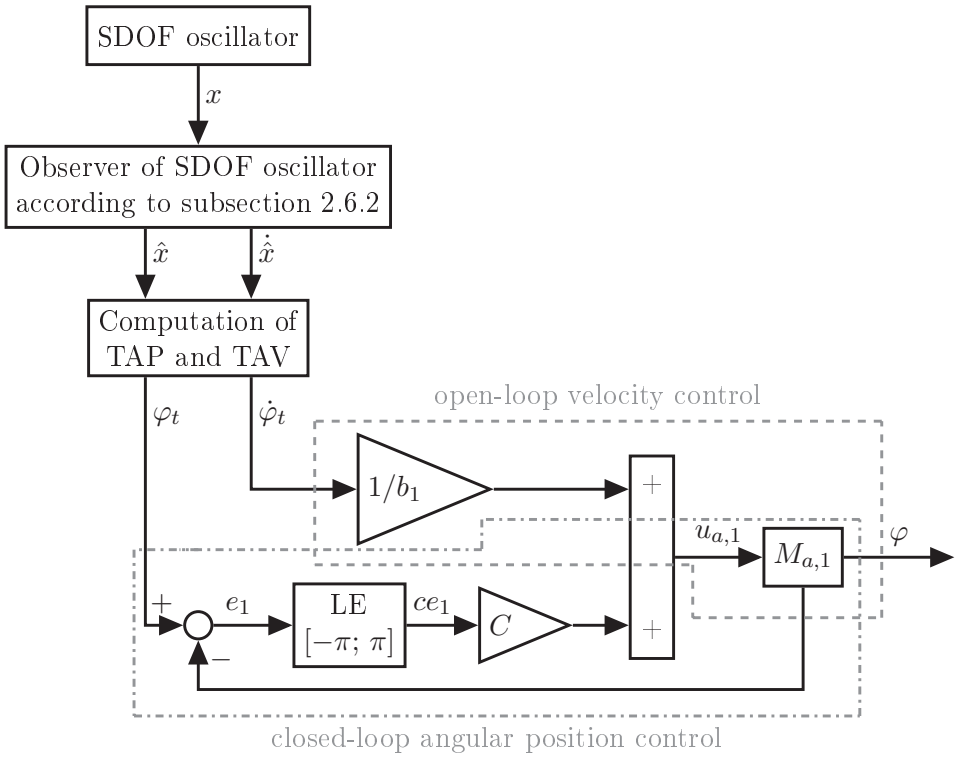

Figure 2.39: Generation of control effort for actuators

For the open-loop velocity control, the TAV is multiplied by $1/b$, see figure 2.39. This multiplication scales the TAV. Therefore, the control effort produced by the open-loop angular velocity control also has a limited output.

The closed-loop angular position control ensures that the (measured) angular position tracks the TAP. The closed-loop controller consists of a simple proportional feedback gain K_P with the additional pole to reduce measurement noise. The unit of K_P is V/(rad), which is dropped in the following. As all actuators are described by transfer functions with the same form, is suffices to check the stability of one actuator. This is done explanatory for actuator one, see (2.146) and table 2.6 ($M_{a,1}(s)$). Note that the block 'LE' restricts the input of the controller to values between $-\pi$ and π, see subsection 2.5.3. This does not alter the dynamics of the closed-loop. A controller as shown in (2.149) was chosen.

$$C(s) = \frac{K_P}{1 + 0.05s} \tag{2.149}$$

The transfer function of actuator one is as given in (2.150), see (2.146) and table 2.6.

$$M_{a,1}(s) = \frac{3.14}{1.50 \cdot 10^{-3}s^2 + s} \tag{2.150}$$

If $C(s)$ is as shown in (2.149), the open-loop transfer function $C(s)M_{a,1}(s)$ is:

$$C(s)M_{a,1}(s) = \frac{3.14K_P}{7.5 \cdot 10^{-5}s^3 + 0.0515s^2 + s} \tag{2.151}$$

The Root Locus of the open-loop configuration is as shown in figure 2.40.

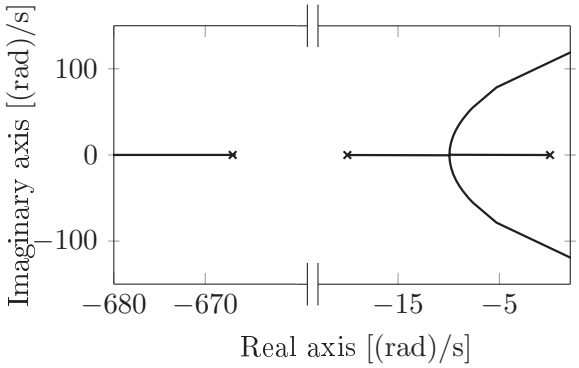

Figure 2.40: Root Locus of open-loop configuration for motor 1

The Root Locus diagrams for the other actuators are nearly the same. With increasing K_P, the left pole moves on the real axis towards minus infinity, whereas the other poles migrate towards each other until they meet; coming together at $s \approx -10\,(\text{rad})/\text{s}$. At that point, they break away from the real axis. At $K_P \approx 220$, they cross into the right half-plane and the controller would become unstable. Thus, the closed-loop angular position control for actuator one is stable for $K_P < 220$. In conjunction with the open-loop angular velocity control, adequate tracking results are already achieved for $K_P = 1$; therefore, K_P is set to one for the free vibration tests of this section for all actuators.

2.6.6 Test results

Tests were performed with a sampling frequency of 500 Hz. Figure 2.41 shows the uncontrolled and controlled displacement response of the SDOF oscillator.

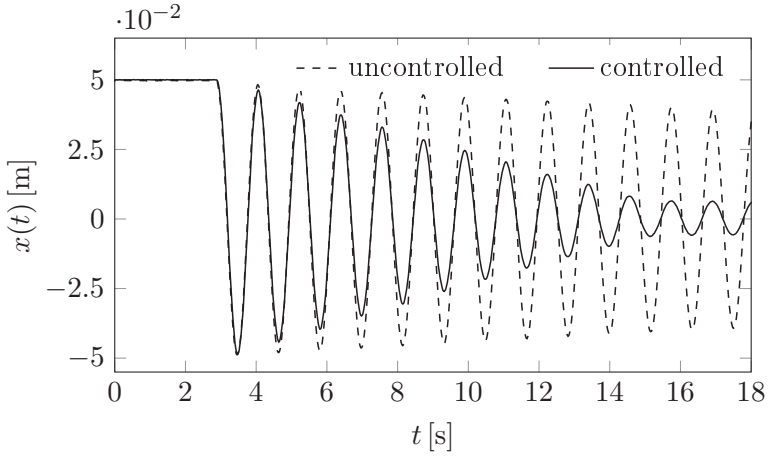

Figure 2.41: Free vibration test showing uncontrolled and controlled displacement response of SDOF oscillator

The table is released from an initial displacement, $x_0 = 0.05\,\text{m}$, at $t = 2.6\,\text{s}$. Until $t = 2.9\,\text{s}$, the uncontrolled and the controlled responses coincide. At $t = 2.9\,\text{s}$, the acceleration response of the SDOF oscillator changes sign from minus to plus. At this instant, the vibration amplitude exceeds A_{on} and the RUP is initiated. It ends at $t = 3.4\,\text{s}$ when the controlled displacement response changes sign from minus to plus (in other words, when the SDOF oscillator completes a half period). After the RUP, the TRD operates in the

continuous rotation mode until the vibration amplitude falls below A_{off}. Considering the uncontrolled displacement response in the time interval from $t = 3.8\,\mathrm{s}$ to $t = 14.3\,\mathrm{s}$, the vibration amplitude decays from 4.82 cm to 4.10 cm; this corresponds to a decay rate of 0.068 cm/s. Considering the controlled displacement response during the same time interval, the vibration amplitude decays from 4.63 cm to 0.81 cm. This corresponds to a decay rate of 0.36 cm/s. This means that by implementing one TRD unit with a mass-radius control product $m_c r$ of 0.0430 kgm, the decay rate is increased by a factor of about 5.3. When the vibrations fall below the lower vibration-amplitude threshold and the TAP surpasses the ramp-down angular position, the RDP is initiated. This is the case at $t = 14.4\,\mathrm{s}$. The rotors are then brought to the starting angular position.

Figure 2.42 shows the TAP computed by the electronic monitoring system.

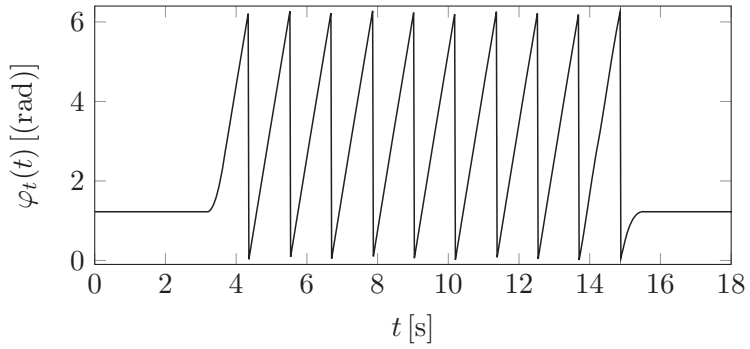

Figure 2.42: TAP $\varphi_t(t)$ computed by the electronic monitoring system belonging to figure 2.41

It becomes evident that the TAP has the desired continuous form; this results in a smooth run of the rotors. The same yields for the target angular velocity $\dot{\varphi}_t(t)$, which is not shown.

Figure 2.43 shows the post-computed angular velocity of rotor one. It is obtained by multiplying the recorded control effort $u_{a,1}$ given to the first actuator (from the electronic monitoring system) with the transfer function $M_{v,1}$, see (2.147) and table 2.6.

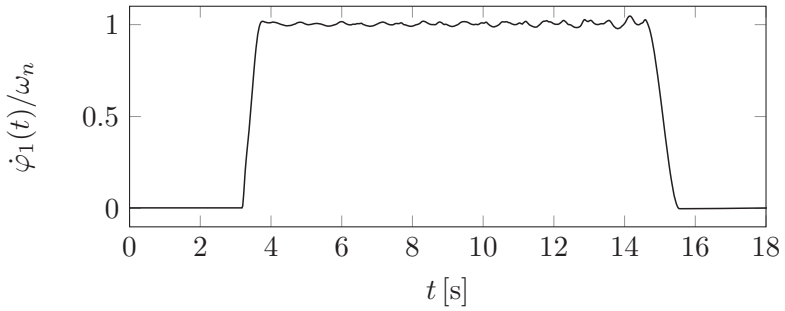

Figure 2.43: Post-computed angular velocity $\dot{\varphi}_1(t)$ belonging to figure 2.41

With the chosen proportional gain K_P of 1.0, the absolute value of the control errors $ce_1(t)$ and $ce_2(t)$ did not exceed 0.09 (rad) ($\approx 5\,^\circ$). By further increasing K_P, more accurate tracking is achieved. However, to calculate the power demands on the actuators, the angular accelerations $\ddot{\varphi}_1(t)$ and $\ddot{\varphi}_2(t)$ are needed. These signals become more noisy the higher K_p is set.

The power of both actuators can be computed with help of a post computation. The power of the TRD unit is

$$P_T(t) = \dot{\varphi}_1(t)M_1(t) + \dot{\varphi}_2(t)M_2(t) \tag{2.152}$$

in which $\dot{\varphi}_1(t)$, $\dot{\varphi}_2(t)$, $M_1(t)$ and $M_2(t)$ refer to the angular velocities of the rotors and the moments created by the actuators. Solving the motor equation of (2.14) for $M(t)$ and inserting this into (2.152) gives:

$$P_T(t) = \dot{\varphi}_1(t)\left[J\ddot{\varphi}_1(t) - 0.5m_c r\ddot{x}(t)\sin\left(\varphi_1(t)\right)\right] + \dot{\varphi}_2(t)\left[J\ddot{\varphi}_2(t) - 0.5m_c r\ddot{x}(t)\sin\left(\varphi_2(t)\right)\right] \tag{2.153}$$

$x(t)$, $\varphi_1(t)$ and $\varphi_2(t)$ are measured states. $\ddot{x}(t)$, $\dot{\varphi}_1(t)$, $\ddot{\varphi}_1(t)$, $\dot{\varphi}_2(t)$ and $\ddot{\varphi}_2(t)$ can be obtained by taking the time derivatives; this results in noisy signals which are unsuitable for further calculations. To cope with this issue, the signals $\ddot{x}(t)$, $\dot{\varphi}_1(t)$, $\ddot{\varphi}_1(t)$, $\dot{\varphi}_2(t)$ and $\ddot{\varphi}_2(t)$ are derived in a different manner. For the acceleration $\ddot{x}(t)$ of the SDOF, the observed velocity $\hat{\dot{x}}$ is differentiated numerically. The observer is tuned as discussed in subsection 2.6.2. To produce the signals $\dot{\varphi}_1(t)$, $\ddot{\varphi}_1(t)$, $\dot{\varphi}_2(t)$ and $\ddot{\varphi}_2(t)$, the models of the actuators from subsection 2.6.3 are used. By recording the control efforts $u_{a,1}$ and $u_{a,2}$ fed to the actuators, the angular velocities ($\dot{\varphi}_1(t)$ and $\dot{\varphi}_2(t)$) of the rotors can be re-produced by using $u_{a,1}$ and $u_{a,2}$ as inputs for the transfer function of (2.146) with the coefficients given in table 2.6. Multiplying the transfer function of (2.147) with the Laplace variable s gives the transfer function

$$M_{ac}(s) = \frac{bs}{as+1} \tag{2.154}$$

It has the control effort u_a as input and the angular acceleration of the corresponding rotor as output. With help of this transfer function, the angular accelerations of the rotors are post-computed. Figure 2.44 shows the power according to (2.153).

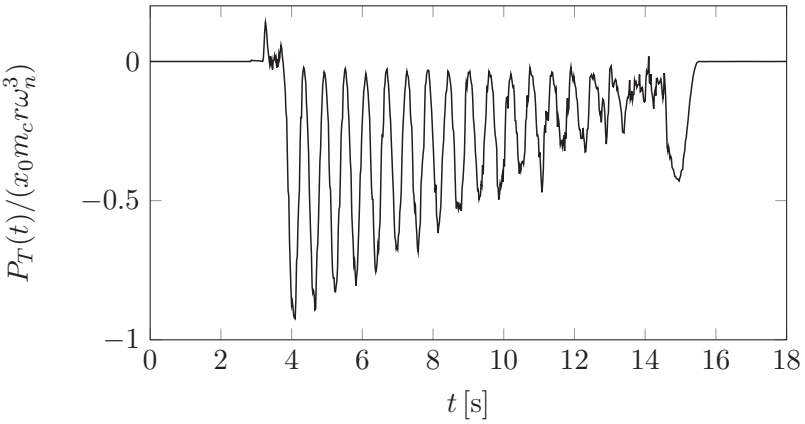

Figure 2.44: Power of TRD belonging to figure 2.41 [24]

The power of the TRD is nearly always smaller than zero, therefore the actuators perform negative work on the rotors (braking). Positive power is only required during the RUP. Integrating the positive power over the RUP from $t = 3.2\,\mathrm{s}$ to $t = 3.7\,\mathrm{s}$ gives the positive work done by the actuators on the rotors. This positive work is approximately $5.0 \cdot 10^{-3}\,\mathrm{J}$ and corresponds to 14 % of the rotational energy the rotors have in the continuous rotation mode. For the design of the RUP, it was only approximately 5 %, see figure 2.36/A for $n = 10$. The difference is due to model inaccuracies. Furthermore, due to the transition, see figure 2.28, a deviation from the optimal trajectory designed in subsection 2.6.4 is prescribed leading to a larger energy consumption.

In the continuous rotation mode, the power curve of the TRD has a similar shape as the power curve of figure 2.22. Note that in figure 2.22, only one vibration period is considered and the vibration amplitude does not decay in time. However, as the acceleration amplitude of the SDOF oscillator decays with time, the power of the TRD also decays.

At $t = 14.5\,\mathrm{s}$, the TRD exits the continuous rotation mode. Therefore, the rotors are decelerated and brought back to the starting angular position. Negative work is done by the actuators of the TRD on the rotors during the RDP.

To validate the experimental verification and the corresponding post computations, i.a. (2.152) and (2.153), the energy balance is checked, see the following equation

$$E_{v,0} + E_T(t) = E_v(t) + E_d(t) \tag{2.155}$$

in which $E_{v,0}$, $E_T(t)$ and $E_d(t)$ refer to the initial vibration energy, the work done by actuators and the dissipated energy given by

$$E_{v,0} = \frac{1}{2}\left(m + m_c\right)\dot{x}(t = t_l)^2 + \frac{1}{2}kx(t = t_l) \tag{2.156}$$

$$E_d(t) = 2\xi\omega_n(m + m_c)\int_{t_l}^{t_u} \dot{x}(t)^2 \mathrm{d}t \tag{2.157}$$

$$E_T(t) = \int_{t_l}^{t_u} P_T(t)\mathrm{d}t \tag{2.158}$$

in which t_l and t_u refer to the time-points at which the RUP is initiated and the RDP is terminated, respectively. As the rotors are at rest at t_l and t_u, the energy stored in the rotors (rotational kinetic energy) can be neglected as the energy terms are zero at these times. The translational kinetic energy stored in the control masses is considered in (2.100) and (2.156). For the velocity $\dot{x}(t)$ in (2.156) and (2.157), the observed velocity $\dot{\hat{x}}(t)$ is used. The computed energy terms are shown in table 2.8.

Table 2.8: Energy terms of (2.155) corresponding to the test of figure 2.41 to 2.44 from $t_l = 3.2\,\mathrm{s}$ to $t_u = 15.5\,\mathrm{s}$

$E_{v,0}$ [J]	$E_T(t_u)$ [J]	$E_v(t_u)$ [J]	$E_d(t_u)$ [J]
1.20	−1.06	0.02	0.18

When calculating the terms on both sides of (2.155), there is an energy difference ΔE of 0.06 J. Comparing this energy difference ΔE to the work done by the actuators gives: $\Delta E / E_T(t) \approx 0.057$. This corresponds to 5.7 % and validates the post-computation in which the power demand on the actuators was estimated. Evaluating the energy balance is an adequate tool for analyzing the quality of post-computations. A comment on the energy balance in given in the Appendix A.1.

2.7 Discussion

In the previous section, a closed-loop control algorithm for operating the TRD in the continuous rotation mode including ramp-up and ramp-down trajectories was presented. The algorithm was validated experimentally, demonstrating the energy and power advantages of the TRD. Some questions arise, which are discussed in the following:

- The TAP was computed using (2.55) which provides a static computation provided that the natural circular frequency of the SDOF oscillator is known. Tracking this TAP ensures the anti-phasing between the velocity of the SDOF oscillator and the control force of the TRD. Alternatively, the phase of the velocity of the SDOF oscillator can be detected using phase-locked loop (PLL) systems [34, 35]. Using the phase of the velocity of the SDOF oscillator, a TAP for the rotors can be calculated such that the resulting control force counteracts the velocity of the SDOF oscillator. However, PLL systems inherit dynamics which must be set accordingly. This requires additional tuning effort. On the other hand, PLL systems additionally and continuously provide the dominant frequency of the signal. However, as the natural circular frequency of the SDOF oscillator is assumed as known, the static computation for the TAP according to (2.55) was and will be used in this work.

- As long as the angular velocity of the rotors is constant, which is the case in the continuous rotation mode, only mono-frequent sinusoidal control forces are generated. This is a disadvantage in the case that the vibrations being damped do not exhibit dominant frequencies but have a broadband spectrum. On the other hand, when the vibrations occur with one or a few dominant frequencies to which the TRD or multiple TRDs can be tuned, the TRD can still be effective for systems under stochastic loading [36]. In [36], numerical simulations were performed with a former, less energy-efficient control algorithm. The numerical and experimental investigation of the TRD for the damping of stochastically forced vibrations is discussed and further developed in chapter 3.

- Another particularity of the continuous rotation mode is that the magnitude of the control force cannot be easily changed during operation. This is a serious disadvantage when the vibration amplitude becomes small and can result in a re-excitation of the SDOF oscillator. However, various methods, presented in [23], have been proposed to prevent this undesired outcome. One method, the on-off method was further elaborated and presented in this section. Two further methods are developed in section 2.9.

- With the control algorithm presented in this section, the TRD cannot bring the vibrations to rest as the device is turned off when the vibration amplitude falls below a certain threshold, see figure 2.41. To bring the SDOF oscillator to rest, an alternative mode of operation, the swinging mode, can be used. A control algorithm which automatically switches between the continuous rotation mode (for large vibration amplitudes) and the swinging mode (for small vibration amplitudes) is presented in chapter 3. With the control algorithm presented in this section, the TRD is only effective for vibrations above a certain vibration-amplitude threshold.

2.8 Steady-state response of SDOF oscillator with and without the twin rotor damper

2.8.1 Introduction

The steady-state damping performance of damping devices can be evaluated with help of frequency-ratio dynamic-amplification relations. Such relations can be derived analytically, numerically or experimentally. Analytic solutions are more elegant; however, for many mechanical systems, especially those with non-linear characteristics, analytic solutions can often not be derived. In such cases, dynamic-amplification frequency-ratio relations are derived numerically or experimentally. In this section, which is partly published in [37, 38], an analytic solution is presented and subsequently validated experimentally.

2.8.2 Uncontrolled response

To investigate the steady-state response of the SDOF oscillator, (2.11) is recalled

$$\ddot{x}(t) + 2\xi\omega_n\dot{x}(t) + \omega_n^2 x(t) = \mu_c r\left[\dot{\varphi}(t)^2\cos\varphi(t) + \ddot{\varphi}(t)\sin\varphi(t)\right] + F_e(t) \tag{2.159}$$

in which $F_e(t)$ is now a (normalized) harmonic excitation force given by

$$F_e(t) = F_0\cos(\omega_e t) \tag{2.160}$$

where ω_e denotes the (angular) excitation frequency and F_0 the (normalized) amplitude of the excitation force.

In this subsection, the uncontrolled response is presented. This is a brief summary presented for the purpose of a simple derivation of the controlled response of the SDOF oscillator. Information regarding the uncontrolled response of the SDOF oscillator can be found in many textbooks, e.g. [1, 25]. For the uncontrolled response, the forces produced by the TRD are neglected. Consequently, with (2.160), (2.159) simplifies to:

$$\ddot{x}(t) + 2\xi\omega_n\dot{x}(t) + \omega_n^2 x(t) = F_0\cos(\omega_e t) \tag{2.161}$$

A variety of techniques to solve (2.161) can be found, see e.g. [**?**]. The steady-state response is described by the particular solution of (2.161). The particular displacement response of a SDOF oscillator with inherent damping under harmonic excitation is:

$$x_p(t) = A_u\cos(\omega_e t - \phi) \tag{2.162}$$

in which A_u and ϕ refer to the displacement amplitude and the phase the displacement response lags behind the excitation force [1]. As shown in [1, 25], A_u and ϕ are given by the following equations

$$A_u = \frac{F_0}{\sqrt{\left(\omega_n^2 - \omega_e^2\right)^2 + \left(2\xi\omega_n\omega_e\right)^2}} \tag{2.163}$$

$$\phi = \operatorname{atan2}\left(2\xi\omega_n\omega_e, \omega_n^2 - \omega_e^2\right) \tag{2.164}$$

In (2.164) and in contrast to [1, 25], the atan2-function is used. It considers the full range of ϕ (zero to 2π) and therefore allows for a more simple detection of the appropriate solution when deriving the controlled steady-state response, see subsection 2.8.3.

Introducing the frequency ratio

$$\eta = \frac{\omega_e}{\omega_n} \tag{2.165}$$

and doing some rearrangements with (2.163) and (2.164), they can be rewritten as shown in (2.166) and (2.167) [1].

$$\frac{A_u \omega_n^2}{F_0} = \frac{1}{\sqrt{(1-\eta^2)^2 + (2\xi\eta)^2}} \tag{2.166}$$

$$\phi = \operatorname{atan2}\left(2\xi\eta, 1-\eta^2\right) \tag{2.167}$$

In many textbooks, the term F_0/ω_n^2 is referred to as static displacement. Note that the fraction $A_u\omega_n^2/F_0$ is dimensionless and is, from here on, referred to as dynamic amplification:

$$D = \frac{A_u \omega_n^2}{F_0} \tag{2.168}$$

The dynamic amplification D and the phase ϕ are plotted against frequency ratio η in figure 2.45.

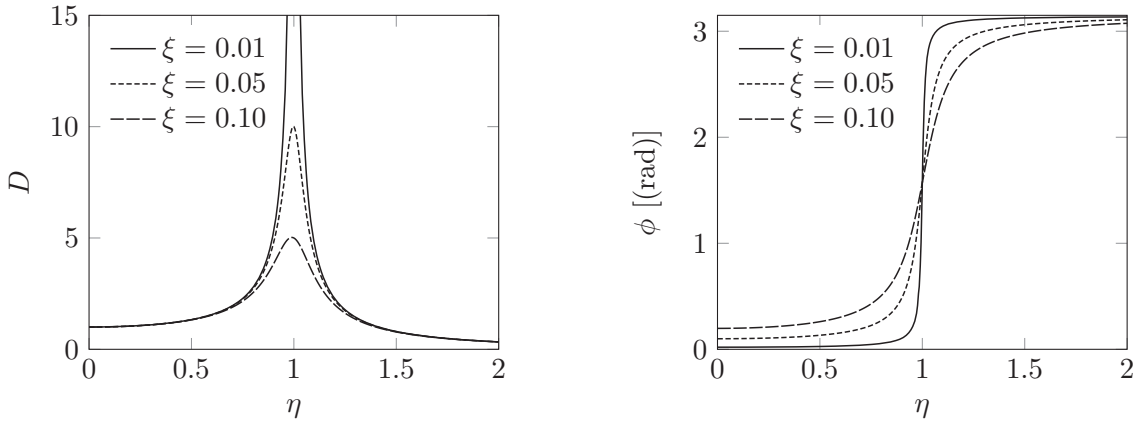

Figure 2.45: Dynamic amplificataion D and phase ϕ plotted against frequency ratio η for several different values of the damping ratio ξ [1]

Curves are plotted for oscillators with small inherent damping ($\xi \leq 0.1$). As the excitation frequency goes against the natural circular frequency ($\eta \to 1$), the dynamic amplification approaches a maximum value, for more information, see [1, 25].

2.8.3 Controlled response

In order to study the steady-state response including the action of the TRD, (2.159) is recalled. Tangential forces produced by the TRD are neglected as it is assumed that the TRD is operated in the continuous rotation mode. Thus, only the radial forces are considered and (2.159) simplifies to:

$$\ddot{x}(t) + 2\xi\omega_n\dot{x}(t) + \omega_n^2 x(t) = \mu_c r \dot{\varphi}(t)^2 \cos\varphi(t) + F_e(t) \tag{2.169}$$

Furthermore, it is assumed that the angular velocity $\dot{\varphi}(t)$ is constant and equal to the excitation frequency ω_e:

$$\dot{\varphi}(t) = \omega_e \tag{2.170}$$

This assumption is further discussed in subsection 2.8.6.

Inserting (2.170) and (2.160) into (2.169), it follows:

$$\ddot{x}(t) + 2\xi\omega_n\dot{x}(t) + \omega_n^2 x(t) = \mu_c r\omega_e^2 \cos\varphi(t) + F_0 \cos(\omega_e t) \tag{2.171}$$

As $\varphi(t)$ changes linearly in time ($\dot{\varphi} = \omega_e$), the control force of the TRD (first term on the right-hand side of (2.171)) is harmonic. Maximum damping action is achieved if the harmonic control force, $\mu_c r\omega_e^2 \cos\varphi(t)$, is set in anti-phase to the excitation force, $F_0 \cos(\omega_e t)$, see (2.171) [23]. To achieve this, information about the phase of the excitation force must be available. However, the excitation force is usually unknown and cannot be easily measured. Alternatively and in contrast to the derivations of [23], the states $x(t)$ and $\dot{x}(t)$ of the SDOF oscillator can be made available and used as feedback. By setting the control force of the TRD in anti-phase to the velocity of the SDOF oscillator, satisfying and realizable damping performance is achieved.

The second term on the left-hand side of (2.171) is the (normalized) inherent damping force of the SDOF oscillator. This inherent damping force acts in anti-phase to the velocity of the SDOF oscillator. The control algorithm presented in section 2.6 is used to ensure the anti-phasing between the control force of the TRD and the velocity of the SDOF oscillator. Taking this into consideration, the control force can be brought to the left-hand side of (2.171) as a function of the velocity $\dot{x}(t)$. This is done by firstly taking the time derivative of (2.162):

$$\dot{x}_p(t) = -A_c\omega_e \sin(\omega_e t - \phi_c) \tag{2.172}$$

in which A_u was replaced by the unknown controlled displacement amplitude A_c and ϕ by the unknown controlled phase ϕ_c. Both A_c and ϕ_c are derived further on. Secondly, dividing (2.172) by the absolute value of its amplitude $A_c\omega_e$ and multiplying it with the amplitude $\mu_c r\omega_e^2$ of the control force (first term on the right-hand side of (2.171)), the control force is now expressed as a function of the velocity on the left-hand side, see the following equation:

$$\ddot{x}(t) + \left[2\xi\omega_n + \frac{\mu_c r\omega_e}{A_c}\right]\dot{x}(t) + \omega_n^2 x(t) = F_0 \cos(\omega_e t) \tag{2.173}$$

The cosine term of the control force of (2.171) drops out as the sign convention and the velocity dependent formulation ensure the anti-phasing between the control force of the TRD and the velocity of the SDOF oscillator. Note that (2.173) is only valid if a control algorithm is available ensuring this anti-phasing.

By setting the term in the square bracket equal to $2\xi_{eq}\omega_n$, an equivalent damping ratio ξ_{eq} can be calculated, see the following equation.

$$2\xi_{eq}\omega_n = 2\xi\omega_n + \frac{\mu_c r\omega_e}{A_c} \tag{2.174}$$

Note that the terms of the left-hand side of (2.173) represent the system forces ($f_i(t)$, $f_d(t)$ and $f_s(t)$) and the normalized control force $f_c(t)$ of the TRD. The term on the right-hand side represents the excitation force $f_e(t)$. These forces are shown in the following equation and will be discussed further later on.

$$\frac{f_i(t)}{m+m_c} = \ddot{x}(t) \qquad \frac{f_d(t)}{m+m_c} = 2\xi\omega_n\dot{x}(t) \qquad \frac{f_c(t)}{m+m_c} = \frac{\mu_c r\omega_e}{A_c}\dot{x}(t) \tag{2.175}$$

$$\frac{f_s(t)}{m+m_c} = \omega_n^2 x(t) \qquad \frac{f_e(t)}{m+m_c} = F_0 \cos(\omega_e t)$$

The second term in the square bracket of (2.173) now describes the control force. Comparing (2.161) with (2.173), the substitution as given in (2.176) must be performed.

$$2\xi\omega_n \rightarrow 2\xi\omega_n + \frac{\mu_c r \omega_e}{A_c} \tag{2.176}$$

Applying the substitution of (2.176) on the uncontrolled solution of (2.163) and (2.164) yields the following two expressions for the previously unknown controlled displacement amplitude A_c and the controlled phase ϕ_c:

$$A_c = \frac{F_0}{\sqrt{(\omega_n^2 - \omega_e^2)^2 + \left(2\xi\omega_n\omega_e + \frac{\mu_c r \omega_e^2}{A_c}\right)^2}} \tag{2.177}$$

$$\phi_c = \operatorname{atan2}\left[\left(2\xi\omega_n + \frac{\mu_c r \omega_e}{A_c}\right)\omega_e, \omega_n^2 - \omega_e^2\right] \tag{2.178}$$

Note that ϕ_c depends now on A_c. Therefore, (2.177) must be solved first for A_c. Doing some rearrangements with (2.177) gives:

$$\left[\left(\omega_n^2 - \omega_e^2\right)^2 + 4\xi^2\omega_n^2\omega_e^2\right] A_c^4 + 4\xi\omega_n\omega_e^3\mu_c r A_c^3 + \left(\mu_c^2 r^2 \omega_e^4 - F_0^2\right) A_c^2 = 0 \tag{2.179}$$

The trivial solutions ($A_c = 0$) are not further considered as they have no physical meaning. A quadratic equation remains. It provides two non-trivial solutions for A_c, which are

$$A_c = \frac{-2\xi\omega_n\omega_e^3\mu_c r \pm \sqrt{F_0^2\left[\left(\omega_n^2 - \omega_e^2\right)^2 + \left(2\xi\omega_n\omega_e\right)^2\right] - \left(\omega_e^2\mu_c r\right)^2\left(\omega_n^2 - \omega_e^2\right)^2}}{\left(\omega_n^2 - \omega_e^2\right)^2 + \left(2\xi\omega_n\omega_e\right)^2} \tag{2.180}$$

As done before for the uncontrolled steady-state response, (2.180) is divided by F_0 and multiplied with ω_n^2. This leads to the normalized controlled displacement amplitude of the SDOF oscillator in steady-state, see (2.181).

$$\frac{A_c\omega_n^2}{F_0} = \frac{\frac{-2\xi\omega_n^3\omega_e^3\mu_c r}{F_0} \pm \omega_n^2\sqrt{\left(\omega_n^2 - \omega_e^2\right)^2 + \left(2\xi\omega_n\omega_e\right)^2 - \left(\frac{\omega_e^2\mu_c r}{F_0}\right)^2\left(\omega_n^2 - \omega_e^2\right)^2}}{\left(\omega_n^2 - \omega_e^2\right)^2 + \left(2\xi\omega_n\omega_e\right)^2} \tag{2.181}$$

Introducing the controlled dynamic amplification

$$D_c = \frac{A_c\omega_n^2}{F_0} \tag{2.182}$$

and doing some further rearrangements with (2.181) using (2.165), it follows:

$$D_c = \frac{\frac{-2\xi\eta^3\omega_n^2\mu_c r}{F_0} \pm \sqrt{\left(1 - \eta^2\right)^2\left[1 - \left(\frac{\eta^2\omega_n^2\mu_c r}{F_0}\right)^2\right] + \left(2\xi\eta\right)^2}}{\left(1 - \eta^2\right)^2 + \left(2\xi\eta\right)^2} \tag{2.183}$$

By setting $\mu_c r$ equal to zero, the uncontrolled dynamic amplification is given, which is in accordance with (2.166).

SDOF oscillator without inherent damping

Considering a SDOF oscillator without inherent damping ($\xi = 0$), (2.183) simplifies to

$$D_c = \frac{\pm\sqrt{1-(\eta^2 K_1)^2}}{1-\eta^2} \tag{2.184}$$

in which K_1 is a positive dimensionless parameter given by:

$$K_1 = \frac{\omega_n^2 \mu_c r}{F_0} \tag{2.185}$$

D_c is real as $1-(\eta^2 K_1)^2 \geq 0$. Solving this inequality for η while considering that $\eta \geq 0$ and $K_1 \geq 0$, yields the following constraint

$$\eta \leq \eta_b = \sqrt[+]{\frac{1}{K_1}} \tag{2.186}$$

in which the border frequency ratio η_b is introduced. D_c can take positive and negative values.

If $D_c > 0$, then $A_c > 0$ as $\omega_n > 0$ and $F_0 > 0$, see (2.182). The TRD contributes positive active damping to the equivalent damping ratio if $A_c > 0$. Otherwise, the influence of the TRD would be negative (the control force of the TRD would be in phase with the velocity of the SDOF oscillator). Therefore, D_c must be greater than or equal to zero. To ensure that the TRD contributes positive damping, the cases

$$D_c = \begin{cases} \dfrac{\sqrt{1-(\eta^2 K_1)^2}}{1-\eta^2} & \text{for} \quad \eta < 1 \\ \text{undefined} & \text{for} \quad \eta = 1 \\ \dfrac{-\sqrt{1-(\eta^2 K_1)^2}}{1-\eta^2} & \text{for} \quad \eta > 1 \end{cases} \tag{2.187}$$

are distinguished.

Using (2.165) and (2.185) and considering that $\xi = 0$, ϕ_c given in (2.178) can be rearranged to:

$$\phi_c = \operatorname{atan2}\left(\frac{\eta^2 K_1}{D_c}, 1-\eta^2\right) \tag{2.188}$$

The controlled dynamic amplification D_c and the phase ϕ_c are plotted against the frequency ratio in figure 2.46 for several values of K_1.

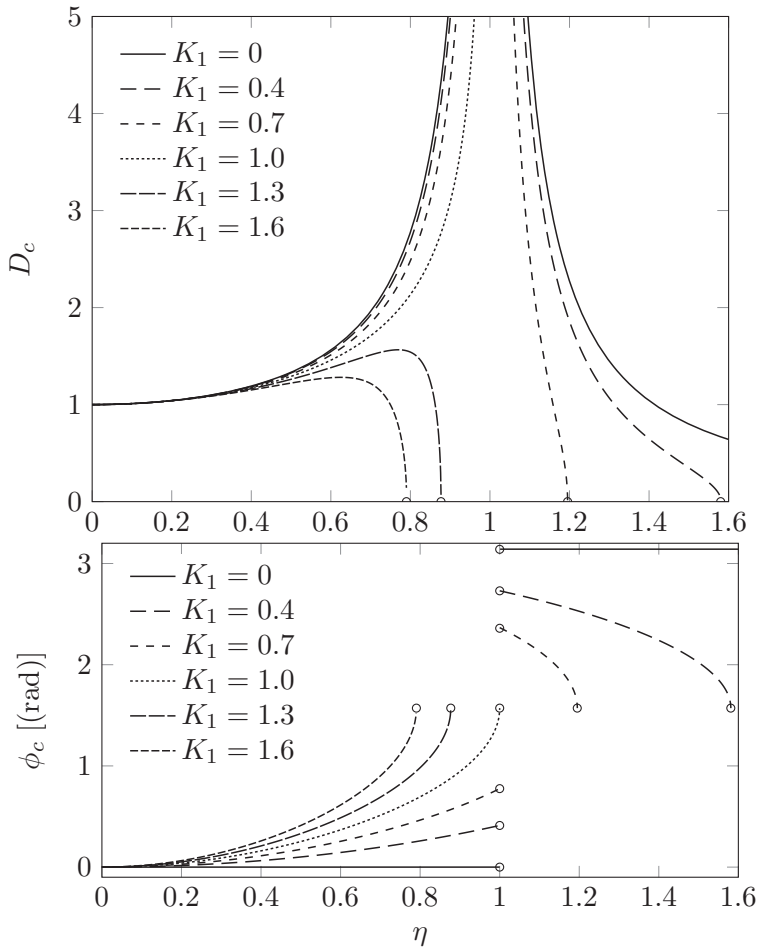

Figure 2.46: Controlled dynamic amplification D_c and phase ϕ_c plotted against frequency ratio η for several different values of K_1 for SDOF oscillators without inherent damping

The higher K_1 is, the higher the steady-state damping performance becomes. For $K_1 < 1$, $\eta_b > 1$. Therefore, the dynamic-amplification to frequency-ratio has a vertical asymptote and a phase jump at $\eta = 1$. In contrast, for $K_1 > 1$, the border frequency η_b is smaller than one. Therefore, the vertical asymptote and the phase jump at $\eta = 1$ do not exist.

The steady-state response can be represented in a pointer diagram. The mass-normalized force terms of (2.175) are additionally divided by ω_n^2 and A_c. Using (2.165), (2.182) and (2.185) and converting to complex notation gives the equations of (2.189). For completeness, $f_d(t)/(m + m_c)/\omega_n^2/A_c$ is also derived.

If K_1 and η are given, D_c can be calculated with (2.187). This was done for $K_1 = 0.5$ and $\eta = 1.2$. The corresponding vector diagram which depicts the forces described in (2.189) is shown in figure 2.47.

All vectors rotate with a constant length in the counterclockwise direction. It can be seen that the force superimposed by the amplitude of the inertial force $f_i(t)$, the control force $f_T(t)$ and the restoring spring force $f_s(t)$ is equivalent to the excitation force $f_e(t)$, see (2.173). If the frequency ratio η approaches η_b, the dynamic amplification D_c converges

to zero and the phase ϕ_c to 0.5π. At $\phi_c = 0.5\pi$, the SDOF oscillator would be at rest. This becomes evident when inserting the border frequency ratio of (2.186) into (2.187). Furthermore, it indicates that the excitation force and the control force of the TRD are in phase in figure 2.47. Note that these forces are on different sides in (2.173) and become infinite, see (2.189). As this state is physically not realizable, the solution at $\eta = \eta_b$ was excluded in figure 2.46.

$$\begin{aligned}
\frac{f_i(t)}{(m+m_c)\omega_n^2 A_c} &= \mathrm{Re}\left[-\eta^2 \mathrm{e}^{i(\omega_e t-\phi_c)}\right] \\
\frac{f_d(t)}{(m+m_c)\omega_n^2 A_c} &= \mathrm{Re}\left[2\xi\eta i \mathrm{e}^{i(\omega_e t-\phi_c)}\right] \\
\frac{f_c(t)}{(m+m_c)\omega_n^2 A_c} &= \mathrm{Re}\left[\frac{K_1\eta^2}{D_c} i \mathrm{e}^{i(\omega_e t-\phi_c)}\right] \\
\frac{f_s(t)}{(m+m_c)\omega_n^2 A_c} &= \mathrm{Re}\left[\mathrm{e}^{i(\omega_e t-\phi_c)}\right] \\
\frac{f_e(t)}{(m+m_c)\omega_n^2 A_c} &= \mathrm{Re}\left[\frac{1}{D_c}\mathrm{e}^{i\omega_e t}\right]
\end{aligned} \tag{2.189}$$

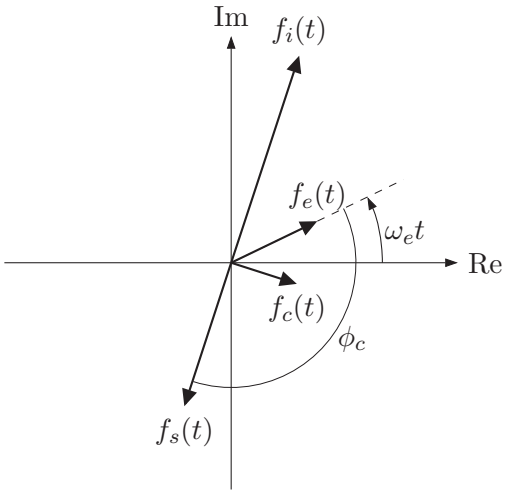

Figure 2.47: Pointer diagram for steady-state responses for $K_1 = 0.5$ and $\eta = 1.2$ [37]

The existence of the border frequency can be explained by considering the control force, see first term on the right-hand side of (2.171). If η is increased, the amplitude of the control force also increases as the angular velocity $\dot{\varphi}$ was set to ω_e, see (2.170). For $\eta < \eta_b$, the amplitude of the control force is smaller than the amplitude of the excitation force and steady-state is reached. At $\eta = \eta_b$, these amplitudes are equivalent.

The equivalent damping ratio ξ_{eq} for oscillators without inherent damping can be computed with (2.174). Doing some rearrangements of (2.174) and using (2.182), (2.185) and (2.187) yields:

$$\xi_{eq} = \left| \frac{1}{2} \frac{(1-\eta^2)\eta K_1}{\sqrt{1-(\eta^2 K_1)^2}} \right| \tag{2.190}$$

in which the absolute value of D_c is calculated to avoid the case distinction of (2.187).

Figure 2.48 shows the equivalent damping ratio plotted against the frequency ratio η for $K_1 = 0.5$ and $K_1 = 1.5$.

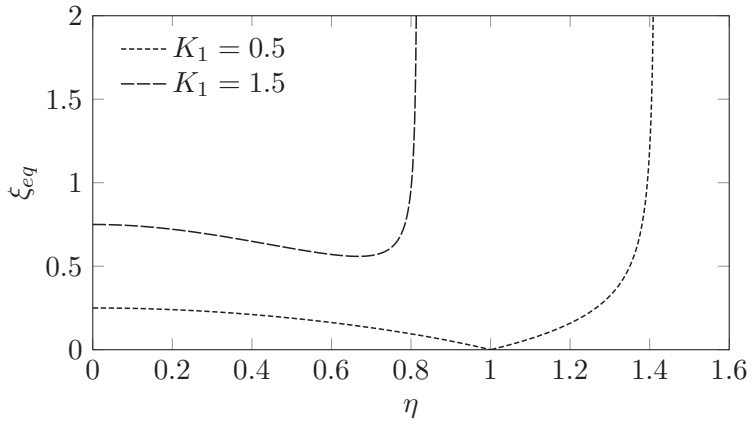

Figure 2.48: Equivalent damping ratio ξ_{eq} according to (2.190)

The equivalent damping ratio goes against infinity (vertical asymptote) for $\eta \to \eta_b$. For $K_1 = 0.5$, ξ_{eq} goes to zero if η approaches one. This means that the TRD does not give damping to the SDOF oscillator for $\eta = 1$. For $\eta > 1$, ξ_{eq} increases with η and goes to infinity if η approaches η_b.

To verify stability, the transfer function

$$G_{ss}(s) = \frac{1}{s^2 + \left(2\xi\omega_n + \dfrac{\mu_c r \omega_e}{A_c}\right) s + \omega_n^2} \tag{2.191}$$

is considered, in which s is the Laplace variable. $G_{ss}(s)$ was derived from (2.173). Its input is the excitation force and the output is x. The positions of the poles of $G_{ss}(s)$ can be represented with a Root Locus, see figure 2.49.

Figure 2.49 is valid for any K_1 and only valid for $\eta_b < 1$. At ①, $\xi_{eq} = 0$ and both poles lie on the imaginary axis at $s_{1,2} = \pm\omega_n j$. With increasing η, the TRD gives more and more damping to the SDOF oscillator until ② at which the poles come together on the real axis and ξ_{eq} reaches the critical damping ratio ($\xi_{eq} = 1$). The corresponding frequency ratio can be calculated by setting (2.190) equal to one. This can be done analytically; however, for simplicity, this is not done in here. From (2.191), it is evident that the damping contribution of the TRD to ξ_{eq} increases with $\mu_c r \omega_e$ and decreases with A_c. By further increasing η beyond ②, the poles run towards the origin and minus infinity. For $\eta \to \eta_b$, they converge to these points.

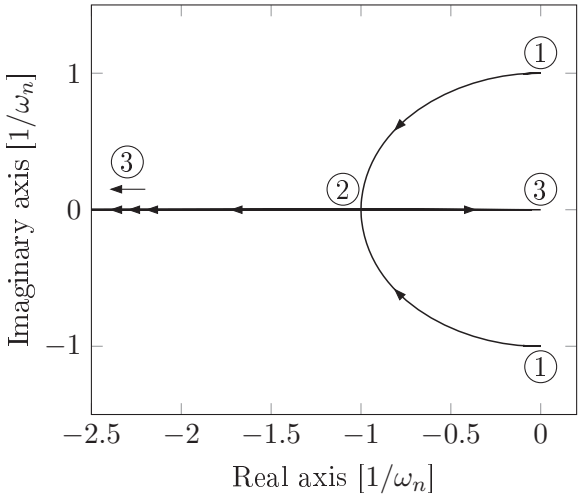

Figure 2.49: Root Locus for varying η [37]

For $\eta_b > 1$, the statements of the previous paragraph are not valid. When $\eta \to 1$, D_c and therefore A_c go to infinity, see figure 2.46. Consequently, the term $2\xi\omega_n + \mu_c r\omega_e/A_c$ approaches zero, which corresponds to an equivalent damping ratio of zero. This means that the poles move back to the point ① and $G_{ss}(s)$ becomes marginally stable again. Because of this, the TRD does not provide damping to the oscillator for $\eta = 1$. When η is increased above $\eta = 1$, the poles migrate towards ② and ξ_{eq} converges to one. By further increasing η, the poles converge to ③, as was the case for $\eta_b < 1$.

The results of the Root Locus of figure 2.49 are in accordance with the results of figure 2.46 and 2.48.

For $\eta > \eta_b$, the control force is larger than the excitation force and a steady-state solution cannot be found. When using the control algorithm of section 2.6, the TRD makes the vibrations decay until the vibrations fall below the vibration-amplitude threshold at which the TRD is turned off. Continued excitation increases the vibrations until an upper vibration-amplitude threshold is exceeded at which the TRD is turned back on.

If inherent damping is not present ($\xi = 0$) and $K_1 = 0$ (uncontrolled), the transient response does not die out and a beat occurs. Therefore, the steady-state with a single frequency can only be achieved by imposing the correct initial conditions to the SDOF oscillator. However, when the oscillator is controlled by the TRD, it adds damping. Therefore, steady-state is reached even though $\xi = 0$, except for $\eta = 1$.

SDOF oscillator with inherent damping

Now considering a SDOF oscillator with inherent damping, (2.185) and (2.183) can be rewritten as follows

$$D_c = \frac{\Xi_3(\eta) \pm \sqrt{\Xi_4(\eta)}}{\Xi_5(\eta)} \tag{2.192}$$

with the terms:

$$\begin{aligned}\Xi_3(\eta) &= -2\xi\eta^3 K_1 \\ \Xi_4(\eta) &= \left(1-\eta^2\right)^2\left[1-\left(\eta^2 K_1\right)^2\right]+(2\xi\eta)^2 \\ \Xi_5(\eta) &= \left(1-\eta^2\right)^2+(2\xi\eta)^2\end{aligned} \tag{2.193}$$

$\Xi_5(\eta) > 0$. The sign of D_c must be greater than zero according to the discussion following (2.186). To achieve this, the plus sign in (2.192) must be used as $\Xi_3(\eta) < 0$. However, it is possible that the nominator of (2.192), $\Xi_3(\eta) \pm \sqrt{\Xi_4(\eta)}$, is negative. At $\eta = 0$, the nominator is equal to one. It is assumed that η_b is reached when the control force amplitude $\mu_c r\omega_e^2$ is equal to the amplitude of the excitation force F_0, as was the case for oscillators without inherent damping. Note that $\mu_c r\omega_e^2$ increases with η, whereas F_0 is constant over η. Setting these amplitudes equal yields

$$\mu_c r\omega_e^2 = F_0 \tag{2.194}$$

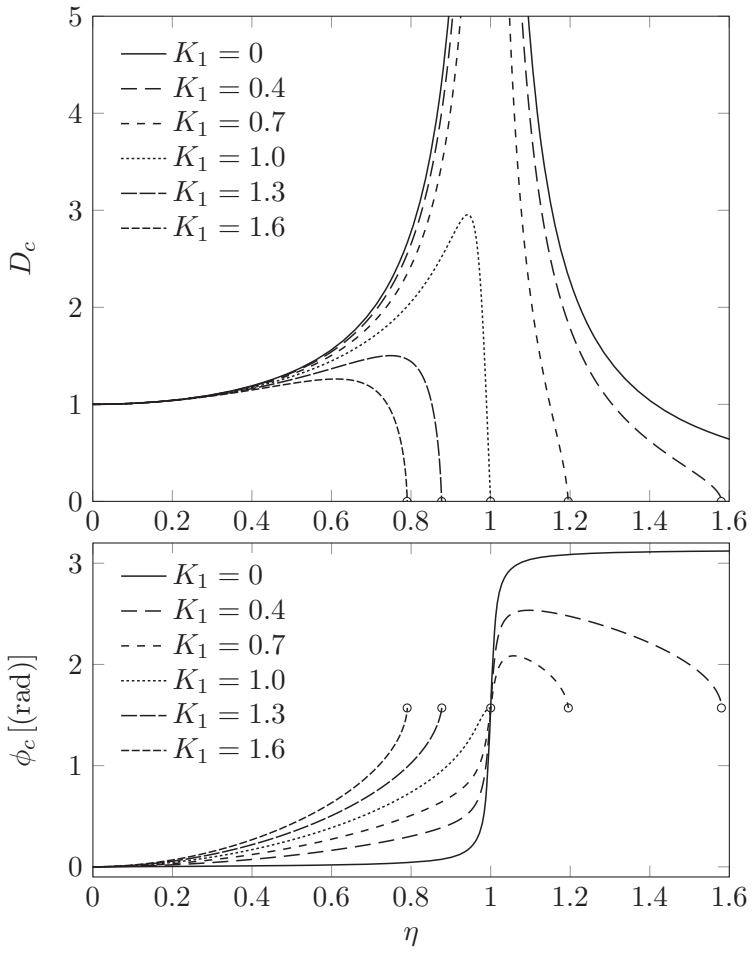

Figure 2.50: Controlled dynamic amplification D_c and phase ϕ_c plotted against frequency ratio η for $\xi = 0.01$ for several different values of K_1 [37]

Rearranging (2.165), (2.185) and (2.194) and replacing η by η_b yields:

$$\eta_b = \sqrt{\frac{1}{K_1}} \tag{2.195}$$

which is equal to (2.186). By varying the parameters according to the ranges given below

$$\begin{aligned} K_1 &> 0 \\ 0 < \xi &< 1 \\ 0 < \eta &< \eta_b \end{aligned} \tag{2.196}$$

it can be shown that the numerator of (2.192), $\Xi_3(\eta) \pm \sqrt{\Xi_4(\eta)}$, is greater than zero. Therefore, D_c is, as desired, greater than zero. By inserting (2.195) into (2.193) and subsequently (2.193) into (2.192), it follows: $D_c(\eta_b) = 0$. Using (2.165), (2.185) and (2.178), the controlled phase ϕ_c for the SDOF oscillator with inherent damping can be written as:

$$\phi_c = \text{atan2}\left[2\xi\eta + \frac{K_1\eta^2}{D_c}, 1-\eta^2\right] \tag{2.197}$$

The dynamic amplification D_c and the corresponding phase ϕ_c are plotted in figure 2.50 for several different values of K_1 and for $\xi = 0.01$. For oscillators with inherent damping and for $K_1 = 1$, D_c tends to zero if η approaches one.

As for oscillators without inherent damping, the forces can be represented in a pointer diagram, see figure 2.51. It shows that the normalized forces on the left hand-side of (2.175) sum up to the force on the right hand-side. The inherent damping force and the control force (both normalized) are in phase and they add together to the total damping force.

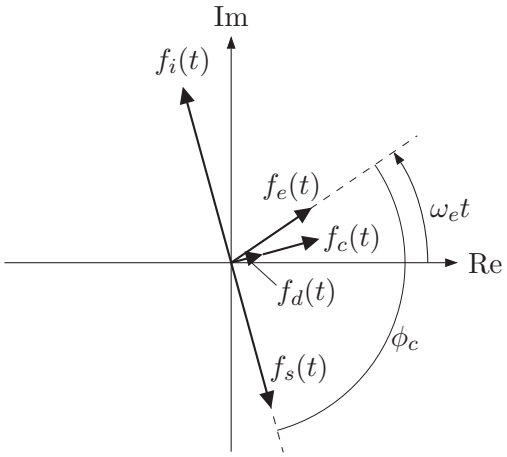

Figure 2.51: Pointer diagram for steady-state responses for $K_1 = 0.5$, $\xi = 0.1$ and $\eta = 1.1$

For $\eta \to \eta_b$, the phase ϕ_c approaches $\pi/2$ and A_c converges to zero, see figure 2.50. If $A_c \to 0$ ($D_c \to 0$), the control force and the inherent damping force go to infinite, see (2.189). Therefore, these points were excluded from the solution shown in figure 2.50.

As for the oscillators without inherent damping, a Root Locus valid for any K_1 can be plotted, see figure 2.52. It is very similar to the one of figure 2.49. The main differences are discussed in the following. For $\eta = 0$ (①), the poles start off in the left half plane, which is due to the inherent damping ξ. The point ② corresponds to the frequency ratio at which the equivalent damping ratio reaches the critical damping ratio. It can be calculated by setting $\xi_{eq} = 1$. Furthermore, for $\eta = 1$, the TRD can give damping to the oscillator, which is due to the fact that D_c does not converge to infinity for $\eta \to 1$. Therefore, the TRD provides damping to the oscillator for $0 < \eta < \eta_b$. This is in contrast to oscillators without inherent damping. For $\eta > \eta_b$, as for the oscillators without inherent damping, steady-state is not reached and the discussion done for oscillators without inherent damping also applies.

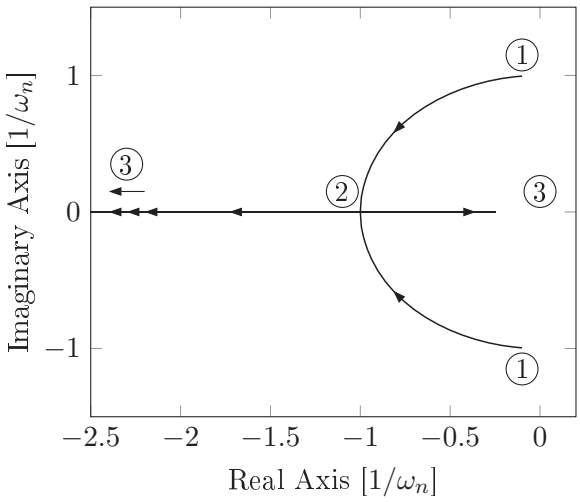

Figure 2.52: Root Locus for varying η and $\xi = 0.1$

2.8.4 Experimental validation of analytical solution

Generation of harmonic excitation force

In this subsection, the analytic solution of subsection 2.8.3 is validated on the test setup described in subsection 2.6.1. The following differential equation governs the motion of the table:

$$m_s\ddot{x}(t) + c\dot{x}(t) + kx(t) = f_{T,1}(t) + f_{T,2}(t) + f_e(t) \tag{2.198}$$

in which $f_{T,1}(t)$ and $f_{T,2}(t)$ denote the control force of the respective TRD unit. For the table, the system properties of table 2.5 are valid, whereas for the TRD units, the mass-radius control products were identified anew with help of (controlled) free vibration tests, see table 2.9 in which m_e is the excitation mass of the linear actuator.

Table 2.9: Mass-radius control products of both TRD units and excitation mass

$(m_c r)_1$ [kgm]	0.0393
$(m_c r)_2$ [kgm]	0.0407
m_e [kg]	2.00

Note m_s refers to the total mass of the table, therefore it includes the control masses of both TRD units and the excitation mass m_e. The harmonic excitation force is applied by moving the excitation mass m_e relative to the table, see figure 2.53.

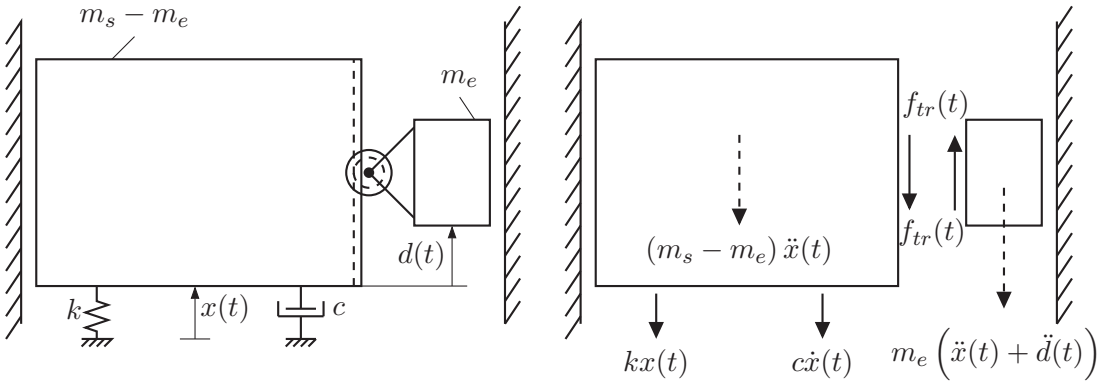

Figure 2.53: Linear actuator and corresponding free body diagram (right) [37]

The relative motion is described by the coordinate $d(t)$, which will be imposed by the linear actuator, see also figure 2.30.

Establishing the dynamic equilibrium of the excitation mass m_e of figure 2.53 yields:

$$f_{tr}(t) = m_e \left[\ddot{x}(t) + \ddot{d}(t)\right] \tag{2.199}$$

in which $f_{tr}(t)$ refers to the transmitted force. The inertial force $m_e\ddot{x}(t)$ is already considered on the left-hand side of (2.198) as $m_s\ddot{x}(t)$ includes the inertial force component created by m_e. The other force term in (2.199), $m_e\ddot{d}(t)$, remains. This is the excitation force $f_e(t)$ given by:

$$f_e(t) = -\ddot{d}(t)m_e \tag{2.200}$$

By imposing a harmonic acceleration $\ddot{d}(t)$, a harmonic excitation force is created. This is realized by tracking a harmonic target position

$$d_t(t) = d_{0,t}\cos(\omega_e t) \tag{2.201}$$

in which $d_{0,t}$ denotes the displacement amplitude of the target position. Taking the time derivative yields the target velocity:

$$\dot{d}_t(t) = -d_{0,t}\omega_e \sin(\omega_e t) \tag{2.202}$$

The dynamics of the linear actuator with the excitation mass m_e were identified with help of system identification methods [32]. The transfer function

$$G_S(s) = \frac{0.126}{2.79 \cdot 10^{-3}s + 1} \tag{2.203}$$

describes the dynamics of the linear actuator. Input is the control effort u_l and output is the velocity $\dot{d}(t)$. Units are V and m/s, respectively. Multiplying (2.203) with $1/s$ (integration over time) gives the transfer function

$$G_{S2}(s) = \frac{0.126}{2.79 \cdot 10^{-3}s^2 + s} \tag{2.204}$$

with the output $d(t)$ in m. The control schemes and stability checks used in this chapter can be found in control theory textbooks, e.g. [33].

The control scheme for the linear actuator is shown in figure 2.54.

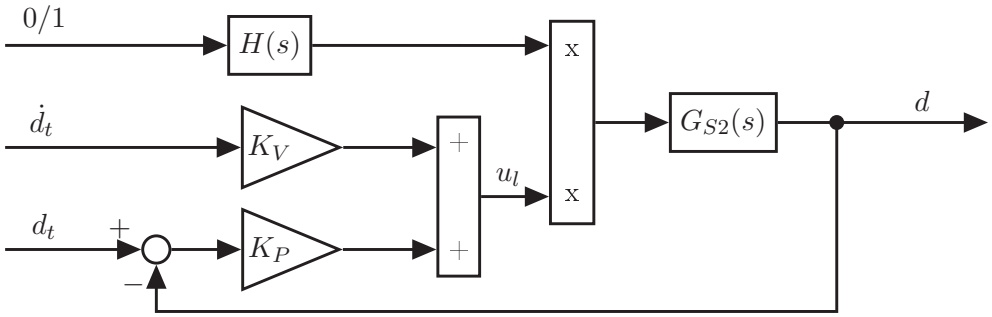

Figure 2.54: Control scheme for control of linear system [37]

The position $d(t)$ is measured and compared with the target position $d_t(t)$ of (2.201). The difference is fed into the controller, which consists of a simple proportional feedback gain K_p. This is a closed-loop position control and stability must be checked. A Root Locus for the open-loop transfer function $K_P G_{S2}(s)$ is shown in figure 2.55.

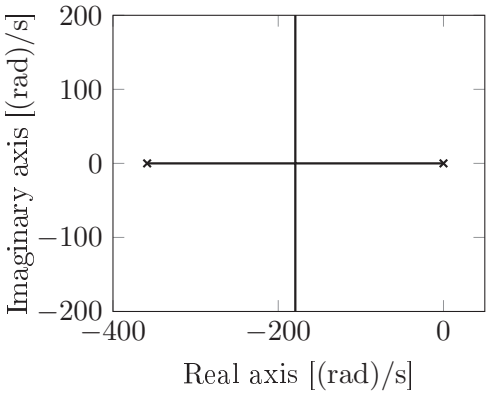

Figure 2.55: Root Locus of open-loop configuration $K_P G_{S2}(s)$ [37]

The poles lie in the left half plane for any K_P. Thus, the closed-loop is stable for any K_P. At $K_P \approx 700\,\mathrm{V/m}$, the poles break off from the real axis. Setting $K_P = 700\,\mathrm{V/m}$ is therefore an appropriate choice. To make the motion of the rotors more constant, an open-loop velocity control in addition to the closed-loop position control is applied. As can be seen from figure 2.54, the target velocity of (2.202) is also input. It is multiplied with the constant gain K_V, which is set to $1/0.126\,\mathrm{Vs/m}$, see (2.203). This is an open-loop velocity control.

Both efforts are added together to the control effort u_l, which is multiplied with another signal (output of $H(s)$). With this signal, the linear actuator can be smoothly turned on and off. When the user manually switches the input of

$$H(s) = \frac{50}{s^2 + 14s + 50} \tag{2.205}$$

from zero to one, the output of $H(s)$ forms a smooth curve. This ensures a smooth ramp-up and ramp-down process for the linear actuator. The presented control scheme was tested. Figure 2.56 shows the measured position $d(t)$ and the error of the position, $d_t(t) - d(t)$, for $\omega_e = 5\,\mathrm{(rad)/s}$ and $d_{0,t} = 0.10\,\mathrm{m}$.

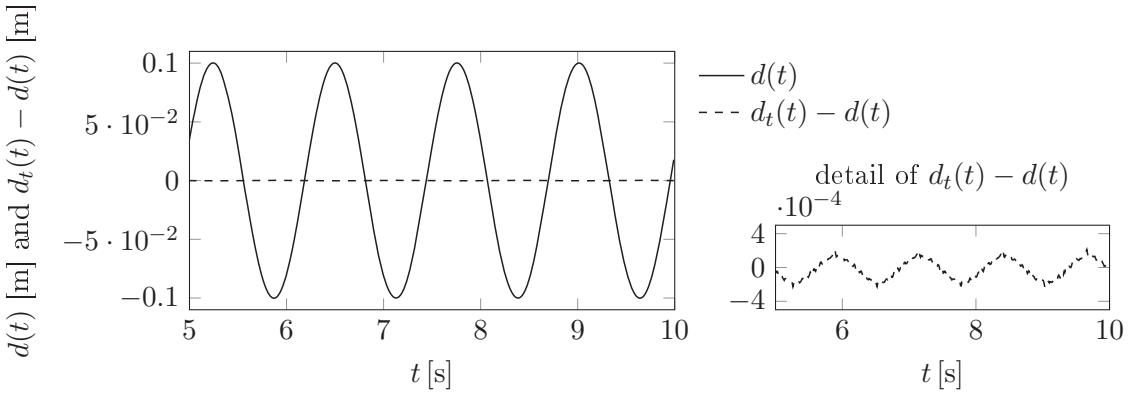

Figure 2.56: Position $d(t)$ and position error $d_t(t) - d(t)$ [37]

In the time sequence of figure 2.56, the position error, $d_t(t) - d(t)$, varies from zero within a value range of $3 \cdot 10^{-4}$ m, see detail; this corresponds to a deviation of 0.3 % of $d_{0,t}$. As the target position $d_t(t)$ is tracked so accurately, it is justified to assume in the following that the amplitude of the target position $d_{0,t}$ equals the (actual, measured) amplitude of the position, d_0. Test were performed for several values of ω_e and $d_{0,t}$, demonstrating that the harmonic target position curves can be tracked adequately accurate with the presented control scheme.

Uncontrolled response

Figure 2.57 shows the dynamic amplification D according to (2.166) and the measured dynamic amplification D_m.

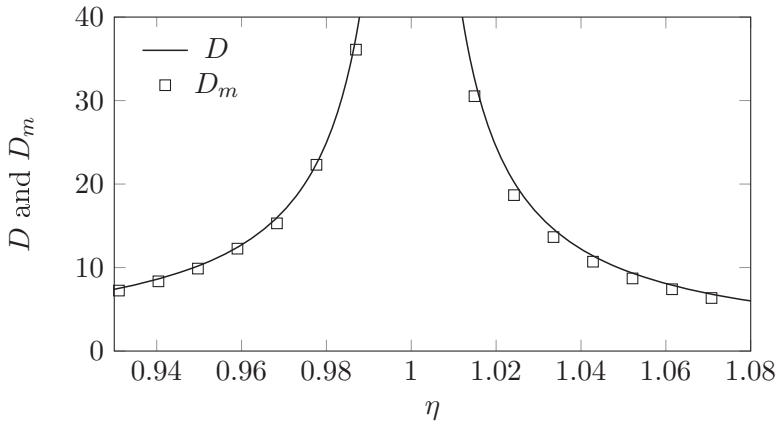

Figure 2.57: Dynamic amplification D and measured dynamic amplification D_m [37]

The values for D_m, which were obtained experimentally, are explained in the following. Harmonic excitation forces with several excitation frequencies ω_e were applied on the table (SDOF oscillator), see first column of table 2.10. All values of figure 2.57 are shown in table B.1.

Table 2.10: Test results of uncontrolled steady-state response [37]

w_e [(rad)/s]	η	d_0 [m]	$A_{0,m}$ [m]	D	D_m	ΔD
5.00	0.93	0.10	0.036	7.51	7.24	0.035
5.15	0.96	0.10	0.065	12.43	12.26	0.013
5.30	0.99	0.04	0.081	37.61	36.10	0.040
5.45	1.01	0.04	0.073	32.63	30.53	0.064
5.60	1.04	0.07	0.047	11.40	10.70	0.061
5.75	1.07	0.10	0.042	6.82	6.35	0.068

When the linear actuator is turned on, transients occur initially. After about ten minutes, these transients are died out and the table responds with the excitation frequency and a certain displacement amplitude $A_{0,m}$ (the additional index m refers to measured), which can be read off from the displacement response. The target position amplitude $d_{0,t}$ was chosen such that the linear actuator does not exceed its maximum stroke is $\pm 0.10\,\mathrm{m}$ and that the displacement response of the table does not exceed $\pm 0.10\,\mathrm{m}$. By limiting $x(t)$, it is ensured that the leaf springs, which support the table, only deform elastically. In the fifth column of table 2.10, the dynamic amplification D is calculated according to (2.166), see also (2.168) using the ξ of table 2.5. In the sixth column, the measured dynamic amplification

$$D_m = \frac{A_{0,m}\omega_n^2}{F_0} \tag{2.206}$$

with

$$F_0 = \frac{m_e d_0 \omega_e^2}{m_s} \tag{2.207}$$

is calculated. In the last column of table 2.10, the error

$$\Delta D = \frac{D - D_m}{D} \tag{2.208}$$

is calculated. The absolute value of ΔD is always smaller than 16.0 %, see also table B.1, except at $\omega_e = 5.35\,(\mathrm{rad})/\mathrm{s}$, which is slightly below resonance. As the frequency-ratio dynamic-amplification function has a steep slope at $\omega_e = 5.35\,(\mathrm{rad})/\mathrm{s}$, small model inaccuracies result is large errors ΔD, which is the explanation for the relatively large error in the vicinity of $\eta = 1$.

From figure 2.57, it becomes evident that the analytic and measured dynamic amplifications (D and D_m) nearly coincide. Therefore, the dynamics of the table can be described sufficiently accurate by a linear model with the properties of table 2.5. Furthermore, the harmonic excitation is applied adequately on the SDOF oscillator.

Controlled response

Before testing the controlled response, pre-calculations are required. The controlled dynamic-amplification relations are additionally described by the parameter K_1, see (2.185). A K_1 of 0.7 was chosen. This was done as, for $K_1 = 0.7$, the displacement amplitudes of the table (SDOF oscillator) in the uncontrolled and the controlled case remain within the experimental displacement limits ($\pm 0.1\,\mathrm{m}$) and are, for an accurate quantification, sufficiently large. The same holds for the amplitude $d_{0,t}$ of the target position for the linear actuator. In the following, the first or both TRD units are activated, see first column of table 2.11.

Table 2.11: Computation of normalized excitation force amplitudes F_0 for $K_1 = 0.7$, $\omega_n = 5.37\,(\text{rad})/\text{s}$ for different active TRD units [37]

TRD unit	$m_c r$ [kgm]	$\mu_c r$ [m]	F_0 [m/s^2]
one	$3.93 \cdot 10^{-2}$	$1.14 \cdot 10^{-3}$	$4.68 \cdot 10^{-2}$
two	$4.07 \cdot 10^{-2}$	$1.18 \cdot 10^{-3}$	$4.85 \cdot 10^{-2}$
both	$8.00 \cdot 10^{-2}$	$2.31 \cdot 10^{-3}$	$9.52 \cdot 10^{-2}$

The corresponding mass-radii control products are given in the second column. Dividing this by m_s yields the respective values for $\mu_c r$, see third column. With $K_1 = 0.7$, ω_n of table 2.5 and (2.185), the required (normalized) excitation force amplitude F_0 can be calculated, see last column of table 2.11.

To apply the same excitation force amplitude, F_0, for different excitation frequencies ω_e, the amplitude $d_{0,t}$ of the target position must be set accordingly. This is discussed in the following. Inserting the first time derivative of (2.202) into (2.200) yields the excitation force:

$$f_e(t) = d_{0,t}\omega_e^2 m_e \cos(\omega_e t) \tag{2.209}$$

Dividing this by m_s, the amplitude of the excitation force is derived

$$F_0 = \frac{d_{0,t}\omega_e^2 m_e}{m_s} \tag{2.210}$$

Solving for $d_{0,t}$

$$d_{0,t} = \frac{F_0 m_s}{\omega_e^2 m_e} \tag{2.211}$$

gives the amplitude of the target position required to apply the same excitation force amplitude F_0 for the different ω_f. To create the harmonic excitation force, the harmonic target position of (2.201) with the amplitude of (2.211) is tracked using the control scheme of figure 2.54. The control scheme for the angular position control of the rotors is explained with the rotor one of TRD unit one, see figure 2.58.

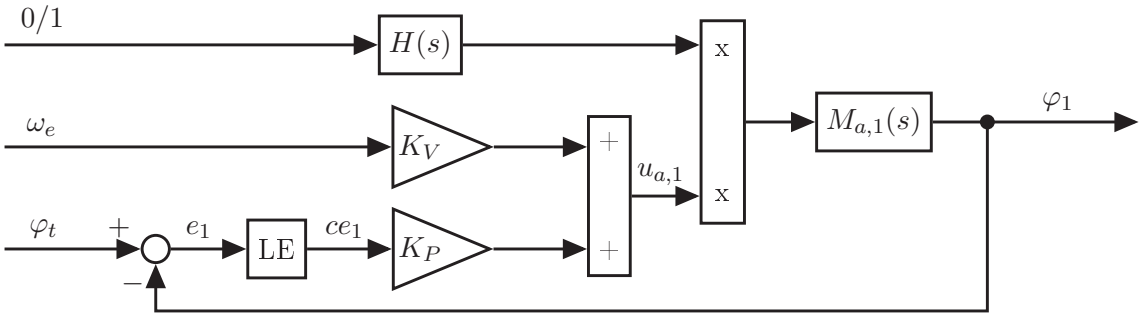

Figure 2.58: Control scheme for angular position control of rotors [37]

The other rotors are controlled equally. The control scheme consists of an open-loop velocity control. Furthermore, a closed-loop angular position control with the TAP $\varphi_t(t)$ as the input is used. The TAP is computed continuously with

$$\varphi_t(t) = \operatorname{atan2}\left[\hat{x}(t); \frac{\dot{\hat{x}}(t)}{\omega_e}\right] + \pi \tag{2.212}$$

in which $\hat{x}(t)$ and $\dot{\hat{x}}(t)$ are obtained from the observer, see subsection 2.6.2. In (2.212) and in contrast to the computation of the TAP $\varphi_t(t)$ in section 2.3, ω_n is replaced by ω_e. In section 2.3, $\varphi_t(t)$ was derived such that the control force of the TRD opposes the free vibrations of the SDOF oscillator, which predominantly responds with the natural frequency ω_n. Therefore, ω_n was used. In this section, the steady-state response is studied, in which the table (SDOF oscillator) responds after some time, primarily with the excitation frequency ω_e. This was also assumed for the analytic solution of subsection 2.8.3.

The TAP is then compared with the measured angular position $\varphi_1(t)$ (upper rotor of TRD unit one, see figure 2.30). The error $e_1(t)$ is then limited to values between $-\pi$ and π by adding integer multiples of 2π to it, see block 'LE' of figure 2.58, which gives $ce_1(t)$. $ce_1(t)$ is then multiplied with K_P, yielding the control effort from the closed-loop angular position control. A stability check of the closed-loop control was given in subsection 2.6.5. The input of the open-loop velocity control is the excitation frequency ω_e, which is multiplied with the constant gain K_V, yielding the control effort from the open-loop velocity control. Both control efforts sum up together to the total control effort $u_{a,1}(t)$, which is then multiplied with another signal. This signal is only used for turning the actuators on and off. When the user manually switches an actuator on, the input of $H(s)$ changes suddenly from zero to one. With the transfer function $H(s)$ given in (2.205), a smooth ramp-up and ramp-down of the rotors is guaranteed. The transfer function $M_{a,1}(s)$ (introduced in subsection (2.6.3)) describes the dynamics of the upper actuator of TRD unit one with the control effort $u_{a,1}(t)$ as the input and the angular position $\varphi_1(t)$ as the output.

For the tests, each actuator is controlled individually. K_P is set to $1.5\,\mathrm{V/(rad)}$. This, in combination with the open-loop velocity control, yields adequate tracking results, see the test described in the following. K_V is computed for each rotor individually by forming the reciprocal value of the numerator of the corresponding transfer function, see subsection 2.6.3, in particular (2.146) and table 2.6. For the first actuator, e.g., K_V is set to $1/3.14\,\mathrm{Vs/(rad)}$.

In the following, the effectiveness of the control scheme for the actuators is demonstrated along with a description of the test procedure for one particular excitation frequency $\omega_e = 5.25\,\mathrm{(rad)/s}$. Both TRD units will be activated. According to table 2.11, F_0 is $9.52 \cdot 10^{-2}\,\mathrm{m/s^2}$. With (2.211), the required amplitude $d_{0,t}$ of the target position is calculated. In figure 2.59/A, the displacement $x(t)$ of the SDOF oscillator is shown.

At $t = 4.5\,\mathrm{s}$, the linear actuator (excitation) is switched on and the displacement amplitude steeply rises to approximately $5.5 \cdot 10^{-2}\,\mathrm{m}$. At $t = 11.5\,\mathrm{s}$, both TRD units are turned on, interrupting the steep rise in the displacement amplitude. The displacement amplitudes then decrease. At $t = 200\,\mathrm{s}$, the (controlled, measured) displacement amplitude $A_{0,c,m}$ is $0.0448\,\mathrm{m}$, which is read off and and used for the computation of the measured controlled dynamic amplification $D_{c,m}$.

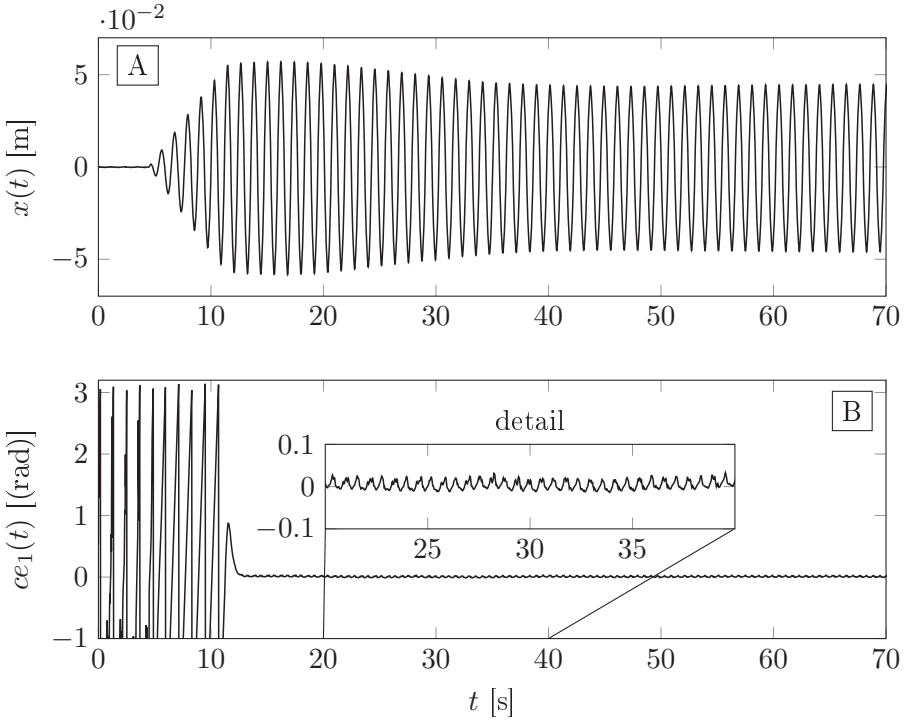

Figure 2.59: Displacement response and control error of steady-state response test for $\omega_e = 5.25\,(\mathrm{rad})/\mathrm{s}$ [38]

In figure 2.59/B, the control error $ce_1(t)$ is shown. $ce_1(t)$ is large up to approximately $t = 11.5\,\mathrm{s}$ as the actuators are not turned on, after which $ce_1(t)$ tends to zero. $ce_1(t)$ deviates from zero in a range of $\pm 0.03\,(\mathrm{rad})$. Therefore, the TAP of (2.212) is tracked quite accurate. The same holds for the other actuators, demonstrating that the control scheme functions as wanted.

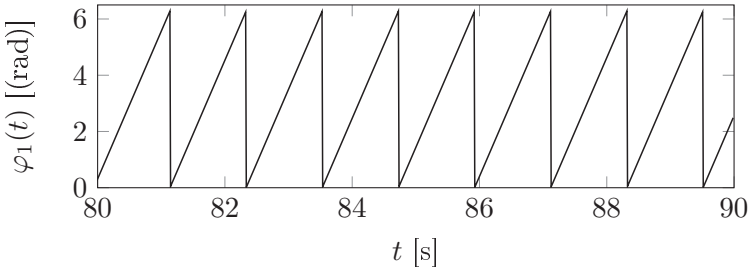

Figure 2.60: Angular position of a rotor corresponding to the test of figure 2.59

Figure 2.60 shows the measured angular position in a time interval in which the SDOF oscillator is in steady-state. It shows a nearly ideal saw-tooth shape illustrating that the rotor is operating, as desired, in the continuous rotation mode.

Table 2.12 and B.2 show the test preparation and the test results for $K_1 = 0.7$. The corresponding results are shown in figure 2.61.

Table 2.12: Test results of controlled steady-state response for $K_1 = 0.7$ [38]

active TRD units	w_e [(rad)/s]	d_0 [m]	D_c	$A_{0,c}$ [m]	$A_{0,c,m}$ [m]	$D_{c,m}$	ΔD
both	4.45	0.0832	2.77	0.0092	0.00897	2.72	0.021
both	4.65	0.0762	3.36	0.0111	0.0103	3.12	0.071
both	4.85	0.0701	4.36	0.0144	0.0132	4.00	0.084
both	5.05	0.0646	6.52	0.0215	0.0194	5.87	0.100
both	5.25	0.0598	14.78	0.0488	0.0448	13.56	0.082
both	5.45	0.0555	18.35	0.0606	0.0581	17.59	0.041
both	5.65	0.0516	5.48	0.0181	0.019	5.75	−0.050
both	5.85	0.0482	2.82	0.0093	0.0107	3.24	−0.147

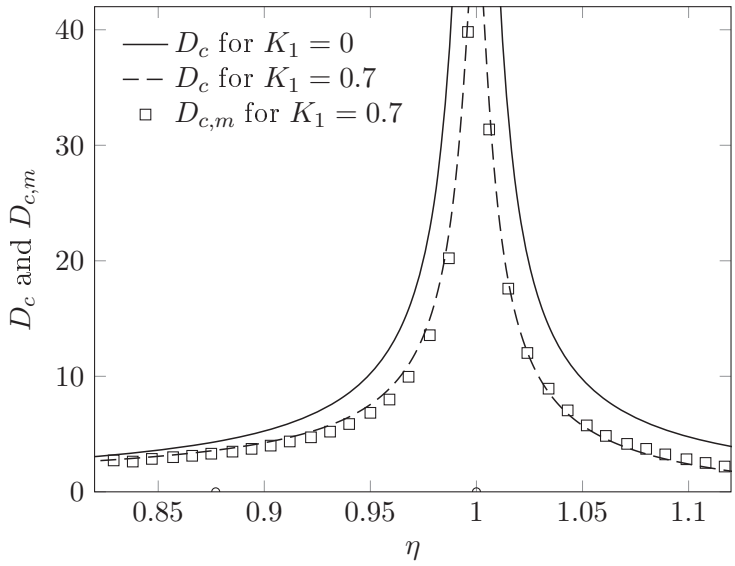

Figure 2.61: Controlled dynamic amplification D_c and $D_{c,m}$ plotted against frequency ratio η for $\xi = 0.00305$ for $K_1 = 0.7$ [38]

The error ΔD of the controlled dynamic amplification is computed by

$$\Delta D = \frac{D_c - D_{c,m}}{D_c} \tag{2.213}$$

Even for frequency ratios close to one, see table B.2, ΔD is smaller than 11 %. This verifies the correctness of the analytic solution.

Test were then repeated for $K_1 = 1.1$, see figure 2.62 with the corresponding table B.3. The analytic solution is confirmed again. However, larger errors ΔD occur, see also table B.3. For a K_1 of 1.1, the dynamic amplification is sensitive to variations in K_1, see figure 2.62, in which D_c is additionally plotted for $K_1 = 1.1 \pm 0.05$.

Furthermore, the error increases with the frequency ratio. With higher frequency ratios, the measured displacement amplitudes $A_{0,c,m}$ become smaller and smaller; the SDOF oscillator is nearly at rest, see $A_{0,c,m}$ of table B.3. For these very small vibrations, the static friction

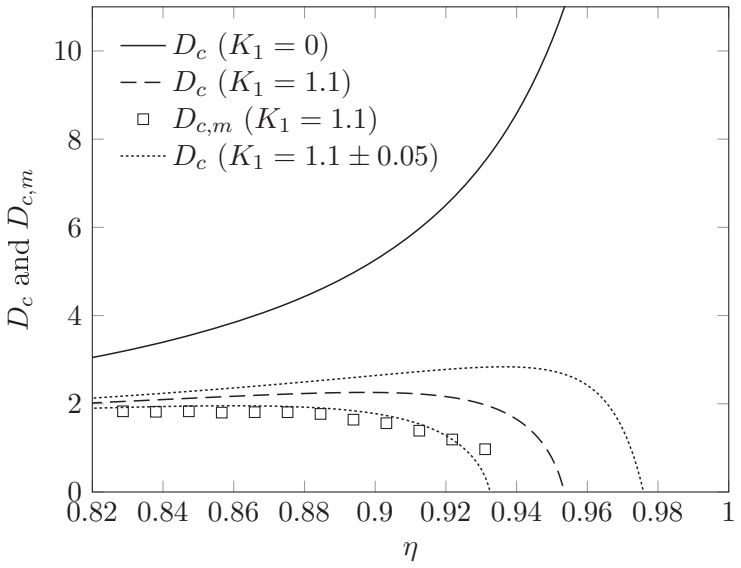

Figure 2.62: Controlled dynamic amplification D_c and $D_{c,m}$ plotted against frequency ratio η for $\xi = 0.00305$ for $K_1 = 1.1$

effects may have a greater impact on the motion than it has for larger vibrations. This is a possible cause for the underestimation of $D_{c,m}$.

Tests were repeated for $K_1 = 1.0$, see figure B.1 and table B.4. The explanations of the previous two paragraphs apply.

2.8.5 Comparison with tuned mass damper

In the following, the steady-state damping performance of the TRD is compared with a tuned mass damper (TMD). The TMD was invented by Frahm [39]. Its theory is explained briefly in the following. For more details, see e.g. [5, 6].

A SDOF oscillator equipped with a TMD as shown in figure 2.63 is considered. The main mass m is attached to the frame by a spring and a damping element. As before, k and c refer to the stiffness of the spring and the damping coefficient of the damping element. The coordinate $x(t)$ describes the motion of m. A control mass m_c is attached to the main mass by a spring with the stiffness k_2 and a damping element with the damping coefficient c_2. The control mass with the spring and the damping element represents the TMD. The relative motion between the mass m and the control mass m_c is described by the coordinate $r_d(t)$. A harmonic excitation force $f_e(t)$ acts on the mass m.

Establishing the dynamic equilibrium and performing some rearrangements yields the displacement amplitude $A_{0,d}$ of the main mass and the relative displacement amplitude $A_{0,r}$ of the control mass in steady-state [5, 6]. Normalizing these displacement amplitudes, as done for the TRD, yields the controlled dynamic amplification D_d of the TMD and $A_{0,r}\omega_n^2/F_0$

$$D_d = \frac{A_{0,d}\omega_n^2}{F_0} = \sqrt{\frac{g_1^2 + g_2^2}{g_3^2 + g_4^2}} \tag{2.214}$$

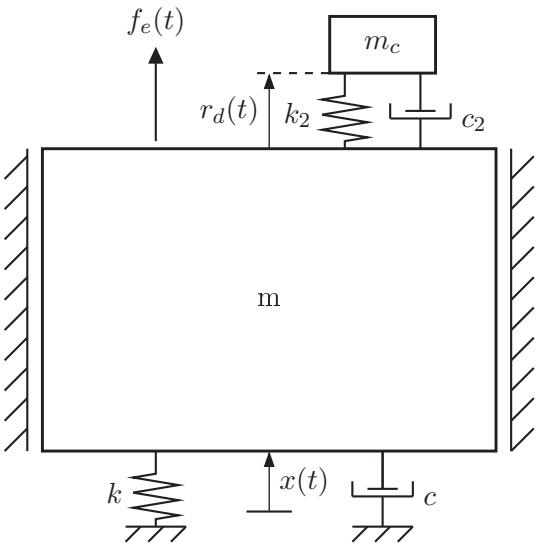

Figure 2.63: Tuned mass damper [5, 6]

$$\frac{A_{0,r}\omega_n^2}{F_0} = \sqrt{\frac{\eta^4}{g_3^2 + g_4^2}} \tag{2.215}$$

with the following terms

$$\begin{aligned} g_1 =& \kappa^2 - \eta^2 \\ g_2 =& 2\eta\kappa\xi_2 \\ g_3 =& \eta^4 - \eta^2\left(1 + \kappa^2 + \mu_2\kappa^2 + 4\kappa\xi\xi_2\right) + \kappa^2 \\ g_4 =& \eta\left[2\xi\left(\kappa^2 - \eta^2\right) + 2\kappa\xi_2\left(1 - \eta^2 - \mu_2\eta^2\right)\right] \end{aligned} \tag{2.216}$$

in which the frequency ratio κ, the damping ratio ξ_2, the mass ratio μ_2, the frequency ratio η and the damping ratio ξ are given by the following equations [5, 6]:

$$\begin{aligned} \kappa &= \frac{\omega_2}{\omega_m} \qquad \text{with} \qquad \omega_m = \sqrt{\frac{k}{m}} \\ \xi_2 &= \frac{c_2}{2m_c\omega_2} \qquad \text{with} \qquad \omega_2 = \sqrt{\frac{k_2}{m_c}} \\ \mu_2 &= \frac{m_c}{m} \qquad \eta = \frac{\omega_e}{\omega_m} \qquad \xi = \frac{c}{2m\omega_m} \end{aligned} \tag{2.217}$$

In (2.217), the frequency ratio η was surreptitiously set equal to the one introduced in (2.165), which considers ω_n according to (2.8) instead of ω_m. The difference is that ω_n considers the inertial forces induced by the total mass $m + m_c$, whereas ω_m only the inertial forces induced by the main mass m. As the control masses are usually small, it can be assumed that $m \approx m + m_c$. Consequently, the frequency ratios η of (2.165) and (2.217) are equal. The discussion also holds for ξ, see (2.217) and (2.9).

The mass ratio μ_2 differs from the mass ratio μ_c given in (2.12). By solving the mass ratio μ_2 of (2.217) for m_c and inserting this into (2.12), a relation between μ_2 and μ_c can be established:

$$\mu_c = \frac{\mu_2}{1 + \mu_2} \tag{2.218}$$

According to [5, 6], the optimal frequency ratio κ_o and the optimal damping ratio $\xi_{2,o}$ are

$$\kappa_o = \frac{1}{1+\mu_2} \tag{2.219}$$

$$\xi_{2,o} = \sqrt{\frac{3\mu_2}{8\,(1+\mu_2)^3}} \tag{2.220}$$

Before discussing figure 2.64 and B.3, the parameters forming the basis for the curves are explained.

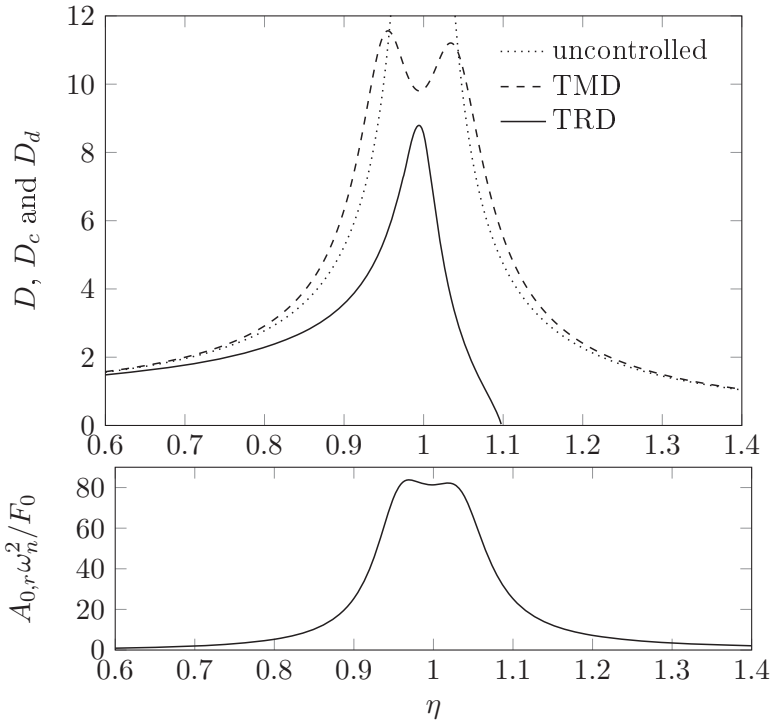

Figure 2.64: Dynamic amplifications D (uncontrolled), D_d (TMD), D_c (TRD) and normalized relative displacement amplitude $A_{0,r}\omega_n^2/F_0$ of the control mass in steady-state, all curves for $\mu_2 = 0.01$ for $\xi = 0.01$ [38]

The damping ratio ξ and the mass ratio μ_2 are inputs. With the given μ_2, the optimal values for κ and ξ_2 are calculated according to (2.219) and (2.220) [5, 6]. Using (2.214) to (2.217), the controlled dynamic amplification D_d and $A_{0,r}\omega_n^2/F_0$ are computed for the TMD. The frequency ratio η is varied in the range in which D_d becomes relatively large. In the lower diagram of figure 2.64, the peak value for $A_{0,r}\omega_n^2/F_0$ can be read off. $A_{0,r}$ corresponds to half of the stroke required for the TMD. To ensure comparability regarding size between the TRD and the TMD, the peak value of $A_{0,r}$ is set equal to the radius r. Therefore: $\max(A_{0,r}\omega_n^2/F_0) = r\omega_n^2/F_0$. By calculating the mass ratio μ_c for the TRD according to (2.218), an equivalent parameter K_1 for the TRD can be calculated with (2.185). This equivalent parameter ensures that the TRD and the TMD have same size and control mass. D_c can then be calculated with (2.192) using the terms of (2.193).

Figure 2.64 shows that the TRD has a better steady-state damping performance than a TMD of comparable size and control mass. In addition, the TRD does not make the frequency range in which relatively large dynamic amplification occurs wider. However, with increasing inherent damping, the advantage of the TRD over the TMD becomes less, see figure B.2, in which D_d and D_c are shown for different damping ratios. In figure B.3, D_d, D_c and $A_{0,r}\omega_n^2/F_0$ are plotted for a different mass ratio. All diagrams show that the TRD lowers steady-state vibrations more effectively than a TMD of comparable size and stroke.

2.8.6 Discussion

- Within this section, the steady-state response of a single degree of freedom oscillator subjected to a harmonic excitation force with and without the TRD was studied. An analytic solution describing the steady-state damping performance of the TRD is derived. It leads to a polynomial equation, a non-trivial solution of which is validated experimentally. The experiments show that with an appropriate control algorithm, the TRD can reach the analytically derived steady-state performance.

- The analytic derivations show that the TRD adds damping to the SDOF oscillator. However, when an oscillator without inherent damping is subject to an excitation force equal to that of the SDOF oscillator, it cannot add damping. Furthermore, it was found that the damping the TRD provides does not only depend on the design parameters of the TRD, namely, the radius and the control mass; it also depends on the steady-state vibration amplitude. The provided damping increases with the design parameters of the TRD and with lower steady-state vibration amplitudes.

- It is shown that above a certain frequency ratio (border frequency ratio), the control force amplitude of the TRD is larger than the harmonic excitation force. In this case, steady-state is not reached. When using the control algorithm presented in section 2.5 and 2.6, the TRD turns itself off when the vibrations fall below a lower threshold and turns itself back on when another upper threshold is exceeded. By doing this, the vibrations are held below the upper threshold. However, the more the considered frequency ratio deviates from the border frequency ratio, the more frequently the TRD must be turned on and off. This is because the control force amplitude increases with larger frequency ratios. It should then be considered to operate the TRD in the swinging mode in which the eccentric control masses oscillate about a certain angular positions. In this mode of operation, the control action is created by continuously accelerating and decelerating the control masses and the TRD possibly loses its power benefit.

- For the tests of subsection 2.8.4, it was assumed that the excitation frequency is known, see figure 2.58. The purpose of these tests was the validation of the analytic solution. If the excitation frequency is not known, it can be made available by firstly assuming an initial excitation frequency, then computing the slope of the TAP, feeding it through a low-pass filter and continuously updating the excitation frequency of (2.212). Alternatively, phase-locked loop systems can be used [34, 35]. Phase-locked loop systems produce phase and frequency of a signal [34, 35]. By detecting the phase of the velocity of the SDOF oscillator, a TAP for the rotors can be computed such that the control force of the TRD opposes the velocity of the SDOF oscillator.

- In subsection 2.8.5, the steady-state damping performance of the TRD was compared with a tuned mass damper (TMD). The frequency-ratio dynamic-amplification diagrams differ in principle. This is because the damping effect is generated in different manners. If a TMD is used, the SDOF oscillator changes to a two-degree-of-freedom oscillator. This produces two lower peaks in the frequency-ratio dynamic-amplification diagrams. Furthermore, this results in a wider frequency range with large dynamic amplification. In contrast to this, the TRD uses the inertial forces of two eccentrically rotating masses. It reduces the dynamic amplification over all frequencies. Furthermore, as the control force increases quadratically with frequency, the TRD can bring the vibrations to rest above a certain frequency ratio (the border frequency ratio). However, as the control algorithm does not work properly for small vibrations, it must be turned off for small vibration amplitudes, see second to last discussion point.

- A TMD is usually tuned to a single frequency (natural frequency) and this frequency can usually not easily be adapted as it requires, for optimal tuning according to (2.219) and (2.220), a replacement of spring and damping element. In contrast to this, the frequency to which the TRD is tuned can be changed easily, see second to last discussion point. When applying the methods of the second to last discussion point, the TRD can even automatically adapt the frequency to which it is tuned.

- The analytic solution is applicable to other active mass dampers which generate their control action by harmonically accelerating and decelerating a control mass between two end positions. Setting the control force of this active mass damper such that it opposes the velocity of the SDOF oscillator, it reaches the same steady-state damping performance as derived analytically in this section.

- The analytic solution can serve as a powerful design tool to dimension the TRD for harmonic excitation. When the uncontrolled vibration amplitude or the amplitude of the harmonic excitation force is known, the design parameters for the TRD can be easily determined.

2.9 Additional re-excitation prevention methods

2.9.1 Introduction

In section 2.5 and 2.6, a method to prevent re-excitation was presented and validated experimentally. In [23], another method to prevent re-excitation was proposed; the use of a second identical TRD unit to counter the first TRD unit for small vibrations. When the vibration amplitudes are large, both units work in unison and damp the motion. When the vibration amplitudes become small, the phasing between both control forces is set such that the control forces increasingly neutralize each other [40]. A control strategy implementing this is presented and validated experimentally in this section.

An alternative method to the one mentioned above is also presented in this section [40]. When the control force of the TRD is set in anti-phase to the velocity of the SDOF oscillator, maximum damping action is produced. By altering this phasing, the damping effect can be regulated. To illustrate this, open-loop studies are presented [41]. Subsequently, a corresponding closed-loop control strategy is derived. This control strategy is similar to the one discussed in [40].

For the simulations and the experiments of this section, a stochastic excitation will be used. This allows for the introduction of several phenomena discussed in more detail in chapter 3.

2.9.2 Two TRD units

The SDOF oscillator is now equipped with two TRD units with equal control mass m_c and radius r, see figure 2.65.

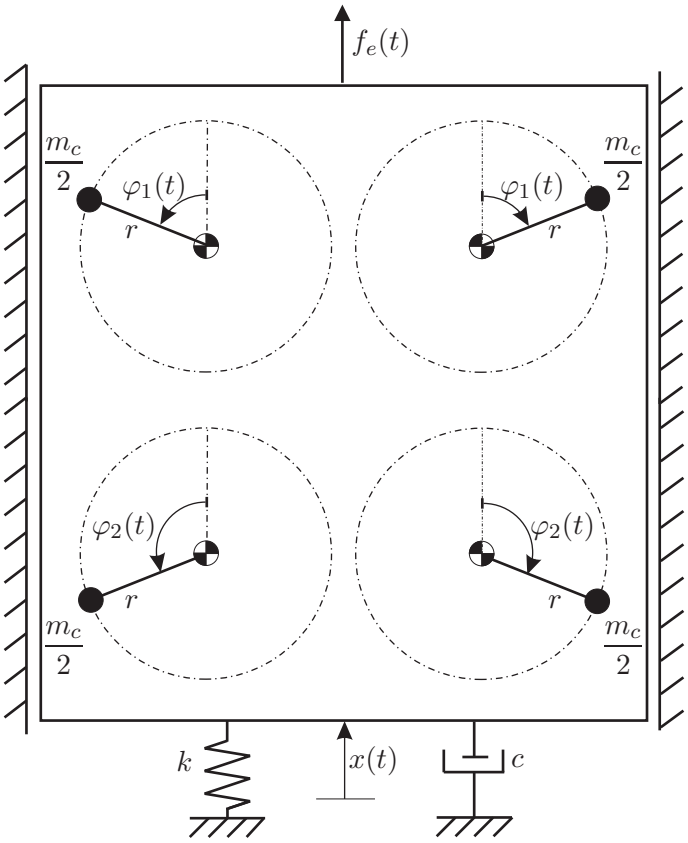

Figure 2.65: SDOF oscillator with two TRD units

The motion of the rotors of the upper TRD unit is described by $\varphi_1(t)$ and the rotors of the lower TRD unit by $\varphi_2(t)$. The motion of the SDOF oscillator under the action of both TRD units and an excitation force $f_e(t)$ is described by

$$m_s\ddot{x}(t) + c\dot{x}(t) + kx(t) = f_{T,1}(t) + f_{T,2}(t) + f_e(t) \tag{2.221}$$

in which m_s is the total mass of the SDOF oscillator and $f_{T,1}(t)$ and $f_{T,2}(t)$ refer to the forces created by each respective TRD unit. These forces are given by:

$$f_{T,1}(t) = m_c r\left[\dot{\varphi}_1(t)^2\cos\varphi_1(t) + \ddot{\varphi}_1(t)\sin\varphi_1(t)\right] \tag{2.222}$$

$$f_{T,2}(t) = m_c r\left[\dot{\varphi}_2(t)^2\cos\varphi_2(t) + \ddot{\varphi}_2(t)\sin\varphi_2(t)\right] \tag{2.223}$$

As before, the first terms in the squared brackets of (2.222) and (2.223) are the radial forces—which superimpose to the respective control forces—and the second terms are the tangential forces—which are to be kept as small as possible in the continuous rotation mode—, see section 2.1.

The SDOF oscillator equipped with two TRD units is identical to the test setup presented in subsection 2.6.1. Therefore, with the properties in table 2.5, c and k can be computed using (2.8) and (2.9) in which $m + m_c$ must be replaced by m_s.

Assuming that both TRD units operate in the continuous rotation mode, each TRD unit creates a harmonic control force. Both harmonic control forces superimpose to a so-called superimposed control force. The magnitude of the superimposed control force is determined by the phasing between the two independent control forces. If both units are in anti-phase to each other, the control forces neutralize each other.

When the system forces (introduced in section 2.2) are large in comparison to the excitation force and the forces generated by the TRD units, the SDOF oscillator responds nearly harmonically with a single frequency ω_n (mono-frequent vibration). In this case, the closed-loop control strategy of subsection 2.6.5 works as wished. Therefore, as desired in the continuous rotation mode, the produced TAPs are saw-tooth like and the angular velocity of the rotors is approximately constant. However, the more the motion of the SDOF oscillator is influenced by excitation forces or tangential forces from the TRD units, the more the motion of the SDOF oscillator deviates from the mono-frequent vibration. This results in a more non-constant angular velocity of the rotors. Due to the non-constant angular velocity, further tangential forces are produced. These additional tangential forces act irregularly on the SDOF oscillator, leading to a response which deviates even more from the previously assumed mono-frequent vibration. Consequently, the target angular velocity becomes even more variable creating more undesired tangential forces. This undesired spiraling effect can be reduced to a certain extent by tuning the controller, which ensures the tracking of the TAP, less aggressive. However, if the controller is not aggressive enough, the anti-phasing between the velocity of the SDOF oscillator and the control forces of the TRD units may be lost. Therefore, the tuning of the controller is a trade-off between ensuring this anti-phasing and producing small tangential forces. The statements of this paragraph are studied and quantified in more detail in chapter 3.

In [40], a control algorithm to prevent the undesired effects described in the previous paragraph is presented. An adapted observer is introduced. This observer makes the states, $\hat{x}(t)$ and $\dot{\hat{x}}(t)$, required for the computation of the TAP available. It re-constructs the displacement and velocity responses of the SDOF oscillator such that for large vibration amplitudes—the system forces are large in comparison to the excitation force and tangential forces produced by the TRD units—, the adapted observer follows the responses of the SDOF oscillator accurately. On the other hand, for small vibration amplitudes—the excitation force and tangential forces produced by TRD units dictate the motion of the SDOF oscillator—, the adapted observer decouples the observed states from the motion of the SDOF oscillator. As a result, the adapted observer continues to produce the desired mono-frequent vibration for small vibration amplitudes. This is realized by coupling and decoupling the adapted observer as a function of the vibration amplitude. In [40], it was shown that the proposed control algorithm works as wanted. However, several tuning variables must be set. This makes the tuning of the control algorithm quite labor-intensive. Therefore, another, simpler control algorithm is presented in the following.

To present the control scheme, an excitation force produced by the linear actuator of figure 2.30 is introduced. For the excitation force $f_e(t)$, a white noise signal (signal with constant spectral power density) is assumed. It is fed through a band-pass filter with a lower and an upper cut-off frequency at $3.37\,(\mathrm{rad})/\mathrm{s}$ and $7.37\,(\mathrm{rad})/\mathrm{s}$, respectively. The filtering is done as the linear actuator, see figure 2.30, is not wanted to apply arbitrary large or small frequencies on the SDOF oscillator. Excitation frequencies much smaller than the natural frequency ω_n cannot be realized as an infinite large stroke of the linear actuator would be required. Furthermore, it is unwanted to drive the linear actuator with arbitrarily high frequencies as this would increase the mechanical wear on the linear actuator without actually exciting the SDOF oscillator.

Dividing the force signal by the excitation mass $m_e = 2.0\,\mathrm{kg}$ produces the acceleration required by the linear actuator to produce the excitation force. Integrating twice over time results in the target position $d_t(t)$ for the linear actuator.

Note that m_e is included in m_s of table 2.5. Therefore, the inertial forces induced by an acceleration $\ddot{x}(t)$ of the table are included on the left-hand side of (2.221), whereas the inertial forces produced by accelerating the excitation mass relative to the table are on the right-hand side of (2.221). See subsection 2.8.4, in particular, figure 2.53 and (2.199) in which $d(t)$ describes the relative motion between the table and the excitation mass. To track $d_t(t)$, a closed-loop control with a proportional feedback gain $K_P = 700\,\mathrm{V/m}$ is sufficient to produce adequate tracking results.

Figure 2.66 shows the displacement of the table for a randomly chosen time interval. The vibration amplitude increases and decreases in time as the excitation force sometimes acts in the direction of the velocity of the SDOF oscillator and sometimes does not. The vibrations magnitude within a restricted time interval can be quantified with the standard deviation (std) of the displacement, $x_{std} = \mathrm{std}(x(t))$. It is used for comparison purposes in the following and is equal to $0.0236\,\mathrm{m}$ for a duration of one hour when both TRD units are inactive (uncontrolled). This result was verified numerically. Repeating the simulation or the test yields nearly the same vibrations magnitude showing that the simulation and testing duration is sufficiently long.

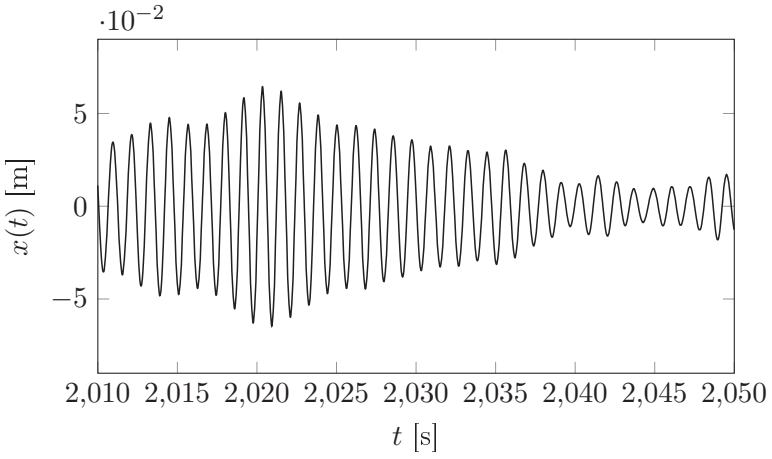

Figure 2.66: Displacement response of SDOF oscillator

The vibration amplitude $A(t)$ and the TAP φ_t are computed according to (2.224)

$$A(t) = \sqrt{\hat{x}(t)^2 + \left[\frac{\dot{\hat{x}}(t)}{\omega_n}\right]^2} \qquad \varphi_t(t) = \text{atan2}\left[\hat{x}(t); \frac{\dot{\hat{x}}(t)}{\omega_n}\right] + \pi \tag{2.224}$$

in which the states produced by the observer, see subsection (2.6.2), are used, see also (2.43) and (2.55).

Due to the stochastic excitation and due to the fact that the SDOF oscillator acts as a band-pass filter itself, the SDOF oscillator responds with several frequencies in the vicinity of its natural frequency. By continuously updating the TAP, the anti-phasing between the velocity of the SDOF oscillator and the superimposed control force is continuously achieved.

To ensure that both TRD units jointly damp the motion for large vibration amplitudes and neutralize each other for small vibration amplitudes, the TAPs, $\varphi_{t,1}(A)$ and $\varphi_{t,2}(A)$, for the individual TRD units are computed as a function of the time-varying vibration amplitude $A(t)$, see figure 2.67. Note that $A(t)$ is a continuous signal as $\hat{x}(t)$ and $\dot{\hat{x}}(t)$, which are produced by the observer, are also continuous signals.

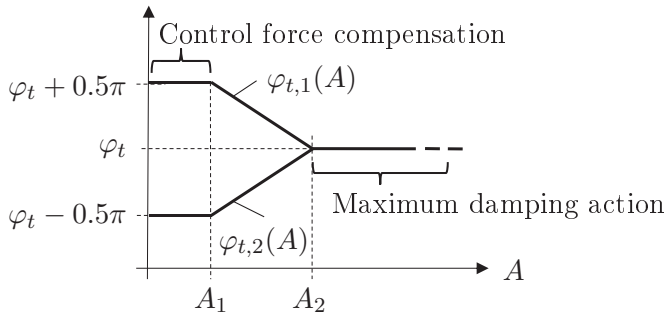

Figure 2.67: Computation of TAPs for each TRD unit

The introduced vibration-amplitude thresholds, A_1 and A_2, are to be set by the designer. When $A(t) \geq A_2$, both TRD-units are required to follow the TAP, $\varphi_t(t)$, see figure 2.67. When $A(t) < A_1$, each TRD unit is required to deviate from $\varphi_t(t)$; one by 0.5π and the other by -0.5π. To achieve this, two individual TAPs, $\varphi_{t,1}(A)$ and $\varphi_{t,2}(A)$ as a function of the time-varying vibration amplitude $A(t)$ for the individual TRD units are formulated, see figure 2.67. As $A(t)$ is a continuous signal, $\varphi_{t,1}(A)$ and $\varphi_{t,2}(A)$ are also continuous signals. Therefore, no discontinuities are produced in $\varphi_{t,1}(A)$ and $\varphi_{t,2}(A)$; see discussion at the end of this subsection.

$\varphi_{t,1}$ and $\varphi_{t,2}$ are then fed through a filter. The filter is shown for $\varphi_{t,1}$ in figure 2.68 in which K_φ refers to a proportional feedback gain. It produces the filtered TAP $\varphi_{t,1,f}$. The input of the integrator refers to the filtered target angular velocity. This filtered target angular velocity is the more variable the larger K_φ. If $K_\varphi = 0$, $\varphi_{t,1,f}$ would have an ideal saw-tooth shape with a constant slope, ω_n, the preferred target angular velocity. However, $\varphi_{t,1,f}$ will not track $\varphi_{t,1}$. If $K_\varphi \to \infty$, $\varphi_{t,1,f}$ will nearly perfectly track $\varphi_{t,1}$. Summarizing the above, $\varphi_{t,1,f}$ tracks $\varphi_{t,1}$ more accurately, the larger K_φ is at the expense of a higher variability of the filtered target angular velocity. The parameter K_φ will be varied in the following. More detailed studies with another, more powerful filter are performed in chapter 3.

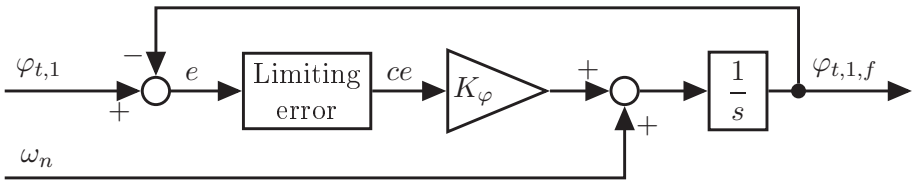

Figure 2.68: Filtering of TAP $\varphi_{t,1}$

Numerical simulations with a duration of one hour were performed. The complete simulation model including the individual blocks is shown in figure 2.69.

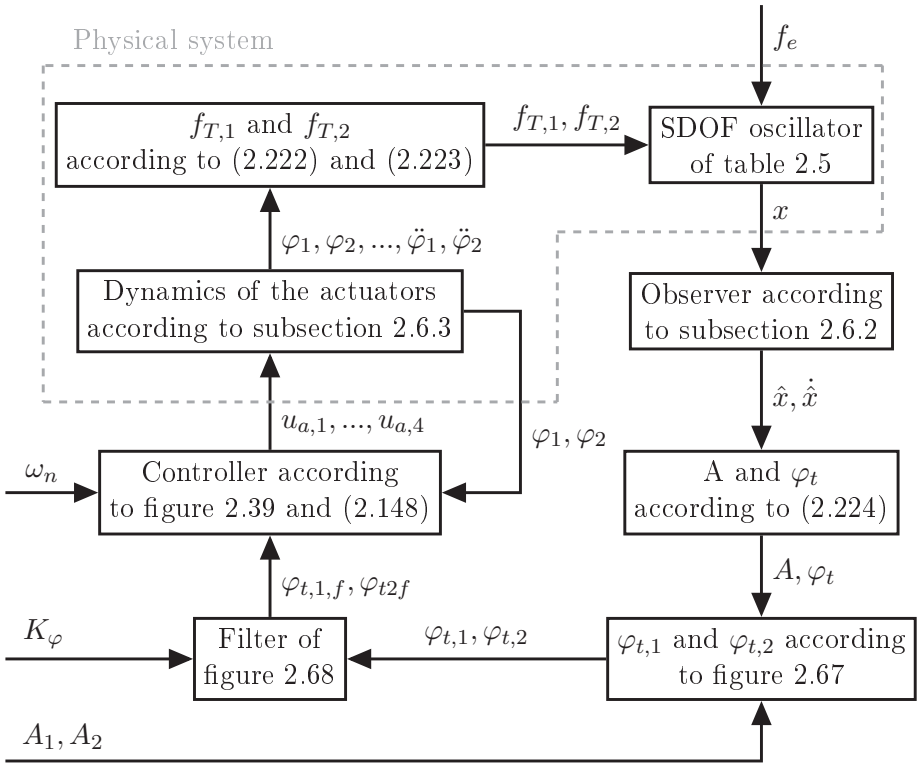

Figure 2.69: Simulation model for tuning

The vibration-amplitude thresholds A_1 and A_2 as well as the gain K_φ were varied in chosen ranges. For the control of the rotors, the control scheme of figure 2.39 is used. It has the filtered TAPs of figure 2.68 as input. The target angular velocity is set to the preferred angular velocity ω_n. Using the controller $C(s)$ of (2.149) with $K_P = 10\,\mathrm{V/(rad)}$ yields adequate tracking results. By adequate it is meant that the rotors accurately track the filtered TAP (i.e. the tracking dynamics of the rotors are much faster than the dynamics of the filter). The dynamics of the actuators were described in subsection 2.6.3.

The simulations are assessed using the standard deviation of the controlled displacement x_{std} and the standard deviations of the angular velocities, $\dot{\varphi}_{std,1}$ and $\dot{\varphi}_{std,2}$, of the individual TRD units, see table 2.13. For the computation of the standard deviations of the rotor velocities, $\dot{\varphi}_1(t)$ and $\dot{\varphi}_2(t)$ represent one rotor of the first and second TRD unit, respectively. This can be done by assuming that the dynamics of both rotors of of one TRD unit are equal.

Table 2.13: Tuning of control algorithm and assessment of numerical simulations (rows written in bold are validated experimentally)

Tuning variables			Assessment criteria		
A_1 [m]	A_2 [m]	K_φ [1/s]	x_{std} [m]	$\dot{\varphi}_{std,1}$ [(rad)/s]	$\dot{\varphi}_{std,2}$ [(rad)/s]
0.01	0.05	0.1	0.0160	0.15	0.14
0.01	0.05	0.5	0.0091	0.28	0.28
0.01	**0.05**	**1.0**	**0.0089**	**0.37**	**0.37**
0.02	0.06	0.1	0.0132	0.09	0.09
0.02	0.06	0.5	0.0126	0.22	0.22
0.02	**0.06**	**1.0**	**0.0126**	**0.30**	**0.30**
0.03	0.07	0.1	0.0157	0.07	0.07
0.03	0.07	0.5	0.0157	0.17	0.17
0.03	**0.07**	**1.0**	**0.0157**	**0.22**	**0.22**

uncontrolled: $x_{std} = 0.0236\,\mathrm{m}$

Table 2.13 shows the assessment of the numerical simulations with the corresponding tuning variables. It becomes evident that the magnitude of the vibrations is lower, the smaller the vibration-amplitude thresholds A_1 and A_2 are set and the higher K_φ is chosen. This is at the expense of larger variations in the angular velocities and represents the main trade-off the design engineer has to make.

Simulation results were then validated experimentally. The excitation force was applied on the table. Subsequently, the control algorithm for the TRD units was initiated. Test duration is, as before, one hour. The data off all required states was recorded at all times. Table 2.14 shows the results for three tuning sets.

Table 2.14: Tuning of control algorithm and assessment of tests

Tuning variables			Assessment criteria		
A_1 [m]	A_2 [m]	K_φ [1/s]	x_{std} [m]	$\dot{\varphi}_{std,1}$ [(rad)/s]	$\dot{\varphi}_{std,2}$ [(rad)/s]
0.01	0.05	1.0	0.0096	0.39	0.39
0.02	0.06	1.0	0.0135	0.27	0.27
0.03	0.07	1.0	0.0170	0.23	0.23

uncontrolled: $x_{std} = 0.0236\,\mathrm{m}$

It becomes evident that the standard deviations of the angular velocities and the displacements of the numerical simulations and the experiments nearly coincide, see table 2.13 and 2.14. Thus, the linear models used for the simulation describe the dynamics of the table, the rotors and the linear actuator adequately accurate. The standard deviation x_{std} of the uncontrolled displacement response is 0.0236 m and it is, depending on the tuning, reduced to 0.0096 m, 0.0135 m and 0.0170 m. This corresponds to a reduction of 59.3 %, 43.0 % and 28.0 %, respectively.

Figure 2.70 shows the vibration amplitude $A(t)$ according to (2.224), the angular positions ($\varphi_1(t)$ and $\varphi_2(t)$) and the angular velocities ($\dot{\varphi}_1(t)$ and $\dot{\varphi}_2(t)$) of the first and second TRD unit in a chosen time interval. As before, the angular positions and angular velocities are shown for the first rotor of the first and second TRD unit, respectively.

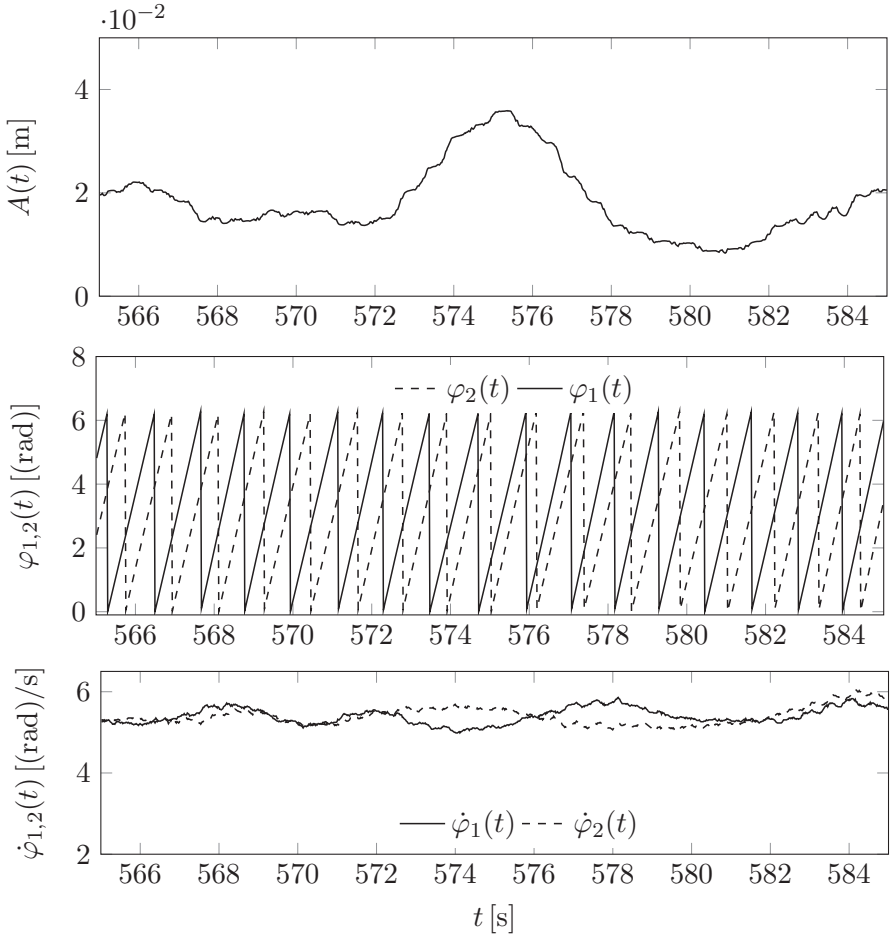

Figure 2.70: Several states of test using two TRD units

At $t = 566\,\mathrm{s}$, $A(t)$ is slightly above A_1. Therefore, the rotors are, as required, nearly in anti-phase to each other, see state $\varphi_{1,2}(t)$. From $t = 573\,\mathrm{s}$ up to $t = 575.5\,\mathrm{s}$, $A(t)$ increases and the rotors become more in phase with each other. To achieve this, $\dot{\varphi}_1(t)$ is decreased and $\dot{\varphi}_2(t)$ is increased. At $t = 575.5\,\mathrm{s}$, $A(t)$ reaches a peak below A_2. Therefore, the phasing between both TRD units is not perfectly the same. From $t = 576\,\mathrm{s}$ up to $t = 580\,\mathrm{s}$, the both TRD units cause the vibrations to decay. Consequently, as $A(t)$ decreases, the control forces of the individual TRD units are set increasingly in anti-phase. This is realized by increasing $\dot{\varphi}_1(t)$ and decreasing $\dot{\varphi}_2(t)$ slightly. At $t = 580\,\mathrm{s}$, as $A(t) \approx A_1$, the control forces of the TRD units are, as at the start, nearly in anti-phase.

Discussion

The simulations and the experiments of this subsection have shown that the proposed control algorithm allows the individual TRD units to work as wished: For small vibration amplitudes ($A(t) < A_1$), the control forces act in anti-phase and for large vibrations ($A(t) > A_2$), in-phase and, simultaneously, in anti-phase to the velocity of the SDOF oscillator. Furthermore, the angular velocity of the rotors is nearly constant. Some aspects for tuning the proposed control algorithm are discussed in the following:

1. The lower the vibration-amplitude thresholds are set, the larger becomes the vibration-amplitude range in which both TRD units jointly damp. Consequently, the vibrations are more reduced. However, as the resulting responses of the SDOF oscillator deviate more from the mono-frequent vibration, the undesired variations in the angular velocities become larger. This also results in larger tangential forces, which can be seen as an additional excitation as they act randomly on the SDOF oscillator. If the effect of the tangential forces becomes too large, a further decrease of the vibration-amplitude thresholds is ineffective.

2. The tuning of the filter of figure 2.68 is a trade-off between ensuring the anti-phasing between the superimposed control force (control force resulting from both TRD units) and the preference of having a nearly constant angular velocities. More studies with a similar filter are performed in chapter 3.

3. The vibration-amplitude thresholds must be set sufficiently far apart from each other. Otherwise, if the vibration amplitude runs through the vibration-amplitude range from A_1 to A_2 or vice versa, see figure 2.67, the computed TAPs $\varphi_{t,1}$ and $\varphi_{t,2}$ are required to change quickly. This leads to undesired high variations in the target angular velocities for $A_1 < A(t) < A_2$. However, it can be checked easily by the designer. If large variations in the angular velocities only occur when the vibration amplitude runs through the considered vibration-amplitude range from A_1 to A_2 or vice versa, A_1 and A_2 must be set further apart from each other.

4. Another issue arises when the vibrations nearly come to rest. When this occurs, the target angular velocity of figure 2.68 (input of the integrator) varies more strongly than by large vibrations. It is even possible that the control error $ce(t)$ in figure 2.68 exceeds the limits of $\pm\pi$. Consequently, discontinuities in the control error $ce(t)$ are formed. Such discontinuities lead to relatively large angular accelerations. They occurred several times within the simulations and the tests. This is because, although the vibrations are nearly at rest and the control forces are set in anti-phase to each other, the filter of figure 2.68 is still required to ensure that the anti-phasing between the velocity of the SDOF oscillator and the superimposed control force is guaranteed for when the vibration amplitude rises again.

   It is possible to continuously update K_φ as a function of the vibration amplitude. By setting K_φ to zero for the case that the vibrations are nearly at rest and to a greater value for larger vibration amplitudes, the filter of figure 2.68 produces a TAP with a saw-tooth shape. Consequently, for the case the vibrations are nearly at rest, a constant target angular velocity is obtained. However, when the vibration amplitude increases again, angular accelerations occur to regain the anti-phasing between the velocity of the SDOF oscillator and the superimposed control force of the TRD; therefore, not solving the issue of the previous paragraph.

2.9.3 Modifying the phasing between the control force and the velocity of the SDOF oscillator

Open-loop studies

To achieve maximum damping performance with the TRD operated in the continuous rotation mode, the control force of the TRD is to be set in anti-phase to the velocity of the SDOF oscillator. By leaving this anti-phasing, the damping effect of the TRD can be varied.

In subsection 2.2.2, an optimal initial angular position $\varphi_{0,opt}$ for particular initial conditions was derived for an open-loop configuration. This ensures optimal damping performance; hence, the anti-phasing between the control force and the velocity of the SDOF oscillator. A phase offset from the optimal initial angular position can be introduced to alter the damping performance. To investigate the damping effect of the TRD with regard to a phase offset from the optimal initial angular position derived in subsection 2.2.2, a phase offset, $\Delta\varphi$, is added to (2.26), see the following equation

$$\ddot{x}(t) + 2\xi\omega_n\dot{x}(t) + \omega_n^2 x(t) = \mu_c r\omega_d^2 \cos\left(\omega_d t + \varphi_{0,opt} + \Delta\varphi\right) \tag{2.225}$$

in which the initial angular position φ_0 is replaced by the optimal value $\varphi_{0,opt}$ according to (2.32) for the particular initial conditions, $x_0 > 0$ and $\dot{x}_0 = 0$, which are assumed for the open-loop studies of this subsection. Furthermore, μ_c of (2.12) is used in the following.

In section 2.3, the angular velocity of the rotors was set to ω_d. When using the optimal initial angular position according to (2.32) and setting $\Delta\varphi$ to zero, positive displacement peaks occur in multiples of T_d provided that re-excitation does not occur within the considered time interval, see figure 2.7. However, when setting $\Delta\varphi$ unequal to zero or multiples of π and considering a single vibration cycle—the time between two successive displacement peaks—, the next positive displacement peak will not occur at $t = T_d$. To ensure that all rotors have the same angular position as at $t = 0$ when the next positive displacement peak occurs, the rotors must be driven with an adjusted (angular) frequency, ω_a. Note in the following, one vibration cycle is considered. As the rotors are driven now with an adjusted frequency ω_a instead of with ω_d, ω_d is replaced by ω_a in (2.225), see the following equation:

$$\ddot{x}(t) + 2\xi\omega_n\dot{x}(t) + \omega_n^2 x(t) = \mu_c r\omega_a^2 \cos\left(\omega_a t + \varphi_{0,opt} + \Delta\varphi\right) \tag{2.226}$$

Assuming that inherent damping is not present ($\xi = 0$) and solving (2.226) for $x(t)$ gives

$$x(t) = \Xi_6 \sin\left(\omega_n t\right) - \Xi_7 \cos\left(\omega_n t\right) + \Xi_8 \cos\left(\omega_a t + \varphi_{0,opt} + \Delta\varphi\right) \tag{2.227}$$

with Ξ_6, Ξ_7 and Ξ_8 given in the following equations:

$$\Xi_6 = \frac{\omega_a^3 \mu_c r \sin\left(\varphi_{0,opt} + \Delta\varphi\right) + \dot{x}_0\left(\omega_n^2 - \omega_a^2\right)}{\omega_n\left(\omega_n^2 - \omega_a^2\right)} \tag{2.228}$$

$$\Xi_7 = \frac{\omega_a^2 \mu_c r \cos\left(\varphi_{0,opt} + \Delta\varphi\right) + x_0\left(\omega_a^2 - \omega_n^2\right)}{\omega_n^2 - \omega_a^2} \tag{2.229}$$

$$\Xi_8 = \frac{\omega_a^2 \mu_c r}{\omega_n^2 - \omega_a^2} \tag{2.230}$$

Taking the time derivative of (2.227) yields:

$$\dot{x}(t) = \Xi_6\omega_n \cos\left(\omega_n t\right) + \Xi_7\omega_n \sin\left(\omega_n t\right) - \Xi_8\omega_a \sin\left(\omega_a t + \varphi_{0,opt} + \Delta\varphi\right) \tag{2.231}$$

To ensure that the oscillator performs a single vibration cycle in the time the rotors also perform one full revolution, (2.232) must hold

$$\dot{x}(t = T_a) = 0 \qquad \text{with} \qquad T_a = \frac{2\pi}{\omega_a} \tag{2.232}$$

in which T_a refers to the actual period length.

The condition of (2.232) is inserted into (2.231) and solved numerically for ω_a. The results are shown in figure 2.71 for several different values of $\mu_c r/x_0$.

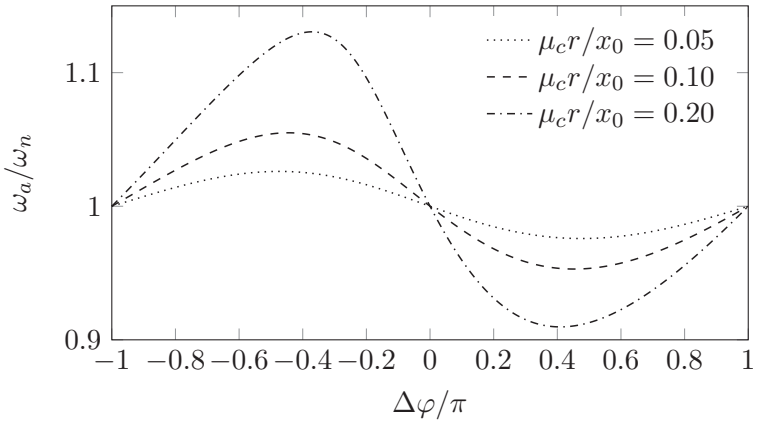

Figure 2.71: Required adjusted frequency ω_a to hold the initial angular position $\varphi_{0,opt}+\Delta\varphi$ with respect to the initial angular position offset $\Delta\varphi$ for several values of $\mu_c r/x_0$

The parameter $\mu_c r/x_0$ can be interpreted as the influence that the control force has on the motion. The higher this value, the larger the control force in comparison to the system forces and the larger the deviation of the actual frequency from the natural circular frequency. For $\Delta\varphi = -\pi$ or π, the control force is in phase with the velocity $\dot{x}(t)$ of the SDOF oscillator, whereas for $\Delta\varphi = 0$, the control force is in anti-phase to $\dot{x}(t)$. When increasing $\Delta\varphi$ from zero to π, the phase of the control force becomes increasingly in phase with $x(t)$, i.e. in anti-phase to $\ddot{x}(t)$. This is equivalent to becoming in phase with the inertial force or in anti-phase to the restoring spring force. Therefore, this is frequently named positive active mass or negative active stiffness, respectively [16]. A decrease of the adjusted frequency is required to hold the phasing between the SDOF oscillator and the control force of the TRD. Conversely, when changing $\Delta\varphi$ from zero to $-\pi$, the control force provides more and more negative active mass or positive active stiffness [16]. Therefore, an increase of the adjusted frequency is required.

The normalized control force of the TRD is given by the right-hand side of (2.226). Multiplying this with the velocity $\dot{x}(t)$ of (2.231) and forming the integral gives the work done by the control force on the SDOF oscillator normalized by the mass $m + m_c$, see (2.233).

$$\frac{W_c}{m + m_c} = \int_{t=0}^{t=T_a} \dot{x}(t)\mu_c r\omega_a^2 \cos\left(\omega_a t + \varphi_{0,opt} + \Delta\varphi\right)\mathrm{d}t \tag{2.233}$$

With $x_0 > 0$ and $\dot{x}_0 = 0$, the initial vibration energy of the SDOF oscillator, see (2.100), is given by: $E_{v,0} = 0.5kx_0^2$. Using (2.8) and normalizing $E_{v,0}$ by $m + m_c$ yields:

$$\frac{E_{v,0}}{m + m_c} = \frac{1}{2}\omega_n^2 x_0 \tag{2.234}$$

The work done by the control force on the SDOF oscillator over the initial vibration energy of the SDOF oscillator can be computed numerically using the adjusted frequency ω_a of figure 2.71. It is shown in figure 2.72 for several different values of $\mu_c r/x_0$.

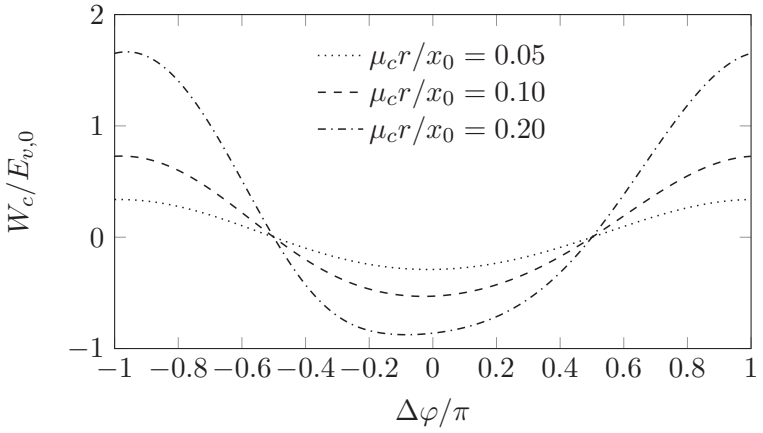

Figure 2.72: Work done by control force over initial vibration energy of the SDOF oscillator, $W_c/E_{v,0}$, during the considered vibration cycle

For $\Delta\varphi = \pm 0.5\pi$, $W_c = 0$. This means that for $\Delta\varphi = \pm 0.5\pi$, the control force does not change the vibration energy of the SDOF oscillator within the considered time interval from $t = 0$ to $t = T_a$. At $\Delta\varphi = 0$, $W_c/E_{v,0}$ is not a minimum. The minimum is slightly below $\Delta\varphi = 0$ and the deviation from $\Delta\varphi = 0$ increases with higher $\mu_c r/x_0$. This can be explained as follows. When a negative phase offset $-\pi < \Delta\varphi < 0$ is assumed, the adjusted frequency increases, see figure 2.71. The higher the actual frequency, the higher the amplitude of the control force. Therefore, W_c decreases further when $\Delta\varphi$ becomes negative. Furthermore, it becomes evident that in the vicinity of $\Delta\varphi = 0$, the slope of W_c is relatively small. Because of this, a deviation from the optimal initial angular position of $\pm 0.2\pi$ can be easily permitted without a great loss in damping performance.

Now considering inherent damping and solving (2.226) for $x(t)$ gives (2.235)

$$x(t) = \mathrm{e}^{-\xi\omega_n t}\left[(x_0 - x_{pa,0})\cos(\omega_d t) + \frac{\dot{x}_0 - \dot{x}_{pa,0} + \xi\omega_n (x_0 - x_{pa,0})}{\omega_d}\sin(\omega_d t)\right] + x_{pa}(t) \tag{2.235}$$

with the particular solution

$$x_{pa}(t) = \omega_a^2 \mu_c r \frac{\left(\omega_n^2 - \omega_a^2\right)\cos(\omega_a t + \varphi_{0,opt} + \Delta\varphi) + 2\omega_a \xi\omega_n \sin(\omega_a t + \varphi_{0,opt} + \Delta\varphi)}{\left(\omega_a^2 - \omega_n^2\right)^2 + \left(2\xi\omega_n\omega_a\right)^2} \tag{2.236}$$

and the initial conditions $x_{pa,0}$ and $\dot{x}_{pa,0}$:

$$x_{pa,0} = x_{pa}(t=0) \qquad \dot{x}_{pa,0} = \dot{x}_{pa}(t=0) \tag{2.237}$$

Taking the time derivative of (2.235) gives (2.238)

$$\dot{x}(t) = \mathrm{e}^{-\xi\omega_n t}\left[\Xi_9 \cos(\omega_d t) + \Xi_{10}\sin(\omega_d t)\right] + \dot{x}_{pa}(t) \tag{2.238}$$

with the velocity $\dot{x}_{pa}(t)$ of the particular response

$$\dot{x}_{pa}(t) = \omega_a^3 \mu_c r \frac{\left(\omega_a^2 - \omega_n^2\right)\sin(\omega_a t + \varphi_{0,opt} + \Delta\varphi) + 2\omega_a \xi\omega_n \cos(\omega_a t + \varphi_{0,opt} + \Delta\varphi)}{\left(\omega_a^2 - \omega_n^2\right)^2 + \left(2\xi\omega_n\omega_a\right)^2} \tag{2.239}$$

and the constants

$$\Xi_9 = \dot{x}_0 - \dot{x}_{pa,0} \tag{2.240}$$

$$\Xi_{10} = \omega_d x_{pa,0} - \omega_d x_0 - \xi\omega_n \frac{\dot{x}_0 - \dot{x}_{pa,0} + \xi\omega_n (x_0 - x_{pa,0})}{\omega_d} \tag{2.241}$$

To ensure, as before, that the SDOF oscillator performs a single vibration cycle in the time the rotors also perform a full revolution, (2.232) must hold.

As done for oscillator without inherent damping, (2.232) is inserted into (2.238). Solving this numerically for ω_a gives the required adjusted frequency to ensure that the rotors perform a single revolution from $t = 0$ to $t = T_a$. Figure 2.73 shows the required adjusted frequencies for several damping ratios and a particular value of $\mu_c r/x_0$. The corresponding work done by the control force on the SDOF oscillator over the initial vibration energy is shown in the right subfigure.

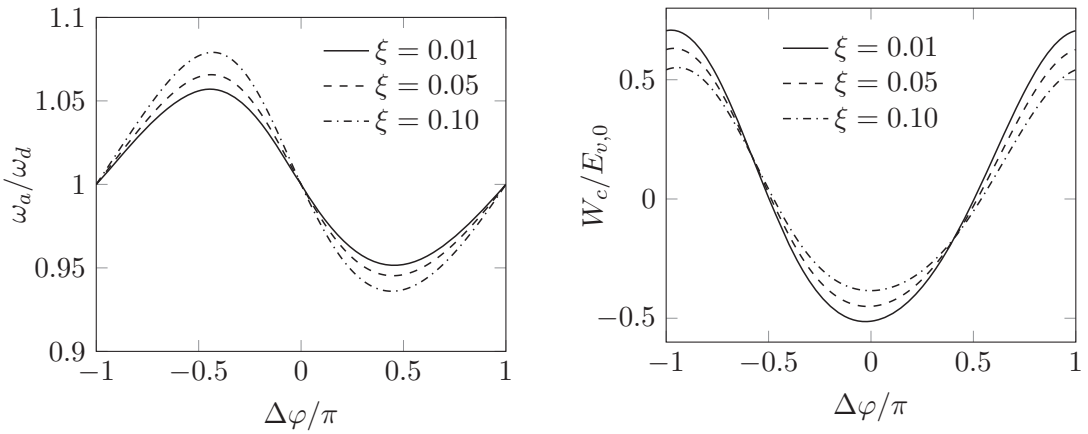

Figure 2.73: Required adjusted frequency ω_a and work done by control force over initial vibration energy of SDOF oscillator with respect to the initial angular position offset $\Delta\varphi$ for $\mu_c r/x_0 = 0.10$ and for several values of ξ

Closed-loop control algorithm

Now a control algorithm is presented to leave and regain the anti-phasing between the control force of the TRD and the velocity of the SDOF oscillator. This is done by continuously varying the phasing between the control force and the velocity of the SDOF oscillator as a function of the vibration amplitude. When the vibrations are above a certain vibration-amplitude threshold A_2, the rotors are required to follow the target angular position φ_t. When the vibrations are below a certain vibration-amplitude threshold A_1, the phase offset from the target angular position φ_t is set such that the damping effect vanishes. This is shown in figure 2.74, producing the adjusted target angular position, $\varphi_{t,a}(A)$.

The control scheme shown in figure 2.69 is implemented anew. However, the block '$\varphi_{t,1}$ and $\varphi_{t,2}$ according to figure 2.68' is replaced by the block 'computation of adjusted TAP according to figure 2.74'. Furthermore, $\varphi_{t,a}$ is used for both TRD units, allowing for a direct comparison with the control algorithm of the previous subsection. The simulation duration is again one hour. The vibration-amplitude thresholds, A_1 and A_2, as well as the gain K_φ were varied. As in the previous section, the standard deviations x_{std} and $\dot{\varphi}_{std,1}$ are used for the assessment of the numerical simulations, see table 2.15.

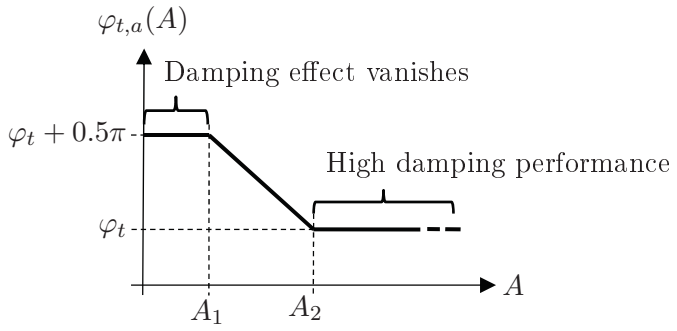

Figure 2.74: Computation of adjusted target angular position $\varphi_{t,a}(A)$ with phase offset from target angular position as a function of the vibration amplitude

Table 2.15: Tuning of control algorithm and assessment of numerical simulations for phase offset (rows written in bold are validated experimentally)

Tuning variables			Assessment criteria	
A_1 [m]	A_2 [m]	K_φ [1/s]	x_{std} [m]	$\dot{\varphi}_{std,1}$ [(rad)/s]
0	**0.02**	**0.5**	**0.0099**	**0.24**
0	**0.03**	**0.5**	**0.0121**	**0.18**
0	0.04	0.1	0.0297	0.03
0	**0.04**	**0.5**	**0.0135**	**0.15**
0	0.04	1	0.0105	0.25
0.01	0.05	0.1	0.0320	0.03
0.01	0.05	0.5	0.0172	0.12
0.01	0.05	1	0.0143	0.18
0.02	0.06	0.1	0.0352	0.03
0.02	0.06	0.5	0.0213	0.10
0.02	0.06	1	0.0187	0.13
uncontrolled: $x_{std} = 0.0236\,\mathrm{m}$				

It suffices to evaluate the variations of one rotor, $\dot{\varphi}_1(t)$, as all rotors are controlled identically and have nearly identical behavior.

The standard deviation of $x(t)$ decreases with increasing K_φ, whereas the standard deviation in $\dot{\varphi}(t)$ increases. This means that higher damping performance can be reached at the expense of higher variations in the angular velocity. Furthermore, the smaller the vibration-amplitude thresholds are set, the higher the damping performance becomes and the larger the undesired variations in the angular velocity.

Tests were then performed using the previously introduced test setup. Results are shown in table 2.16. The test results nearly coincide with the numerical simulations. The same tendency can be identified: The smaller the vibration-amplitude thresholds are set, the lower the vibrations at the expense of larger variations in the angular velocity.

Figure 2.75 shows several states of a test using the tuning variables of the first row of table 2.16 for an arbitrarily chosen time interval.

Table 2.16: Assessment of tests with phase offset

Tuning variables			Assessment criteria	
A_1 [m]	A_2 [m]	K_φ [1/s]	x_{std} [m]	$\dot{\varphi}_{std,1}$ [(rad)/s]
0	0.02	0.50	0.0099	0.33
0	0.03	0.50	0.0115	0.22
0	0.04	0.50	0.0130	0.19

uncontrolled: $x_{std} = 0.0236\,\mathrm{m}$

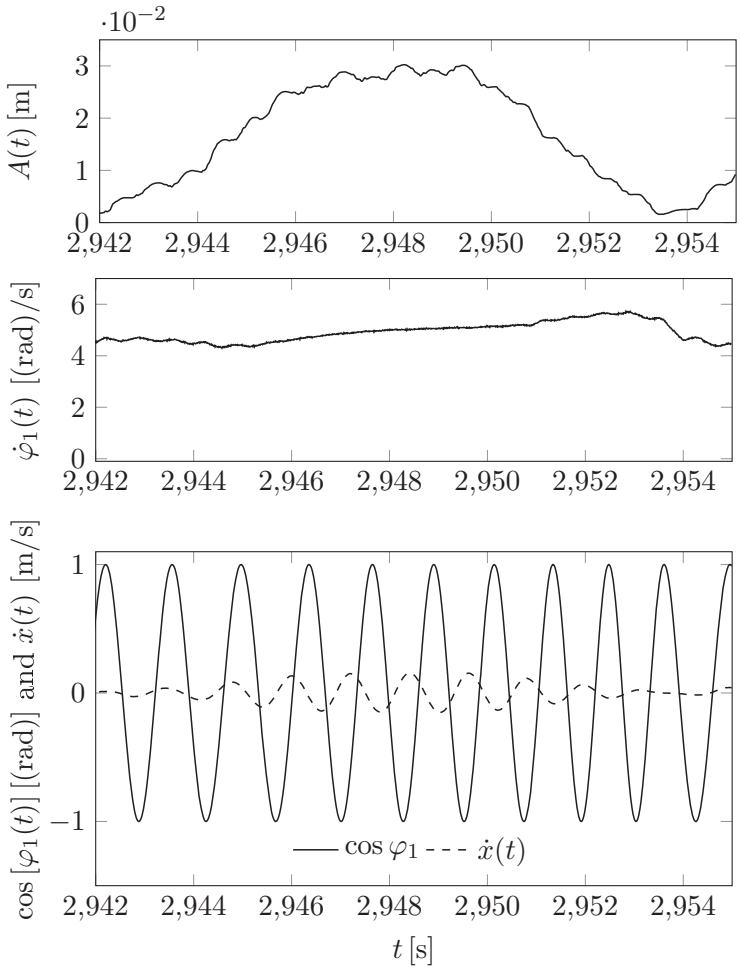

Figure 2.75: Several states of test with phase offset from optimal angular position for small vibration amplitudes

In the lower sub-diagram, the velocity $\dot{x}(t)$ of the SDOF oscillator and $\cos[\varphi_1(t)]$ are shown. $\cos[\varphi_1(t)]$ is used to indicate the phase of the control force. At $t = 2942\,\mathrm{s}$, the vibrations are nearly at rest. Due to the filtering of $\varphi_{t,a}$, $\dot{\varphi}_1(t)$ is nearly constant. From $t = 2944\,\mathrm{s}$ to $t = 2946\,\mathrm{s}$, the vibration amplitude rises. Consequently, as required, the control algorithm sets the control force increasingly in anti-phase to $\dot{x}(t)$. At $t = 2950\,\mathrm{s}$, these states are nearly in anti-phase, consequently, $A(t)$ decreases.

Discussion
The simulations and the experiments of this subsection have shown that the proposed control algorithm allows the TRD units to work as wished: For large vibration amplitudes ($A(t) > A_2$), the control force acts in anti-phase to the velocity of the SDOF oscillator and for smaller vibration amplitudes, the TRD units leave this anti-phasing. The discussion points 1,2 and 3 of subsection 2.9.2 also apply to the control algorithm presented in this subsection. Discussion point 4 must be adapted:

For small vibrations, the control algorithm is still required to ensure a certain phasing between the control force and the phase of vibration (introduced in subsection 2.3.2). When the vibrations nearly come to rest, the discontinuities explained in discussion point 4 of subsection 2.9.2 occur. They lead to additional undesired angular accelerations. Therefore, the comments regarding K_φ in discussion point 4 of subsection 2.9.2 also apply to the control algorithm of this subsection.

2.9.4 Discussion on damping small vibrations using the continuous rotation mode

Before starting off with the discussion, the term 'controllability', which is frequently used in the field of control engineering, is introduced in the following [33]. A system is controllable if it can be brought from an arbitrary state point to a second, desired state point in any time interval. For the SDOF oscillator, the second, desired state point is the rest position ($x = 0$ and $\dot{x} = 0$). Controllability can be checked by computing the Controllability Gramian. This was done for the SDOF oscillator in [23, p. 233]. As the Controllability Gramian has full rank, the SDOF oscillator is controllable [23]. However, this implies that an arbitrary input, which is a force, of the SDOF oscillator must be available. As the TRD cannot provide such an arbitrary force, at least in the continuous rotation mode, it can be stated that the SDOF oscillator is not controllable by the TRD in the continuous rotation mode.

To illustrate this, figure 2.2 is reconsidered and the following is assumed: At an initial time-point, $t = 0$, the SDOF oscillator is at rest ($x_0 = 0$ and $\dot{x}_0 = 0$). Furthermore, $\varphi_0 = 0$ and $\dot{\varphi}_0 = \omega_d$ as desired in the continuous rotation mode. This means that a force in positive x-direction is produced by the TRD at $t = 0$. At the next time-point, the SDOF oscillator will have a positive velocity $\dot{x}(t)$ and $\varphi(t)$ will be slightly above zero. Due to the constraint of the continuous rotation mode, $\dot{\varphi} = \omega_d$, the TRD is forced to continue generating a control force in the positive direction of $\dot{x}(t)$. Thus, the TRD will further excite the SDOF oscillator. For this reason, the TRD is unable to control small vibrations of the SDOF oscillator in the continuous rotation mode.

The argumentation of the previous paragraph can be adapted to apply to the method of subsection 2.9.3.

The method of subsection 2.9.2 is now considered. The SDOF oscillator is considered again with the particular initial conditions $x_0 = 0$ and $\dot{x}_0 = 0$. Furthermore, at $t = 0$, the TRD units are, as wanted, operating in anti-phase to each other such that the superimposed control force vanishes. Besides that, an excitation force is assumed to accelerate the SDOF oscillator. Therefore, the velocity of the SDOF oscillator $\dot{x}(t)$ is unequal to zero at the next time-point. To make the superimposed control force damp this motion, two states must be reached:

1. The anti-phasing between both TRD units must be varied such that the superimposed control force amplitude is unequal to zero. This is realized by increasing the angular velocity of the first TRD unit and decreasing the angular velocity of the other TRD unit.

2. The anti-phasing between $\dot{x}(t)$ and the superimposed control force must be regained. If the superimposed control force is coincidentally in phase with $\dot{x}(t)$, the SDOF oscillator will be further excited, whereas if they are occasionally in anti-phase, the TRD units will damp the motion. The time it takes until the anti-phasing between the superimposed control force and $\dot{x}(t)$ is regained depends on the tuning of the filter of figure 2.68. The more aggressive it is set, the faster the anti-phasing is regained. This is done at the expense of larger variations in the target angular velocity. Consequently, larger tangential forces are produced. These tangential forces can be seen as an additional excitation force as they act randomly on the SDOF oscillator.

It became apparent that for regaining the anti-phasing between $\dot{x}(t)$ and the superimposed control force, angular accelerations generating tangential forces are needed. It would be more beneficial to directly use these tangential forces for vibration control, instead of generating those in an arbitrary manner for regaining the anti-phasing between $\dot{x}(t)$ and the superimposed control force. Note again that up to the time-point at which the anti-phasing is regained, the tangential forces act randomly and can be seen as an additional excitation force.

It will be shown in chapter 3 that there exists a vibration amplitude below which an operation in the continuous rotation is no longer beneficial.

*

3

Twin rotor damper for the damping of stochastically forced vibrations

3.1 Influence of excitation force

3.1.1 Introduction

The applicability of the TRD for the damping of stochastically forced vibrations is studied in this chapter. A summary of this chapter can be found in [42]. A SDOF oscillator under the action of a stochastic excitation force is considered. The excitation force affects the states of the SDOF oscillator, $\ddot{x}(t)$, $\dot{x}(t)$ and $x(t)$. These states are used for the computation of the target angular position (TAP), see section 2.3. To study the effect of the excitation force on the SDOF oscillator, (2.11) is recalled. Neglecting the action of the TRD and solving (2.11) for $\ddot{x}(t)$ yields:

$$\ddot{x}(t) = F_e(t) - 2\xi\omega_n\dot{x}(t) - \omega_n^2 x(t) \tag{3.1}$$

in which $F_e(t)$ is given in (2.13). A block diagram representing (3.1) is shown in figure 3.1.

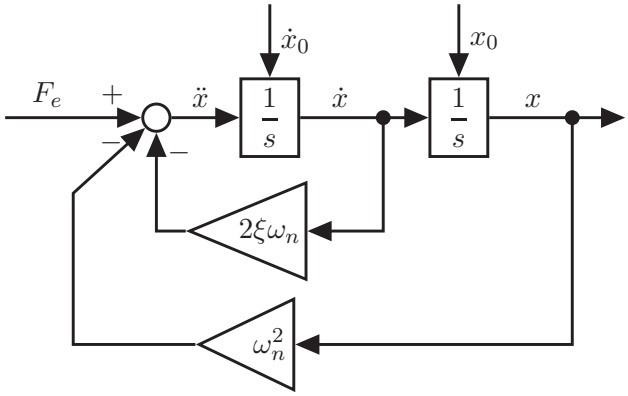

Figure 3.1: Block diagram representing (3.1)

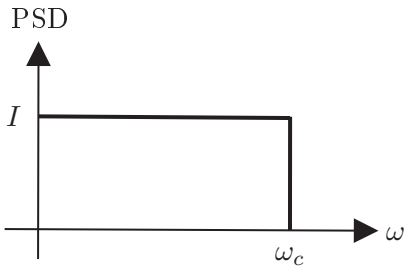

Figure 3.2: Power spectral density of band-limited white noise

Due to the direct influence of $F_e(t)$ on $\ddot{x}(t)$, $\ddot{x}(t)$ is most strongly influenced by the excitation force and therefore the most disrupted signal. This disruption is reduced (smoothed) due to the integration, see figure 3.1, therefore enhancing the quality (smoothness) of $\dot{x}(t)$ and $x(t)$.

3.1.2 Excitation force

White noise is assumed for the excitation force $F_e(t)$. White noise signals have a zero mean and a constant power spectral density (PSD) [43, 44]. A random signal containing all frequencies is generated. Because of these properties, white noise is frequently used as a test signal. However, when performing numerical simulations, only frequencies up to a

certain corner frequency ω_c are generated. This is due to sampling in time. Therefore, such signals are named band-limited white noises. The power spectral density (PSD) of such signals is constant over a finite range of frequencies and vanishes above ω_c, see figure 3.2, in which I refers to the magnitude of the white noise (height of rectangular spectrum). In the following, this magnitude I is referred to as excitation power.

Within the numerical simulations performed in this section, the sampling time for the generation of the excitation force and the solver are set as given by the following equation

$$T_s = \frac{1}{100} \frac{2\pi}{\max(\omega_n, \omega_f)} \tag{3.2}$$

in which $\max(\omega_n, \omega_f)$ refers to the larger value of ω_n and ω_f; ω_f will be defined later on.

3.1.3 Signal norms

To evaluate the numerical simulations done in the following, some signal norms are introduced [45, 46]. The instantaneous power $P_{in}(t)$ of a signal $s(t)$ is given by the squared magnitude of the signal [46]:

$$P_{in}(t) = |s(t)|^2 \tag{3.3}$$

Note that the upper-case P now refers to the power of a signal and no longer to the mechanical power of one actuator. The power, P_{si}, of the signal $s(t)$ within the time interval from t_l to t_u is computed as given in (3.4).

$$P_{si}[s(t)] = \frac{1}{t_u - t_l} \int_{t_l}^{t_u} s(t)^2 \mathrm{d}t \tag{3.4}$$

The power $P_{si}[s(t)]$ of (3.4) is, in many textbooks, frequently referred to as time-averaged power or average power [46]. The variance of a signal $s(t)$ is

$$\mathrm{Var}\,[s(t)] = \frac{1}{t_u - t_l} \int_{t_l}^{t_u} [s(t) - \mu_s]^2 \,\mathrm{d}t \qquad \mu_s = \frac{1}{t_u - t_l} \int_{t_l}^{t_u} s(t) \mathrm{d}t \tag{3.5}$$

in which μ_s is the mean value of $s(t)$ [47]. If $\mu_s = 0$, the variance $\mathrm{Var}\,[s(t)]$ of a signal is equal to its power $P_{si}[s(t)]$. The standard deviation of a signal $s(t)$ is as given in the following equation [47]:

$$\mathrm{std}(s(t)) = \sqrt{\frac{1}{t_u - t_l} \int_{t_l}^{t_u} [s(t) - \mu_s]^2 \,\mathrm{d}t} \tag{3.6}$$

When evaluating signal magnitudes in terms of power $P_{si}[s(t)]$ or the rms-value according to (2.96), the deviation of the signal from zero is quantified, whereas when computing in terms of standard deviation or variance, the deviation from the mean value is quantified.

Now considering the signal $F_e(t)$, which has the unit $\mathrm{m/s^2}$, its units of $P_{in}(t)$ and $P_{si}[F_e(t)]$ are $\mathrm{m^2/s^4}$, see (3.3) and (3.4). Considering the PSD diagram of figure 3.2, the excitation power I of the excitation force has the unit $\mathrm{m^2/s^4}$ per (rad)/s. Furthermore, when a certain excitation power is assumed, it must also be clarified if the excitation power refers to a one-sided (only positive frequencies) or two-sided spectrum (positive and negative frequencies).

3.1.4 Power of displacement response with initial conditions and excitation force

Considering a free vibration, the motion of the SDOF oscillator is governed by:

$$\ddot{x}(t) + 2\xi\omega_n\dot{x}(t) + \omega_n^2 x(t) = 0 \tag{3.7}$$

If inherent damping is not present, the vibration amplitude is constant. It is only dependent on the initial conditions, see the following equation.

$$A = \sqrt{x_0^2 + \left(\frac{\dot{x}_0}{\omega_n}\right)^2} \tag{3.8}$$

The power of the displacement can be evaluated with (3.4). Inserting the solution of (3.7) (see (2.18) with $\mu_c r = 0$) into (3.4) and integrating over a number of full vibration periods, e.g. one vibration period from $t_l = 0$ to $t_u = 2\pi/\omega_n$, gives the power, P_i, of the displacement due to the initial conditions for $\xi = 0$:

$$P_i = \frac{1}{2}\left[x_0^2 + \left(\frac{\dot{x}_0}{\omega_n}\right)^2\right] \qquad \text{for} \qquad \xi = 0 \tag{3.9}$$

Substituting the initial conditions, x_0 and $\dot{x}_0$, in (3.9) by the corresponding continuous signals, $x(t)$ and $\dot{x}(t)$, the power of the displacement can be computed continuously:

$$P_x(t) = \frac{1}{2}\left[x(t)^2 + \left(\frac{\dot{x}(t)}{\omega_n}\right)^2\right] \tag{3.10}$$

Considering a free vibration without inherent damping, $P_x(t)$ is constant in time, whereas it varies in time if an excitation force acts on the SDOF oscillator. $P_x(t)$ can also be seen as the (normalized) squared vibration amplitude or as the (normalized) vibration energy stored in the SDOF oscillator.

When taking inherent damping into consideration ($0 < \xi < 1$), the solution for $x(t)$ is as given in (2.27) with $\mu_c r = 0$. Taking $x(t)$, inserting it into (3.4) and solving for a number of full vibration periods gives the power of the displacement due to the initial conditions. It considers the decay due to the inherent damping. As the calculation does not provide more insight nor it is used for further derivations, it is not presented. Furthermore, assuming that the inherent damping is small ($0 < \xi < 0.1$), the vibration amplitude remains nearly constant within one vibration period. Therefore, for oscillators with small inherent damping, (3.9) can be used as an approximation for the power of the displacement response due to the initial conditions. To compute the power $P_x(t)$ for oscillators with inherent damping, ω_n is substituted with ω_d in (3.10), see the following equation:

$$P_x(t) = \frac{1}{2}\left[x(t)^2 + \left(\frac{\dot{x}(t)}{\omega_d}\right)^2\right] \tag{3.11}$$

In the following, the SDOF oscillator is additionally disturbed by an excitation force (band-limited white noise introduced in subsection 3.1.1 and 3.1.2) and the following conditions: $x_0 > 0$ and $\dot{x}_0 = 0$. The simulations can also be performed with different initial conditions. Furthermore, single vibration periods with a duration of T_n are considered.

By starting the simulation of a single vibration period with particular initial conditions and applying additionally an excitation force on the SDOF oscillator, the total power of the displacement response can be decomposed into: the power produced due to the initial conditions and the power produced by the excitation force. Considering the case that $F_e(t) = 0$ ($I = 0$), the system forces (defined in section 2.2) dictate the motion, the vibration amplitude remains nearly constant for $0 < \xi < 0.1$ and the total power of the displacement is only due to the initial conditions. Consequently, the resulting motion is mono-frequent. When the excitation power I is increased, the motion of the SDOF oscillator becomes more and more dictated by the excitation force. As a result, the response of the SDOF oscillator increasingly deviates from the mono-frequent vibration.

Starting the simulation of a single vibration period with $x_0 > 0$, $\dot{x}_0 = 0$ and $I = 0$, the next positive displacement peak will occur at $t = T_n$. If an excitation force additionally acts on the SDOF oscillator, the actual period length can the shortened or elongated and the vibration amplitude may increase or decrease within the considered time interval from $t = 0$ to $t = T_n$. This corresponds to giving positive or negative damping as well as positive or negative stiffness to the SDOF oscillator [16]. The effects of positive and negative damping as well as of positive and negative stiffness vanish when simulating a very large number of vibration periods with the same initial conditions and the same excitation power I while considering the mean values for the actual period length and the decay within the considered vibration periods.

The power of the displacement due to the initial conditions can be computed according to (3.9). The total power, P_t, of the displacement is computed according to (3.12)

$$P_t = \frac{1}{t_u - t_l} \int_{t_l}^{t_u} x(t)^2 \mathrm{d}t \tag{3.12}$$

in which the signal $s(t)$ in (3.4) is substituted by the displacement $x(t)$. It follows the power, P_e, produced by the excitation force

$$P_e = P_t - P_i \tag{3.13}$$

with P_i of (3.9). Figure 3.3 shows the normalized displacement and velocity responses of the SDOF oscillator disturbed by the excitation force and initial conditions for a single vibration period in which the power ratio

$$P_r := \frac{P_i}{P_t} \tag{3.14}$$

is introduced which is obtained with a post computation, see (3.9) and (3.12) (with $t_l = 0$ and $t_u = T_n$).

P_r can be changed by varying the excitation power I or the magnitude of x_0. All diagrams were produced using an excitation force with the same seed (same excitation force) and different magnitudes of x_0. This explains the similarities between the deviation of the displacement and of the velocity responses from the free vibration response ($P_r = 1$).

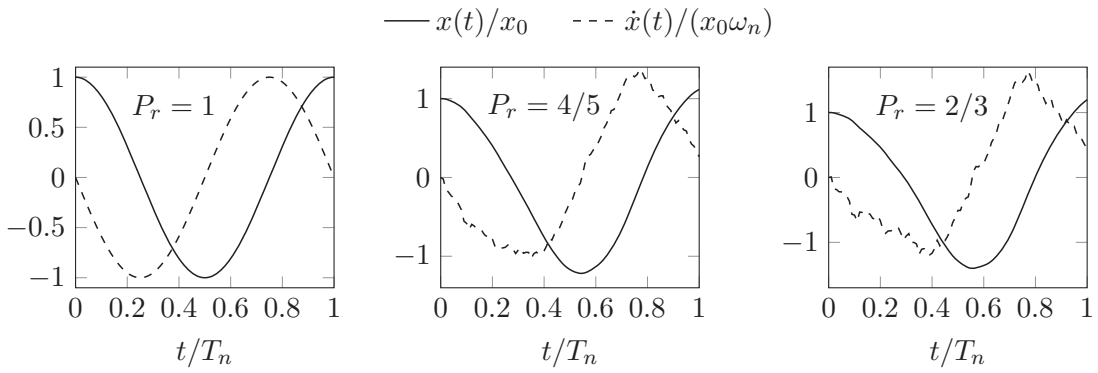

Figure 3.3: Normalized displacement $x(t)/x_0$ and velocity $\dot{x}(t)/(x_0\omega_n)$ for several ratios P_r for $\xi = 0$

Due to the properties of linear dynamic systems, the following statement holds:

Dividing the excitation power by the natural frequency ω_n gives the excitation power per natural frequency, I/ω_n (normalized excitation power with the unit $\mathrm{m}^2/\mathrm{s}^4$ per $((\mathrm{rad})/\mathrm{s})^2$). Furthermore, normalizing the initial condition x_0 ($\dot{x}_0 = 0$) by ω_n^2, x_0/ω_n^2—note the scaling of the initial condition x_0 with ω_n^2 in figure 3.1—, ensures that the same restoring spring force power due to the initial conditions is produced. Thus, by normalizing the excitation power I and the initial condition x_0 as discussed above and using the same seed for the excitation force, the same restoring-spring-force to excitation-force power ratio for the considered vibration period is produced. As a result, the same normalized curves ($x(t/T_n)/x_0$, $\dot{x}(t/T_n)/(x_0\omega_n)$) are obtained for any ω_n. This allows for considerations independent of ω_n.

It became evident that the deviation of the displacement and the velocity responses from their harmonic responses (free vibration) are larger, the smaller the ratio P_r becomes. Furthermore, the normalized displacement responses are less disturbed than the corresponding normalized velocity responses. This is due to the additional integration discussed in subsection 3.1.1. The corresponding normalized acceleration signals, which are not plotted in figure 3.3, are even more disturbed than the corresponding normalized velocity signals; for this reason, they are not shown.

It is of particular interest to continuously calculate or estimate the ratio P_r as it can be an interesting parameter for feedback or to schedule a subsequent filter. Therefore, an approach to estimate P_r is briefly discussed. It is possible to estimate the ratio P_r by continuously evaluating the preceding vibration period. P_t can be estimated continuously by forming the integral over the preceding vibration period providing the total power of the displacement:

$$P_t(t) = \frac{1}{T_n} \int_{t_l=-T_n}^{t_u=t} x(t)^2 \mathrm{d}t \tag{3.15}$$

The power of the displacement due to the actual conditions can be computed with (3.10). Subsequently, the ratio $P_x(t)/P_t(t)$ can be calculated. The calculation of $P_x(t)$ and $P_t(t)$ can be made over arbitrary time intervals. For $P_x(t)$, mean values for the preceding time interval can be computed. For $P_t(t)$, the integration limits in (3.15) can be adapted accordingly. The longer the considered time interval, the smaller the variance of $P_x(t)$ and $P_t(t)$ and consequently their ratio. This is at the expense of an increased time delay.

3.1.5 Resulting target angular positions

The TAPs corresponding to $P_r = 2/3$ of figure 3.3 are computed using (2.55), (2.56) and (2.58), see figure 3.4. To distinguish the signals from each other, offsets in the vertical axis of plus and minus two, respectively, were added. The TAPs increase by approximately 2π with the same mean slope (ω_n). For each curve, one can imagine an ideal straight line with a slope of ω_n starting at $t = 0$ with the values $3/2\pi-2$, $3/2\pi+2$ and $3/2\pi$, respectively. The deviations from the corresponding straight lines are lowest for $\varphi_t(t)$ according to (2.55) as for the computation of this TAP, the least disrupted states $x(t)$ and $\dot{x}(t)$ are used. For $\varphi_t^*(t)$ according to (2.56) with (2.52), the most disrupted states $\dot{x}(t)$ and $\ddot{x}(t)$ are used, producing the largest deviations from the straight line. For $\varphi_{t,s}(t)$, the three states $x(t)$, $\dot{x}(t)$ and $\ddot{x}(t)$ are used, producing an average deviation from the straight line.

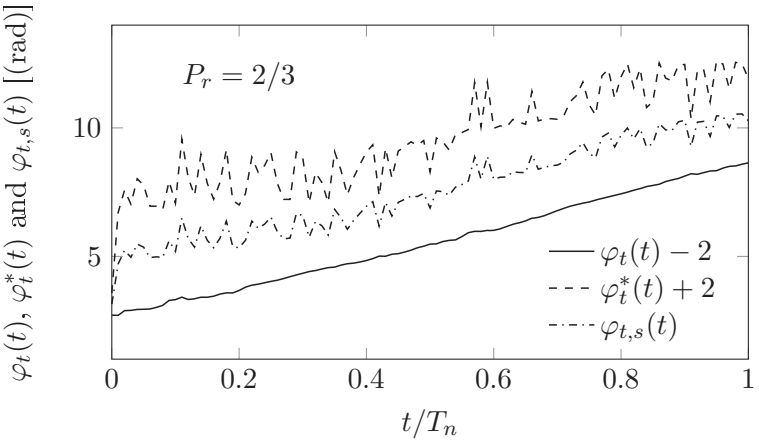

Figure 3.4: TAPs according to (2.55), (2.56) and (2.58) derived with the states of figure 3.3

Because of this, it is recommended to use $\varphi_t(t)$ according to (2.55) for the computation of the TAP, which is done henceforth.

The deviations from the corresponding straight line decrease with higher ratios of P_r. This holds for $\varphi_t(t)$, $\varphi_t^*(t)$ and $\varphi_{t,s}(t)$. Deviations of the TAP from the assumed straight line correspond to variations in the target angular velocity $\dot{\varphi}_t(t)$ (TAV). Therefore, the higher P_r is, the lower the variations of the TAV.

3.2 Discussion and objective

In the previous section, it became apparent that the TAV deviates more from the desired TAV, ω_n, the higher the influence of the excitation force on the motion of the SDOF oscillator. Furthermore, it was shown that there is a state, P_r, that can continuously describe the influence of the excitation force on the motion.

To make the TAV more constant, simulated dynamics can be added. For instance, by filtering the states $x(t)$, $\dot{x}(t)$ and $\ddot{x}(t)$ before computing the TAP and changing the filter parameters as a function of a parameter describing the influence of the excitation force on the motion on the SDOF oscillator, more harmonic responses can be created when the influence of the excitation force is large. However, a filter must be designed, requiring additional design effort. Alternatively, an observer as presented in [40] can be used. By changing the coupling between the SDOF oscillator and the observer as a function of the parameter used to describe the influence of the excitation force, more constant target angular velocities can be produced. Another powerful method is the so-called phase-locked loop (PLL) system [34, 35]. A controller continuously synchronizes the phase of an oscillating model with the phase of the SDOF oscillator. This controller can be parametrized as a function of the influence of the excitation force. The method presented in the following section uses several of the stated ideas.

Before doing this, the objectives for the computation of the TAP for the continuous rotation mode are clarified:

- To keep the power demand on the actuators low in the continuous rotation mode, the variations of the TAV are to be kept as small as possible.
- When the rotors are accelerated or decelerated, tangential forces are additionally generated. These tangential forces can be seen as an additional excitation force as they randomly damp or excite the motion. Therefore, these tangential forces are to be kept as small as possible.
- To ensure that the harmonic control force of the TRD (introduced in section 2.1) effectively damps the vibrations, the anti-phasing between the control force and velocity of the SDOF oscillator must be guaranteed. When the SDOF oscillator is disturbed by a stochastic excitation, its actual frequency deviates from ω_n. To further ensure this anti-phasing, the TRD must adapt its motion by appropriately accelerating and decelerating the rotors.

These objectives are in conflict with each other. In the following section, section 3.3, a phase-locked loop filter with a single tuning parameter is presented. By varying the tuning parameter, the following effects are investigated:

- The variations of the TAV.
- The creation of undesired tangential forces.
- The damping effect (anti-phasing).

3.3 Filtering of target angular position

3.3.1 Method

To filter the TAP, a control-loop as shown in figure 3.5 is proposed.

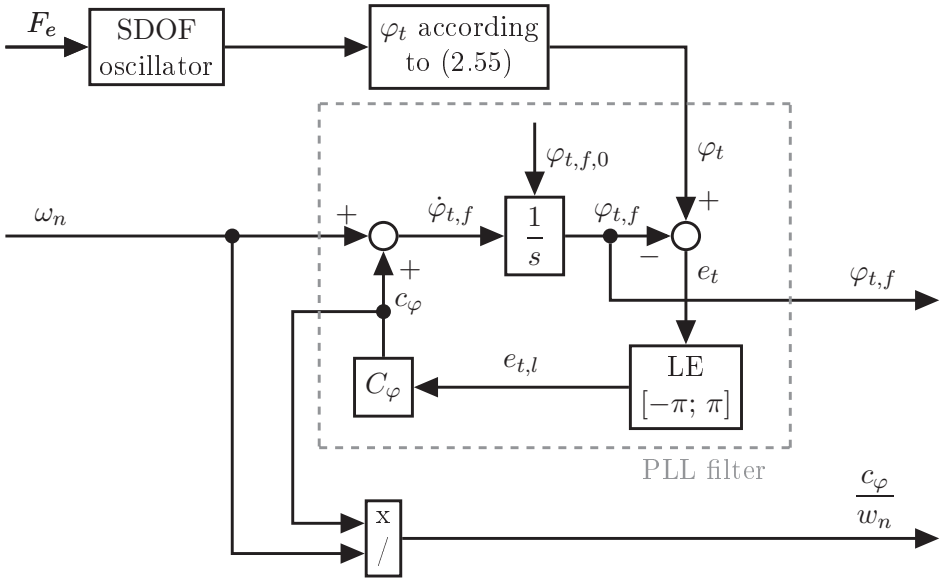

Figure 3.5: Phase-locked loop filter

The TAP $\varphi_t(t)$ is computed according to (2.55). $\varphi_t(t)$ and ω_n are the inputs of the so-called PLL filter. With this filter, a more uniform saw-tooth like TAP is produced. It is assumed that the natural frequency ω_n is known. The filter outputs are the filtered TAP, $\varphi_{t,f}(t)$, and $c_\varphi(t)/\omega_n$ discussed later. The filter compares $\varphi_t(t)$ with $\varphi_{t,f}(t)$, producing the error $e_t(t)$ of the TAP. By limiting $e_t(t)$ to values between $-\pi$ and π, $\varphi_{t,f}(t)$ converges towards to the next possible $\varphi_t(t)$. With an appropriate design of the PLL filter, $e_t(t)$ does not approach the limit values, $-\pi$ and π, of the block 'LE'. By doing this, discontinuities in the filtered TAP are avoided. Output of this block is the limited error, $e_{t,l}(t)$, of the TAP, which is the input of the controller $C_\varphi(s)$. The control effort, $c_\varphi(t)$, is then added to the natural frequency of the oscillator ω_n. This sum is fed into the integrator with an initial value $\varphi_{t,f,0}$. This summation does not change the dynamics of the closed-loop from $\varphi_t(t)$ to $\varphi_{t,f}(t)$. Input of the integrator is the filtered TAV $\dot{\varphi}_{t,f}(t)$. The output of the controller $c_\varphi(t)$ represents the deviation of $\dot{\varphi}_{t,f}(t)$ from ω_n. Therefore, to describe the deviation of $\dot{\varphi}_{t,f}(t)$ from ω_n, $c_\varphi(t)/\omega_n$ is evaluated.

To keep the closed-loop from $\varphi_t(t)$ to $\varphi_{t,f}(t)$ simple, a transfer function from $\varphi_t(t)$ to $\varphi_{t,f}(t)$ as given by

$$G_{cl}(s) = \frac{\omega_f^2}{s^2 + 2\xi_f\omega_f s + \omega_f^2} \tag{3.16}$$

is chosen in which ω_f is the filter frequency and ξ_f the damping ratio of the closed-loop.

To damp out high frequency components, ξ_f is set to one. By doing this, noise in $x(t)$ and $\dot{x}(t)$ which results in noise in $\varphi_t(t)$, see (2.55), is reduced in $\varphi_{t,f}(t)$.

The closed-loop from $\varphi_t(t)$ to $\varphi_{t,f}(t)$ can also be described with help of the compensator

$C_\varphi(s)$ and the integrator $1/s$, see the following equation [33].

$$G_{cl}(s) = \frac{C_\varphi(s)/s}{1 + C_\varphi(s)/s} \tag{3.17}$$

Setting (3.16) equal to (3.17) and solving for $C_\varphi(s)$ gives the form of the controller:

$$C_\varphi(s) = \frac{\omega_f^2}{s + 2\omega_f} \tag{3.18}$$

The two poles of $G_{cl}(s)$ of (3.16) with $\xi_f = 1.0$ lie both at $s = -\omega_f$. Therefore, this closed-loop is stable for $\omega_f > 0$.

To illustrate the effect of the filter of figure 3.5, the SDOF oscillator is disturbed by the excitation force defined in subsection 3.1.2. A single vibration period is considered with the initial condition $x_0 > 0$ and $\dot{x}_0 = 0$. The initial value of the integrator $\varphi_{t,f,0}$ is set equal to the TAP at $t = 0$, which is $3/2\pi$ according to (2.55) for the given initial conditions; thus, $e_t(t = 0) = 0$.

Figure 3.6/A shows the unfiltered and filtered TAP. Subfigure B shows the corresponding deviation of the filtered TAV from the natural frequency. The filter frequency was set equal to the natural frequency, $\omega_f = \omega_n$. In figure 3.6/A, the noise damping effect becomes evident when inspecting $\varphi_t(t)$ and $\varphi_{t,f}(t)$.

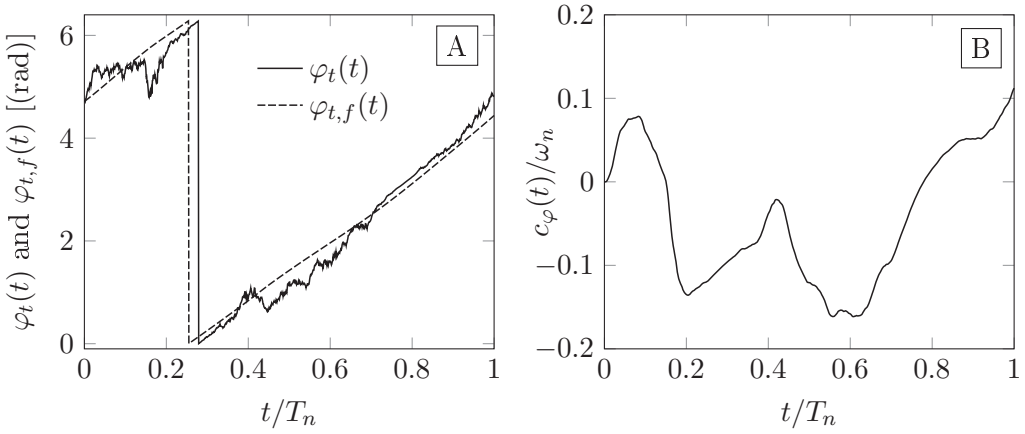

Figure 3.6: Chosen states for illustration of figure 3.5 with $P_r = 2/3$ and $\omega_f/\omega_n = 1.0$

The filter frequency w_f was then increased by a factor of ten and the simulation was repeated using the same seed for the excitation force, see figure 3.7. Therefore, $\varphi_t(t)$ in figure 3.6/A and 3.7/A are identical. In figure 3.7, $\varphi_t(t)$ is tracked more accurately than in figure 3.6. To reach this, the filtered TAV must be varied more. This can be seen in figure 3.7/B. $c_\varphi(t)/\omega_n$ reaches almost minus three at $t/T_n \approx 0.15$.

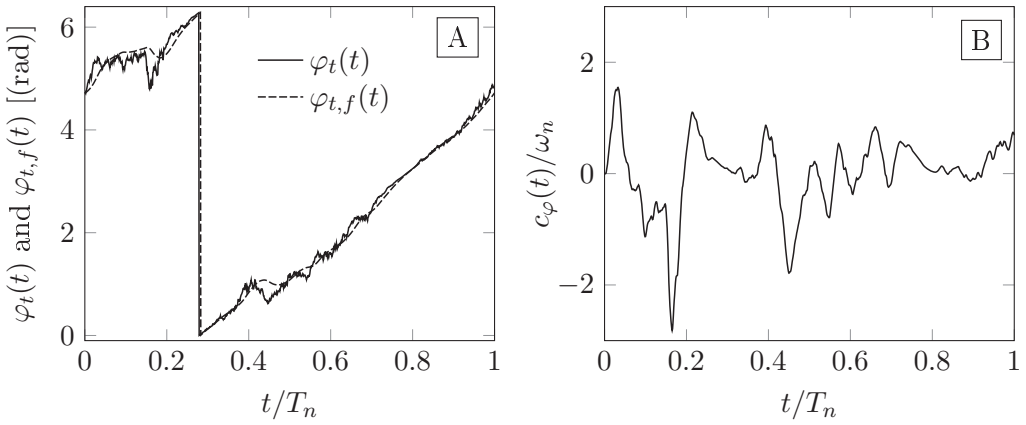

Figure 3.7: Chosen states for illustration of phase-locked loop of figure 3.5 with $P_r = 2/3$ and $\omega_f/\omega_n = 10$

The variance and the standard deviation of c_φ/ω_n are calculated for figure 3.6 and 3.7 in table 3.1. When increasing the filter frequency ω_f by a factor of ten, the variance and the standard deviation are increased by a factor of approximately 65 and 8.1, respectively.

Table 3.1: Calculation of variance and standard deviation of $c_\varphi(t)/\omega_n$ corresponding to figure 3.6 and 3.7

w_f/ω_n	$\mathrm{Var}(c_\varphi(t)/\omega_n)$	$\mathrm{std}(c_\varphi(t)/\omega_n)$
1.0 (figure 3.6)	0.0065	0.0804
10 (figure 3.7)	0.4247	0.6519

The variations of $c_\varphi(t)/\omega_n$ from $t = 0$ to $t = T_n$ were evaluated with help of the variance and the standard deviation, see (3.5), (3.6), and table 3.1. Note the quantity $c_\varphi(t)/\omega_n$ describes the deviation from a continuous motion. By limiting this quantity, an upper limit for the power demand on the actuators required to accelerate and decelerate the rotors in the continuous rotation mode is set. In figure 3.6, $c_\varphi(t)/\omega_n$ varies within a range of ± 0.15. This corresponds to a maximum deviation from ω_n of $\pm 15\,\%$. To the author, this deviation from the continuous motion seems to be acceptable for a power-efficient operation and an initial upper limit for $\mathrm{std}(c_\varphi(t)/\omega_n)$ is set in the following to 0.10. Further comments regarding this initial upper limit are given subsection 3.3.5.

The filtered TAP $\varphi_{t,f}(t)$ is the input of a subsequent system, which drives the rotors to $\varphi_{t,f}(t)$. For the rest of this section, it is assumed that this subsequent system is much faster than the PLL filter of figure 3.5, in other words, $\varphi_{t,f}(t)$ is 'perfectly' tracked. By assuming this, the variations in the actual TAV are reduced with help of the PLL filter.

In the following subsections, the influences of the PLL filter on the objectives enumerated in section 3.2 are quantified.

3.3.2 Limiting variations of filtered target angular velocity

Oscillator without inherent damping

Within the simulations performed for figure 3.6 and 3.7, a single vibration period was considered for a certain power ratio P_r. In order to increase the statistical significance,

n single vibration periods are simulated and the mean values of the individual standard deviations $\mathrm{std}(c_{\varphi,i}(t)/\omega_n)$ are calculated by

$$V_{\dot{\varphi}} = \frac{1}{n}\sum_{i=1}^{i=n}[\mathrm{std}(c_{\varphi,i}(t)/\omega_n)] \tag{3.19}$$

in which $V_{\dot{\varphi}}$ refers to the expected variations of the filtered TAV. With $n = 5000$, reproducibility is ensured meaning that when simulating 5000 single vibration periods another time, nearly the same values for $V_{\dot{\varphi}}$ are obtained. Therefore, n is set to 5000 in the following.

Using the same initial conditions, different excitation force seeds and the same excitation power I, the mean power ratio P_r remains approximately constant. The filter frequency ω_f was then varied within a chosen range ($0 < \omega_f/\omega_n < 2$). For these simulations, $V_{\dot{\varphi}}$ can be plotted against ω_f/ω_n for multiple power ratios P_r, see figure 3.8. To obtain different values for P_r, the excitation power I was varied. Alternatively, the magnitude of x_0 could be changed. Note that the diagram of figure 3.8 is valid for any ω_n.

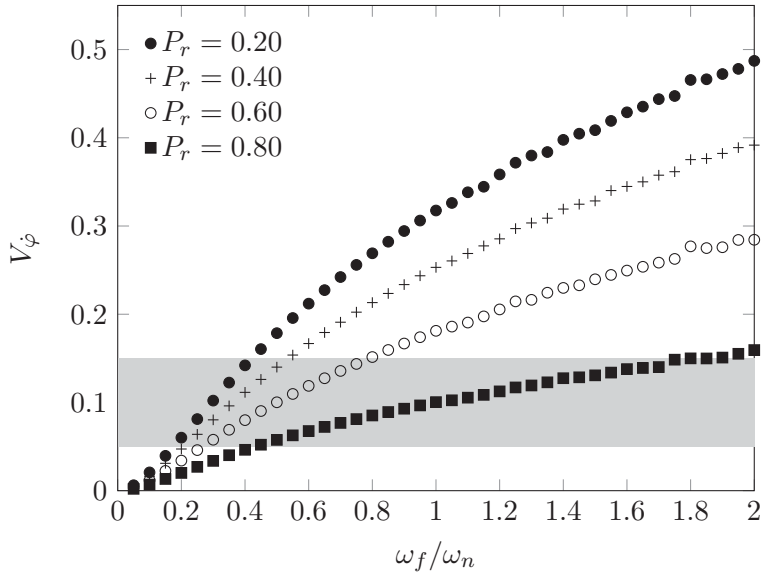

Figure 3.8: Expected variations of the filtered TAV $V_{\dot{\varphi}}$ plotted against frequency ratio ω_f/ω_n for different power ratios P_r

The curves of figure 3.8 can be approximated using simple linear regression in the region of $V_{\dot{\varphi}} = 0.1$ (initial upper limit for $\mathrm{std}[c_{\varphi}(t)/\omega_n]$ of subsection 3.3.1) [48]. With simple linear regression it is meant that there is only one explanatory variable, which is ω_f/ω_n. The least square approach is used. It minimizes the sum of the squared errors in which an error is the difference between the approximated value, $A_{\dot{\varphi}}(\omega_f/\omega_n)$ given in (3.20), and the numerically simulated value $V_{\dot{\varphi}}$ [48].

$$A_{\dot{\varphi}}(\omega_f/\omega_n) = a_v\frac{\omega_f}{\omega_n} + b_v \tag{3.20}$$

In (3.20), a_v is the slope and b_v the value at $\omega_f/\omega_n = 0$. The values of $V_{\dot{\varphi}}$ in the value range from $V_{\dot{\varphi}} = 0.05$ to $V_{\dot{\varphi}} = 0.15$ are used for the approximation. The considered data is marked with a gray background, see figure 3.8.

The parameters a_v and b_v describing the linear regression lines corresponding to the curves of figure 3.8 are shown in table 3.2. To derive a relation between P_r and the parameters a_v and b_v, a_v and b_v were evaluated for different power ratios P_r, see figure 3.9. This is justified by the assumption that the power ratio P_r and the filter frequency ω_f independently influence $V_{\dot{\varphi}}$.

Table 3.2: Parameters a_v and b_v of (3.20) for the curves of figure 3.8

P_r	a_v	b_v
0.20	0.41	−0.022
0.40	0.30	−0.011
0.60	0.19	0.0031
0.80	0.069	0.028

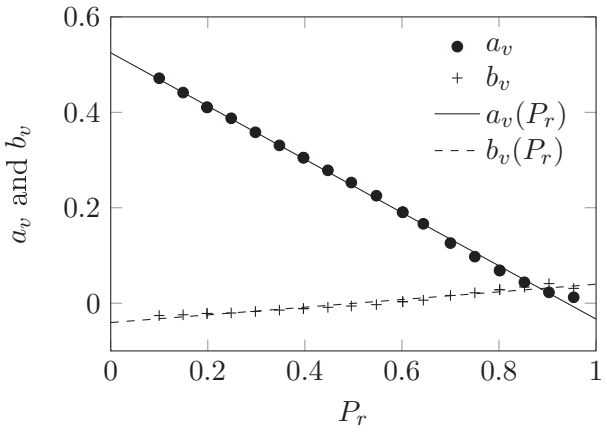

Figure 3.9: Parameters a_v and b_v and corresponding regression lines $a_v(P_r)$ and $b_v(P_r)$ of (3.21) with coefficients of (3.22)

Approximations for a_v and b_v can be found using linear regression with the values of $V_{\dot{\varphi}}$ in the value range from $V_{\dot{\varphi}} = 0.05$ to $V_{\dot{\varphi}} = 0.15$ for multiple values of P_r [48]. The explanatory variable is now P_r and the least square approach is applied [48]. Thus, the parameters a_v and b_v can be approximated by

$$a_v(P_r) = a_{v,1}P_r + a_{v,0} \qquad b_v(P_r) = b_{v,1}P_r + b_{v,0} \tag{3.21}$$

with the coefficients

$$a_{v,1} = -0.5581 \qquad a_{v,0} = 0.5248 \qquad b_{v,1} = 0.0804 \qquad b_{v,0} = -0.0405 \tag{3.22}$$

The linear regression lines are also depicted in figure 3.9.

Inserting (3.21) into (3.20) yields:

$$A_{\dot{\varphi}}(\omega_f/\omega_n, P_r) = (a_{v,1}P_r + a_{v,0})\,\frac{\omega_f}{\omega_n} + b_{v,1}P_r + b_{v,0} \tag{3.23}$$

(3.23) gives an approximation of the variations in the filtered TAV as a function of the filter frequency ω_f/ω_n and the power ratio P_r. Solving (3.23) for ω_f/ω_n and requiring that the variations in the filtered TAV are equal or below a specified threshold, $A_{v,t}$, it follows:

$$\omega_f/\omega_n \leq \frac{A_{v,t} - b_{v,1}P_r - b_{v,0}}{a_{v,1}P_r + a_{v,0}} \tag{3.24}$$

Note that P_r is a time-varying parameter, which can be estimated. (3.24) sets an upper threshold for ω_f/ω_n. This threshold limit the variations of the filtered TAV; therefore the power demand required for accelerating and decelerating the rotors. For the determination of the coefficients $a_{v,1}$, $a_{v,0}$, $b_{v,1}$ and $b_{v,0}$, only the data in the region of $A_{v,t} = 0.1$ (initial upper limit of subsection 3.3.1) was used, see figure 3.8. If another value for $A_{v,t}$ is chosen, the linearizations of (3.20) and (3.21) must be repeated with the data in the region of the new value for $A_{v,t}$, see figure 3.8.

Oscillators with inherent damping

Taking an oscillator with inherent damping into consideration, ω_n must be substituted by ω_d in the respective computations of the previous subsection. Furthermore, the analysis is done with respect to the frequency ratio ω_f/ω_d instead of ω_f/ω_n.

Figure 3.10 shows the expected variations $V_{\dot{\varphi}}$ of the filtered TAV as a function of ω_f/ω_d for $P_r = 0.4$ and for several damping ratios ξ. $V_{\dot{\varphi}}$ increases with the damping ratio ξ. This is because the decay due to the inherent damping is not neglected, see comments before (3.11). Therefore, the mean influence of the excitation force on the motion of the SDOF oscillator increases in time within the considered vibration periods. This explains the increased influence of the excitation force.

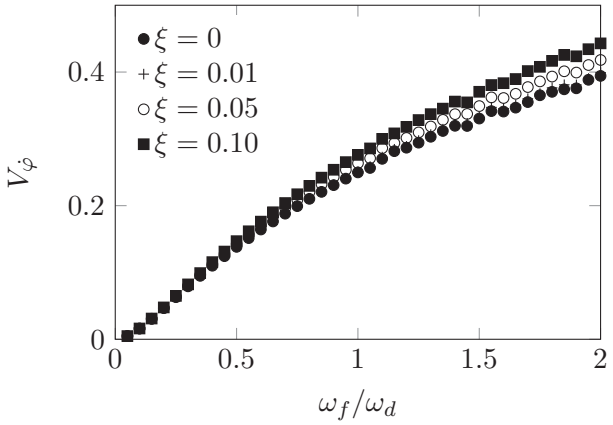

Figure 3.10: Expected variations of the filtered TAV $V_{\dot{\varphi}}$ plotted against frequency ratio ω_f/ω_d for $P_r = 0.4$ for several different damping ratios ξ

However, the influence of the inherent damping is small for $0 < \xi < 0.1$. This was checked for several values of P_r. Therefore, considerations in the following are pursued for oscillators without inherent damping but they are also a good estimate for oscillators with small inherent damping.

In this subsection, the influence of the filter frequency ω_f and the power ratio P_r on the variations of the filtered TAV was studied. (3.24) gives the maximum value for ω_f such that the variations of the filtered TAV do not exceed $A_{v,t} = .1$ (initial upper limit of subsection 3.3.1).

3.3.3 Limiting tangential forces

When the rotors are driven with a constant angular velocity, only radial forces are created. However, variations in the TAV are required to ensure the anti-phasing between the control force of the TRD and the velocity of the SDOF oscillator. As a result, tangential forces

are additionally produced. The tangential forces act randomly on the SDOF oscillator. Therefore, they can be seen as an additional excitation force and are to be kept small. In this subsection, an upper limit for the PLL filter frequency will be set such that the tangential forces are small with respect to the radial forces. To study the tangential to radial force ratio, (2.3) is recalled:

$$f_T(t) = m_c r \left[\dot{\varphi}(t)^2 \cos\varphi(t) + \ddot{\varphi}(t) \sin\varphi(t)\right] \tag{3.25}$$

Note that for the investigation of this subsection, the force of the TRD is still not applied to the SDOF oscillator.

The first term in the square bracket of (3.25) describes the radial forces and the second the tangential forces produced by the TRD. The factor $m_c r$ can be dropped as it contributes equally to both force terms. As done in the previous subsection, numerous single vibration periods will be considered. In a single vibration period, $\varphi_t(t)$ changes by approximately 2π. Therefore, the contributions of both trigonometric functions are equal and can, for this comparison, be neglected when considering numerous single vibration periods and computing average values. To make both force terms dimensionless, they are normalized by the squared natural frequency, see the following equation

$$f_{r,c}(t) = \frac{\dot{\varphi}(t)^2}{\omega_n^2} \qquad\qquad f_{t,c}(t) = \frac{\ddot{\varphi}(t)}{\omega_n^2} \tag{3.26}$$

in which the index c stands for comparison. The objective is to find a constraint for the filter frequency such that the tangential forces are low in comparison to the radial forces. $f_{r,c}(t)$ is evaluated with help of the rms-function as it varies about one in the continuous rotation mode. Thus, $\mathrm{rms}[f_{r,c}(t)]$ can be approximated as follows:

$$\mathrm{rms}[f_{r,c}(t)] = \mathrm{rms}\left[\frac{\dot{\varphi}(t)^2}{\omega_n^2}\right] \approx 1 \tag{3.27}$$

For $f_{t,c}(t)$, the std-function is used as $f_{t,c}(t)$ varies about zero (it would be equivalent to use the rms-function). As $\mathrm{rms}[f_{r,c}(t)] \approx 1$, only $f_{t,c}(t)$ must be computed to evaluate the tangential to radial force ratio. As before, 5000 single vibration periods are considered and the average standard deviation of $f_{t,c}(t)$, see (3.26), is calculated:

$$E_t = \frac{1}{n} \sum_{i=1}^{i=n} \left[\mathrm{std} \frac{\ddot{\varphi}(t)}{\omega_n^2}\right] \tag{3.28}$$

E_t is referred to as the expected tangential force component. For the following numerical simulations, $\ddot{\varphi}(t)$ is derived numerically by differentiating $\dot{\varphi}_{t,f}(t)$ with respect to time. This is based on the assumption that the filtered TAP is perfectly tracked. To begin with, E_t is studied with respect to the filter parameter ω_f/ω_n for different P_r. The results are shown in figure 3.11.

As done in the previous subsection, the curves of figure 3.11 can be approximated in the region of $0.1 < E_t < 0.3$ using simple linear regression. An initial upper threshold, $E_{t,t} = 0.2$, for E_t is set. Using the least square approach for the values about this threshold from $0.5E_{t,t}$ to $1.5E_{t,t}$, an approximation for E_t can be derived for each P_r:

$$A_t(\omega_f/\omega_n) = a_t \frac{\omega_f}{\omega_n} + b_t \tag{3.29}$$

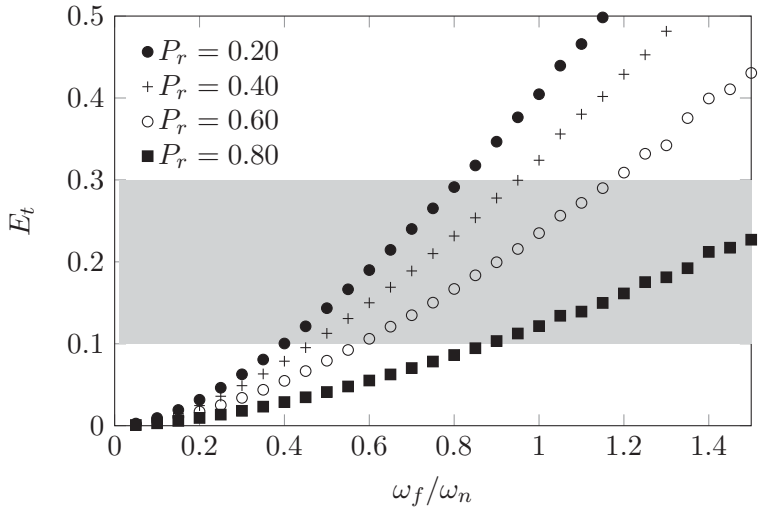

Figure 3.11: Expected tangential force component plotted against frequency ratio ω_f/ω_n for different power ratios P_r

A_t will be referred to as the estimated tangential force component.

As done before, the coefficients a_t and b_t can be described as a function of P_r. a_t and b_t were evaluated for various P_r, see figure 3.12.

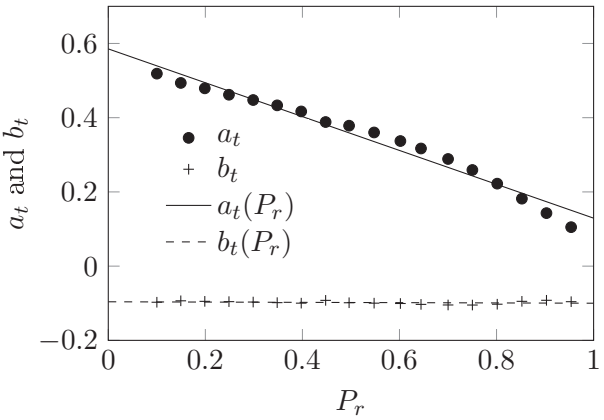

Figure 3.12: Parameters a_t and b_t and corresponding regression lines $a_t(P_r)$ and $b_t(P_r)$ of (3.30) with coefficients of (3.31)

Using the least square approach with P_r as the explanatory variable, the parameters a_t and b_t can be expressed by:

$$a_t(P_r) = a_{t,1}P_r + a_{t,0} \qquad b_t(P_r) = b_{t,1}P_r + b_{t,0} \tag{3.30}$$

with the following coefficients

$$a_{t,1} = -0.4560 \qquad a_{t,0} = 0.5853 \qquad b_{t,1} = -0.0039 \qquad b_{t,0} = -0.0961 \tag{3.31}$$

The corresponding linear regression lines are plotted in figure 3.12. Inserting (3.30) into (3.29) yields:

$$A_t(\omega_f/\omega_n, P_r) = (a_{t,1}P_r + a_{t,0})\frac{\omega_f}{\omega_n} + b_{t,1}P_r + b_{t,0} \tag{3.32}$$

(3.32) gives an approximation of the tangential force component as a function of ω_f/ω_n and P_r. An upper threshold for the filter frequency ω_f is found by solving (3.32) for ω_f/ω_n while setting $A_t(\omega_f/\omega_n, P_r)$ equal to the upper threshold $E_{t,t}$, see (3.33).

$$\frac{\omega_f}{\omega_n} \leq \frac{E_{t,t} - b_{t,1}P_r - b_{t,0}}{a_{t,1}P_r + a_{t,0}} \tag{3.33}$$

The coefficients of (3.31) were derived with an initial upper threshold $E_{t,t} = 0.2$, which is further discussed in subsection 3.3.5.

3.3.4 Anti-phasing between control force and velocity of SDOF oscillator

Within the last two subsections, two upper thresholds for the filter frequency ω_f were derived. The first constraint ensures that the variations in the angular velocity are held below a certain threshold and the second constraint ensures that the tangential to radial force ratio is held below a certain threshold.

To guarantee the anti-phasing between the control force of the TRD and the velocity of the SDOF oscillator, the filter frequency ω_f must lie above a lower threshold, $\omega_{f,l}$. The objective of this subsection is to find an appropriate lower threshold $\omega_{f,l}$ for ω_f to complement the upper thresholds previously derived. If $\omega_f = 0$, there is no feedback within the PLL filter. Therefore, $\varphi_t(t)$ and $\varphi_{t,f}(t)$ are independent from each other. Consequently, the anti-phasing between the control force of the TRD and the velocity of the SDOF oscillator is no longer guaranteed. The higher ω_f, the faster $e_{t,l}(t)$ of figure 3.5 (difference between $\varphi_t(t)$ and $\varphi_{t,f}(t)$) goes to zero. The closed-loop transfer function, $G_{cl}(s)$ from $\varphi_t(t)$ to $\varphi_{t,f}(t)$, is as given in (3.16) with $\xi_f = 1$.

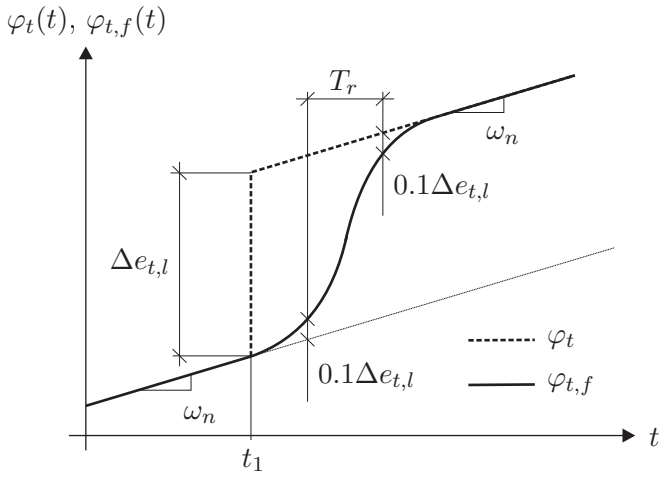

Figure 3.13: Re-synchronization time T_r

The rise time is the time required for the response of a signal to rise from 10 % of the steady-state value to 90 % of the steady-state value due to a unit-step [49]. What does this mean for the filter in figure 3.5? In figure 3.13, the unfiltered TAP $\varphi_t(t)$ and the filtered $\varphi_{t,f}(t)$ TAP coincide and increase with ω_n until $t = t_1$. Now assuming that $\varphi_t(t)$ suddenly changes by $\Delta e_{t,l}$, control action must be taken to re-synchronize $\varphi_{t,f}(t)$ with $\varphi_t(t)$ ($\Delta e_{t,l}$ decays back to zero). The time it takes to bring the error from $0.9\Delta e_{t,l}$ to $0.1\Delta e_{t,l}$ is the rise time [49]; henceforth, this time will be referred to as the re-synchronization time. Due to the fact that the PLL filter is a linear dynamic system, the re-synchronization time is

independent from the magnitude of the error $\Delta e_{t,l}(t)$ (deviation of $\varphi_t(t)$ from $\varphi_{t,f}(t)$) in figure 3.13.

For $\xi_f = 1$ and for the closed-loop transfer function of (3.16), the relation between the re-synchronization time T_r and the filter frequency ω_f is as given by

$$T_r = \frac{3.359}{\omega_f} \tag{3.34}$$

in which the re-synchronization time T_r is given in s and the filter frequency in (rad)/s [49]. The re-synchronization time is an adequate performance index for evaluating the speed of response. Replacing the re-synchronization time in (3.34) by the re-synchronization frequency $\omega_r = 2\pi/T_r$, dividing both sides by ω_n, doing some rearrangements and forming and inequality gives a lower threshold for ω_f/ω_n for a certain required re-synchronization frequency, $\omega_{r,t}$:

$$\frac{\omega_f}{\omega_n} \geq \frac{3.359}{2\pi}\frac{\omega_{r,t}}{\omega_n} \approx 0.5346\frac{\omega_{r,t}}{\omega_n} \tag{3.35}$$

(3.35) provides a lower threshold for the filter frequency, ensuring that $\varphi_{t,f}(t)$ and $\varphi_t(t)$ are re-synchronized adequately fast; therefore, ensuring a fast recovery of the anti-phasing between the control force and the velocity of the SDOF oscillator. A re-synchronization frequency of $\omega_{r,t}/\omega_n = 1$ is deemed to be an appropriate initial value. It follows: $\omega_f/\omega_n = 0.5346$. Further considerations regarding the lower threshold for the filter frequency are given in subsection 3.3.6.

3.3.5 Synthesis of constraints

In this subsection, the constraints of subsection 3.3.2, 3.3.3 and 3.3.4 are synthesized. This results in two upper and a lower threshold (UT and LT) for ω_f, see figure 3.14. It becomes apparent that all constraints are only met if $P_r > 0.64$.

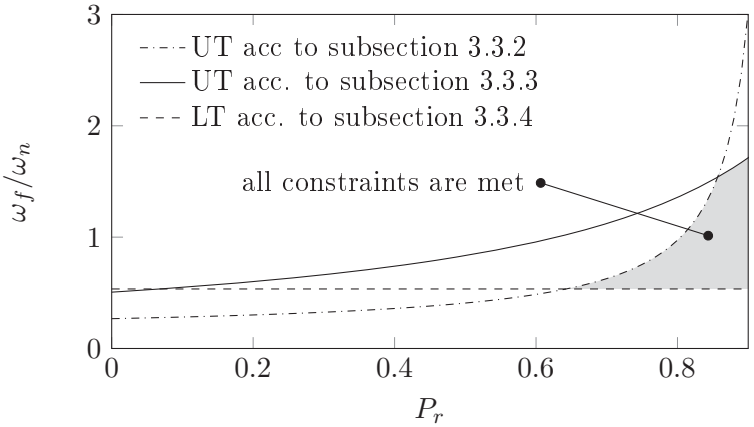

Figure 3.14: Constraints for ω_f to achieve desired performance with the TRD in the continuous rotation mode

For illustration purposes, a simulation is now performed with the phase-locked-loop filter of figure 3.5. As before, the excitation of subsection 3.1.2 is used. The initial conditions as well as the excitation power are randomly chosen. They do not have an impact on the following considerations. The filter frequency ω_f is set equal $0.5346\,\omega_n$ (initial value of previous subsection). Some signals which are discussed in the following are shown in

figure 3.15. The force of the TRD is not acting on the SDOF oscillator and a time interval of from zero to $30\,T_n$ is considered.

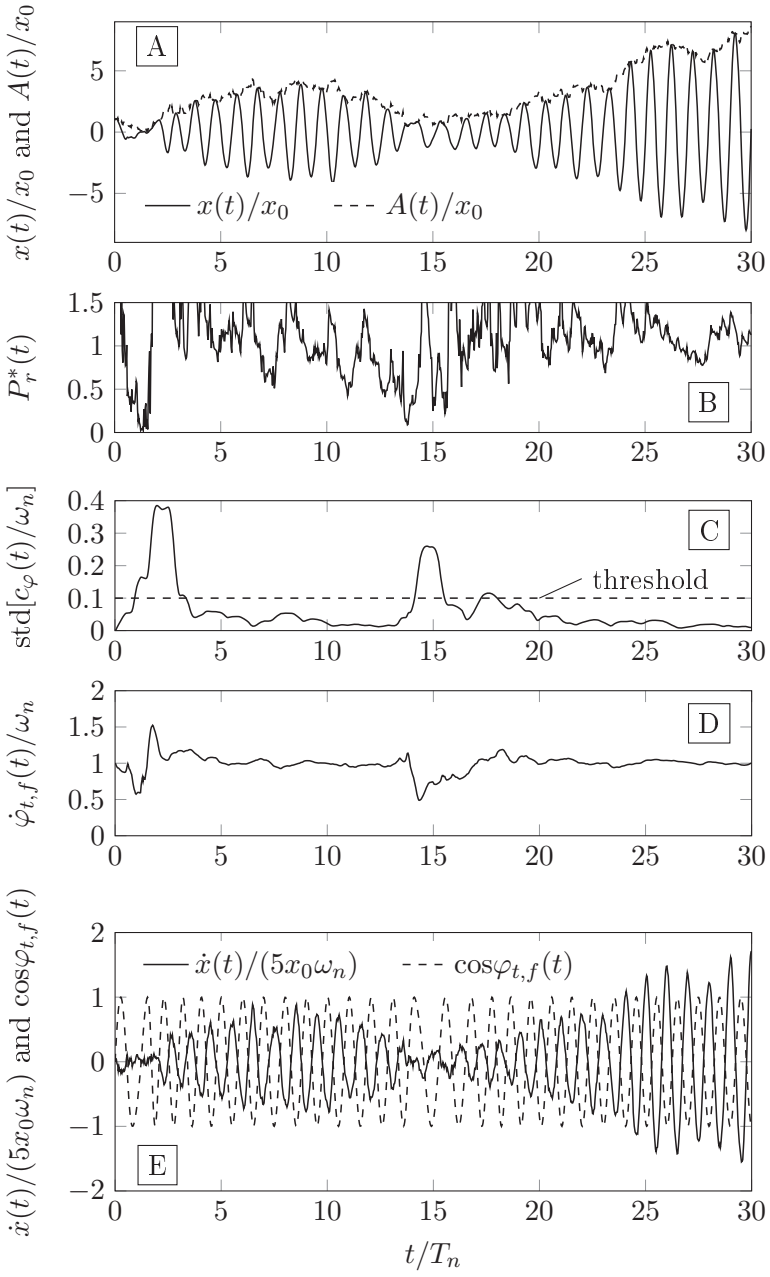

Figure 3.15: Numerical simulation of PLL filter with $x_0 > 0$, $\dot{x}_0 = 0$ and $\xi = 0$

Figure 3.15/A shows the displacement and the vibration amplitude due to the excitation force. It can be see that the excitation force randomly damps and excites the SDOF oscillator. Subfigure/B shows the continuously estimated power ratio, $P_r^*(t)$, computed

according to (3.36), which is further discussed in the following.

$$P_r^*(t) = \frac{\frac{1}{2}\left[x(t)^2 + \left(\frac{\dot{x}(t)}{\omega_n}\right)^2\right]}{\frac{1}{T_n}\int\limits_{t=-T_n}^{t} x(t)^2 \mathrm{d}t} \tag{3.36}$$

See also (3.15) and corresponding comments. The numerator of (3.36), see also (3.11), refers to the actual states and can be seen as a normalized, squared vibration amplitude. The denominator calculates the power of the displacement response of the preceding vibration period (integration from $t = -T_n$ up to t). It becomes evident that this continuously estimated power ratio $P_r^*(t)$ is, in comparison to the vibration amplitude $A(t)$ shown in subfigure A, more disrupted. Therefore, $A(t)$ is more suitable for further computations. To reduce the disruption of $P_r^*(t)$, one can consider multiple rather than single vibration periods or implement a low-pass filter. The longer the considered time interval and the more aggressive the low-pass filter, respectively, the smoother the response of $P_r^*(t)$ at the expense of a larger time delay.

To evaluate the variations of the filtered TAV continuously, the standard deviation of $c_\varphi(t)/\omega_n$ of the preceding vibration period is calculated according to (3.6). With $t_l = -T_n$ and $t_u = t$ and $s(t) = c_\varphi(t)/\omega_n$, (3.6) becomes

$$\mathrm{std}[c_\varphi(t)/\omega_n] = \sqrt{\frac{1}{T_n}\int\limits_{-T_n}^{t}\left[\frac{c_\varphi(t)}{\omega_n} - \mu_\varphi(t)\right]^2 \mathrm{d}t} \tag{3.37}$$

in which $\mu_\varphi(t)$ refers to the mean value of $c_\varphi(t)/\omega_n$ from $t_l = -T_n$ to $t_u = t$. When the vibration amplitude is relatively small, as is the case in the following time intervals, $T_n < t < 3T_n$ and $13T_n < t < 17T_n$, the motion is more influenced by the excitation force compared to when the displacement amplitudes are larger. Consequently, $P_r^*(t)$ has the tendency to decrease and the variations of the filtered TAV increase.

$\dot{x}(t)$ and $\cos\varphi_t^*(t)$, which indicates the phase of the control force, are shown in subfigure E. $\dot{x}(t)$ is normalized such that the magnitudes of both signals are approximately equal. As the control force continuously opposes $\dot{x}(t)$, ω_f is set adequately high. At $t = 13.5\,\mathrm{s}$, the displacement amplitude becomes relatively small. As a result, the excitation force increasingly dictates the motion of the SDOF oscillator, making the actual frequency of the SDOF oscillator deviating from ω_n. The vibration amplitude then increases. To regain the anti-phasing, the filtered TAV $\varphi_{t,f}(t)$ is lowered in the time range from $t = 14\,\mathrm{s}$ up to $t = 16\,\mathrm{s}$.

When setting ω_f to a lower value, the undesired variations in the filtered TAV will decrease at the expense of a poorer anti-phasing between the control force and the velocity $\dot{x}(t)$. Furthermore, the tangential forces will decrease.

The simulation of figure 3.15 validates the considerations done in subsection 3.3.2. When the power ratio $P_r^*(t)$ falls below the value 0.65, it can be seen that the $\mathrm{std}[c_\varphi(t)/\omega_n]$ exceeds the chosen threshold of 0.1. Due to the PLL filter, $\mathrm{std}[c_\varphi(t)/\omega_n]$ crosses its threshold of 0.1 slightly delayed from $P_r^*(t) = 0.65$, see subfigure B and C.

The continuously computed power ratio $P_r^*(t)$ is an estimate, see (3.36). $P_r^*(t)$ is the ratio of the power of the displacement expected to be performed in the impending vibrations over the total power performed in the preceding vibration period. Therefore, $P_r^*(t)$ can detect changes in the excitation power, which was assumed as constant so far. However, the power ratio $P_r^*(t)$ of figure 3.15/B is strongly disrupted and can, in this form, not used for feedback; filtering is required.

The higher P_r, the more harmonic the responses $x(t)$ and $\dot{x}(t)$ of the SDOF oscillator. The same applies to $P_r^*(t)$ and $A(t)$ according to (2.43). Both states, $P_r^*(t)$ and $A(t)$, can be seen as continuous measures quantifying the harmonic components of the response of the SDOF oscillator—in frequency domain, the concentration of frequencies in the vicinity of ω_n. However, $P_r^*(t)$ is, in comparison to $A(t)$, more disrupted. Therefore, $A(t)$ will be used in the following. However, for some practical purposes, $P_r^*(t)$ can be more useful as it can directly detect variations in the excitation power. It is therefore of particular interest when excitation force scenarios with varying excitation power are considered.

An excitation force was assumed and the motion of the rotors of the TRD was analyzed assuming the filtered TAP generated by the PLL filter is perfectly tracked. Until now, the forces created by the TRD were not fed back to the SDOF oscillator ($\mu_c r = 0$). In particular, the tangential forces would make the response of the SDOF more non-harmonic. This disturbing tangential force effect increases with the mass-ratio-radius control product $\mu_c r$. It is possible to repeat all the simulations done in this section while additionally varying $\mu_c r$. It is evident that these additional tangential forces would increase the values for $V_{\dot{\varphi}}$ and E_t of figure 3.8 and 3.11, respectively, therefore tightening the corresponding constraints of figure 3.14.

It is the opinion of the author that it is more beneficial to give recommendations regarding the tuning of the PLL filter and the design of the TRD than performing numerous further simulations while varying $\mu_c r$. This is done in the following subsection.

3.3.6 Design recommendations

1. Setting of filter frequency

In a first step, recommendations regarding setting the filter frequency ω_f are given. From subsection 3.3.4, it became apparent that setting ω_r to approximately ω_n is an appropriate initial assumption. The objective of the PLL filter is to bring $\varphi_{t,f}$ and φ_t in phase while minimizing the variations of the filtered TAV. The worst case scenario is that $\varphi_{t,f}$ and φ_t differ from each other by π. This is studied in the following.

A free vibration ($F_e(t) = 0$) of a SDOF oscillator with $\xi = 0$ is assumed with the initial conditions $x_0 > 0$ and $\dot{x}_0 = 0$. To impose the worst case scenario at the time-point $t = 0$, the initial value $\varphi_{t,f,0}$ of the filtered TAV is set to 0.5π. This corresponds to a deviation of π from the TAP according to (2.55). Simulation results are shown in figure 3.16 for different frequency ratios ω_r/ω_n.

It becomes evident that with $\omega_r/\omega_n = 1$, the anti-phasing between $\dot{x}(t)$ and $\cos\varphi_{t,f}(t)$ (phase of the control force) is almost achieved after a single vibration period ($t/T_n = 1$), see subfigure A. The larger ω_r/ω_n, the faster the anti-phasing is regained at the expense of larger variations in the filtered TAV, see subfigure B. For $\omega_r/\omega_n = 1.2$ at $t/T_n \approx 0.2$, the

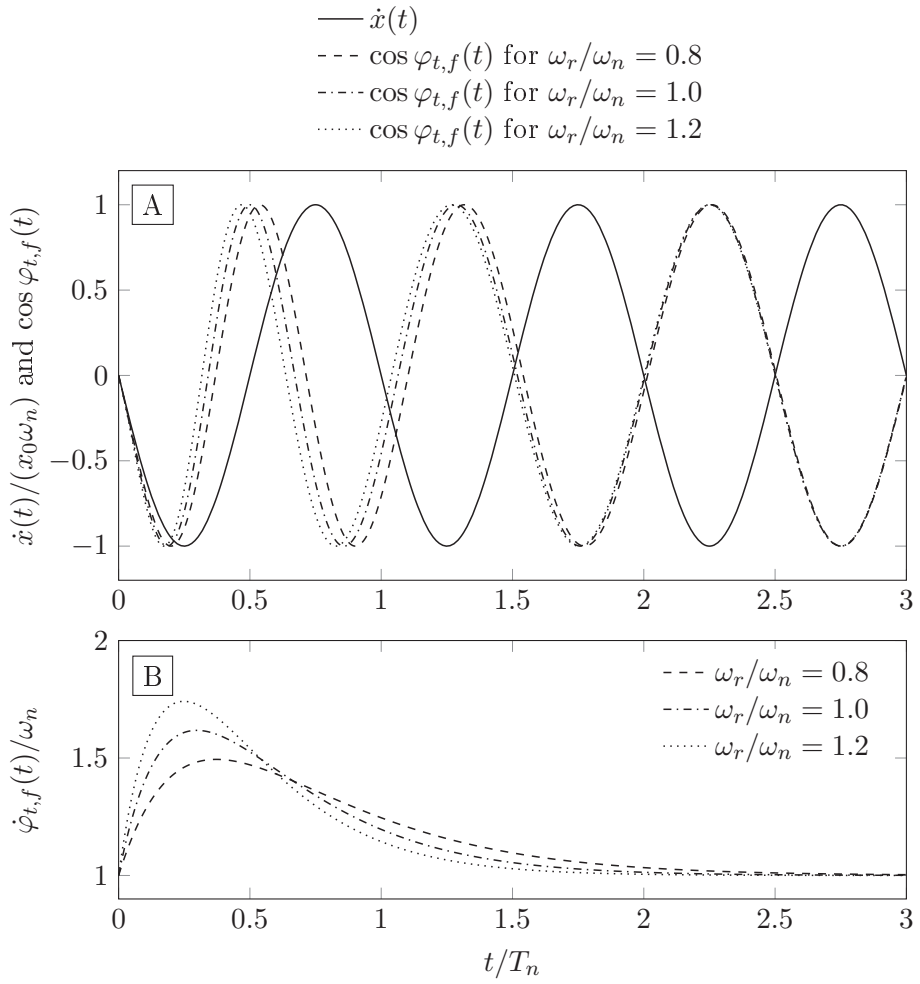

Figure 3.16: Simulation of worst case scenario with $x_0 > 0$, $\dot{x}_0 = 0$ and $\varphi_{t,f,0} = 0.5\pi$

TAV is required to increase by approximately 70 %, whereas only by 50 % for $\omega_r/\omega_n = 0.8$. As this is the worst case scenario, an increase of the TAV of 50 % is deemed to be acceptable. Therefore, $\omega_{r,t}/\omega_n$ is set according to (3.38).

$$\omega_{r,t}/\omega_n = 0.8 \tag{3.38}$$

It follows according to (3.35) that $\omega_f/\omega_n \approx 0.428$.

The simulations of figure 3.16 can also be performed for oscillators with $0 < \xi$. As the influence of inherent damping for $0 < \xi < 0.1$ is small, these simulations are not presented.

2. Critical vibration-amplitude threshold

In the second step, the critical vibration-amplitude threshold below which an operation in the continuous rotation mode is not beneficial is set. In chapter 2, two vibration-amplitude thresholds A_{on} and A_{off} were introduced. When the vibration amplitude $A(t)$ exceeds A_{on} and other conditions are met (see subsection 2.6.4), the TRD turns on and operates in the continuous rotation mode. As soon as $A(t)$ falls below the lower vibration-amplitudes threshold A_{off}, the TRD is shut down. In the following, a critical vibration-amplitude threshold is found.

The displacement response is shown in figure 3.17/A.

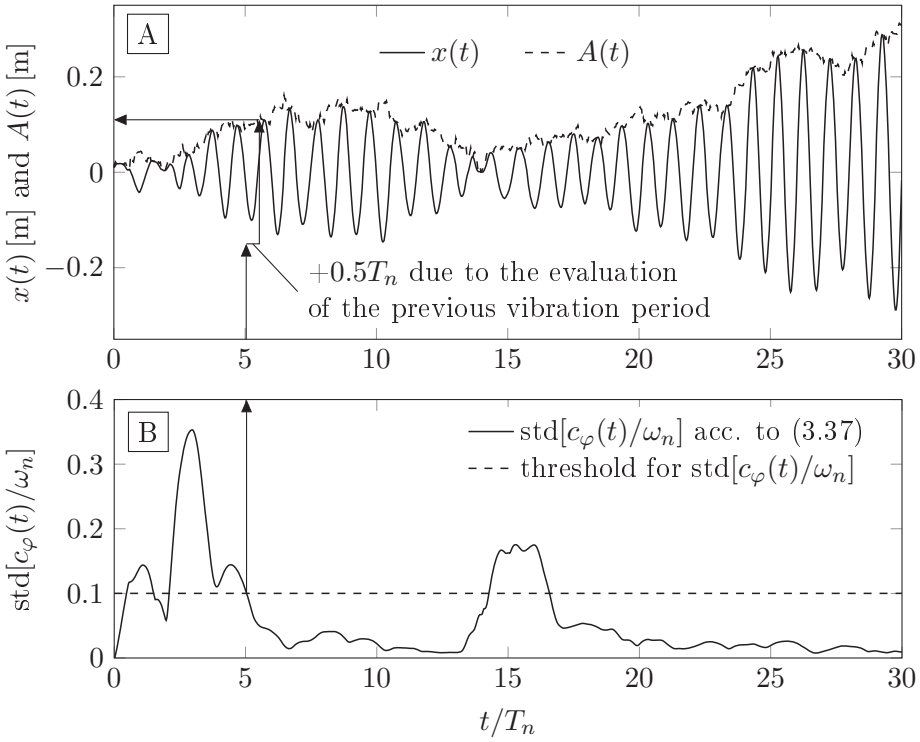

Figure 3.17: Numerical simulation with $x_0 = 0.01\,\mathrm{m}$, $\dot{x}_0 = 0$, a excitation power $I = 0.0675\,\mathrm{m^2/s^4}$ per Hz using a two-sided spectrum, a step size T_s of $0.005\,\mathrm{s}$, $\varphi_{t,f,0} = 0.5\pi$, $\omega_n = 2\pi\,(\mathrm{rad})/\mathrm{s}$, $\xi = 0$ and $\omega_r/\omega_n = 0.8$

The SDOF oscillator is disturbed by the excitation $F_e(t)$ introduced in subsection 3.1.2. Subfigure A shows the displacement $x(t)$ and the vibration amplitude $A(t)$ according to (2.43). Subfigure B shows the std$[c_\varphi(t)/\omega_n]$, which assesses the variations in the filtered TAV within the preceding vibration period (from $t_l = -T_n$ to $t_u = t$), see (3.37). From both subfigures, it becomes evident that when the vibration amplitude $A(t)$ falls below approximately $0.11\,\mathrm{m}$, the variations of the filtered TAV exceed the desired threshold, see arrows in both subfigures.

Therefore, the critical vibration amplitude A_c is set equal to $0.11\,\mathrm{m}$. The operation of the TRD in the continuous rotation mode is, with the chosen initial upper threshold of subsection 3.3.1 (std$[c_\varphi(t)/\omega_n] < 0.1$), only beneficial if $A(t) > A_c$.

3. Mass-ratio-radius control product

The third step is to choose a mass-ratio-radius control product. Figure 3.18 is discussed later on. So far, the force effect of the TRD on the SDOF oscillator has been neglected. This force effect is considered in the following. Furthermore, it is assumed that the angular positions $\varphi(t)$ perfectly tracks the filtered TAP $\varphi_{t,f}(t)$. Taking the force effect of the TRD in (3.1) into account yields

$$\ddot{x}(t) = F_e(t) - 2\xi\omega_n\dot{x}(t) - \omega_n^2 x(t) + F_T(t) \tag{3.39}$$

with the force $F_T(t)$ of the TRD given by

$$F_T(t) = \mu_c r\left[\dot{\varphi}_{t,f}(t)^2\cos\varphi_{t,f}(t) + \ddot{\varphi}_{t,f}(t)^2\sin\varphi_{t,f}(t)\right] \tag{3.40}$$

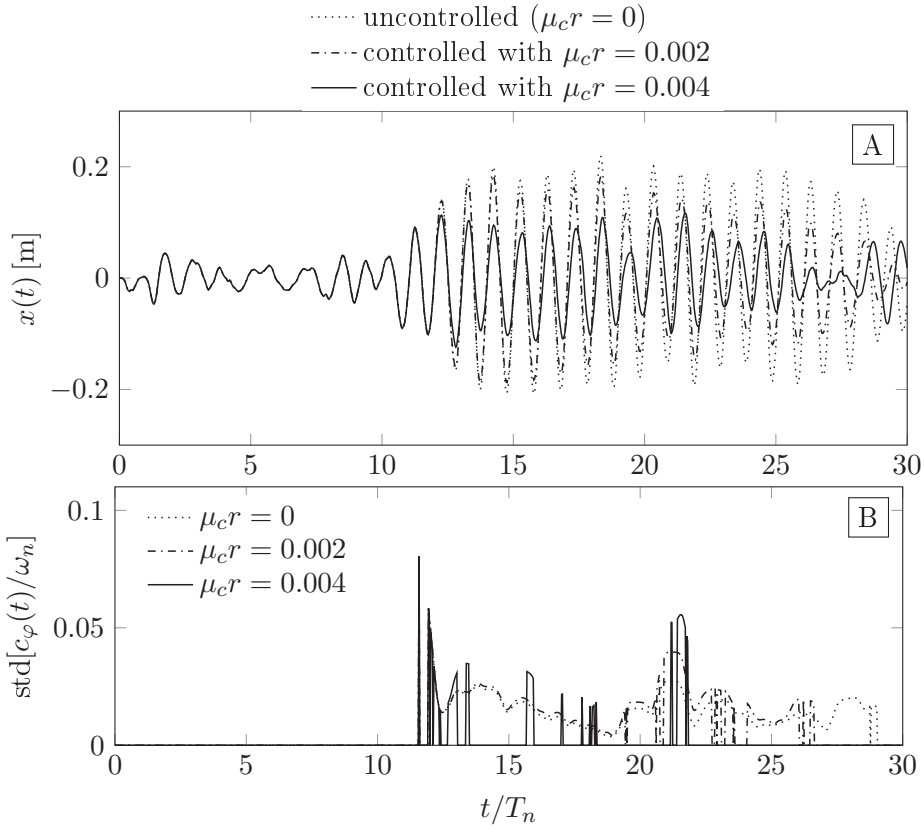

Figure 3.18: Numerical simulation with same simulation tuning as in figure 3.17 but with a different seed and the force effect $F_T(t)$ of (3.41) of the TRD described by $\mu_c r$ and with std$[c_\varphi(t)/\omega_n]$ according to (3.42) with $c_\varphi(t)$ of (3.37)

The magnitude of the force effect is determined by the mass-ratio-radius control product, $\mu_c r$. In the following simulation, $F_T(t)$ is set to zero if $A(t) < A_c$.

$$F_T(t) = \begin{cases} \mu_c r \left[\dot{\varphi}_{t,f}(t)^2 \cos\varphi_{t,f}(t) + \ddot{\varphi}_{t,f}(t)^2 \sin\varphi_{t,f}(t)\right] & \text{for } A(t) \geq A_c \\ 0 & \text{for } A(t) < A_c \end{cases} \tag{3.41}$$

Furthermore, std$[c_\varphi(t)/\omega_n]$ according to (3.37), which describes the variations of the filtered TAV, is set to zero if $A(t) < A_c$, see (3.42). Therefore, the variations of the filtered TAV are only taken into consideration when the TRD is operated in the continuous rotation mode.

$$\text{std}[c_\varphi(t)/\omega_n] = \begin{cases} \text{std}[c_\varphi(t)/\omega_n] & \text{for } A(t) \geq A_c \\ 0 & \text{for } A(t) < A_c \end{cases} \tag{3.42}$$

Figure 3.18/A shows the displacement for different mass-ratio-radius control products $\mu_c r$. The higher $\mu_c r$, the greater the damping effect is. However, as can be seen from figure 3.18/B, the higher $\mu_c r$ is, the larger the undesired variations of the filtered TAV in the time ranges when $A(t) \geq A_c$. This is because the higher $\mu_c r$, the lower the mean vibration amplitudes consequently the disrupting force effect of the excitation and tangential forces is larger. From figure 3.18/B, it becomes evident that the variations of the filtered TAV are below the chosen initial upper threshold of 0.1 for all $\mu_c r$ and $A(t) > A_c$.

3.4 Summary and discussion

- The upper and lower thresholds of figure 3.14 were derived based on initial values ($A_{v,t}$ of subsection 3.3.2, $E_{t,t}$ of subsection 3.3.3 and $\omega_{r,t}$ of subsection 3.3.4). When different initial values are chosen, the lower and upper thresholds change. However, the shapes of the curves of figure 3.14 will remain, coming to the same conclusion: The operation in the continuous rotation mode is only effective if P_r is above a specific value.

- The presented numerical study has shown that the operation of the TRD in the continuous rotation mode using the proposed control algorithm below a certain power ratio P_r is ineffective. The power ratio defined in (3.14) describes the influence of the excitation force on the motion of the SDOF oscillator; the lower the power ratio is, the greater the influence of the excitation force. Considering a constant excitation power, the statement of the first discussion point can be modified: The operation of the TRD in the continuous rotation mode is only effective above a certain vibration-amplitude threshold, A_c.

- For simplicity, the filter frequency will be set equal to the lower threshold according to (3.35) with the recommendation of (3.38). It follows: $\omega_f/\omega_n = 0.428$. When a constant filter frequency is used, the variations of the filtered TAV become lower with larger vibration amplitude $A(t)$. This is because the larger the vibration amplitude $A(t)$, the more the motion of the SDOF oscillator is influenced by its actual conditions ($x(t)$ and $\dot{x}(t)$) instead of by the stochastic excitation.

- The simplicity of the proposed control algorithm allows for a straightforward tuning to operate the TRD in the continuous rotation mode. A tuning procedure was proposed to set the filter frequency ω_f, the critical vibration amplitude A_c and the mass-ratio-radius control product $\mu_c r$. Firstly, the filter frequency ω_f is to be chosen, secondly, the critical vibration-amplitude threshold A_c is to be set and lastly, the mass-ratio-radius control product is determined. All tuning variables (ω_f, A_c and $\mu_c r$) influence the damping effect of the TRD in the continuous rotation mode and the variations of the angular velocity, consequently the power demand on the actuators for accelerating and decelerating the rotors in the continuous rotation mode.

- If only vibrations with $A(t) > A_c$ are to be damped, the TRD can simply be turned on and off at the respective vibration-amplitude thresholds, see section 2.5 and 2.6. Alternatively, if vibrations with $A(t) < A_c$ are additionally required to be damped, the TRD can be operated in the swinging mode in which the tangential forces produced by the TRD are used for the control of small vibrations. A corresponding control algorithm is presented in section 3.5.

- In [28], a SDOF oscillator is disturbed by an excitation force characterized by a band-limited spectrum symmetric about the natural frequency of the oscillator. It was found that the energy consumption, power demand and damping efficiency of the TRD operating in the continuous rotation mode becomes better the more narrow this spectrum is [28]. Vibration reductions (measured in terms of standard deviation) of 25 %, 50 % and 75 % were required. To achieve this, $m_c r$ was set accordingly and a former, less efficient control algorithm for the continuous rotation mode with the ON/OFF method was used. The same reductions were then also required using the same $m_c r$ and the swinging mode. It was found that the TRD performs bet-

ter regarding energy consumption and damping performance when operating in the continuous rotation mode.

- In this chapter, a SDOF oscillator was disturbed by an excitation force in the form of white noise and a tuning procedure was proposed. When the SDOF oscillator is subject to this type of excitation, the SDOF oscillator mainly responds with frequencies in the vicinity of its natural frequency, allowing for the operation in the continuous rotation mode.

  If the SDOF oscillator is disturbed by a different type of excitation, e.g. a stochastic wind excitation, the presented tuning procedure can still be applied. However, if the variations of the filtered TAV are continuously above the chosen threshold, an operation of the TRD in the continuous rotation mode is not beneficial.

  The mean vibration amplitude decreases with the damping ratio when considering inherent damping, an infinite long time interval and a specific excitation force scenario, e.g. a white noise. This holds for any excitation force scenario. Considering inherent damping, a very long time interval and a specific excitation force scenario, e.g. a white noise for $F_e(t)$, the mean vibration amplitude decreases with the damping ratio. Due to the decrease in the mean vibration amplitude, the time intervals in which the vibration amplitude exceeds the critical vibration amplitude become shorter; therefore, the time intervals in which an operation in the continuous rotation mode is beneficial are also shortened.

- The PLL filter was derived under the assumption that the natural frequency ω_n is known. If it is unknown, it can be made available by continuously calculating the slope of the filtered TAP and updating ω_n (input of PLL filter, see figure 3.5) with this slope. The slope of the TAP is noisy when stochastically forced vibrations are considered. Therefore, it must be fed through a low-pass filter, which must be tuned. Alternatively, phase-locked loop systems can be used [34, 35]. The additional tuning of the low-pass filter and the PLL system, respectively, increase the tuning effort. However, further findings regarding the damping performance of the TRD in the continuous rotation mode for stochastically forced vibrations would not be gained. Therefore, ω_n was assumed as known and constant.

3.5 Swinging mode

3.5.1 Formulation of the problem

In this section, a control algorithm for the operation of the TRD in the swinging mode is presented. In this mode, the tangential forces produced by accelerating (swinging) the rotors about the angular positions $\varphi = \pi/2$ or $\varphi = 3/2\pi$ are used for vibration control.

Recalling (2.11) and solving for $\ddot{x}(t)$ yields

$$\ddot{x}(t) = -2\xi\omega_n\dot{x}(t) - \omega_n^2 x(t) + \mu_c r\left[-\dot{\theta}(t)^2\sin\theta(t) + \ddot{\theta}(t)\cos\theta(t)\right] + F_e(t) \tag{3.43}$$

in which $\varphi(t)$ is replaced by

$$\theta(t) = \varphi(t) - \frac{1}{2}\pi \tag{3.44}$$

The angular position offset of (3.44) makes it possible to stabilize the rotors about their new zero positions ($\theta(t) = 0$). From here on, time dependencies are dropped in this subsection.

Solving (2.14) for $\ddot{\varphi}$ and performing the substitution of (3.44) yields:

$$\ddot{\theta} = \frac{\ddot{x}\cos\theta}{r} + \frac{2M}{m_c r^2} \tag{3.45}$$

Inserting (3.45) into (3.43) and doing some rearrangements gives:

$$\ddot{x} = \frac{2\xi\omega_n\dot{x} + \omega_n^2 x + \mu_c r\dot{\theta}^2\sin\theta}{\mu_c\left(\cos\theta\right)^2 - 1} + \frac{2\mu_c\cos\theta}{m_c r\left[1-\mu_c\left(\cos\theta\right)^2\right]}M + \frac{1}{1-\mu_c\left(\cos\theta\right)^2}F_e \tag{3.46}$$

Inserting (3.46) into (3.45) yields, after further rearrangements:

$$\begin{aligned}\ddot{\theta} =& \frac{\cos\theta}{r}\frac{2\xi\omega_n\dot{x} + \omega_n^2 x + \mu_c r\dot{\theta}^2\sin\theta}{\mu_c\left(\cos\theta\right)^2 - 1} + \left\{\frac{2}{m_c r^2}\left[\frac{1}{1-\mu_c(\cos\theta)^2}\right]\right\}M + ... \\ & \frac{\cos\theta}{r\left[1-\mu_c\left(\cos\theta\right)^2\right]}F_e\end{aligned} \tag{3.47}$$

Introducing the state vector

$$\boldsymbol{z} = [z_1, z_2, z_3, z_4]^{\mathrm{T}} = \left[x, \dot{x}, \theta, \dot{\theta}\right]^{\mathrm{T}} \tag{3.48}$$

the differential equations of (3.46) and (3.47) can be rewritten by a set of four first order differential equations

$$\begin{cases}\dot{z}_1 = z_2 \\ \dot{z}_2 = a_{nl,1}(\boldsymbol{z}) + b_{nl,1}(\boldsymbol{z})M + w_{nl,1}(\boldsymbol{z})F_e \\ \dot{z}_3 = z_4 \\ \dot{z}_4 = a_{nl,2}(\boldsymbol{z}) + b_{nl,2}(\boldsymbol{z})M + w_{nl,2}(\boldsymbol{z})F_e\end{cases} \tag{3.49}$$

with $a_{nl,1}(\boldsymbol{z})$, $a_{nl,2}(\boldsymbol{z})$, $b_{nl,1}(\boldsymbol{z})$, $b_{nl,2}(\boldsymbol{z})$, $w_{nl,1}(\boldsymbol{z})$ and $w_{nl,2}(\boldsymbol{z})$ given in the following equations

$$a_{nl,1}(\boldsymbol{z}) = \frac{2\xi\omega_n\dot{x} + \omega_n^2 x + \mu_c r\dot{\theta}^2\sin\theta}{\mu_c\left(\cos\theta\right)^2 - 1} \qquad a_{nl,2}(\boldsymbol{z}) = \frac{\cos\theta}{r}\frac{2\xi\omega_n\dot{x} + \omega_n^2 x + \mu_c r\dot{\theta}^2\sin\theta}{\mu_c\left(\cos\theta\right)^2 - 1} \tag{3.50}$$

$$b_{nl,1}(\boldsymbol{z}) = \frac{2\mu_c\cos\theta}{m_c r\left[1-\mu_c\left(\cos\theta\right)^2\right]} \qquad b_{nl,2}(\boldsymbol{z}) = \frac{2}{m_c r^2}\left[\frac{1}{1-\mu_c\left(\cos\theta\right)^2}\right] \tag{3.51}$$

$$w_{nl,1}(\boldsymbol{z}) = \frac{1}{1-\mu_c\left(\cos\theta\right)^2} \qquad w_{nl,2}(\boldsymbol{z}) = \frac{\cos\theta}{r\left[1-\mu_c\left(\cos\theta\right)^2\right]} \tag{3.52}$$

The control input of the system of (3.49) is the moment M. Unfortunately, many entries of the state vector $\boldsymbol{z}$ influence the system of (3.49) non-linearly. This makes the controller design challenging. However, similar systems have been treated in the past. In [28], a linear-parameter-varying (LPV) controller was presented. It was developed by the Institute of Control Systems at the Hamburg University of Technology. Further control strategies to control such systems are, for instance, sliding mode controllers and adaptive control strategies, see e.g. [50, 51, 52, 53]. Alternatively, as shown in the following subsection, the rotors can be stabilized about their zero positions, $\theta = 0$, by making the system of (3.49) linear about $\theta = 0$. To achieve this, some assumptions must be made, which are discussed in the following. Similar issues are discussed in [54].

3.5.2 Locally stabilizing controller

Assuming that the rotors oscillate about their zero positions ($\theta = 0$) with small values of θ, the small-angle approximation can be used:

$$\sin\theta \approx \theta \qquad\qquad \cos\theta \approx 1 \tag{3.53}$$

Furthermore, it is assumed that the third term, $\mu_c r\dot{\theta}^2 \sin\theta$, of the nominator of $a_{nl,1}(\boldsymbol{z})$ and $a_{nl,2}(\boldsymbol{z})$, respectively, see (3.50), is much smaller than the second term, see (3.54).

$$\omega_n^2 x \gg \mu_c r\dot{\theta}^2 \sin\theta \tag{3.54}$$

The term on the left-hand side of (3.54) represents the acceleration induced by the restoring spring force and the term on the right-hand side represents the acceleration induced by the radial forces. To substantiate the assumption of (3.54) for free vibrations, a harmonic oscillation of the SDOF oscillator is assumed with a displacement amplitude x_a and frequency ω_n. Furthermore, the rotors oscillate about $\theta = 0$ with the frequency ω_n and an amplitude θ_a of $\pm\pi/6$ ($\pm 30°$) such that the resulting tangential forces oppose $\dot{x}$. Assuming a harmonic response of the rotors with the amplitude θ_a and the frequency ω_n, the amplitude of the angular velocity of the rotors is $\theta_a\omega_n$. To compare the amplitudes on both sides of (3.54) (therefore the sin-function is neglected), the assumed amplitudes (x_a, θ_a and $\theta_a\omega_n$) are inserted into (3.54):

$$\omega_n^2 x_a \gg \mu_c r(\omega_n\theta_a)^2 \tag{3.55}$$

Assuming a mass ratio μ_c of 0.01 and $\theta_a = \pi/6$ and doing some rearrangements with (3.55) yields

$$\frac{x_a}{r} \gg 0.01\left(\frac{\pi}{6}\right)^2 \approx 2.7\cdot 10^{-3} \tag{3.56}$$

x_a and r are, for many applications, not largely different from each other. In these cases, (3.54) holds. However, the inequality (3.54) must be checked by the designer. Therefore, the accelerations induced by the third term in the numerator of $a_{nl,1}(\boldsymbol{z})$ and $a_{nl,2}(\boldsymbol{z})$ of (3.50) are dropped in the following. With the small-angle approximation of (3.53) and (3.54), a linear system is derived for (3.49):

$$\dot{\boldsymbol{z}} = \boldsymbol{A}\boldsymbol{z} + \boldsymbol{B}M + \boldsymbol{W}F_e \tag{3.57}$$

with the matrices $\boldsymbol{A}$, $\boldsymbol{B}$ and $\boldsymbol{W}$ given by

$$\boldsymbol{A} = \begin{bmatrix} 0 & 1 & 0 & 0 \\ \dfrac{\omega_n^2}{\mu_c - 1} & \dfrac{2\xi\omega_n}{\mu_c - 1} & 0 & 0 \\ 0 & 0 & 0 & 1 \\ \dfrac{\omega_n^2}{r\,(\mu_c - 1)} & \dfrac{2\xi\omega_n}{r\,(\mu_c - 1)} & 0 & 0 \end{bmatrix} \quad \boldsymbol{B} = \begin{bmatrix} 0 \\ \dfrac{2\mu_c}{m_c r\,(1-\mu_c)} \\ 0 \\ \dfrac{2}{m_c r^2(1-\mu_c)} \end{bmatrix} \quad \boldsymbol{W} = \begin{bmatrix} 0 \\ \dfrac{1}{1-\mu_c} \\ 0 \\ \dfrac{1}{r\,(1-\mu_c)} \end{bmatrix} \tag{3.58}$$

For the linear system of (3.57), the controllability matrix $\boldsymbol{U} = [\boldsymbol{B}, \boldsymbol{A}\boldsymbol{B}, \boldsymbol{A}^2\boldsymbol{B}, \boldsymbol{A}^3\boldsymbol{B}]$ can be calculated [30]. Using the Gaussian elimination, the matrix $\boldsymbol{U}$ can be broken down to the identity matrix, which has a full rank [30]. Thus, the linear system of (3.57) with $\boldsymbol{A}$ and $\boldsymbol{B}$ of (3.58) is controllable.

As the system has two degrees of freedom (x and θ), which are to be controlled, and only one actuator, the system of (3.57) is under-actuated [54]. Another definition of under-actuation is given in (3.59)

$$\operatorname{rank}(\boldsymbol{A}) < \dim(\boldsymbol{z}) \tag{3.59}$$

in which the rank-function computes the rank of a matrix and the dim-function the dimension of a vector [54]. As the rank of A, see (3.58), is three and the dimension of $\boldsymbol{z}$ is four, the system of (3.57) is under-actuated [54].

To control the system of (3.57), a linear quadratic regulator (LQR) as shown in figure 3.19 is used.

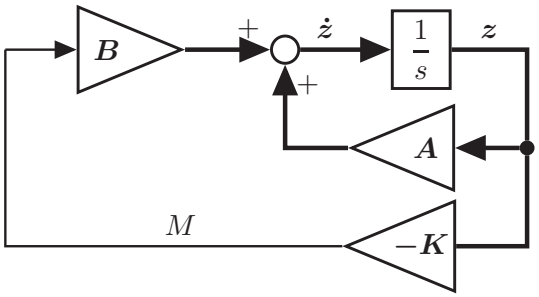

Figure 3.19: Linear quadratic regulator

The excitation force F_e is neglected and free vibrations are considered in the following. A LQR controller is a full state feedback controller [30]. It minimizes the cost function

$$J_c = \int_0^\infty \boldsymbol{z}^T \boldsymbol{Q} \boldsymbol{z} + MRM \mathrm{d}t \tag{3.60}$$

in which $\boldsymbol{Q}$ is a diagonal 4x4 matrix penalizing the states $\boldsymbol{z}$ and R is a scalar value penalizing the moment M (control effort) [30]. $\boldsymbol{Q}$ and R are to be set by the designer. By solving the algebraic Riccati equation, a constant feedback gain $\boldsymbol{K}^{1\mathrm{x}4}$ is calculated. Therefore, the moment is given by:

$$M = -\boldsymbol{K}\boldsymbol{z} \tag{3.61}$$

A controller gain $\boldsymbol{K}$ was then calculated with help of MATLAB using the `lqr` command for the design example of table 3.3.

Table 3.3: Design example

ω_n [(rad)/s]	μ_c [1]	m_c [kg]	r [m]	ξ [1]
2π	0.01	0.1	0.1	0.01

$\boldsymbol{Q}$ and R were set for the initial conditions $\boldsymbol{z} = [0.05\,\mathrm{m}, 0, 0, 0]$ such that θ does not exceed $\pm\pi/2$. Such controllers are referred to as regulators because they bring the system states to rest. With help of the weighting matrix $\boldsymbol{Q}$, the states of the system are punished and with R the control effort M. Therefore, the diagonal entries of $\boldsymbol{Q}$ punish the respective entries of $\boldsymbol{z}$. Consequently, if the range of θ is too low, the third entry of $\boldsymbol{Q}$ can be lowered. Alternatively, the punishment on M can be relaxed by lowering R.

With the system properties of table 3.3, a matrix $\boldsymbol{Q} = \mathrm{diag}(1, \omega_n, 5 \cdot 10^{-4}, 5 \cdot 10^{-4}\omega_n)$ and $R = 1.0 \cdot 10^{-5}$ yields a controller gain $\boldsymbol{K} = [3.23 \cdot 10^3, -14.81, 7.07, 17.76]$. Units were dropped for $\boldsymbol{Q}$, R and $\boldsymbol{K}$.

The controller with the gain $\boldsymbol{K}$ was then used for the linear model of (3.57) and for the non-linear system described by (3.49) to (3.52). The results are shown in figure 3.20.

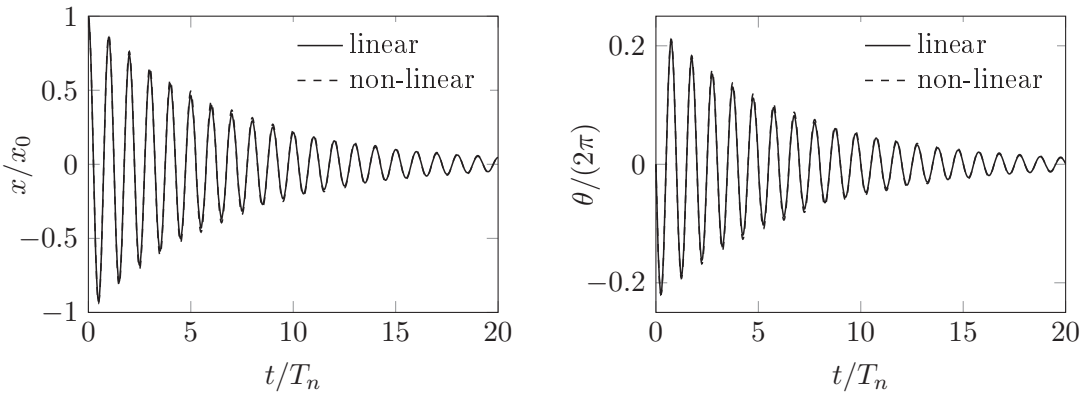

Figure 3.20: Numerical simulation of linear quadratic regulator

It becomes evident that all states decay, as desired, to zero. Even though the rotors oscillate within a working range of nearly $\pm\pi/2$, the curves for the linear and the non-linear system nearly coincide. This is a indicator that the assumptions of (3.53) and (3.54) are correct, at least for free vibrations.

Figure 3.21 depicts the force of the TRD F_T and the velocity of the SDOF oscillator belonging to the non-linear system of figure 3.20.

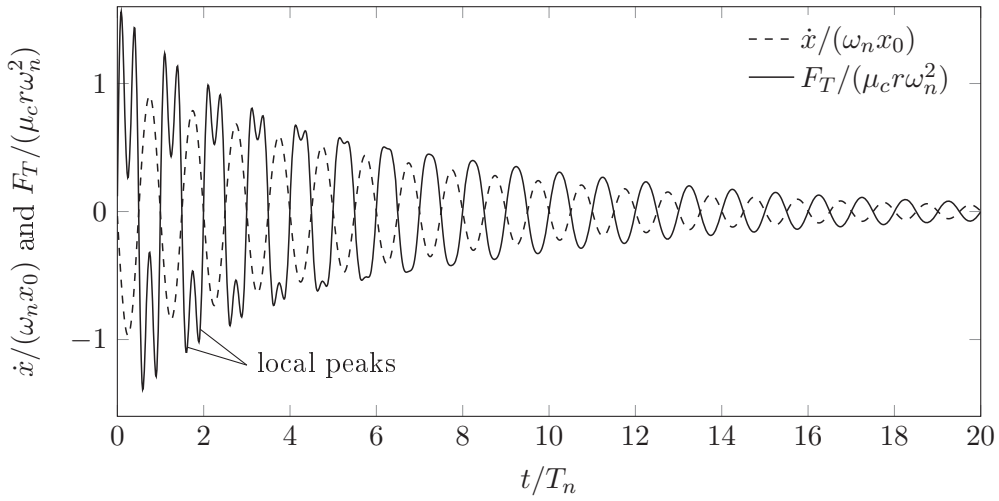

Figure 3.21: Normalized force generated by TRD and normalized velocity of SDOF oscillator belonging to the non-linear system of figure 3.20

For small vibration amplitudes (see $t/T_n > 6$), F_T and $\dot{x}$ are in anti-phase. Note that the radial forces are small in comparison to the tangential forces when the rotors oscillate with small amplitudes. However, for larger vibration amplitudes ($t/T_n < 5$), the working range of the rotors reaches nearly $\pm\pi/2$, see figure 3.20, and the effect of the tangential forces becomes smaller in comparison to the radial forces. The radial forces create two local peaks in the force curve, see figure 3.21. Fortunately, the components of the radial and the tangential forces in the x-direction have the same sign. Therefore, the radial forces additionally damp the system. However, the damping effect due to the tangential forces decreases with a larger working range of θ as the sin-function of (3.43) reduces the effect of the tangential forces.

3.6 Design example: Switching between the continuous rotation and the swinging mode

3.6.1 Excitation force

In this section, the SDOF oscillator is disturbed by a stochastic excitation force and the TRD is tuned such that it operates in the continuous rotation mode for large vibrations and in the swinging mode for small vibrations. Numerical simulations are performed with the test setup presented in subsection 2.6.1. These simulations are then validated experimentally.

The excitation force is created using the linear actuator of figure 2.30. The excitation mass m_e is increased from 2.0 kg to 4.0 kg, allowing for a stronger excitation. Due to the increase of the excitation mass, the properties of the SDOF oscillator change and are now as given in table 3.4.

Table 3.4: System properties of SDOF oscillator with excitation mass $m_e = 4.0\,\text{kg}$

m_s [kg]	36.6
ω_n [(rad)/s]	5.28
ξ [%]	0.272

To induce a stochastic excitation force, a band-limited white noise signal is created. It is then led through a Butterworth band-pass filter of the order 20 with a lower edge frequency of $\omega_{l,e} = 2.28\,(\text{rad})/\text{s}$ and an upper edge frequency of $\omega_{u,e} = 8.28\,(\text{rad})/\text{s}$ [44], that is $\omega_n \pm 3\,(\text{rad})/\text{s}$. As the linear actuator has a limited stroke, the lower frequencies must be canceled out. In addition, inappropriately high frequencies are not applied as they may damage the linear actuator.

Due to the filtering described in the previous paragraph, the excitation force in frequency domain is symmetric about the natural circular frequency of the SDOF oscillator, see table 3.4, producing the preliminary filtered excitation force $\tilde{f}_e(t)$. This signal is then divided by $m_e = 4.0\,\text{kg}$, yielding the target acceleration $\ddot{d}_t(t)$, see figure 3.22. Integrating once yields the target velocity $\dot{d}_t(t)$ and twice the target position $d_t(t)$.

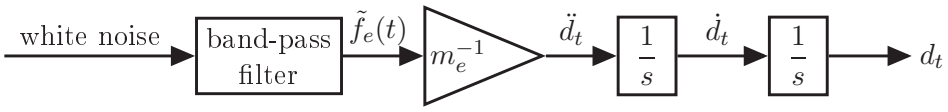

Figure 3.22: Generation of excitation force

Using an excitation power of $0.9\,\text{N}^2$ per Hz and a two-sided spectrum, $d_t(t)$ remains within the physical limits of $\pm 0.1\,\text{m}$.

To track $d_t(t)$, a method from the field of modern control theory, which is named mixed-sensitivity design, is applied [55]. Hence, a controller is designed that is robust to model inaccuracies and insensitive to measurement noise for the tracking of $d_t(t)$. The transfer function $G_{S2}(s)$ from (2.204) is reconsidered. System identification was performed anew as the dynamics of the linear actuator change due to the increased excitation mass m_e. The modified transfer function with the control effort $u_a(t)$ as input and the position $d(t)$

as output is:

$$G_{s2}(s) = \frac{0.124}{6.16 \cdot 10^{-3} s^2 + s} \tag{3.62}$$

With the state vector $\boldsymbol{x}_a(t) = [d(t), \dot{d}(t)]^{\mathrm{T}}$, a state-space representation of (3.62) is formed

$$\dot{\boldsymbol{x}}_a(t) = \boldsymbol{A}_a \boldsymbol{x}_a(t) + \boldsymbol{B}_a u_a(t) \qquad d(t) = \boldsymbol{C}_a \boldsymbol{x}_a(t) + d_d(t) \tag{3.63}$$

with

$$\boldsymbol{A}_a = \begin{bmatrix} 1 & 0 \\ -162.3 & 0 \end{bmatrix} \qquad \boldsymbol{B}_a = \begin{bmatrix} 0 \\ 20.13 \end{bmatrix} \qquad \boldsymbol{C}_a = \begin{bmatrix} 1 & 0 \end{bmatrix} \qquad D_a = 0 \tag{3.64}$$

in which the units are dropped. $d_d(t)$ will be discussed later.

The mixed-sensitivity controller design in described roughly in the following; for more details, see [55]. The chosen generalized plant of figure 3.23 has two inputs, $d_t(t)$ and $u_a(t)$. $d_n(t)$ and $d_d(t)$ are introduced and discussed later.

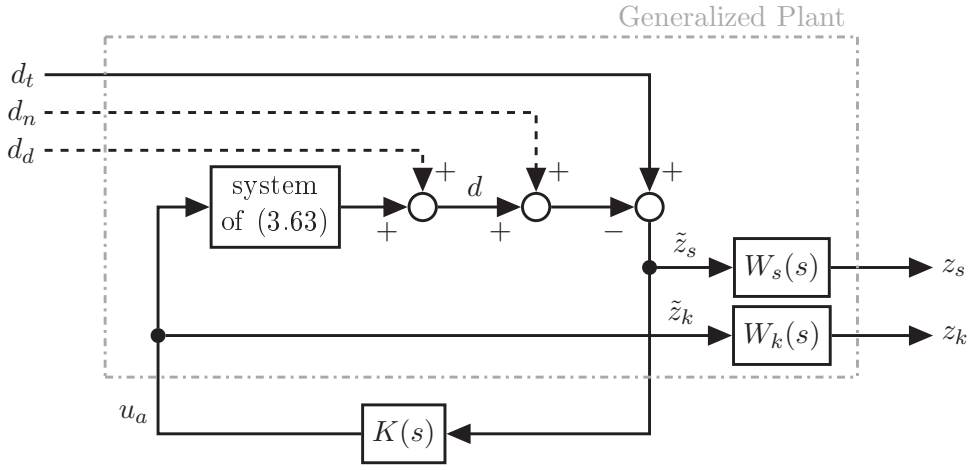

Figure 3.23: Generalized plant for linear actuator

Considerations regarding the mixed-sensitivity design are done in frequency domain in the following. Therefore, for the rest of this subsection, time dependencies are dropped. The generalized plant has two fictitious outputs, z_s and z_k. The relation between the inputs and the preliminary fictitious outputs, $\tilde{z}_s$ and $\tilde{z}_k$, are given by

$$\begin{bmatrix} \tilde{z}_s \\ \tilde{z}_k \end{bmatrix} = \tilde{P} \begin{bmatrix} d_t \\ u_a \end{bmatrix} \qquad \tilde{P} = \left[\begin{array}{c|cc} \boldsymbol{A}_a & \boldsymbol{0} & \boldsymbol{B}_a \\ \hline -\boldsymbol{C}_a & 1 & 0 \\ \boldsymbol{0} & 0 & 1 \end{array}\right] \tag{3.65}$$

with the preliminary generalized plant $\tilde{P}$. $\boldsymbol{0}$ refers to a zero matrix with the appropriate dimensions.

Before $\tilde{z}_s$ and $\tilde{z}_k$ leave the generalized plant, each is fed through a filter $W_s(s)$ and $W_k(s)$, see figure 3.23. The fictitious outputs z_s and z_k are given by

$$\begin{bmatrix} z_s \\ z_k \end{bmatrix} = \begin{bmatrix} W_s(s) & 0 \\ 0 & W_k(s) \end{bmatrix} \begin{bmatrix} \tilde{z}_s \\ \tilde{z}_k \end{bmatrix} \tag{3.66}$$

Before explaining the purpose of $W_s(s)$, the sensitivity function $S(s)$ is discussed. The measurement noise d_n and the output disturbance d_d are now additionally considered. From figure 3.23, the following two equations can be derived

$$d = G_{s2}(s)u_a + d_d \tag{3.67}$$

$$u_a = K(s)\left(d_t - d - d_n\right) \tag{3.68}$$

Substituting (3.68) into (3.67) and solving for d yields

$$d = S(s)d_d + S(s)G_{s2}(s)K(s)\left(d_t - d_n\right) \tag{3.69}$$

where the sensitivity function is

$$S(s) = \left(G_{s2}(s)K(s) + I\right)^{-1} \tag{3.70}$$

From (3.69), it becomes evident that $S(s)$ is the transfer function from d_d to d. Therefore, to reject the output disturbance d_d, it is required that $|S(s)| = 0$. As can be seen in [55], there are further interpretations of $S(s)$. It is also the transfer function from d_t, d_n and d_d to the error (difference between d and d_t) [55, 56]. To perfectly track d_t, it is required that $|S(s)| = 0$, whereas to suppress measurement noise, $|S(s)| = 1$ is required. Therefore, the tracking and suppression of measurement noise are conflicting design objectives. A trade-off is required. Therefore, $|S(s)| = 0$ is chosen for small frequencies to achieve output disturbance rejection and adequate tracking. Furthermore, $|S(s)| = 1$ is chosen for large frequencies in order to suppress measurement noise.

To limit the control effort u_a and also make the controller act in a desired frequency range, the so-called control sensitivity function, $S(s)K(s)$, is also evaluated and limited. For more information regarding the sensitivity and the control sensitivity function, see [55].

To shape $S(s)$ such that it has high-pass behavior—$|S(s)| = 0$ at low frequencies and $|S(s)| = 1$ at high frequencies—, shaping filters are used [55]. Before explaining the shaping filters, the H_∞ norm is briefly discussed. It computes the maximum singular value, $\sigma(..)$, over frequency. The operator $||...||_\infty$ is used to denote this [55, 56]. Within the mixed sensitivity synthesis, a controller $K(s)$ is constructed such that the maximum singular values in frequency domain are pushed down. Shaping $W_s(s)$ as a high-pass filter, using the constraint of (3.71) and applying a mixed sensitivity design (with the Robust Control Toolbox in Matlab), the desired shape of $S(s)$ is imposed. $W_s(s)$ amplifies $S(s)$ at low frequencies, therefore $W_s(s)$ is used to additionally punish $S(s)$ at low frequencies.

$$||W_s(s)S(s)||_\infty < 1 \tag{3.71}$$

This implies (3.72). Note that $1/|W_s(jw)|$ gives an upper limit for $S(s)$.

$$|S(jw)| < \frac{1}{|W_s(jw)|} \tag{3.72}$$

A form for $W_s(s)$ as shown in (3.73) was chosen.

$$W_s(s) = \frac{1}{M_s}\frac{1}{s/w_s + 1}\frac{1}{s/w_{s2} + 1} \tag{3.73}$$

The values for M_s, w_s and w_{s2} are to be chosen by the designer. The frequency w_{s2} is set to a very small value such that $W_s(s)$ starts off at $s = 0$ with a negative slope of

20 dB/dec. This ensures that low frequencies in the sensitivity function are additionally punished, resulting in an amplification of low frequencies of the controller.

Furthermore, it is wanted that (3.74) holds.

$$||W_k(s)K(s)S(s)||_\infty < 1 \tag{3.74}$$

This allows to limit the control effort u_a. $W_k(s)$ is chosen as shown in (3.75)

$$W_k(s) = \frac{1}{M_k}\frac{s/w_{kz}+1}{s/w_{kp}+1} \tag{3.75}$$

in which the constants M_k, w_{kz} and w_{kp} are to be chosen by the designer.

The transfer function matrix $T_{\boldsymbol{z}d_t}(s)$ from d_t to the output $\boldsymbol{z} = [z_s, z_k]^{\mathrm{T}}$ is given by

$$\boldsymbol{T}_{\boldsymbol{z}d_t}(s) = \begin{bmatrix} W_s(s)S(s) \\ W_k(s)K(s)S(s) \end{bmatrix} \tag{3.76}$$

A controller $K(s)$ is now searched for such that (3.77) holds.

$$\left|\left|\begin{bmatrix} W_s(s)S(s) \\ W_k(s)K(s)S(s) \end{bmatrix}\right|\right|_\infty = \gamma < 1 \tag{3.77}$$

In MATLAB, algorithms generating a controller $K(s)$ while minimizing γ are available. If $\gamma < 1$, the constraint of (3.77) holds. If not, the constraints set with (3.73) and (3.75) must be relaxed. Otherwise, they can be tightened. With the tuning parameters of table 3.5, which were set in an iterative process, adequate tracking results are achieved for the plant of (3.62).

Table 3.5: Tuning parameters for mixed-sensitivity design

M_s	w_s [(rad)/s]	w_{s2} [(rad)/s]	M_k	w_{kz} [(rad)/s]	w_{kp} [(rad)/s]
$1.5 \cdot 10^{-11}$	1.0	$1.0 \cdot 10^{-8}$	1000	42	$6.0 \cdot 10^5$

The inverse weighting filter functions $1/|W_s(s)|$ and $1/|W_k(s)|$ corresponding to the tuning of table 3.5 are shown in figure 3.24 including the singular values of the corresponding sensitivity function $S_1(s)$ and control sensitivity function $K_1(s)S_1(1)$.

As $\gamma < 1$, the constraint of (3.77) holds. When applying the controller on the test setup, the linear actuator starts a jerking motion as the controller is too aggressive. In MATLAB, tools are available to generate a less aggressive controller. By setting the GMIN-value to 1.05γ, a second controller with $\sigma(S_2(s))$ and $\sigma(K_2(s)S_2(s))$ is calculated. With regard to figure 3.24, note that $\sigma(S_1(s) \approx S_2(s))$ and $\sigma(K_1(s)S_1(s)) \approx \sigma(K_2(s)S_2(s))$ for $\omega < 100\,(\mathrm{rad})/\mathrm{s}$. However, for $\omega > 100\,(\mathrm{rad})/\mathrm{s}$, the control sensitivity $\sigma(K_2(s)S_2(s))$ function has a steeper negative slope, therefore the controller $K_2(s)$ amplifies these frequencies less.

Using this controller and tracking d_t leads to satisfying tracking results. Figure 3.25 shows d_t and d for a randomly chosen time sequence. It becomes evident that d_t nearly coincides with d.

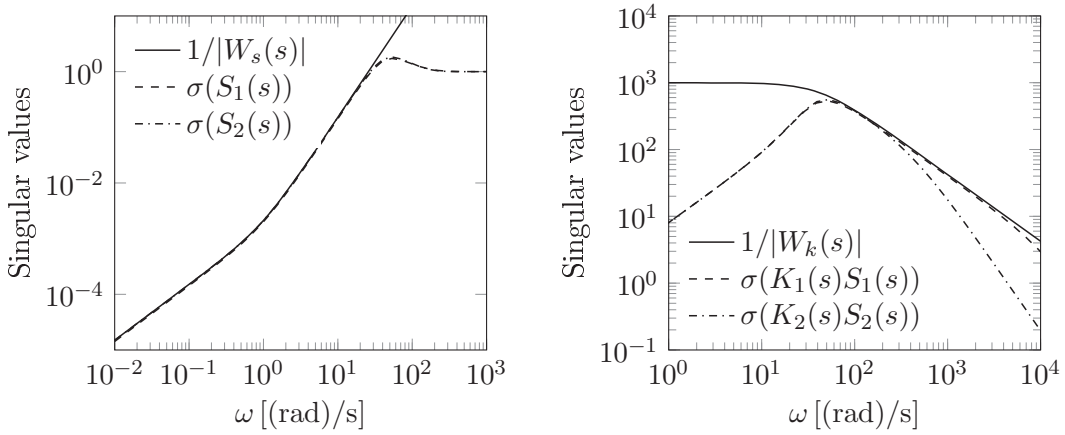

Figure 3.24: Singular values of sensitivity and control sensitivity function including chosen constraints of designed controllers

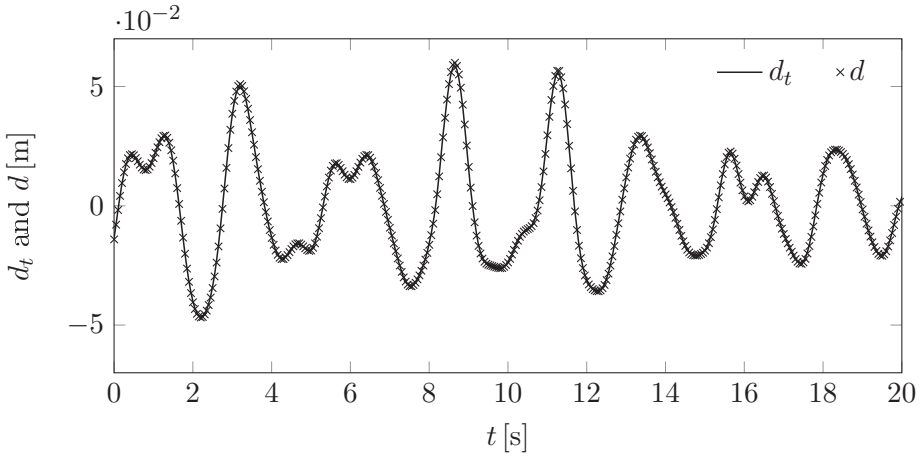

Figure 3.25: Target position d_t and position d of linear actuator for a randomly chosen time interval

The excitation force described at the beginning of this subsection was then applied to the SDOF oscillator of table 3.4. This was done experimentally and numerically. The experiment was conducted first. The TAP d_t generated by the real-time system for the linear actuator and the displacement x of the table were recorded. To eliminate inaccuracies in the generation of the time course for d_t, the previously recorded time course of d_t is subsequently used for the numerical simulations. The standard deviations of the uncontrolled displacement responses were calculated. The standard deviation x_{std} of the displacement of the numerical simulation was 0.0200 m and 0.0207 m for the experiment. The values nearly coincide. This shows that the SDOF oscillator with the properties of table 3.4 describes the dynamical behavior sufficiently accurate. Such tests were performed several times. The standard deviations did not vary considerably. Therefore, the time duration of one hour is sufficiently long.

3.6.2 Tuning of continuous rotation mode

Setting of ON/OFF thresholds

Numerical simulations are performed in the following to set the vibration-amplitude thresholds for the excitation described in subsection 3.6.1. This excitation produces varying vibration amplitudes between zero and 0.09 m. According to the recommendation of subsection 3.3.6, the filter frequency is set as follows: $\omega_f/\omega_n = 0.428$. The variations of the filtered TAV are measured with help of the $\mathrm{std}\,[c_\varphi(t)/\omega_n]$, see (3.37). The vibration amplitude $A(t)$ and $\mathrm{std}\,[c_\varphi(t)/\omega_n]$ are shown in figure 3.26.

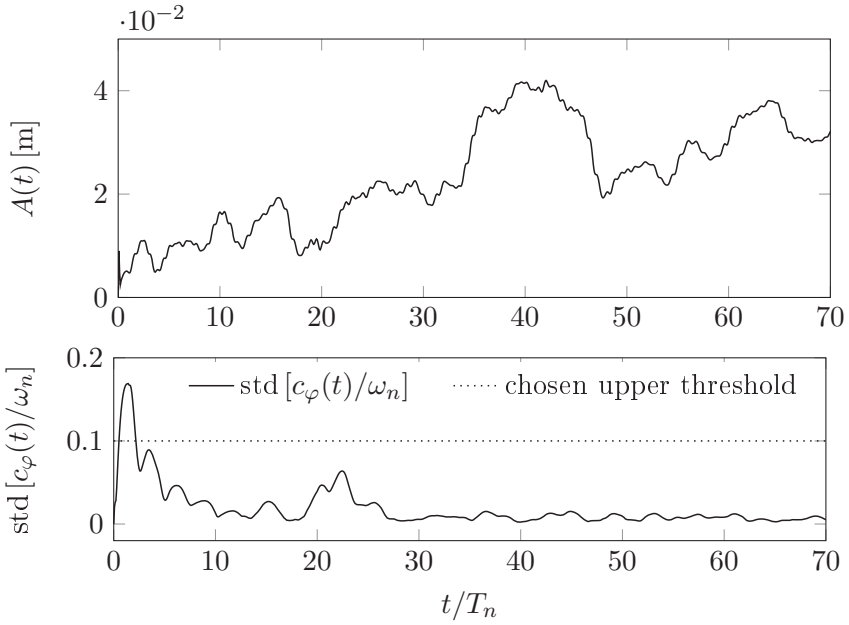

Figure 3.26: Vibration amplitude $A(t)$ and $\mathrm{std}\,[c_\varphi(t)/\omega_n]$ for setting on/off vibration-amplitude thresholds

Previously in this chapter, it was found that if $\mathrm{std}\,[c_\varphi(t)/\omega_n]$ is smaller than 0.1, the variations of the filtered TAV are acceptable. From figure 3.26, it becomes evident that when $A(t)$ is larger than approximately 0.01 m, this threshold is held. To ensure that the continuous rotation mode is not entered and left too frequently, the vibration-amplitude thresholds are set as follows: $A_{on} = 0.015\,\mathrm{m}$ and $A_{off} = 0.010\,\mathrm{m}$.

Simulations are performed to tune the continuous rotation mode as shown in the block diagram of figure 3.27.

$m_c r$ will be set in the following to $4.28 \cdot 10^{-2}\,\mathrm{kgm}$. Note the similarities of the values for ω_f/ω_n and $m_c r$ are coincidental. This mass-radius control product corresponds to one active TRD unit with the mass-radius control product shown in table 2.5. This is the largest mass-radius control product considered for this investigation. Note for smaller mass-radius control products, the disturbing effect due to the tangential forces is reduced when using identical control algorithms. Therefore, the same control algorithm derived in the following can be used for all smaller mass-radius control products.

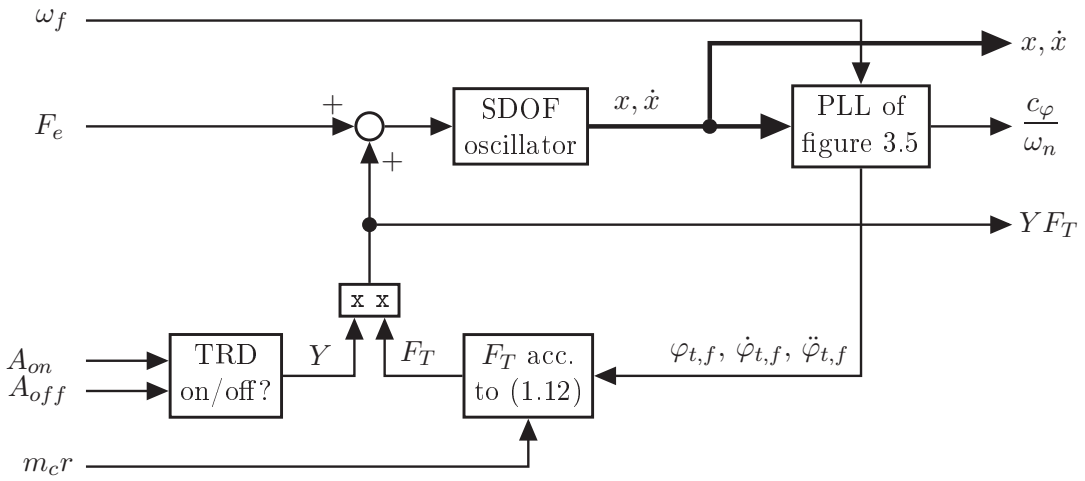

Figure 3.27: Block diagram for tuning of continuous rotation mode

According to figure 3.27, the force of the TRD is only applied when it is operated in the continuous rotation mode. This is done as in this step, only the continuous rotation mode is tuned. The logical output Y of the block 'TRD on/off?' is set to one when $A(t)$ exceeds A_{on} and back to zero when $A(t)$ falls below A_{off}; thus switching the control action generated in the continuous rotation mode on and off. Note that Y is only zero or one and its time dependency is not depicted.

Furthermore, it is assumed that the filtered TAP $\varphi_{t,f}(t)$ is perfectly tracked. This means that the dynamics of the actuators have no influence: $\varphi(t) = \varphi_{t,f}(t)$, $\dot{\varphi}(t) = \dot{\varphi}_{t,f}(t)$ and $\ddot{\varphi}(t) = \ddot{\varphi}_{t,f}(t)$. $\dot{\varphi}_{t,f}(t)$ is directly available from the filter of figure 3.5. $\ddot{\varphi}_{t,f}(t)$ is obtained by numerically taking the time derivative of $\dot{\varphi}_{t,f}(t)$.

The continuous rotation mode was then tuned. The simulation results using the final tuning parameters are shown in figure 3.28.

Subfigure A shows the uncontrolled and the controlled displacement response. If the damping effect of the TRD is not sufficient, a larger $m_c r$ must be chosen. However, from subfigure A, it is evident that the chosen $m_c r$ effectively damps the vibrations. By further increasing $m_c r$, the damping effect can be increased. Subfigure B and C show that the variations of the filtered TAV are within the desired limits. Simultaneously, the anti-phasing between the control force of the TRD and the velocity of the SDOF oscillator is ensured. If the variations of the filtered TAV would be too high, the filter frequency ω_f must be lowered or the formerly chosen vibration-amplitude thresholds must be increased. Subfigure D shows the power demand of the TRD unit, which is computed as follows. Solving (2.14) for $M(t)$ and substituting $\varphi(t)$ and $\ddot{\varphi}(t)$ by $\varphi_{t,f}(t)$ and $\ddot{\varphi}_{t,f}(t)$ yields

$$M(t) = 0.5 m_c r^2 \ddot{\varphi}_{t,f}(t) - 0.5 m_c r \ddot{x}(t) \sin \varphi_{t,f}(t) \tag{3.78}$$

Multiplying this by two and with the filtered TAV $\dot{\varphi}_{t,f}(t)$ gives the power demand of the TRD unit

$$P_T(t) = 2M(t)\dot{\varphi}_{t,f}(t) \tag{3.79}$$

Multiplying (3.79) with Y gives the required power demand of one TRD unit in the continuous rotation mode. As can be seen from figure 3.28/D, $YP_T(t)$ is nearly always smaller

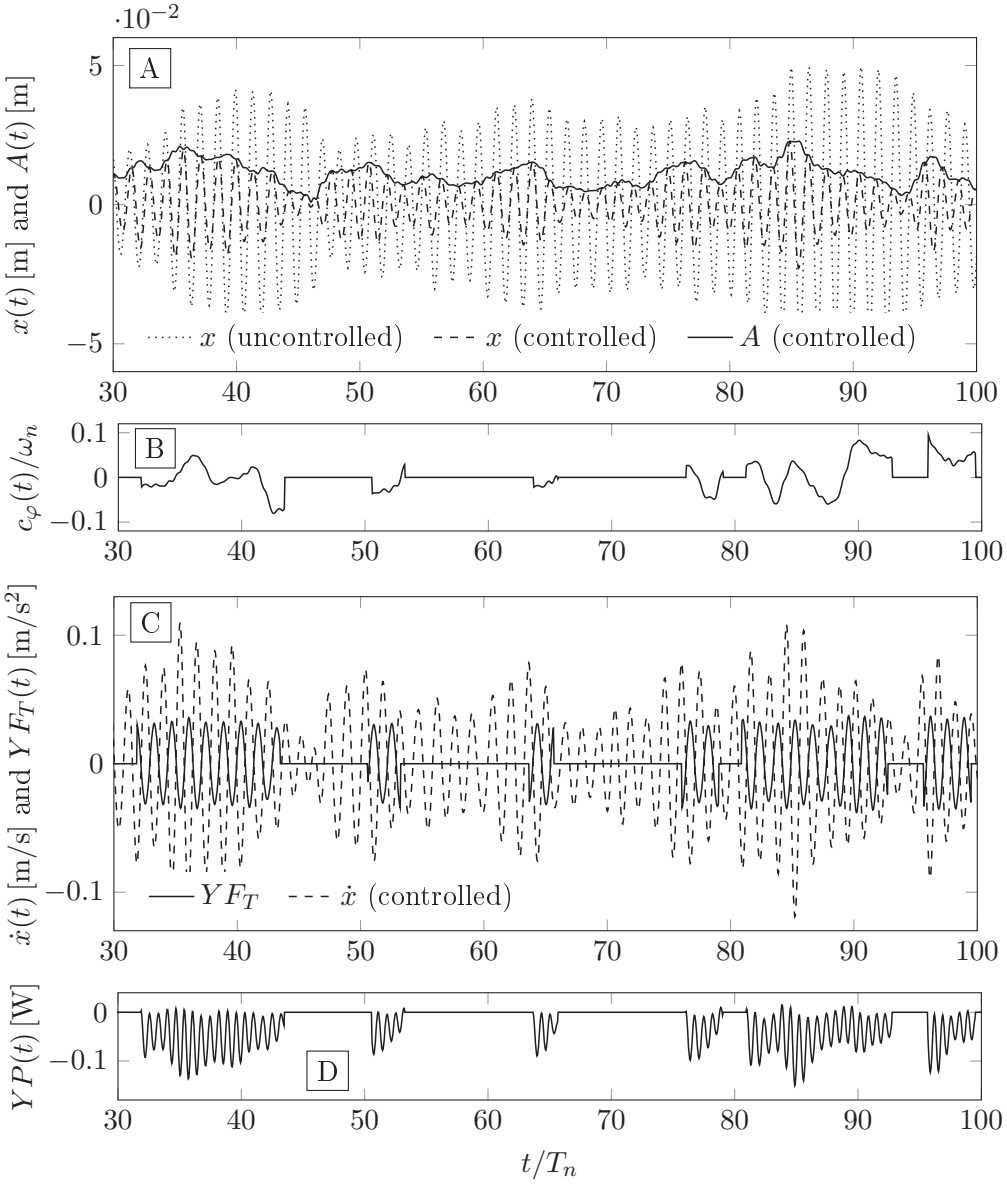

Figure 3.28: States for evaluation of continuous rotation mode

than zero. Hence, the TRD dissipates energy from the SDOF oscillator and the actuators are required to brake. The power demand on the actuator in the continuous rotation mode depends on several parameters tuned in this step. From figure 3.28, it becomes evident that $YP_T(t)$ increases with the vibration amplitude $A(t)$. This is because with larger $A(t)$, the acceleration $\ddot{x}(t)$ increases, requiring larger braking power. Furthermore, the angular accelerations guaranteeing the anti-phasing also influence $M(t)$ and therefore $P_T(t)$. This term was bounded by limiting c_φ/ω_n and, due to this, the power demand is not considerably increased by the angular accelerations $\ddot{\varphi}_{t,f}$.

To evaluate the power demand of one TRD unit in the continuous rotation mode, the rms-value, see (2.96), of $YP_T(t)$ according to (3.80) is calculated

$$P_{rms,rot} = \mathrm{rms}(YP_T(t)) = \sqrt{\frac{1}{T_Y}\int_{t=0}^{t=1\,\mathrm{h}} |YP_T(t)|^2 \mathrm{d}t} = 0.052\,\mathrm{W} \tag{3.80}$$

in which T_Y refers to the time duration the TRD operates in the continuous rotation mode. Using T_Y rather than the complete time duration of one hour is equivalent to consider the power only in the time intervals the TRD operates in the continuous rotation mode.

For comparison purposes, the power demand, $P_{rms,sw}$, required to operate the TRD in the swinging mode will also be calculated later on. $P_{rms,sw}$ will be calculated in the same manner as it is done with (3.80) for the continuous rotation mode. However, the power demand will only be considered when $Y = 0$.

For the derivation of (3.78), the rotational inertia of the rotors is only composed of that of a single lumped control mass. For practice, the rotational inertias of all parts of the TRD set into rotational motion, i.e. transmission, rod, etc. must be considered. Furthermore, in (3.78) friction is neglected.

The power demand on the actuators for the experiments of subsection 3.6.5 and 3.6.6 is determined in the same manner as it was done for the experiments of subsection 2.6.6.

Tuning of controller for tracking filtered target angular position
In a next step, the controller for tracking the TAP $\varphi_{t,f}(t)$ for the test setup is tuned. The open-loop velocity and closed-loop angular position control shown in figure 2.39 is used again. The TAV is set to ω_n and $\varphi_{t,f}(t)$ is produced by the PLL filter. Using a controller of the form as shown in the following equation

$$C(s) = \frac{K_P}{s\omega_P^{-1} + 1} \tag{3.81}$$

with the proportional feedback gain $K_P = 1\,\mathrm{V/(rad)}$ and a pole with $\omega_P = 70\,\mathrm{(rad)/s}$ yields adequate tracking results for the actuators identified in subsection 2.6.3. With adequate is meant that the control error is negligibly small when the TRD is operated in the continuous rotation mode. The control effort $u_{a,c}(t)$ for the continuous rotation mode is then given by

$$u_{a,c}(t) = \frac{1}{b}\omega_n + C(s)ce(t) \tag{3.82}$$

with the corresponding b of table 2.6. As in section 2.6, each rotor is controlled individually.

3.6.3 Tuning of controller for swinging mode

For the tuning of the swinging mode, the dynamical behavior of the actuators must be determined. Their dynamical behavior is described by the transfer function of (2.146) with the coefficients of table 2.6. Rearranging (2.146) and substituting $\varphi(t)$ by $\theta(t)$, see subsection 3.5.1, the following equation is derived:

$$\ddot{\theta}(t) = -\frac{\dot{\theta}(t)}{a} + \frac{b}{a}u_a(t) + w_\theta(t) \tag{3.83}$$

in which $u_a(t)$ is the control effort and $w_\theta(t)$ denotes disturbance due to accelerations of the SDOF oscillator. Time dependencies will no longer be indicated in this subsection. Reconsidering (3.43) and the discussion done in subsection 3.5.2—the radial forces are small in comparison to the tangential forces—and using the small-angle approximation of (3.53), (3.43) simplifies to:

$$\ddot{x} = -2\xi\omega_n\dot{x} - \omega_n^2 x + \mu_c r\ddot{\theta} + F_e \tag{3.84}$$

Inserting (3.83) into (3.84) yields

$$\ddot{x} = -2\xi\omega_n\dot{x} - \omega_n^2 x + \mu_c r\left(-\frac{\dot{\theta}}{a} + \frac{b}{a}u_a + w_\theta\right) + F_e \tag{3.85}$$

Introducing the state vector of (3.48), the equations of (3.83) and (3.85) can be written in a state space representation

$$\dot{\boldsymbol{z}} = \boldsymbol{A}\boldsymbol{z} + \boldsymbol{B}u_a + \boldsymbol{w} \tag{3.86}$$

in which the vector $\boldsymbol{w} = [0, F_e, 0, \mu_c r w_\theta]^{\mathrm{T}}$ describes the process noise (disturbances) with $\boldsymbol{A}$ and $\boldsymbol{B}$:

$$\boldsymbol{A} = \begin{bmatrix} 0 & 1 & 0 & 0 \\ -\omega_n^2 & -2\xi\omega_n & 0 & -\dfrac{\mu_c r}{a} \\ 0 & 0 & 0 & 1 \\ 0 & 0 & 0 & -\dfrac{1}{a} \end{bmatrix} \qquad \boldsymbol{B} = \begin{bmatrix} 0 \\ \mu_c r\dfrac{b}{a} \\ 0 \\ \dfrac{b}{a} \end{bmatrix} \tag{3.87}$$

The controllability matrix of (3.86) with the matrices of (3.87) has, as before, full rank; thus, the system is controllable. Furthermore and as before, the system is under-actuated. The output equation is given by

$$\begin{bmatrix} x \\ \theta \end{bmatrix} = \begin{bmatrix} 1 & 0 & 0 & 0 \\ 0 & 0 & 1 & 0 \end{bmatrix} \boldsymbol{z} + \boldsymbol{n}_{x,\theta} \tag{3.88}$$

in which $\boldsymbol{n}_{x,\theta}$ represents the measurement noise vector in x and θ.

In section 3.5, a LQR regulator was designed. Such a regulator assumes that all states of $\boldsymbol{z}$ are available. For the test setup, only x and θ are available for feedback. The linear-quadratic Gaussian (LQG) regulator design approach generating the controller $\boldsymbol{C}(s)$, see figure 3.29, is suitable for such a control problem [33, 55]. In contrast to the LQR, the LQG regulator design approach additionally constructs an observer to estimate the non-measured states, see [33, 55].

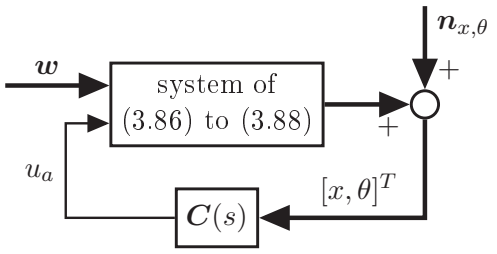

Figure 3.29: Linear quadratic Gaussian regulator

The LQG regulator constructs a controller $\boldsymbol{C}(s)$ such that the cost function J_c of (3.89) is minimized.

$$J_c = \int_0^\infty \begin{bmatrix} \boldsymbol{z}^{\mathrm{T}} & u_a \end{bmatrix} \boldsymbol{Q} \begin{bmatrix} \boldsymbol{z} \\ u_a \end{bmatrix} \mathrm{d}t \qquad \text{with} \qquad \boldsymbol{Q} = \mathrm{diag}\left[q_x, q_{\dot{x}}, q_\theta, q_{\dot{\theta}}, q_u\right] \tag{3.89}$$

In (3.89), $\boldsymbol{Q}$ is the diagonal weighting matrix punishing the states of $\boldsymbol{z}$ and the control effort u_a. With the weighting matrix $\boldsymbol{Q}$, the individual states of $\boldsymbol{z}$ are punished. If, for instance, the working range of θ becomes too large (the rotors oscillate by more than $\pm\pi/2$ about their zero position), the designer can increase the penalty on q_u. This results in a more restricted working range of θ and a lower damping action. The entries of $\boldsymbol{Q}$ are to be set by the designer. The `lqg`-command in MATLAB has three inputs:

1. The system defined in (3.86) to (3.88),
2. the matrix $\boldsymbol{Q}$ and
3. a matrix $\boldsymbol{Q}_m$ estimating the measurement noise $\boldsymbol{n}_{x,\theta}$ and the disturbance $\boldsymbol{w}$. It is assumed that $\boldsymbol{Q}_m = \text{diag}\left[10^{-2}, 10^{-2}, 10^{-2}, 10^{-2}, 10^{-2}, 10^{-2}\right]$.

Multiple LQG regulators were designed for the excitation force of subsection 3.6.1 in an iterative process for multiple $m_c r$. The simulation time is, as before, one hour. 'Tuning 1' is considered first and refers to a tuning of $\boldsymbol{Q}$ in which the required power demand in the swinging mode $P_{rms,sw}$ is equal to the one in the continuous rotation mode $P_{rms,rot}$, see (3.80) and the corresponding comments above and below. Note that in table 3.6, $Y = 0$ refers to the operation of the TRD in the swinging mode. For the ease of tuning, only the states q_x, q_θ and q_u were punished.

Table 3.6: Weighting matrix $\boldsymbol{Q}$ for LQG regulator design (units are dropped)

	q_x	$q_{\dot{x}}$	q_θ	$q_{\dot{\theta}}$	q_u	Power demand is considered when
Tuning 1	10,000	0	0.1	0	varied	$Y = 0$
Tuning 2	10,000	0	0.1	0	varied	$Y = 0$ and $A > 0.01\,\text{m}$

In the continuous rotation mode, the power demand does, contrary to in the swinging mode, not vary considerably for $m_c r = 0.0428\,\text{kgm}$, see figure 3.28. In the swinging mode, the variation of the power demand increases with the vibration amplitude. This is due to the fact that the working range of the rotors becomes wider with larger vibration amplitude, resulting in larger angular accelerations. Because of this, a second tuning scenario for $\boldsymbol{Q}$, 'tuning 2' is investigated. 'Tuning 2' considers the power demand in the swinging mode ($Y = 0$) only when $A > 0.01\,\text{m}$, see table 3.6. The reason for the two tunings will be further discussed in subsection 3.6.6.

Controllers $\boldsymbol{C}_s(s)$ for the swinging mode for both tunings and various $m_c r$ are then generated. $\boldsymbol{C}_s(s)$ can be represented by a 1-by-2 transfer matrix. The control effort for the swinging mode is then as given by

$$u_{a,s} = \boldsymbol{C}_s(s) \begin{bmatrix} x \\ \theta \end{bmatrix} \tag{3.90}$$

As for the continuous rotation mode, each rotor is controlled individually.

3.6.4 Switching between both modes of operation

Initially, the control algorithm operates in the swinging mode ($Y = 0$). The continuous rotation mode is activated if the following constraints are fulfilled:

$$A(t) > A_{on} \qquad \text{and} \qquad \varphi_{t,f}(t) \text{ passes } \varphi(t) \tag{3.91}$$

The TRD switches back to the swinging mode if

$$A(t) < A_{off} \qquad \text{and} \qquad \varphi(t) \text{ passes } \frac{1}{2}\pi\,(\theta(t) = 0) \tag{3.92}$$

The second constraints of (3.91) and (3.92), respectively, ensure that jerking motion is avoided when switching. When Y switches from zero to one or vice versa, one mode of

operation is required to be ramped down and the other one is required to be ramped up. To ensure a smooth ramp-up/down process between the individual and continuously calculated control efforts $u_{a,c}$ and $u_{a,s}$, the following switching algorithm is implemented when Y changes:

- The control effort of the mode of operation to be ramped down is calculated as follows. When Y switches, the control effort fed to the corresponding actuator is stored and the time variable t_{sw} is set to zero. From this instant on, the stored control effort is weighted with

$$w_{sw}(t_{sw}) = a_5 t_{sw}^5 + a_4 t_{sw}^4 + a_3 t_{sw}^3 + a_2 t_{sw}^2 + a_1 t_{sw} + a_0 \tag{3.93}$$

  The coefficients a_5, ..., a_0 can be calculated by inserting the boundary conditions

$$w_{sw}(t_{sw} = 0) = 1 \qquad \dot{w}_{sw}(t_{sw} = 0) = 0 \qquad \ddot{w}_{sw}(t_{sw} = 0) = 0 \tag{3.94}$$

$$w_{sw}(t_{sw} = T_{sw}) = 0 \qquad \dot{w}_{sw}(t_{sw} = T_{sw}) = 0 \qquad \ddot{w}_{sw}(t_{sw} = T_{sw}) = 0 \tag{3.95}$$

  in which T_{sw} denotes the switching time, into (3.93). With the chosen boundary conditions, a smooth ramp-up/down transition is guaranteed. Solving the system of equations yields a_5, ..., a_0. Once $t_{sw} > T_{sw}$, the weight function w_{sw} is set to zero. Setting the switching time to $0.25T_n$ often results in an adequately fast transition.

- The control effort of the mode of operation to be ramped up is weighted with zero until a switch is required. For $0 < t_{sw} < T_{sw}$, it is weighted with $1 - w_{sw}(t_{sw})$ up to $t_{sw} = T_{sw}$. For $t_{sw} > T_{sw}$, the control effort to be ramped up is weighted with one until the next switch is required.

Switching between both modes of operations as described above leads to a smooth motion of the rotors, even during switching. The energy consumption and the power demand during switching can be further improved by developing switching trajectories similar to the ramp up/down trajectories of subsection 2.5.2. However, the design of such switching trajectories is more complex than the design of the ramp-up/down trajectories of subsection 2.5.2. This is because the initial conditions, which were constant for the ramp-up process of subsection 2.5.2, are no longer constant, see e.g. (2.107); instead, as the swinging mode is used before switching into the continuous rotation mode, the initial conditions for each switching trajectory would vary. This requires adaptive trajectories which take varying initial conditions into account. This issue is not further studied in this work and is part of future work.

As discussed in subsection 3.6.3, the swinging mode will be tuned such that it requires the same power demand as in the continuous rotation mode. For the evaluation of the power demands, the switching time intervals are not taken into account. This is justified by the assumption that the actuators driving the rotors can be overloaded for short periods of time.

3.6.5 Free vibration tests

Controlled free vibration tests were performed with the tuning parameters shown in table 3.7 using 'tuning 1' with $q_u = 0.29$ and 'tuning 2' with $q_u = 0.63$. The results for the free vibration tests are shown in figure 3.30.

Table 3.7: Tuning for numerical and experimental validation

A_{on} [m]	A_{off} [m]	T_{sw} [s]	K_P [V/(rad)]	ω_P [(rad)/s]	ω_f/ω_n
0.015	0.010	0.3	1	70	0.428

The table is excited by hand until the continuous rotation mode is turned on and a displacement amplitude of approximately 0.02 m is reached, see subfigure A. The TRD remains in the continuous rotation mode until $t = 4.15\,\mathrm{s}$ at which the switching process is initiated. From $t = 4.45\,\mathrm{s}$, the TRD operates in the swinging mode. It becomes evident that the decay of the displacement amplitudes is much smaller when the TRD is operated in the swinging mode. Furthermore, in the continuous rotation mode, the displacement amplitudes decay approximately linearly, whereas exponentially in the swinging mode.

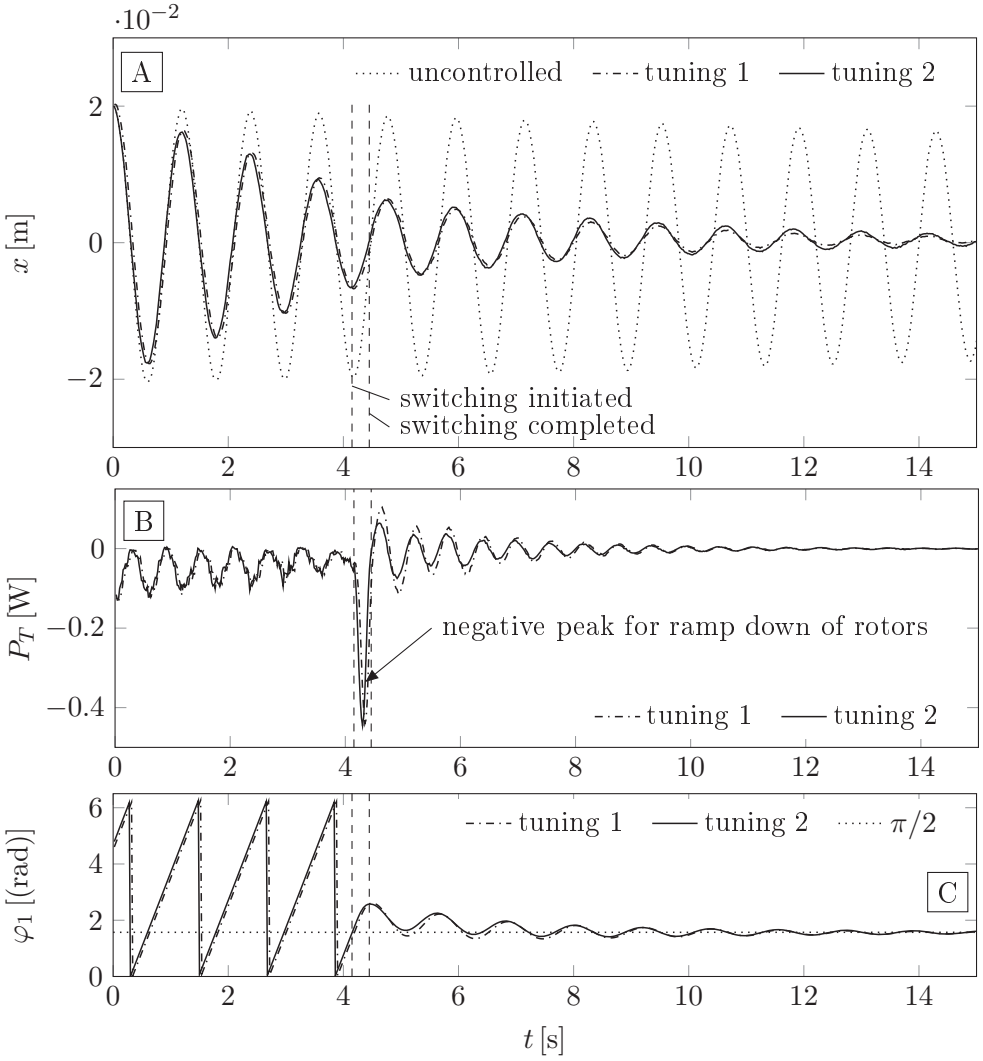

Figure 3.30: Free vibration test

The power curve is obtained as discussed in subsection 2.6.6. Before switching, the power curve is nearly always smaller than zero. During switching, a negative peak in the power curve occurs. This is because the actuators are required to brake the rotors. After switching into the swinging mode, positive as well as negative powers are required for accelerating

and decelerating the rotors about the position $\varphi = \pi/2$, see subfigure C.

Comparing 'tuning 1' and 'tuning 2', it can be seen that the power demand in the swinging mode for 'tuning 2' is slightly lower at the expense of a lower decay of the displacement amplitudes. Calculating the equivalent damping ratio as in subsection 2.6.1 for the time interval from $t = 4.7\,\mathrm{s}$ to $t = 13.0\,\mathrm{s}$ yields an equivalent damping ratio of $3.77\,\%$ for 'tuning 1' and of $2.91\,\%$ for 'tuning 2'. This corresponds to an increase of the equivalent damping ratio by a factor of approximately 13.9 for 'tuning 1' and 10.7 for 'tuning 2', see table 3.4.

3.6.6 Stochastically forced vibrations

The table is now disturbed by the stochastic excitation force of subsection 3.6.1 and the action of the TRD. This is done numerically and experimentally for various mass-radius control products for 'tuning 1' and 'tuning 2', see table 3.7. To reach the same power demand for both modes of operation for 'tuning 1' and 'tuning 2', q_u is set as shown in table 3.8.

Table 3.8: Evaluation of power demand and vibrations amplitude of numerical simulations and experiments

			numerical simulations			experiments		
$m_c r$ [kgm]	tuning	q_u	$P_{rms,rot}$ [W]	$P_{rms,sw}$ [W]	x_{std} [m]	$P_{rms,rot}$ [W]	$P_{rms,sw}$ [W]	x_{std} [m]
0.0428	1	0.29	0.056	0.056	0.0060	0.058	0.054	0.0058
	2	0.63	0.058	0.058	0.0064	0.062	0.060	0.0063
0.0310	1	0.40	0.042	0.042	0.0068	0.047	0.046	0.0072
	2	0.74	0.043	0.043	0.0072	0.047	0.045	0.0075
0.0214	1	0.48	0.032	0.032	0.0080	0.033	0.031	0.0078
	2	0.73	0.032	0.032	0.0082	0.034	0.033	0.0080
0.0155	1	0.47	0.025	0.025	0.0091	0.026	0.026	0.0097
	2	0.74	0.032	0.032	0.0082	0.026	0.025	0.0099
uncontrolled: $x_{std} = 0.0207\,\mathrm{m}$ (experiment)								

Several states are shown in figure 3.31 for 'tuning 1'.

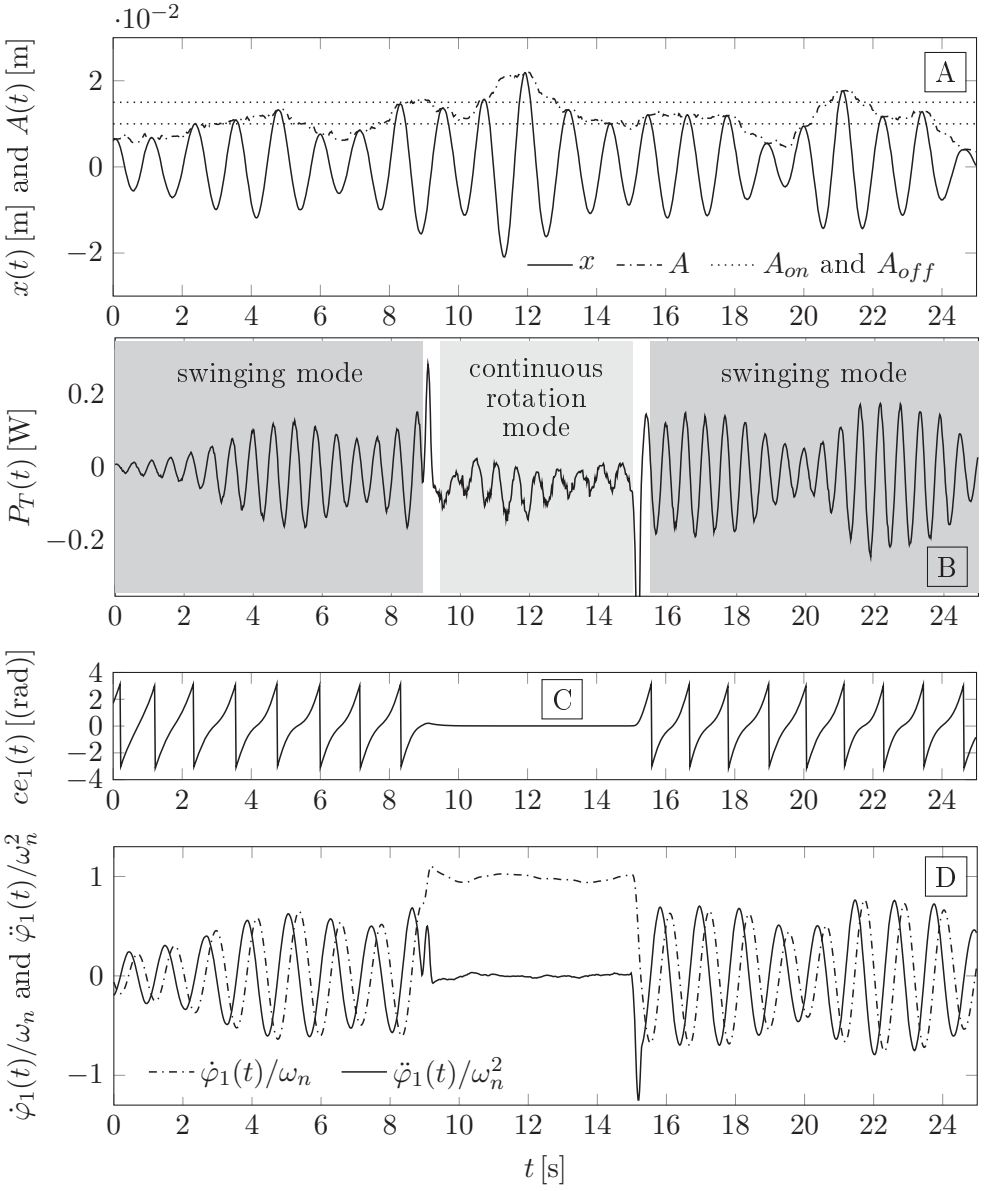

Figure 3.31: Several states of a test using 'tuning 1' and $m_c r = 0.0428\,\mathrm{kgm}$ in a chosen time sequence

From subfigure A, it can be seen that $A(t)$ exceeds the threshold A_{on} at $t \approx 8.5\,\mathrm{s}$, however, switching is not started before $t \approx 8.9\,\mathrm{s}$; this is due to the second constraint of (3.91). Afterwards, the TRD operates in the continuous rotation mode until $t \approx 15.0\,\mathrm{s}$. This can be seen from subfigure D. Furthermore, from subfigure C, it becomes evident that the control error for the first rotor is nearly zero in the continuous rotation mode, to be more precise, the absolute deviation from zero does not exceed $5.0 \cdot 10^{-3}\,(\mathrm{rad})$ in the time interval from $10.0\,\mathrm{s}$ to $15.0\,\mathrm{s}$.

Comparing the power demands in subfigure B, it seems apparent that the power demand in the swinging mode is larger than in the continuous rotation mode. However, for the complete evaluation duration of one hour, both power demands are approximately equal as required. It must be taken into consideration that in figure 3.31, only 25 s of the entire duration of one hour are shown. Time intervals such as the one from $t = 0\,\mathrm{s}$ to $t = 2.0\,\mathrm{s}$ in subfigure B dominate the evaluation of the power demand $P_{rms,sw}$ in the swinging mode. To avoid this, numerical and experimental tests were also performed with 'tuning 2' which also ensures that the power demand in both modes of operation are approximately equal; however, the power in the swinging mode is only considered when $A > 0.01\,\mathrm{m}$, see table 3.6.

The evaluation of the numerical simulations and the experiments with a duration of one hour is shown in table 3.8.

Comparing the numerical simulations with the experiments, it becomes evident that the computed values for the power demands as well as for the standard deviations of the controlled displacement responses are in accordance. The most relevant relations are discussed in the following using the data of the experiments.

The larger the mass-radius control product $m_c r$, the greater the damping performance, in other words, the higher the reductions of the standard deviations of the displacement response. However, with the largest $m_c r$ and 'tuning 1', the TRD operates for the majority of the time in the swinging mode, to be more precise, it operates only 183 s of the 3600s in the continuous rotation mode and 3351 s in the swinging mode. This is because for this case, when the TRD is operated in the swinging mode, it is tuned relatively aggressive (the penalty on q_u is lowest). This aggressive controller in combination with the large mass-radius control product $m_c r$ leads to the fact that the vibration amplitude $A(t)$ only rarely exceeds A_{on}. For this case, the standard deviation of the displacement is reduced from 0.0207 m to 0.0058 m. This corresponds to a reduction of 72 % ($(0.0207 - 0.0058)/0.0207$) and is reached with a mean power demand of 0.056 W ($0.5P_{rms,rot} + 0.5P_{rms,sw}$).

Now considering $m_c r = 0.0155\,\mathrm{kgm}$ and 'tuning 1', the TRD operates 1368 s in the continuous rotation mode and 2112 s in the swinging mode. The standard deviation of the displacement is reduced from 0.0207 m to 0.0097 m. This corresponds to a reduction of 53 %. However, it is reached with a power demand of 0.026 W; 54 % lower than the case considered in the previous paragraph.

The higher the mass-radius control product, the larger the damping performance. However, the higher the mass-radius control product is chosen, the larger the power demand on the actuators.

*

4

Oscillator with two degrees of freedom

4.1 Introduction

In chapter 2 and 3, the twin rotor damper was studied for an oscillator with a single translational degree of freedom. As described in section 2.1, in a preferred mode of operation, a harmonic control force working in a single direction can be created. The device presented in this chapter has a similar layout as the TRD. However, the control masses rotate about a single axis. Furthermore, the operational constraints will differ, to be more precise, small variations in the angular velocity of the rotors are allowed and wanted. This enables the control force to change direction in a plane. The idea for this modified version of the TRD (adapted TRD) arose while analyzing the horizontal motion of wind turbines and high-rise buildings [57, 58]. Such cantilever structures mainly vibrate in the first mode of vibration in two horizontal directions and their motion can be approximated by an oscillator with two translational degrees of freedom, which is introduced in section 4.3. Results of this chapter are also published in [59].

In this chapter, a control algorithm is derived for the operation of the adapted TRD in the continuous rotation mode. Subsequently, one control algorithm is tested experimentally for free vibrations and numerically for stochastically forced vibrations. Finally, the power demand of the adapted TRD is compared with the power demand of a conventional active mass damper.

4.2 Adapted twin rotor damper

As indicated in figure 4.1, the adapted TRD consists of two eccentrically rotating control masses, $0.5m_c$, each hinged by a mass-less rod with a length r to a single axis. Each rotor (control mass with mass-less rod) can move independently from the other and their motion is defined by the individual angular positions, $\varphi_1(t)$ and $\varphi_2(t)$. These two angular positions are measured from the positive Y-axis, see figure 4.1. In a preferred mode of operation, both rotors turn in opposite directions with a constant angular velocity $\dot{\varphi}$. As a result, each control mass creates a radial force given by (4.1).

$$f_r = \frac{m_c}{2} r \dot{\varphi}^2 \tag{4.1}$$

As shown in (4.2) and (4.3), the radial forces can be decomposed in X- and Y-direction.

$$f_{r,X}(t) = \frac{m_c}{2} r \dot{\varphi}^2 \left[-\sin\varphi_1(t) + \sin\varphi_2(t) \right] \tag{4.2}$$

$$f_{r,Y}(t) = \frac{m_c}{2} r \dot{\varphi}^2 \left[\cos\varphi_1(t) + \cos\varphi_2(t) \right] \tag{4.3}$$

The direction, φ_D, of the resultant force is given by:

$$\varphi_D = \frac{\varphi_1(t) - \varphi_2(t)}{2} \tag{4.4}$$

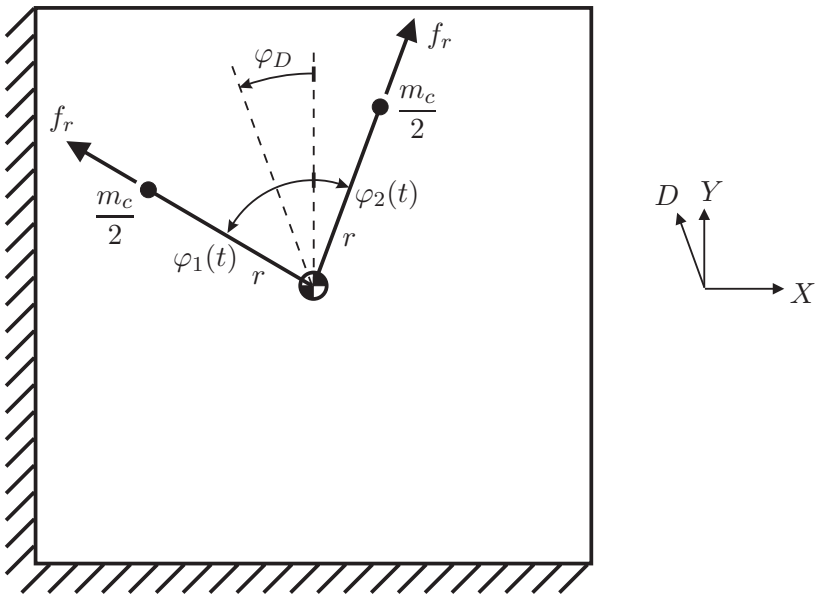

Figure 4.1: Adapted twin rotor damper for generating a directed control force [59]

Henceforth, this resultant force will be referred to as the control force. The direction of the control force is defined by the angle φ_D, which is measured counterclockwise from the positive Y-axis, see figure 4.1. Note that due to the equal and constant angular velocities of the rotors, φ_D is constant and a harmonic control force in D-direction is created.

By allowing small variations in the angular velocities of the rotors, the direction of the harmonic control force can be varied during operation. Consequently, φ_D becomes $\varphi_D(t)$. $\dot{\varphi}$ must then be replaced by $\dot{\varphi}_1(t)$ in (4.2) and by $\dot{\varphi}_2(t)$ in (4.3). Furthermore, tangential forces are additionally created. These tangential forces act perpendicular to the radial forces and are not denoted in figure 4.1. They are given by

$$f_{t,X}(t) = \frac{m_c}{2} r \left[\ddot{\varphi}_1(t) \cos\varphi_1(t) - \ddot{\varphi}_2(t) \cos\varphi_2(t)\right] \tag{4.5}$$

$$f_{t,Y}(t) = \frac{m_c}{2} r \left[\ddot{\varphi}_1(t) \sin\varphi_1(t) + \ddot{\varphi}_2(t) \sin\varphi_2(t)\right] \tag{4.6}$$

in which the indices t, X and t, Y indicate the tangential forces in X- and Y-direction. In the preferred mode of operation, the tangential forces are to be kept small in comparison to the radial forces.

If the angular accelerations of the rotors differ ($\ddot{\varphi}_1(t) \neq \ddot{\varphi}_2(t)$), moments are additionally generated. As the corresponding rotational degree of freedom is neglected, the presented control algorithm for the device is confined to systems without rotational vibrations. If the damping device is used for systems with rotational vibrations, the moments induced by the angular accelerations of the rotors must be considered.

4.3 Two degree of freedom oscillator

An oscillator with two translational degrees of freedom is considered, see figure 4.2. The rotational degree of freedom of this TDOF oscillator is neglected.

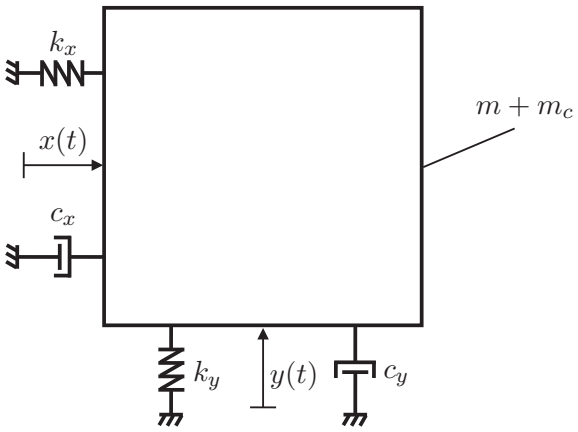

Figure 4.2: Oscillator with two translational degrees of freedom [59]

The free vibration of the two degree of freedom (TDOF) oscillator in $X-$ and $Y-$direction is described by

$$(m + m_c)\,\ddot{x}(t) + c_x\dot{x}(t) + k_x x(t) = 0 \qquad (m + m_c)\,\ddot{y}(t) + c_y\dot{y}(t) + k_y y(t) = 0 \tag{4.7}$$

where $m + m_c$ is the total mass of the oscillator, c is the damping coefficient and k is the stiffness. The indices of c and k in (4.7) indicate the degree of freedom. As before, the forces on the left-hand side of (4.7) will be referred to as system forces. The differential equations of (4.7) are linear and decoupled. However, if the damping device of section 4.2 with the radial and the tangential forces of (4.2), (4.3), (4.5) and (4.6) is applied, it will affect the motion in both directions and therefore couple these equations through $\varphi_1(t)$ and $\varphi_2(t)$ and their time derivatives.

The damped natural frequencies are given in (4.8).

$$\omega_{d,x} = \omega_{n,x}\sqrt{1 - \xi_x^2} \qquad \omega_{d,y} = \omega_{n,y}\sqrt{1 - \xi_y^2} \tag{4.8}$$

where $\omega_{n,x}$ and $\omega_{n,y}$ are the natural (circular) frequencies, see (4.9), and ξ_x and ξ_y are the damping ratios given in (4.10) [25].

$$\omega_{n,x} = \sqrt{\frac{k_x}{m + m_c}} \qquad \omega_{n,y} = \sqrt{\frac{k_y}{m + m_c}} \tag{4.9}$$

$$\xi_x = \frac{c_x}{2\,(m + m_c)\,\omega_{n,x}} \qquad \xi_y = \frac{c_y}{2\,(m + m_c)\,\omega_{n,y}} \tag{4.10}$$

In the following, it is assumed that the natural frequencies in $X-$ and $Y-$direction coincide, see (4.11). It follows that $k_x = k_y$.

$$\omega_n = \omega_{n,x} = \omega_{n,y} \tag{4.11}$$

By doing this, the control-loop developed hereinafter is confined to such systems. Furthermore, the following derivations are made under the assumption that inherent damping is not present, see (4.12).

$$\xi_x = \xi_y = 0 \tag{4.12}$$

The presence of inherent damping only makes the derivations more complex without producing additional insight.

4.4 Free vibration

4.4.1 Vibration phases of TDOF oscillator

To study the motion path of the TDOF oscillator, it is illustrative to consider the vibration phase and the vibration amplitude in both directions, see figure 4.3.

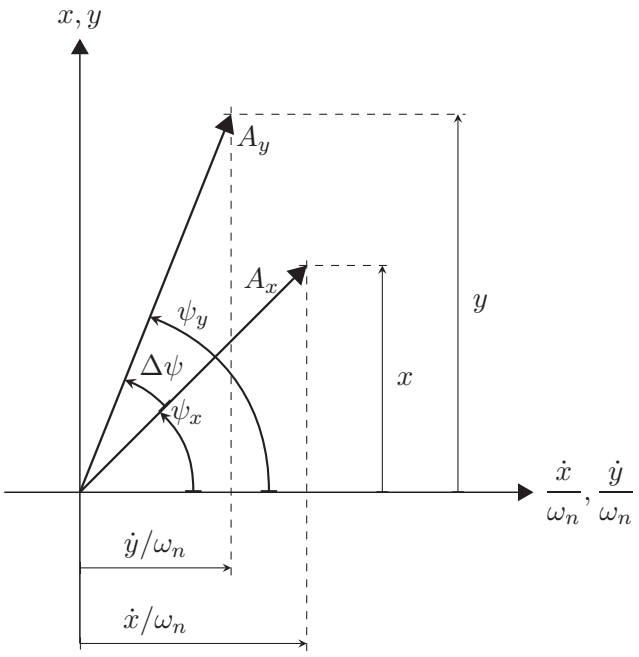

Figure 4.3: Vibration phases and vibration amplitudes of both directions

The vibration amplitudes, $A_x(t)$ and $A_y(t)$, and the vibration phases, $\psi_x(t)$ and $\psi_y(t)$, are given by

$$A_x(t) = \sqrt{x(t)^2 + \left[\frac{\dot{x}(t)}{\omega_n}\right]^2} \qquad A_y(t) = \sqrt{y(t)^2 + \left[\frac{\dot{y}(t)}{\omega_n}\right]^2} \tag{4.13}$$

$$\psi_x(t) = \text{atan2}\left[x(t), \frac{\dot{x}(t)}{\omega_n}\right] \qquad \psi_y(t) = \text{atan2}\left[y(t), \frac{\dot{y}(t)}{\omega_n}\right] \tag{4.14}$$

The phase difference, $\Delta\psi(t)$, is given by

$$\Delta\psi(t) = \psi_y(t) - \psi_x(t) \tag{4.15}$$

Considering a free vibration, the vectors A_x and A_y of figure 4.3 rotate counterclockwise with a constant length and an angular velocity ω_n. Consequently, for free vibrations, the phase difference $\Delta\psi$ is constant.

Figure 4.4 shows various motion paths of the TDOF oscillator for different initial conditions, see (4.16).

$$x(t=0) = x_0 \qquad y(t=0) = y_0 \qquad \dot{x}(t=0) = \dot{x}_0 \qquad \dot{y}(t=0) = \dot{y}_0 \tag{4.16}$$

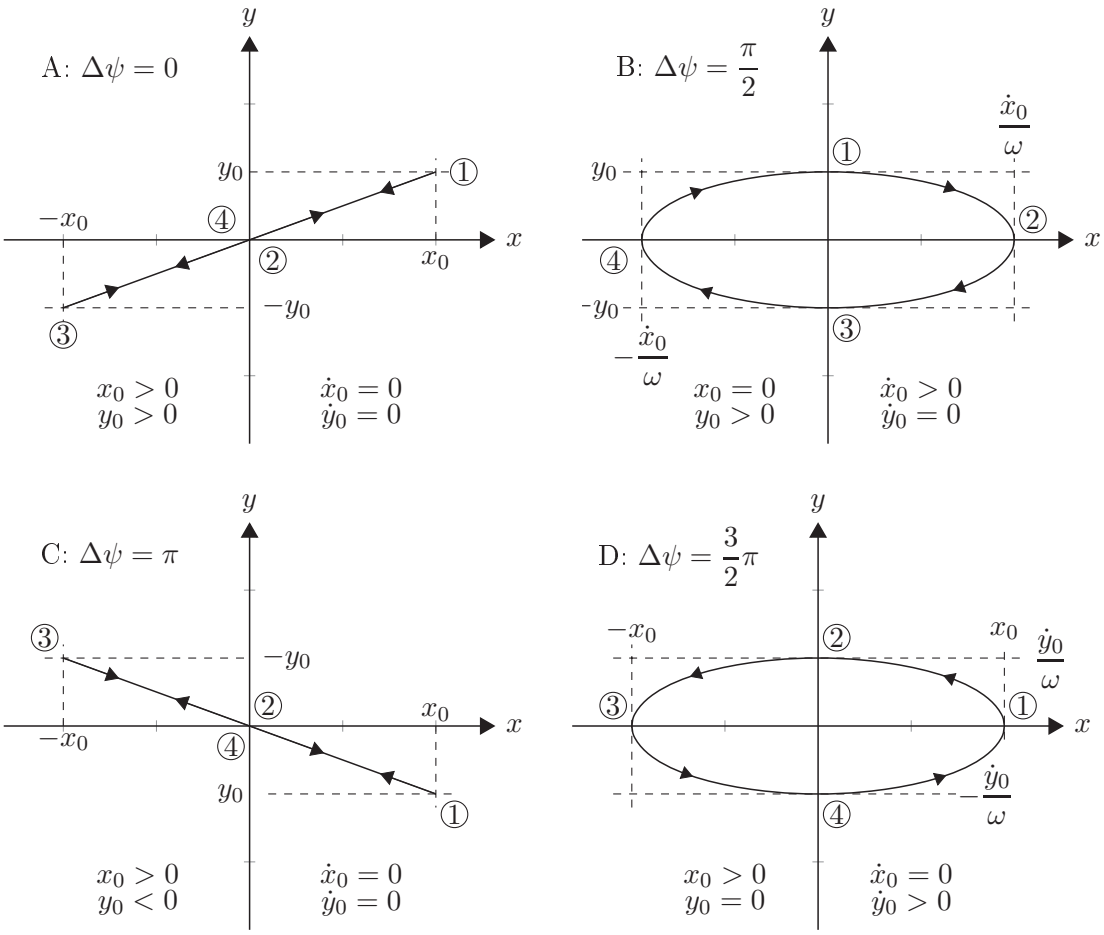

Figure 4.4: Free vibration motion paths of TDOF oscillator for particular initial conditions

As free vibrations without damping are considered and the natural frequencies in both directions coincide, the initial conditions of (4.16) determine the phase difference $\Delta\psi$. In figure 4.4, the circled numbers indicate the progress within one vibration cycle, where ①, ②, ③ and ④ stand for $t = nT$, $t = 0.25T + nT$, $t = 0.5T + nT$ and $t = 0.75T + nT$, respectively, in which n is an integer number.

If $\Delta\psi = 0$, see figure 4.4/A, the vibrations in X- and Y-direction are in phase. Therefore, the displacement and velocity peaks coincide (occur simultaneously). The TDOF oscillator moves along a line through the origin and the second and fourth quadrants. If $\Delta\psi = \pi$, see figure 4.4/C, this line goes through the origin and the second and fourth quadrant. If $\Delta\psi = 0.5\pi$, see figure 4.4/B, the motion path forms an ellipse moving in clockwise direction. The TDOF oscillator moves clockwise for $0 < \Delta\psi < \pi$. In contrast to this, it moves counterclockwise for $\pi < \Delta\psi < 2\pi$ as shown in figure 4.4/D.

From figure 4.4, it becomes evident that the TDOF oscillator forms an elliptical motion path. Furthermore, no relation between the phase difference $\Delta\psi$ and the major axis (introduced and defined in subsection 4.4.2) has been found. This becomes apparent by considering figure 4.4/A and assuming different values for x_0 and y_0. The larger x_0/y_0, the more the motion line converges to the X-axis and vice versa. When considering different ratios for x_0/y_0, the direction of the major axis changes, but $\Delta\psi$ remains constant.

4.4.2 Major axis of ellipse

If the TDOF oscillator of figure 4.2 performs free vibrations, the motion path of the point, O (TDOF oscillator), forms an ellipse in the $X-Y$ plane, see figure 4.5.

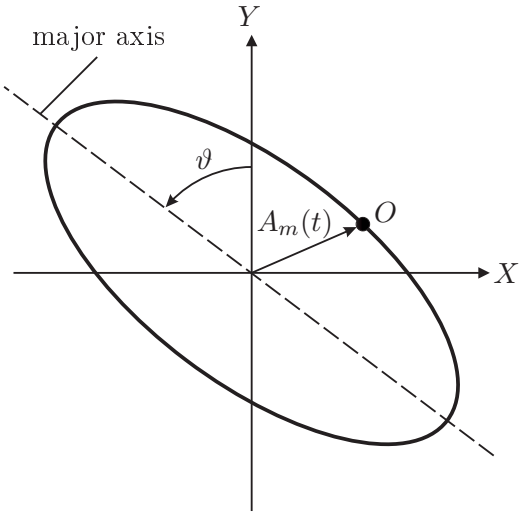

Figure 4.5: Major axis and its direction [59]

The largest distance between two antipodal points of an ellipse defines the so-called major axis, see figure 4.5 [60]. The direction of the major axis (DOMA) is defined by the angle, $\vartheta(t)$, which is constant when considering free vibrations. Two methods to compute the DOMA are proposed in this work; one in this subsection, another one at the end of subsection 4.6.2.

The amplitude, $A_m(t)$, is defined as the vector connecting the origin with the point O, see figure 4.5 and (4.17).

$$A_m(t) = \sqrt{x(t)^2 + y(t)^2} \tag{4.17}$$

The DOMA can be calculated by determining the maximum of $A_m(t)$. Assuming the free vibrations of (4.7), the displacement responses are as given in (4.18) with the initial conditions of (4.16) [1, 25].

$$x(t) = x_0 \cos(\omega_n t) + \frac{\dot{x}_0}{\omega_n} \sin(\omega_n t) \qquad y(t) = y_0 \cos(\omega_n t) + \frac{\dot{y}_0}{\omega_n} \sin(\omega_n t) \tag{4.18}$$

Inserting (4.18) into (4.17) and forming the derivative with respect to time yields (4.19)

$$\frac{\mathrm{d}A_m}{\mathrm{d}t} = \frac{\left[x_0 c_{\omega_n} + \frac{\dot{x}_0}{\omega_n} s_{\omega_n}\right]\left[-x_0 \omega_n s_{\omega_n} + \dot{x}_0 c_{\omega_n}\right] + \left[y_0 c_{\omega_n} + \frac{\dot{y}_0}{\omega_n} s_{\omega_n}\right]\left[-y_0 \omega_n s_{\omega_n} + \dot{y}_0 c_{\omega_n}\right]}{\sqrt{\left[x_0 c_{\omega_n} + \frac{\dot{x}_0}{\omega_n} s_{\omega_n}\right]^2 + \left[y_0 c_{\omega_n} + \frac{\dot{y}_0}{\omega_n} s_{\omega_n}\right]^2}} \tag{4.19}$$

using the substitutions of (4.20).

$$s_{\omega_n}(t) = \sin(\omega_n t) \qquad c_{\omega_n}(t) = \cos(\omega_n t) \tag{4.20}$$

Equating (4.19) to zero and solving for t yields the times t_1 and t_2 at which $A_m(t)$ is maximum or minimum. These times $t_{1/2}$ are shown in (4.21) with the substitutions of (4.22)

and (4.23).

$$t_{1/2} = \frac{1}{\omega_n}\text{atan}\left[\frac{-\omega_n^2 x_0^2 + \dot{x}_0^2 - \omega_n^2 y_0^2 + \dot{y}_0^2 \pm \sqrt{\Xi_3^2 + \Xi_4^2 + \Xi_5^2 - \Xi_6^2 + \Xi_7}}{2\left(\omega_n x_0 \dot{x}_0 + \omega_n y_0 \dot{y}_0\right)}\right] \tag{4.21}$$

$$\Xi_3 = \omega_n^2 y_0^2 + \dot{y}_0^2 \qquad \Xi_4 = \omega_n^2 x_0^2 + \dot{x}_0^2 \qquad \Xi_5 = \sqrt{2}\omega_n^2 x_0 y_0 + \sqrt{2}\dot{x}_0 \dot{y}_0 \tag{4.22}$$

$$\Xi_6 = \sqrt{2}\omega_n\left(x_0 \dot{y}_0 + y_0 \dot{x}_0\right) \qquad \Xi_7 = 8\omega_n^2 x_0 y_0 \dot{x}_0 \dot{y}_0 \tag{4.23}$$

The solutions for t_1 and t_2 repeat in π/ω_n, see (4.21); in other words, each type of extrema occurs twice per vibration period. To check whether t_1 or t_2 corresponds to the maximum or minimum, both time values are inserted into (4.18) and subsequently into (4.17). This gives $A_m(t_1)$ and $A_m(t_2)$. If $A_m(t_1) > A_m(t_2)$, t_1 corresponds to the major axis and t_2 to the minor axis; otherwise, vice versa. The DOMA can then be computed as given in (4.24).

$$\vartheta = \begin{cases} -\text{atan}\dfrac{x_0\cos\left(\omega_n t_1\right) + \dfrac{\dot{x}_0}{\omega_n}\sin\left(\omega_n t_1\right)}{y_0\cos\left(\omega_n t_1\right) + \dfrac{\dot{y}_0}{\omega_n}\sin\left(\omega_n t_1\right)} & \text{for} \quad A_m(t_1) > A_m(t_2) \\ -\text{atan}\dfrac{x_0\cos\left(\omega_n t_2\right) + \dfrac{\dot{x}_0}{\omega_n}\sin\left(\omega_n t_2\right)}{y_0\cos\left(\omega_n t_2\right) + \dfrac{\dot{y}_0}{\omega_n}\sin\left(\omega_n t_2\right)} & \text{for} \quad A_m(t_1) < A_m(t_2) \\ \text{undefined} & \text{for} \quad A_m(t_1) = A_m(t_2) \end{cases} \tag{4.24}$$

If $A_m(t_1) = A_m(t_2)$, the TDOF oscillator performs circular motion, the DOMA is undefined and $A_m(t)$ is constant. This issue is discussed further in the following.

4.5 Target angular positions using an energy approach

4.5.1 Open-loop configuration

In subsection 2.3.6, two assumptions used in section 2.3 were emphasized. First, small inherent damping can be neglected. Second, by assuming a free vibration response of a SDOF oscillator and minimizing the work that the control force would perform on the motion of the SDOF oscillator, adequate results for the target angular position (TAP) are derived. The same assumptions are used in this subsection for the derivation of the TAPs for the vibration control of the TDOF oscillator.

A continuous rotor motion of the rotors is assumed

$$\varphi_1(t) = \omega_n t + \varphi_{0,1} \qquad \varphi_2(t) = \omega_n t + \varphi_{0,2} \tag{4.25}$$

in which $\varphi_{0,1}$ and $\varphi_{0,2}$ refer to the initial angular positions of the rotors. Note that the angular velocity of the rotors was set to the natural (circular) frequency of the TDOF oscillator. Assuming additionally a free vibration response of the TDOF oscillator, its velocity response can be derived by taking the time derivative of (4.18):

$$\dot{x}(t) = -x_0\omega_n \sin\left(\omega_n t\right) + \dot{x}_0 \cos\left(\omega_n t\right) \qquad \dot{y}(t) = -y_0\omega_n \sin\left(\omega_n t\right) + \dot{y}_0 \cos\left(\omega_n t\right) \tag{4.26}$$

The power of the control force in each direction is derived by multiplying the radial force components of (4.2) and (4.3) with the corresponding velocities of (4.26)

$$P_x(t) = f_{r,X}(t)\dot{x}(t) \qquad P_y(t) = f_{r,Y}(t)\dot{y}(t) \tag{4.27}$$

Note that the tangential forces vanish as the angular velocities of the rotors are assumed as constant. Integrating (4.27) from $t = 0$ to $t = 2\pi l/\omega_n$ yields the work done by the control force in each direction for l vibration periods, see (4.28) and (4.29).

$$W_{c,x} = \int_0^{\frac{2l\pi}{\omega_n}} f_{r,X}(t)\dot{x}(t)\mathrm{d}t = \frac{1}{2}m_c r l\omega_n\pi\left[\dot{x}_0(\sin\varphi_{0,2} - \sin\varphi_{0,1}) + x_0\omega_n(\cos\varphi_{0,1} - \cos\varphi_{0,2})\right] \tag{4.28}$$

$$W_{c,y} = \int_0^{\frac{2l\pi}{\omega_n}} f_{r,Y}(t)\dot{y}(t)\mathrm{d}t = \frac{1}{2}m_c r l\omega_n\pi\left[\dot{y}_0(\cos\varphi_{0,1} + \cos\varphi_{0,2}) + y_0\omega_n(\sin\varphi_{0,1} + \sin\varphi_{0,2})\right] \tag{4.29}$$

The total work done by the control force is given by the sum:

$$W_c = W_{c,x} + W_{c,y} \tag{4.30}$$

(4.30) is now seen as a function of the initial angular positions $\varphi_{0,1}$ and $\varphi_{0,2}$. The extrema of (4.30) are identified by setting the partial derivatives with respect to $\varphi_{0,1}$ and $\varphi_{0,2}$ equal to zero, see the following equations:

$$\frac{\partial W_c}{\partial\varphi_{0,1}} = \frac{1}{2}m_c r l\omega_n\pi\left(-\dot{x}_0\cos\varphi_{0,1} - x_0\omega_n\sin\varphi_{0,1} - \dot{y}_0\sin\varphi_{0,1} + y_0\omega_n\cos\varphi_{0,1}\right) = 0 \tag{4.31}$$

$$\frac{\partial W_c}{\partial\varphi_{0,2}} = \frac{1}{2}m_c r l\omega_n\pi\left(\dot{x}_0\cos\varphi_{0,2} + x_0\omega_n\sin\varphi_{0,2} - \dot{y}_0\sin\varphi_{0,2} + y_0\omega_n\cos\varphi_{0,2}\right) = 0 \tag{4.32}$$

Solving these equations for $\varphi_{0,1}$ and $\varphi_{0,2}$ gives:

$$\varphi_{0,1} = \operatorname{atan}\frac{y_0\omega_n - \dot{x}_0}{\dot{y}_0 + x_0\omega_n} \qquad\qquad \varphi_{0,2} = \operatorname{atan}\frac{y_0\omega_n + \dot{x}_0}{\dot{y}_0 - x_0\omega_n} \tag{4.33}$$

To identify the type of extremum, it is required to calculate the second partial derivative of W_c with respect to $\varphi_{0,1}$ and $\varphi_{0,2}$:

$$\frac{\partial^2 W_c}{\partial\varphi_{0,1}^2} = \frac{1}{2}m_c r l\omega_n\pi\left(\dot{x}_0\sin\varphi_{0,1} - x_0\omega_n\cos\varphi_{0,1} - \dot{y}_0\cos\varphi_{0,1} - y_0\omega_n\sin\varphi_{0,1}\right) \tag{4.34}$$

$$\frac{\partial^2 W_c}{\partial\varphi_{0,2}^2} = \frac{1}{2}m_c r l\omega_n\pi\left(-\dot{x}_0\sin\varphi_{0,2} + x_0\omega_n\cos\varphi_{0,2} - \dot{y}_0\cos\varphi_{0,2} - y_0\omega_n\sin\varphi_{0,2}\right) \tag{4.35}$$

By inserting the solutions of (4.33) into the respective second derivatives of (4.34) and (4.35), it can be determined if the extremum is a minimum or maximum. If the second derivative is smaller than zero, the extremum is a maximum. Note that the solutions for $\varphi_{0,1}$ and $\varphi_{0,2}$ of (4.33) repeat in π. Therefore, to assure that both rotors start with the (optimal) initial angular position corresponding to damping (the work done by the control force is minimal), π needs to be added if the respective second partial derivative is smaller than zero. Hence, the optimal initial angular positions $\varphi_{0,1,opt}$ and $\varphi_{0,2,opt}$ are as follows:

$$\varphi_{0,1,opt} = \begin{cases} \varphi_{0,1} & \text{for } \frac{\partial^2 W_c}{\partial\varphi_{0,1}^2} > 0 \\ \varphi_{0,1} + \pi & \text{for } \frac{\partial^2 W_c}{\partial\varphi_{0,1}^2} < 0 \end{cases} \qquad \varphi_{0,2,opt} = \begin{cases} \varphi_{0,2} & \text{for } \frac{\partial^2 W_c}{\partial\varphi_{0,2}^2} > 0 \\ \varphi_{0,2} + \pi & \text{for } \frac{\partial^2 W_c}{\partial\varphi_{0,2}^2} < 0 \end{cases} \tag{4.36}$$

Applying the radial forces of (4.2) and (4.3) to the free vibrations of the TDOF oscillator, the equations of motion can be formed

$$\ddot{x}(t) + \omega_n^2 x(t) = \frac{1}{2}\mu_c r\omega_n^2\left[\sin\left(\omega_n t + \varphi_{0,2,opt}\right) - \sin\left(\omega_n t + \varphi_{0,1,opt}\right)\right] \tag{4.37}$$

$$\ddot{y}(t) + \omega_n^2 y(t) = \frac{1}{2}\mu_c r \omega_n^2 \left[\cos\left(\omega_n t + \varphi_{0,2,opt}\right) + \cos\left(\omega_n t + \varphi_{0,1,opt}\right)\right] \tag{4.38}$$

with μ_c of (2.12). The optimal initial angular positions according to (4.36) are utilized for the open-loop configuration. Solving these equations of motion for the displacement responses of the TDOF oscillator yields the displacement responses, see (4.39) and (4.40).

$$\begin{aligned} x(t) = \frac{\dot{x}_0}{\omega_n}\sin\left(\omega_n t\right) + x_0\cos\left(\omega_n t\right) + \frac{\mu_c r}{4}\{ & \sin\left(\omega_n t\right)\left(\cos\varphi_{0,2,opt} - \cos\varphi_{0,1,opt}\right) + ... \\ & \omega_n t[\cos\left(\omega_n t + \varphi_{0,1,opt}\right) - ... \\ & \cos\left(\omega_n t + \varphi_{0,2,opt}\right)]\} \end{aligned} \tag{4.39}$$

$$\begin{aligned} y(t) = \frac{\dot{y}_0}{\omega_n}\sin\left(\omega_n t\right) + y_0\cos\left(\omega_n t\right) + \frac{\mu_c r}{4}\{ & -\sin\left(\omega_n t\right)\left(\sin\varphi_{0,2,opt} + \sin\varphi_{0,1,opt}\right) + ... \\ & \omega_n t\left[\sin\left(\omega_n t + \varphi_{0,2,opt}\right) + \sin\left(\omega_n t + \varphi_{0,1,opt}\right)\right]\} \end{aligned} \tag{4.40}$$

Figure 4.6 shows a trajectory of the TDOF oscillator, see (4.39) and (4.40).

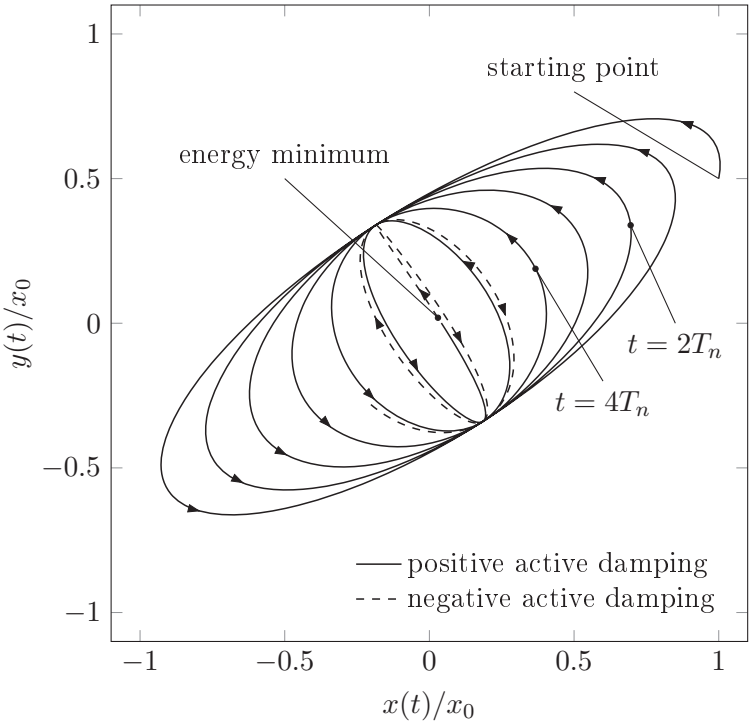

Figure 4.6: Open-loop trajectory of the TDOF oscillator with $\mu_c r/x_0 = 0.06$, $y_0 = 0.5x_0$, $\dot{y}_0 = 0.5x_0\omega_n$ and $\dot{x}_0 = 0.1x_0\omega_n$ [61]

All initial states are normalized with respect to the initial displacement x_0. The unitless ratio $\mu_c r/x_0$ determines the decay rate. The higher this ratio, the larger the decay becomes. The arrows depict the direction in which the TDOF oscillator is moving. The solid line shows the TDOF oscillator being effectively damped (positive active damping). Note that the direction of the control force does not change in time. It acts in the direction of the major axis corresponding to the time-point $t = 0$. Therefore, it damps the motion along the major axis from $t = 0$ until approximately $t = 4T_n$, the time-point at which the

motion becomes circular. The motion is then further damped until approximately $t = 6T_n$, where an energy minimum is reached. After this time-point, the motion is re-excited.

From figure 4.6, it becomes evident that when using the optimal initial angular positions, the control force acts, as desired, along the major axis from $t = 0$ until the motion becomes circular. It is evident from figure 4.6 that the open-loop configuration succeeds to identify the initial major axis and damps this motion. However, after reaching a circular motion path, the control force proceeds to act along the initial direction of the major axis.

4.5.2 Closed-loop configuration

A closed-loop control algorithm is now derived. To continuously compute the TAPs for the rotors, the initial states of (4.33) and (4.36) are replaced by continuous states, see (4.41) and (4.42).

$$\varphi_{t,1}(t) = \operatorname{atan}\frac{y(t)\omega_n - \dot{x}(t)}{\dot{y}(t) + x(t)\omega_n} \qquad \varphi_{t,2}(t) = \operatorname{atan}\frac{y(t)\omega_n + \dot{x}(t)}{\dot{y}(t) - x(t)\omega_n} \tag{4.41}$$

$$\varphi_{t,1,opt} = \begin{cases} \varphi_{t,1} & \text{for } \frac{\partial^2 W_c}{\partial \varphi_{t,1}^2} > 0 \\ \varphi_{t,1} + \pi & \text{for } \frac{\partial^2 W_c}{\partial \varphi_{t,1}^2} < 0 \end{cases} \qquad \varphi_{t,2,opt} = \begin{cases} \varphi_{t,2} & \text{for } \frac{\partial^2 W_c}{\partial \varphi_{t,2}^2} > 0 \\ \varphi_{t,2} + \pi & \text{for } \frac{\partial^2 W_c}{\partial \varphi_{t,2}^2} < 0 \end{cases} \tag{4.42}$$

Note that in (4.42), the time dependencies of the TAPs $\varphi_{t,1}$, $\varphi_{t,2}$, $\varphi_{t,1,opt}$ and $\varphi_{t,2,opt}$ and of the energy derivatives are not indicated. Within the closed-loop configuration, all these signals are continuously updated. $\varphi_{t,1,opt}$ and $\varphi_{t,2,opt}$ are then fed to a closed-loop angular position control, ensuring that these TAPs are tracked.

Numerical simulations were performed using the closed-loop configuration. They are presented in [61] and summarized in the following. When tracking the TAPs of (4.42), the adapted TRD operates as long in the continuous rotation mode as the TDOF oscillator performs an elliptical motion. In this case, the control force acts along the major axis and the velocity component of the TDOF oscillator along the major axis is in anti-phase to the control force. Once the motion of the TDOF oscillator becomes circular, the TAPs of (4.42) become discontinuous; in other words, the shape of the TAP strongly deviates from the desired saw-tooth like shape. As a result, the rotors stop rotating with a constant angular velocity and the tangential forces become large in comparison to the radial forces. Therefore, the control algorithm of [61] fails when the motion of the TDOF oscillator becomes circular. To cope with this issue, the DOMA can be fed through a low-pass filter. An enhanced damping strategy ensuring this is presented in section 4.6.

The damping strategy presented in this section is applicable when the TDOF oscillator vibrates along a line through the origin, to be more precise, when the phase difference $\Delta\psi$ equals zero or π, see figure 4.4.

4.6 Enhanced damping strategy

4.6.1 Damping strategy

In the preferred mode of operation, maximum damping action is achieved if the harmonic control force counteracts the velocity along the major axis. To reach this goal, the control algorithm has to ensure that firstly the direction of the harmonic control force coincides with the major axis of the ellipse and secondly the harmonic control force is in anti-phase

to the velocity along the major axis. The control algorithm presented in the following was presented in [59].

4.6.2 Direction of major axis

Considering a TDOF oscillator under a stochastic excitation force or the forces of the damping device, the DOMA can change in time. The approximated time it takes $A_m(t)$ to reach the next extrema, see figure 4.5, can be computed continuously by replacing the initial states of (4.21) by continuous states, see (4.43) to (4.45), in which the index a refers to signals which are continuously updated.

$$t_{a,1/a,2} = \frac{1}{\omega_n}\text{atan}\left[\frac{-\omega_n^2 x_a^2 + \dot{x}_a^2 - \omega_n^2 y_a^2 + \dot{y}_a^2 \pm \sqrt{\Xi_{a,3}^2 + \Xi_{a,4}^2 + \Xi_{a,5}^2 - \Xi_{a,6}^2 + \Xi_{a,7}}}{2\left(\omega_n x_a \dot{x}_a + \omega_n y_a \dot{y}_a\right)}\right] \tag{4.43}$$

$$\Xi_{a,3} = \omega_n^2 y_a^2 + \dot{y}_a^2 \qquad \Xi_{a,4} = \omega_n^2 x_a^2 + \dot{x}_a^2 \qquad \Xi_{a,5} = \sqrt{2}\omega_n^2 x_a y_a + \sqrt{2}\dot{x}_a \dot{y}_a \tag{4.44}$$

$$\Xi_{a,6} = \sqrt{2}\omega_n \left(x_a \dot{y}_a + y_a \dot{x}_a\right) \qquad \Xi_{a,7} = 8\omega_n^2 x_a y_a \dot{x}_a \dot{y}_a \tag{4.45}$$

This is justified by the assumption that the system forces primarily dictate the motion.

To check whether $t_{a,1}$ or $t_{a,2}$ corresponds to the maximum or minimum, the initial conditions of (4.18) are also replaced by continuous states, see (4.46) and (4.47) with the time values of (4.43).

$$x_{a,1} = x_a \cos\left(\omega_n t_{a,1}\right) + \frac{\dot{x}_a}{\omega_n}\sin\left(\omega_n t_{a,1}\right) \qquad y_{a,1} = y_a \cos\left(\omega_n t_{a,1}\right) + \frac{\dot{y}_a}{\omega_n}\sin\left(\omega_n t_{a,1}\right) \tag{4.46}$$

$$x_{a,2} = x_a \cos\left(\omega_n t_{a,2}\right) + \frac{\dot{x}_a}{\omega_n}\sin\left(\omega_n t_{a,2}\right) \qquad y_{a,2} = y_a \cos\left(\omega_n t_{a,2}\right) + \frac{\dot{y}_a}{\omega_n}\sin\left(\omega_n t_{a,2}\right) \tag{4.47}$$

By inserting the state points $(x_{a,1}, y_{a,1})$ and $(x_{a,2}, y_{a,2})$ corresponding to the first and second extremum into (4.48),

$$A_{a,1} = \sqrt{x_{a,1}^2 + y_{a,1}^2} \qquad A_{a,2} = \sqrt{x_{a,2}^2 + y_{a,2}^2} \tag{4.48}$$

the length of the vectors $A_{a,1}$ and $A_{a,2}$ are obtained. If $A_{a,1} > A_{a,2}$, the first extremum $(x_{a,1}, y_{a,1})$ corresponds to the major axis; otherwise, $(x_{a,2}, y_{a,2})$, see (4.49). The unfiltered DOMA, $\vartheta^*(t)$ is then given by

$$\vartheta^*(t) = \begin{cases} \text{atan}\dfrac{-x_{a,1}}{y_{a,1}} & \text{for} \quad A_{a,1} \geq A_{a,2} \\ \text{atan}\dfrac{-x_{a,2}}{y_{a,2}} & \text{for} \quad A_{a,1} < A_{a,2} \end{cases} \tag{4.49}$$

In (4.49) and in contrast to (4.24), vectors with equal length ($A_{a,1} = A_{a,2}$) are assigned to the first case. This assignment can be done arbitrarily as, in practice, the state $A_{a,1} = A_{a,2}$ will most likely not occur and if it occurs, it will only exist for a short period of time. Due to the filter presented in the following subsection, this arbitrary assignment will not affect the control algorithm.

The DOMA can be computed in an alternative way. By replacing $\varphi_1(t)$ and $\varphi_2(t)$ in (4.4) by $\varphi_{0,1,opt}$ and $\varphi_{0,2,opt}$ of (4.36), respectively, the DOMA can be computed by (4.50), which is further discussed below and in which the additional index al stands for alternative.

$$\vartheta_{al}^*(t) = \frac{1}{2}\left[\varphi_{1,opt}(t) - \varphi_{2,opt}(t)\right] \tag{4.50}$$

In (4.50), the initial states $\varphi_{0,1,opt}$ and $\varphi_{0,2,opt}$ were replaced by continuous states $\varphi_{1,opt}(t)$ and $\varphi_{2,opt}(t)$. To compute $\varphi_{1,opt}(t)$ and $\varphi_{2,opt}(t)$ according to (4.36), (4.33), (4.34) and (4.35) are used. In these equations, the initial states (x_0, y_0, $\dot{x}_0$, $\dot{y}_0$) must be replaced by continuous states ($x(t)$, $y(t)$, $\dot{x}(t)$, $\dot{y}(t)$). Furthermore, the energy derivatives in (4.34), (4.35) and (4.36) are also continuously updated.

4.6.3 Dynamics of DOMA

In the following, the DOMA according to (4.49) is filtered to prevent sudden changes. Considering an elliptical motion path of the TDOF oscillator and a control force which acts in anti-phase to the velocity along the major axis, the harmonic control force would damp the motion of the TDOF oscillator along the major axis until the motion of the TDOF oscillator becomes circular, after which, the harmonic control force would be required to suddenly change its direction by 0.5π; this results in large tangential forces in comparison to the radial forces. To prevent this undesired outcome, the DOMA is filtered. A filter as shown in figure 4.7 is used.

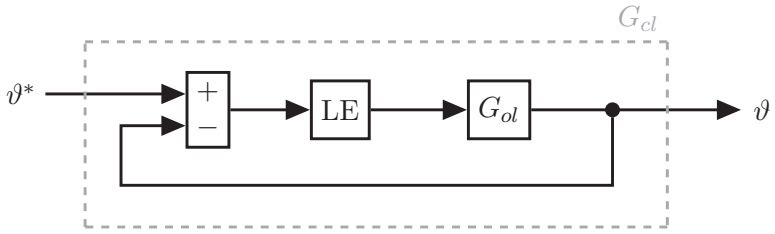

Figure 4.7: Filtering of direction of major axis [59]

Due to the periodicity of (4.49) in π, an infinite number of solutions for the unfiltered DOMA, $\vartheta^*(t)$, exits. To drive $\vartheta^*(t)$ to the next possible solution, the difference between the filtered, $\vartheta(t)$, and the unfiltered DOMA $\vartheta^*(t)$ is fed into the block 'LE', which adds multiples of π to limit the difference to values between -0.5π and 0.5π. This ensures that the DOMA is driven to the next possible solution. For the closed-loop dynamics, a second-order transfer function $G_{cl}(s)$ from $\vartheta^*(t)$ to $\vartheta(t)$ as shown in (4.51) was chosen

$$G_{cl}(s) = \frac{\omega_{cl}^2}{s^2 + 2\xi_{cl}\omega_{cl}s + \omega_{cl}^2} \tag{4.51}$$

in which ξ_{cl} is the damping ratio and ω_{cl} the natural frequency of the closed-loop [33]. By choosing high values for ξ_{cl} $(0.85 - 1.0)$, noise is suppressed. Furthermore, the speed of response can be set with ω_{cl}. It follows the open-loop transfer function $G_{ol}(s)$, see (4.52).

$$G_{ol}(s) = \frac{\omega_{cl}^2}{s^2 + 2\xi_{cl}\omega_{cl}s} \tag{4.52}$$

The filtered DOMA $\vartheta(t)$ is then as given by

$$\vartheta = G_{cl}(s)\vartheta^* \tag{4.53}$$

Henceforth, the filtered DOMA is referred to as DOMA. The displacement, $d_m(t)$, and velocity, $\dot{d}_m(t)$, along the filtered DOMA are then computed as given in (4.54), see also figure 4.5.

$$d_m(t) = y(t)\cos\vartheta(t) - x(t)\sin\vartheta(t) \qquad \dot{d}_m(t) = \dot{y}(t)\cos\vartheta(t) - \dot{x}(t)\sin\vartheta(t) \tag{4.54}$$

4.6.4 Computation of target angular position

As done for the SDOF oscillator, see (2.55), the TAPs referring to the DOMA can be computed by

$$\varphi_t(t) = \text{atan2}\left[d_m(t), \frac{\dot{d}_m(t)}{\omega_n}\right] + \pi \tag{4.55}$$

(4.55) is valid for systems without and with small inherent damping, see section 2.3 and ensures the anti-phasing between the control force and the velocity along the major axis. Subsequently, the TAPs referring to the Y-axis, see figure 4.1, can be calculated as shown in (4.56).

$$\varphi_{1,t}(t) = \varphi_t(t) + \vartheta(t) \qquad \varphi_{2,t}(t) = \varphi_t(t) - \vartheta(t) \tag{4.56}$$

To distinguish the TAPs of (4.56) from the TAPs of (4.41), the indices were interchanged.

The TAPs of (4.56) are now considered and it is assumed that these positions are perfectly tracked with a suitable controller. When the TDOF oscillator performs elliptical motion, the control force damps down the motion along the major axis and the DOMA will not vary considerably in time. Thus, with regard to (4.56), $|\dot{\vartheta}(t)| << |\dot{\varphi}_t(t)|$ in which $\dot{\varphi}_t(t) \approx \omega_n$. Therefore, the damping device operates in the preferred mode of operation in which the angular velocities of the rotors are approximately ω_n and the radial forces are much larger than the tangential forces. However, when the DOMA is required to change (e.g. the motion becomes circular or some excitation makes the DOMA changing), the filter for the DOMA influences $\dot{\varphi}_{1,t}(t)$ and $\dot{\varphi}_{2,t}(t)$, respectively, resulting in a varying amplitude of the radial forces. Furthermore, the tuning of the filter of figure 4.7 also determines the angular accelerations. These accelerations directly determine the amplitude of the created tangential forces which should be kept low in comparison to the radial forces. Note that the variations of the target angular velocities are needed to change the direction of the control force. To ensure that the created tangential forces are not too large in comparison to the radial forces when such a change is required, it is recommended to set ω_{cl} to ω_n. However, it must be checked that the effect of the tangential forces in comparison to the radial forces is small when a change in the DOMA is required.

The closed-loop angular position control is explained in an exemplary way for motor 1, see figure 4.8. Motor 2 is controlled in the same manner. The TAP $\varphi_{1,t}(t)$, see (4.56), is compared to the (measured) angular position, $\varphi_1(t)$. The error, $e_1(t)$, is then limited to values between $-\pi$ and π by adding multiples of 2π. This is indicated by the block 'LE' in figure 4.8. The limited error, $ce_1^*(t)$, is then fed through the filter given in (4.57).

$$F(s) = \frac{\omega_f^2}{s^2 + 2\xi_f\omega_f s + \omega_f^2} \tag{4.57}$$

$F(s)$, defined by the filter properties ω_f and ξ_f, exhibits low-pass behavior. With $3\omega_n < \omega_f < 5\omega_n$ and $0.85 < \xi_f < 1.0$, measurement noise is nicely suppressed.

The filtered control error $ce_1(t)$ is then fed into the controller. In addition to $ce_1(t)$, the on-off signal, $w_1(t)$, is also a controller input. This state and the controller are discussed in subsection 4.6.5. The output of the controller is the control effort $u_{a,1}$, which is fed into the actuator to track the TAP. This is also indicated in figure 4.8.

Note that some variables of figure 4.8 are not introduced yet. They are explained in the following subsection and section.

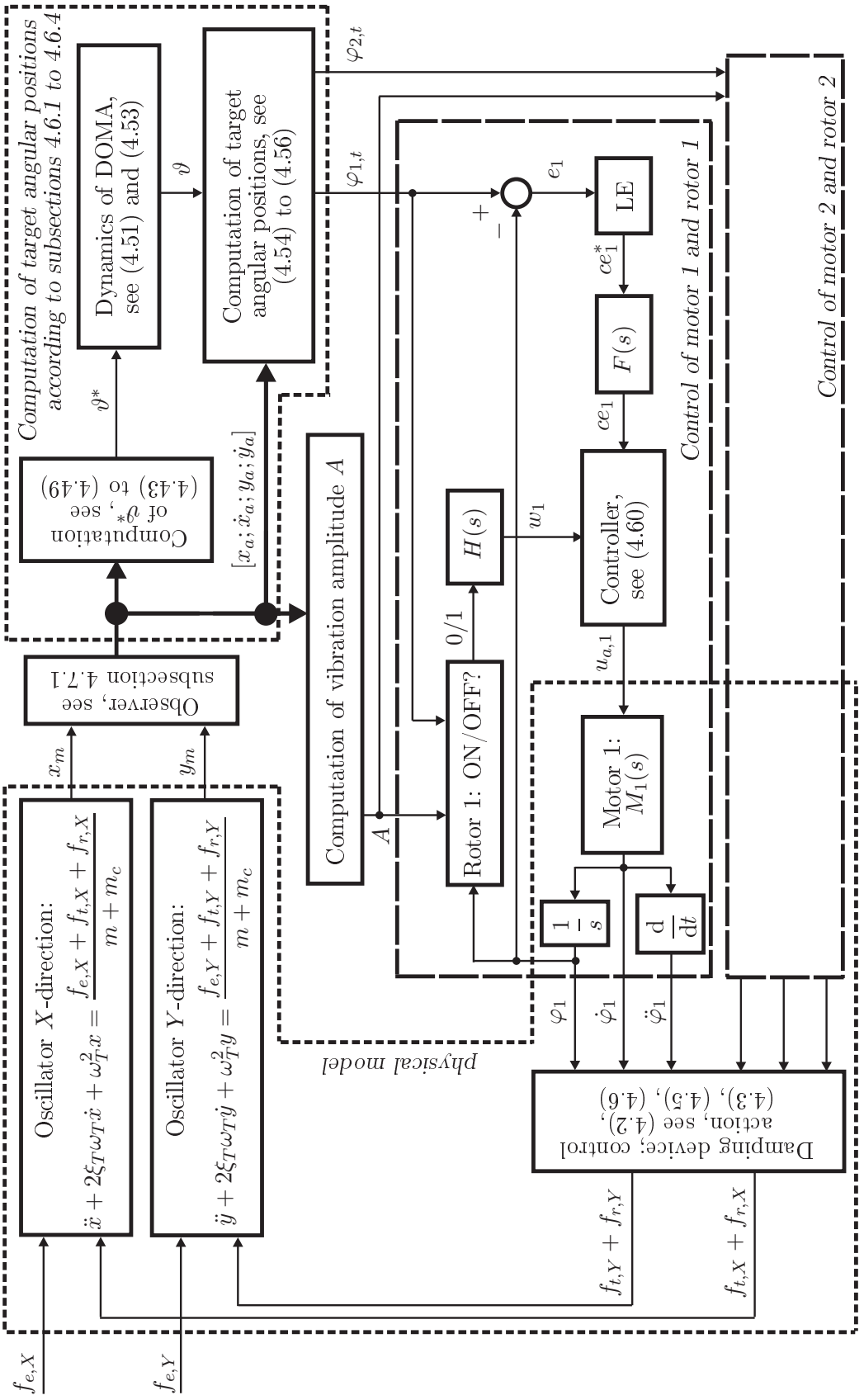

Figure 4.8: Control algorithm for adapted TRD to control the vibrations of a TDOF oscillator [59]

4.6.5 Ramp-up and ramp-down process

The adapted TRD has a similar issue as the TRD; in the continuous rotation mode, the amplitude of the control force cannot be varied during operation. As a result, both devices can re-excite the motion when the vibrations become small. For the TRD, several methods have been developed to avoid this undesired outcome. One method is turning the device off when the vibrations fall below a lower vibration threshold, A_{off}, and back on when an upper threshold, A_{on}, is exceeded. This method will be used for the adapted TRD in the following. For the TDOF oscillator, the vibration amplitude $A(t)$ along the major axis is computed as given by

$$A(t) = \sqrt{d_m(t)^2 + \left(\frac{\dot{d}_m(t)}{\omega_n}\right)^2} \tag{4.58}$$

When A_{on} is exceeded and the TAP passes the corresponding angular position of the rotor, the rotor is turned on (output of block 'Rotor 1: ON/OFF?' in figure 4.8 is set to one). When $A(t) < A_{off}$, the rotor is turned back off. A smooth ramp-up and ramp-down process is guaranteed (in contrast to section 2.5, in which an energy- and power-efficient ramp-up is guaranteed) using the transfer function $H(s)$ given in (4.59).

$$H(s) = \frac{\omega_H^2}{s^2 + 2\xi_H\omega_f s + \omega_H^2} \tag{4.59}$$

By choosing adequate values for ω_H and ξ_H, $H(s)$ exhibits low-pass behavior. With $3\omega_n < \omega_H < 5\omega_n$ and $0.85 < \xi_H < 1.0$, a smooth ramp-up and ramp-down process is achieved. The higher ω_H, the faster the device is ramped-up and down, resulting in larger tangential forces during the ramp-up and ramp-down processes.

In addition to the closed-loop angular position control of subsection 4.6.4, an open-loop velocity control is applied. The control effort for the first rotor, $u_{a,1}(t)$, is given by

$$u_{a,1}(t) = K_P ce_1(t) w_1(t) + \frac{1}{b}\omega_n w_1(t) \tag{4.60}$$

in which K_P is the proportional feedback gain of the closed-loop angular position control, $w_1(t)$ is the ramp-up/ramp-down weight signal and b is a coefficient describing the dynamics of the actuator, see the following section. The open-loop velocity control results in a more constant angular velocity of the rotors, see also subsection 2.6.5. Note that with $F(s)$, the measurement noise is already suppressed and a simple proportional feedback gain can be used for the closed-loop angular position control. The control effort $u_{a,2}(t)$ for the second rotor is computed analogously.

4.7 Tests

4.7.1 Setup

The TDOF oscillator is attached via three steel wires (each with a length of approximately 0.30 m) to a stiff frame, see figure 4.9.

The oscillating body can move in the horizontal plane (perpendicular to gravity). This horizontal motion can be described by two identical, decoupled single degree of freedom oscillators with the properties shown in table 4.1, see also figure 4.2.

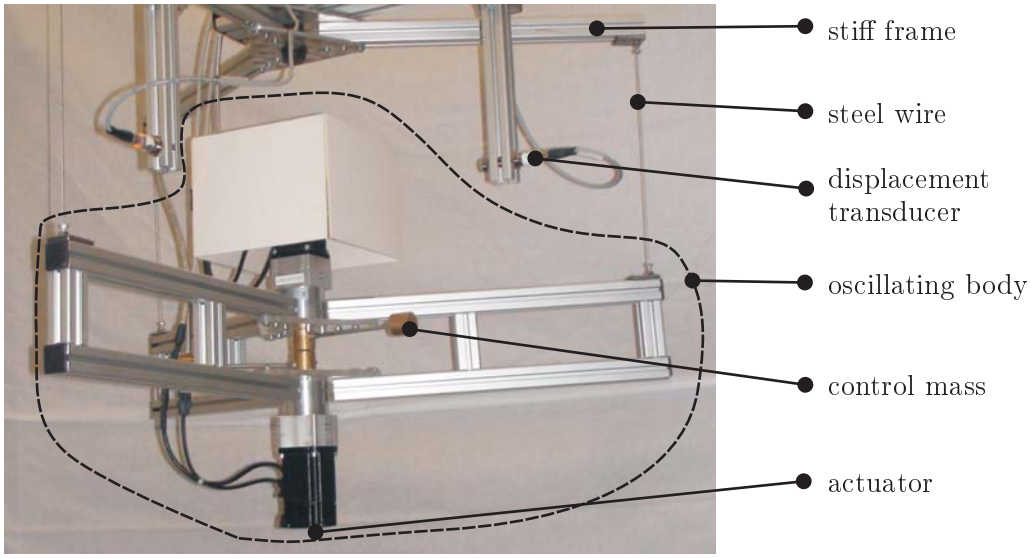

Figure 4.9: Test setup

Table 4.1: System properties of TDOF oscillator and damping device

Total mass	$m + m_c$ [kg]	9.96
Damped natural frequency	ω_T [(rad)/s]	5.85
Damping ratio	ξ_T [%]	0.935
Mass-radius control product	$0.5 m_c r$ [kgm]	$2.55 \cdot 10^{-2}$
Control mass	m_c [kg]	0.300

Two displacement transducers detect the horizontal displacement in X- and Y-direction, $x_m(t)$ and $y_m(t)$. The index m indicates measured signals. To detect the DOMA, the velocities in both directions $\dot{x}_a$ and $\dot{y}_a$ are also required, see (4.43) to (4.49). They are made available using an observer as shown in figure 2.34 for both directions. This is done with the feedback gain $\boldsymbol{L} = [-2263.3, -92.2]^{\mathrm{T}}$ (units are dropped) for both directions; for more information, see subsection 2.6.2. The observers have as input the measured displacements (x_m and y_m) and as output x_a, $\dot{x}_a$, y_a, $\dot{y}_a$, see figure 4.8.

The properties of table 4.1 were obtained via various free vibration tests. The oscillator was displaced several times by hand in $X-$, $Y-$ and in both directions simultaneously. Mean values of the (measured) damped natural frequency, ω_T, and damping ratio, ξ_T, from the different free vibration tests were calculated.

The oscillating body is only excited in translational directions. Furthermore, the control algorithm is tuned such that the angular accelerations of the rotors are small. This leads to negligibly small rotational vibrations of the oscillating body during tests.

In section 4.6, the control algorithm was derived using the natural frequency of the TDOF oscillator. However, the damped (measured) natural frequency ω_T of the test setup is now used for the control algorithm. Taking the effects of inherent damping into consideration would only make the derivation of the control algorithm more complex without producing additional insight. Therefore, ω_n is replaced by ω_T in (4.43) to (4.47) and (4.55).

The mass-radius control products $0.5 m_c r$ of both rotors are identical.

Before the tests, system identifications of both actuators were performed [32]. The actuators are voltage controlled and their dynamical behavior can be described by the transfer functions $M_v(s)$ given in (2.147) with the coefficients of table 4.2.

Table 4.2: Coefficients a and b describing dynamic behavior of actuators

	b	a
$M_{v,1}(s)$	3.09	$3.88 \cdot 10^{-3}$
$M_{v,2}(s)$	3.88	$3.65 \cdot 10^{-3}$

Input is the control effort in V and the output is the angular velocity in (rad)/s. For the tests, the angular positions of the rotors $\varphi_1(t)$ and $\varphi_2(t)$ are measured and used for the closed-loop angular position control. To obtain the angular position for the simulations of section 4.8, the angular velocity is integrated over time, see figure 4.8. The transfer functions of subsection 2.6.3 with the coefficients of table 4.2 and the system properties of table 4.1 will also be used for the numerical simulations of section 4.8.

4.7.2 Tuning

The control algorithm for the test setup was tuned with the help of simulations. The parameters ξ_{cl} and ω_{cl}, which determine the dynamics of the DOMA, were set to 0.9 and 5.0 (rad)/s. ω_H and ξ_H of the filter $H(s)$ were set to 20 (rad)/s and 0.9. The properties of the filter $F(s)$ (ω_F and ξ_F) were set to the same values. For the free vibration tests, the upper vibration-amplitude threshold A_{on} is set to 0.06 m and the lower threshold A_{off} to 0.01 m. The controller gain for the closed-loop angular position control was set to 1.00 V/(rad). In subsection 4.7.3, the test results are presented. In section 4.9, the effects that the tuning variables inherit are further discussed.

4.7.3 Test results

Figure 4.10 shows the states of the TDOF oscillator performing free vibrations while being damped by the adapted TRD. Time dependencies are no longer indicated in this chapter.

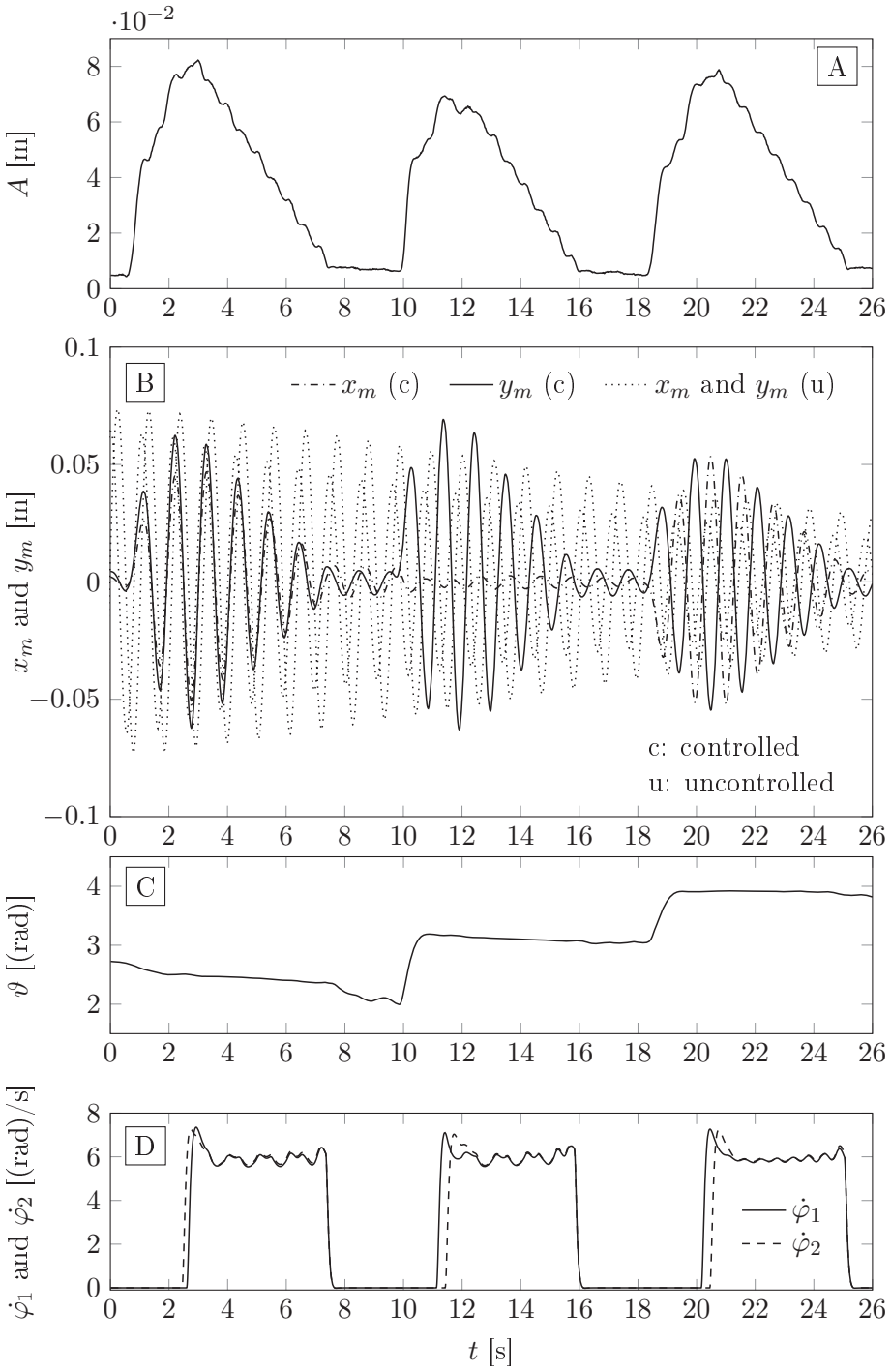

Figure 4.10: Test results for excitation in different directions [59]

The TDOF oscillator is displaced by hand in different directions. The states x_m and y_m are measured and the states A, ϑ, $\dot{\varphi}_1$ and $\dot{\varphi}_2$ are calculated by the control system. x_m and y_m are additionally shown for an uncontrolled free vibration, see subfigure B. This illustrates the effectiveness of the adapted TRD.

From $t = 0.8\,\mathrm{s}$ to $t = 3.0\,\mathrm{s}$, the oscillating body is excited, see states A, x_m (c), y_m (c) in figure 4.10/A and B. At $t = 2.5\,\mathrm{s}$, the upper vibration-amplitude threshold A_{on} is exceeded and the damping device turns on. At this instant, excitation by hand is stopped. It can be seen from the states $\dot{\varphi}_1$ and $\dot{\varphi}_2$ that the rotors are turned on at different time-points. This is because the TAP of each rotor passes the corresponding (measured) angular position at different instants. From $t = 3.0\,\mathrm{s}$ to $t = 7.5\,\mathrm{s}$, the device produces the desired damping action in the continuous rotation mode, see states $\dot{\varphi}_1$, $\dot{\varphi}_2$, A, x_m (c) and y_m (c) of figure 4.10. At $t = 7.5\,\mathrm{s}$, the vibration amplitude A falls below the lower vibration-amplitude threshold and the device is ramped down. At $t = 10.0\,\mathrm{s}$, the oscillating body is excited in a different direction by hand. This direction is detected by the control algorithm, see ϑ of figure 4.10/C. At $t = 11.3\,\mathrm{s}$, the device is turned back on and the excitation is again temporarily stopped. From $t = 11.3\,\mathrm{s}$ to $t = 16.0\,\mathrm{s}$, the device operates once again in the continuous rotation mode. From $t = 18.5\,\mathrm{s}$ to $t = 25.2\,\mathrm{s}$, another damping sequence in a third direction is shown.

Considering figure 4.10 for the first damping sequence ($t = 4.2\,\mathrm{s}$ to $t = 6.8\,\mathrm{s}$), the vibration amplitude A decays from 0.06 m to 0.02 m within 2.6 s. In this time interval, the vibration performs approximately 2.42 cycles. The equivalent damping ratio is 7.21 %. This corresponds to an increase of the damping ratio by a factor of 7.7, see table 4.1.

The oscillating body was then displaced by hand such that an elliptical motion path of the TDOF oscillator is produced, see figure 4.11.

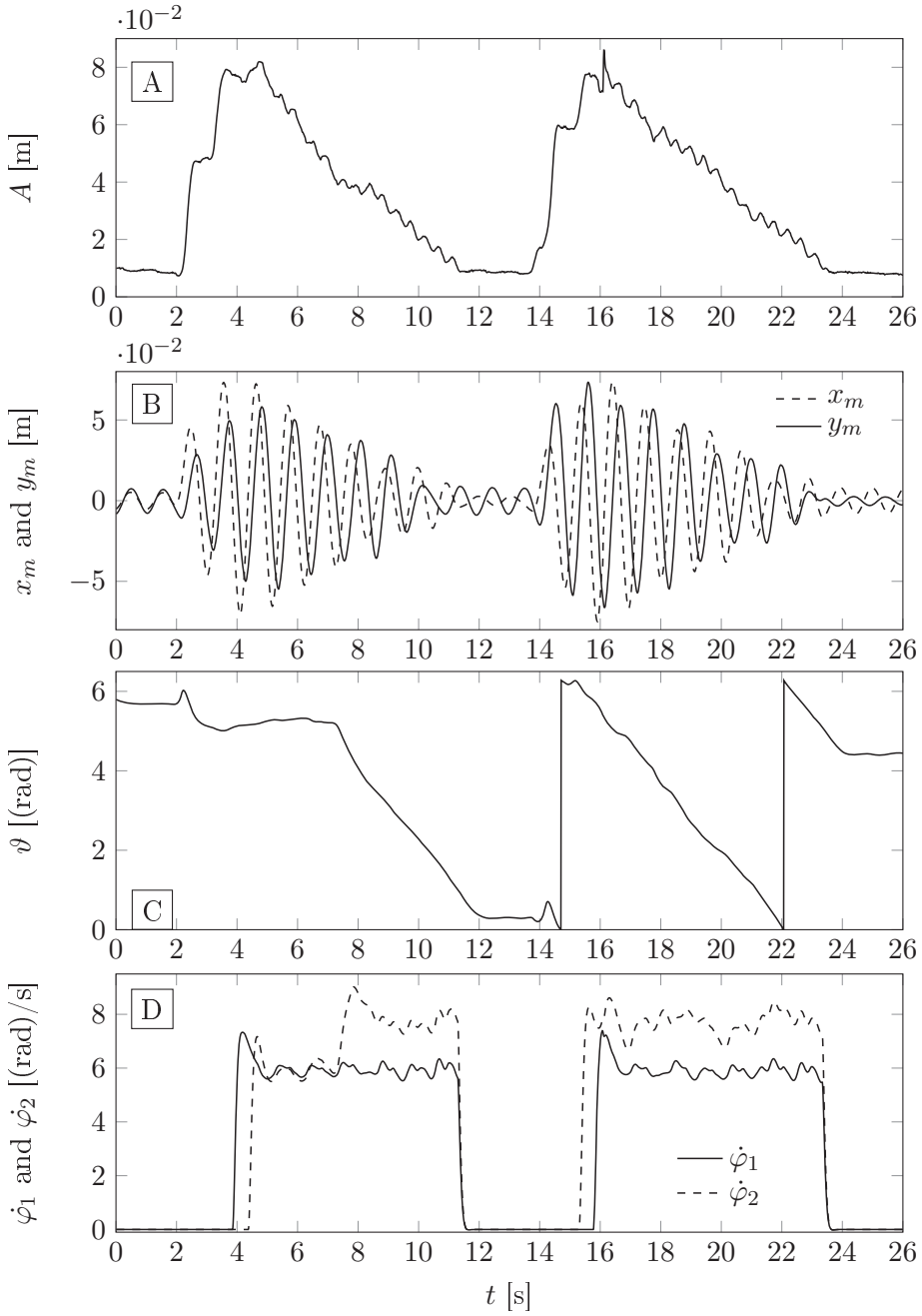

Figure 4.11: Test results for elliptic excitation by hand [59]

From $t = 2.1\,\mathrm{s}$ to $t = 4.0\,\mathrm{s}$, the oscillating body is excited and the device turns on at $t = 3.9\,\mathrm{s}$. At this instant, the DOMA is already detected, see state ϑ of figure 4.11. The device operates in the continuous rotation mode and damps the vibration along the major axis from $t = 4.0\,\mathrm{s}$ to $t = 7.3\,\mathrm{s}$. Within this time interval, the DOMA does not change and the elliptical motion path of the TDOF oscillator becomes more and more circular. This can be seen from the states x_m and y_m in figure 4.11. When the displacement amplitudes of x_m and y_m coincide and reach a phase offset of 0.5π to each other, the motion path is approximately a circle. This is the case at $t = 7.3\,\mathrm{s}$. From this instant on, the DOMA changes with respect to time. The change rate is determined by the natural frequency ω_{cl} of the closed-loop from ϑ^* to ϑ, see subsection 4.6.3. Furthermore, the angular velocity

of one rotor increases while the other one remains nearly constant. The decay rate in the vibration amplitude is slightly smaller, see state A of figure 4.11/A. Considering the damping sequence from $t = 14.0\,\mathrm{s}$ to $t = 23.5\,\mathrm{s}$, it can be seen that the excitation directly results in a circular motion path. The DOMA starts changing once the device becomes active. An increased angular velocity of the second rotor can be observed in the complete damping interval from $t = 16.0\,\mathrm{s}$ to $t = 23.0\,\mathrm{s}$.

Once the motion path of the TDOF oscillator has a circular form (vibration amplitudes on major and minor axis coincide), an operation of the adapted TRD with a constant angular velocity is no longer possible. As a result, tangential forces which act randomly on the TDOF oscillator are created in addition to the radial forces. Therefore, the resulting motion and rotor behavior is not easily assessed. However, pre-simulations and tests show that the angular velocities of the rotors deviate from the damped natural frequency once the motion path has a circular form and that this deviation is larger, the higher ω_{cl} is chosen.

4.8 Stochastically forced vibrations

4.8.1 Uncontrolled response and simulation settings

For the numerical simulations, the TDOF oscillator is excited by a stochastic excitation. The simulation duration for all simulations performed in this section is 5000 s. For the excitation, white noise with an intensity of $1.0\,\mathrm{N}^2/\mathrm{Hz}$ using a two-sided spectrum is assumed. This stochastic excitation (see $f_{e,X}$ and $f_{e,Y}$ in figure 4.8) leads to a mean standard deviation in the uncontrolled displacement in both directions of approximately, $u_{std,x,y} = 0.0379\,\mathrm{m}$ ($u_{std,x,y} = 0.5\mathrm{std}(x) + 0.5\mathrm{std}(y)$). Note that u refers now to the uncontrolled displacement response. The simulations were done in MATLAB/Simulink using a sampling frequency of 2000 Hz and ode3 (Bogacki-Shampine method) as the numerical solver. The same settings and excitation force are used for all simulations in this section. The complete simulation model is illustrated in figure 4.8. The observer is not used for the numerical simulations as the velocities of the TDOF oscillator are directly available.

4.8.2 Control parameters

In this subsection, the control parameters for the control algorithm are chosen. The parameters of minor importance are only set, whereas the parameters with major importance are varied within an optimization.

As recommended in section 4.6.4 and 4.6.5, the filter parameters ω_H, ξ_H, ω_F and ξ_F are set as given in table 4.3. They are not varied as they play a minor role. The filter $H(s)$ determines the ramp-up/ramp-down process, which only occurs over short periods of time, and the filter $F(s)$ suppresses measurement noise.

Table 4.3: Setting and variation ranges of control parameters

$\omega_{H/F}\,[(\mathrm{rad})/s]$	$\xi_{H/F}$	$\omega_{cl}\,[(\mathrm{rad})/s]$	ξ_{cl}	$A_{on}\,[\mathrm{m}]$	$A_{off}\,[\mathrm{m}]$	$K_P\,[\mathrm{V}/(\mathrm{rad})]$
20	0.9	$0.5 - 20$	0.9	$0.01 - 0.1$	$0.01 - 0.07$	$0.1 - 1.5$

ω_{cl}, which determines the dynamics of the DOMA, is varied as given in table 4.3. ξ_{cl} is set to 0.9.

Due to the excitation, the displacement peaks of the uncontrolled displacement response reach 0.1 m to 0.12 m. Therefore, the upper vibration-amplitude thresholds A_{on} and the lower one A_{off} are varied as shown in table 4.3.

The proportional feedback gain K_P for the angular position closed-loop control is set to values between 0.1 V/(rad) and 1.5 V/(rad). Note that the choice of the range for K_P depends on the dynamics of the actuators. However, some recommendations regarding tracking objectives can be given. In the continuous rotation mode, the error ce^* should not exceed $\pm 0.2\,(\text{rad})$ ($\approx 11.5°$), however, during the ramp-up ramp-down processes, it should not exceed $\pm\pi/2$. It is beneficial to add an open-loop angular velocity control. This allows the closed-loop angular position control to be designed less aggressive, resulting into a more continuous motion of the rotors.

4.8.3 Evaluation

To calculate the power demand and the energy consumption, the moments required to be created by the actuators are needed. They are given by (4.61) and (4.62).

$$M_1 = 0.5r^2 m_c \ddot{\varphi}_1 - 0.5 m_c r \left(\ddot{y}\sin\varphi_1 + \ddot{x}\cos\varphi_1\right) \tag{4.61}$$

$$M_2 = 0.5r^2 m_c \ddot{\varphi}_2 + 0.5 m_c r \left(-\ddot{y}\sin\varphi_2 + \ddot{x}\cos\varphi_2\right) \tag{4.62}$$

(4.61) and (4.62) are obtained by forming the dynamic equilibrium about the center of the axis of each actuator; tangential forces (forces induced by an angular acceleration of the rotors) and inertial forces induced by the translational accelerations of the TDOF oscillator must be considered. The moments by the actuators, M_1 and M_2, are assumed to act in the same direction as the corresponding angular position, φ_1 and φ_1, see figure 4.1. A free body diagram of rotor one is shown in figure 4.12.

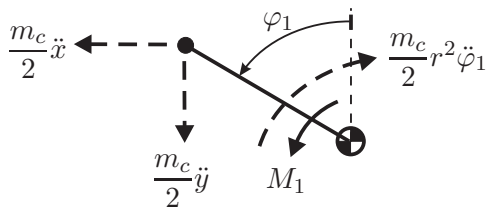

Figure 4.12: Free body diagram of first rotor [59]

Friction is neglected. The rotational inertia of one rotor is assumed to be $0.5 m_c r^2$ (rotational inertia of a point mass). Hence, the rotational inertia of the rod, shaft of the actuator, etc. is not considered. The same assumption will be made for the other active mass damper used for the comparison. Henceforth, the other active mass damper will be referred to as conventional active mass damper (CAMD).

The power of each actuator is given by (4.63).

$$P_1 = M_1\dot{\varphi}_1 \qquad\qquad P_2 = M_2\dot{\varphi}_2 \tag{4.63}$$

The work done by each actuator is given by

$$E_1 = \int_{t=0}^{t=T} P_1 \mathrm{d}t \qquad E_2 = \int_{t=0}^{t=T} P_2 \mathrm{d}t \tag{4.64}$$

in which T is the simulation time. The work done by the actuators will be referred to as consumed energy. In (4.64), positive as well as negative energy is considered. This means that braking energy can be regained. Because of this, the positive energy consumed by the actuators is also computed; such energies will be labeled with the index plus, e.g. E_1^+.

The excitation force directly acts on the acceleration of the TDOF oscillator, therefore influencing the moments and powers, see (4.61) to (4.63). However, due to the low-pass filter of (4.57), the actuators would not react to the high frequency components of the excitation forces. Therefore, before further evaluation, a filter with the same form as in (4.57) will also be used to process the powers of (4.63), in which ξ_F and ω_F were set to 1 and 50 (rad)/s, yielding the powers $P_{1,f}$ and $P_{2,f}$. Using the filtered powers $P_{1,f}$ and $P_{2,f}$ instead of P_1 and P_2 in (4.64) gives the (filtered) works done by the actuators, $E_{1,f}$, $E_{2,f}$, $E_{1,f}^+$ and $E_{1,f}^+$. For all simulations, the energy balance was checked to validate the filtered and unfiltered power courses, confirming the filter process described in this paragraph, see Appendix A.2.

To evaluate the required power of the actuators, the root mean square values of the (filtered) powers of the individual actuators are computed, giving $P_{rms,1} = \mathrm{rms}(P_{1,f})$ and $P_{rms,2} = \mathrm{rms}(P_{2,f})$. Furthermore, to evaluate the vibration reduction, the standard deviations of the controlled displacement responses, $x_{std} = \mathrm{std}(x(t))$ and $y_{std} = \mathrm{std}(y(t))$, are computed. Mean values, P_{rms} and $c_{std,x,y}$, in which c stands for controlled, are used as a measure for the required power of one actuator and for the controlled vibration, see (4.65).

$$P_{rms} = 0.5\,[P_{rms,1} + P_{rms,2}] \qquad c_{std,x,y} = 0.5\,[x_{std} + y_{std}] \tag{4.65}$$

The parameters described in subsection 4.8.2 were varied and the performance was evaluated with help of the product $P_{rms}c_{std,x,y}$, which is to be minimized. Additionally, a certain vibration reduction R was required, see (4.66).

$$R = \frac{u_{std,x,y} - c_{std,x,y}}{u_{std,x,y}} \tag{4.66}$$

Note that the evaluation of the power demand in this chapter differs from the evaluation of the power demand in chapter 3 in which the power demand was only considered when the TRD is in the continuous rotation mode, see subsection 3.6.2. In this chapter, an overall power demand is calculated including the times the TRD is off, the ramp-up and ramp-down processes and the power demand required for the continuous rotation mode. Further comments regarding this are given later on.

4.8.4 Simulation results

Table 4.4 shows the results of a stochastically forced vibration. A reduction R of at least 50 % was required. The standard deviation of the uncontrolled displacement response of $u_{std,x,y} = 0.0379\,\mathrm{m}$ was reduced to 0.0177 m. This corresponds to a reduction R of approximately 53.4 %. This reduction was achieved with an actuator power P_{rms} of 0.140 W and a mean positive energy consumption, $E^+ = 0.5E_{1,f}^+ + 0.5E_{2,f}^+$, of one actuator of 101 J.

Table 4.4: Setting and simulation results with adapted TRD [59]

A_{on} [m]	A_{off} [m]	ω_{cl} [(rad)/s]	K_P [V]	P_{rms} [W]	$c_{std,x,y}$ [m]	R [1]	E^+ [J]
0.030	0.015	7	0.3	0.140	0.0177	0.534	101

In the following, comments regarding some tuning parameters are given. The damping effect increases with lower vibration-amplitude thresholds as the vibration amplitude range in which the device is active is wider. However, the vibration-amplitude thresholds cannot be set to arbitrary small values. The smaller the vibration amplitude, the higher the influence of the excitation forces is in comparison to the system forces; consequently, the more non-harmonic d_m and $\dot{d}_m$ become. This results in a more non-constant TAV for small vibration amplitudes and therefore to relatively large angular accelerations of the rotors, creating a larger tangential force to radial force ratio. If the effect of the tangential forces—which can be seen as a random excitation force—becomes too large, the vibration-amplitude thresholds must be set to higher values.

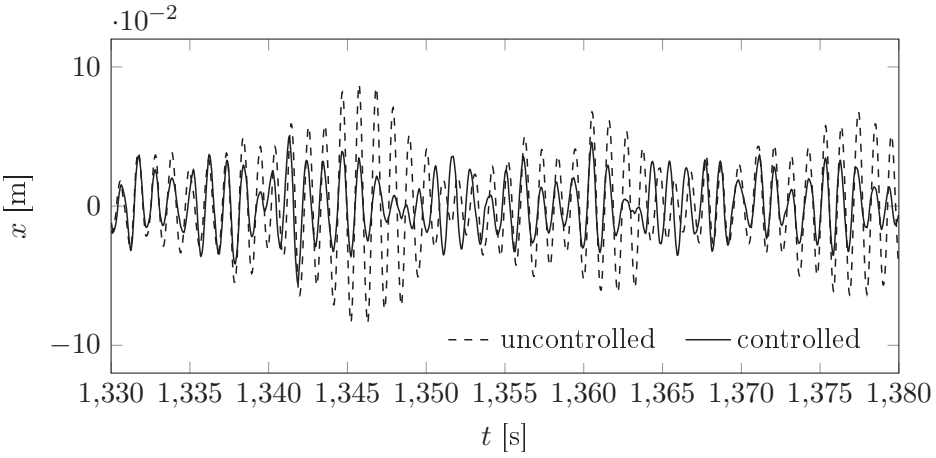

Figure 4.13: Uncontrolled and controlled displacement response in a single direction [59]

In figure 4.13, the uncontrolled and the controlled displacement responses in $X-$direction are shown for a chosen time interval. It can be seen that the device effectively damps the stochastically forced vibrations.

With the gain K_P, the closed-loop angular position controller is tuned. The larger the gain K_P is set, the more accurate the tracking of the TAPs at the expense of larger actuator power. However, even for TAPs which deviate from the current angular positions by $\pi/6$, the damping effect is still large in the continuous rotation mode. Therefore, control errors of $\pi/2$ can even be allowed for short periods of time during the continuous rotation mode and the ramp-up process.

4.8.5 Comparison with conventional active mass damper

A conventional active mass damper (CAMD) which generates its control action by accelerating and decelerating control masses is shown in figure 4.14.

d_x and d_y describe the relative displacements between the mass m and the control masses.

The motion in $X-$direction is governed by (4.67), whereas $f_{e,X}$ (not indicated in figure 4.14) is the same excitation force as described in subsection 4.8.1.

$$(m + m_c)\,\ddot{x} + c_x\dot{x} + k_x x = -0.5 m_c \ddot{d}_x + f_{e,X} \tag{4.67}$$

Using direct linear velocity feedback

$$\ddot{d}_x = g_x \dot{x} \tag{4.68}$$

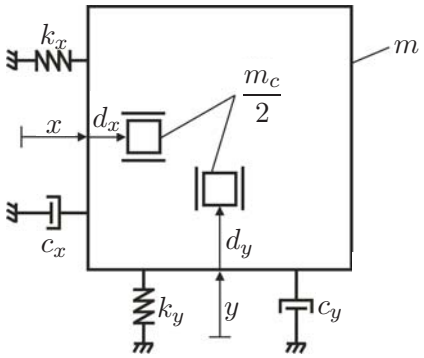

Figure 4.14: Two degree of freedom oscillator with conventional active mass damper [59]

the differential equation of (4.67) can be rearranged in

$$(m + m_c)\,\ddot{x} + (c_x + 0.5 m_c g_x)\,\dot{x} + k_x x = f_{e,X} \tag{4.69}$$

With help of the gain g_x, the damping effect can be governed; the larger the gain, the higher the damping effect.

Direct linear velocity feedback is an easy and effective technique to control the TDOF oscillator with the CAMD [17]. Using the direct linear velocity feedback of (4.68), it may occur that the control masses drift away from their center positions (very large stroke would be required). However, this did not occur. If it occurs, an additional position control is required ensuring that the control masses move back and forth about their center positions. The power of the actuator dictating the motion between the mass and the control masses is given in (4.70)

$$P_x = 0.5 m_c \left(\ddot{x} + \ddot{d}_x\right) \dot{d}_x \tag{4.70}$$

The power of (4.70) is filtered as the powers of (4.63), giving the filtered power, $P_{x,f}$. The consumed energy is as given by

$$E_x = \int_{t=0}^{t=T} P_{x,f} \mathrm{d}t \tag{4.71}$$

(4.67) to (4.70) can be derived for the $Y-$direction analogously. However, as the differential equations are decoupled and equal in both directions, the evaluation of one direction suffices. As in (4.65), the required power of one actuator $P_{rms,c} = \mathrm{rms}(P_{x,f})$ and the vibration $c_{std,c} = \mathrm{std}(x)$ are quantified using the rms-value and the and the standard deviation. The additional index c refers to the CAMD. The controller gain g_x was set such that approximately the same reduction R as in subsection 4.8.4 is achieved, see table 4.5.

Table 4.5: Simulation results of conventional active mass damper

g_x [1/s]	$c_{std,c}$ [m]	R	$P_{rms,c}$ [W]	E_x^+ [J]
25	0.0178	0.53	0.180	175.9

The simulations show that the power demand and positive energy consumption is lower with the adapted TRD. This is because the CAMD is required to continuously accelerate and decelerate the control masses, whereas for the adapted TRD, large power demands are only required during the ramp-up and ramp-down processes.

Figure 4.15 shows the power demands for a single actuator of the adapted TRD $P_{1,f}$ and the CAMD $P_{x,f}$ in a chosen time interval. With figure 4.15, only the characteristics of the power demands are discussed. For a direct quantitative comparison, such a short time interval is not representative; however, it is done as before using P_{rms} and $P_{rms,c}$, see table 4.4 and 4.5. In the time interval of figure 4.15, the adapted TRD is turned on and off two times. At $t = 1440.0\,\mathrm{s}$, the adapted TRD is ramped up and operates in the continuous rotation mode up to $t = 1445.0\,\mathrm{s}$ at which it is ramped down as can be seen from the peaks in the power demand. From $t = 1446\,\mathrm{s}$ until $t = 1454\,\mathrm{s}$, a second damping sequence is shown. When the adapted TRD operates in the continuous rotation mode, power is only required for aligning the control force along the DOMA and for ensuring the anti-phasing between the control force and the velocity along the major axis. Note the power $P_{1,f}$ is still noisy, which is due to the manner the power demand is calculated, see (4.63) and the following two paragraphs. This noise increases the power demand P_{rms} on the adapted TRD. In contrast to the power demand on the adapted TRD, the CAMD is required to continuously accelerate and decelerate the control masses, increasing its power demand $P_{x,f}$. The larger the vibration amplitude, the larger the power demand of the CAMD becomes, see e.g. $t = 1448\,\mathrm{s}$ until $t = 1454\,\mathrm{s}$.

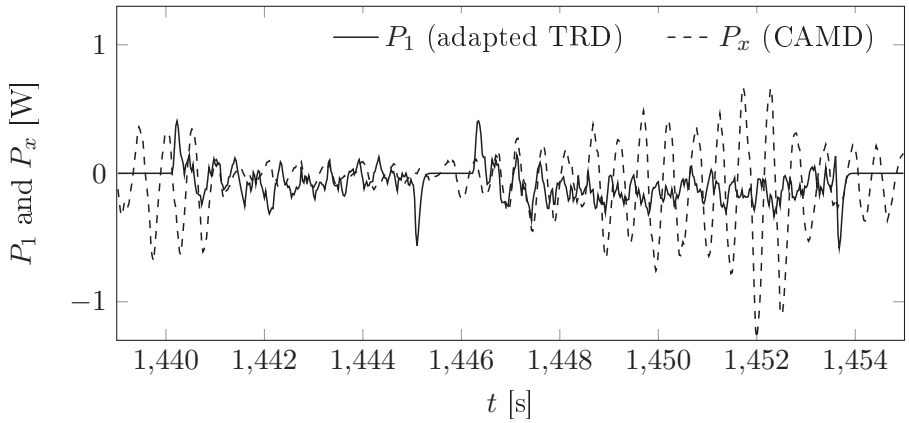

Figure 4.15: Power demand of adapted TRD and CAMD [59]

The reduction R is now varied. To achieve this with the adapted TRD, only the radius r is varied; the larger the radius r, the greater the radial forces. Consequently, the control force amplitude increases and therefore the damping effect. Varying the radius corresponds to a change in size. To achieve different reductions with the CAMD, only the gain g_x is varied. This also corresponds to a change in size as the required stroke increases with g_x. Figure 4.16 shows the power demands, P_{rms} and $P_{rms,c}$, of both damping devices for different reductions R. Furthermore, the mean values of the power demand are shown.

The mean power demands, P_{mean} and $P_{mean,c}$, nearly coincide as the energies both devices dissipate from the TDOF oscillator are equal when the same reductions are required. These mean powers are accounted for in the rms values P_{rms} and $P_{rms,c}$. The rms value (P_{rms}) of the power demand of the adapted TRD further includes the powers required for: the ramp-up and ramp-down processes, aligning the control force along the major axis and ensuring the anti-phasing. For the CAMD, rms value $P_{rms,c}$ of the power demand further includes the powers required for accelerating and decelerating the control masses.

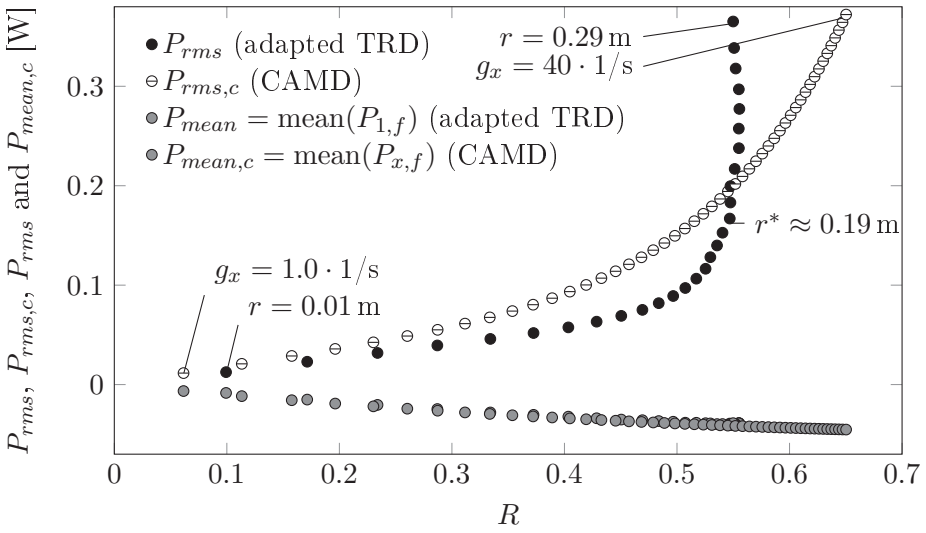

Figure 4.16: Power demands for different reductions R [59]

In the following, P_{rms} and $P_{rms,c}$ are discussed. The radius r is varied from 0.01 m to 0.29 m and the gain g_x from 1.0 1/s to 40 1/s. For reductions smaller than 0.50, the power demand is lower with the adapted TRD (P_{rms}), to be more precise, the power demand is 30 % to 45 % smaller. With the adapted TRD, vibration reductions larger than 0.55 were not achieved with the described control algorithm. This means that choosing a radius larger than a certain radius limit r^* would lead to a larger control force amplitude, but not to a larger reduction. If r is larger than r^*, the vibration amplitudes are held most of the time below the upper vibration-amplitude threshold. However, the vibration amplitudes decay stronger (a stronger decay does not lead to a further reduction) than with a smaller radius r. On the contrary, the power demand required to ramp the device up and down increases with the radius (yielding a larger rotational inertia of the rotors). Additionally, the increased decay in the vibration amplitude requires the device to turn on and off more frequently. Due to this, for $r > r^*$, the power demand increases without producing a further vibration reduction. The CAMD can reach large reductions ($R > 0.55$) at the expense of an over-proportionally increasing power demand. Simulations with $g_x > 40 \cdot 1/\text{s}$ were not performed.

4.9 Discussion

4.9.1 Control algorithm

In the following, the derived control algorithm is discussed. Furthermore, some assumptions are reconsidered.

Natural frequencies

It was assumed that the natural frequencies of the TDOF oscillator in both directions coincide, see (4.11). Removing this assumption and assuming that these frequencies slightly differ, the motion path of the TDOF oscillator is also elliptic. However, due to the frequency difference, the DOMA changes in time when a free vibration as in section 4.4 is considered. The mean value of the natural frequencies can be used for the control algorithm of section 4.6 ($\omega_n = 0.5\omega_x + 0.5\omega_y$ for a TDOF oscillator with small inherent damping). Due to the continuous change of the DOMA, the target angular velocities deviate from ω_n; the larger the frequency difference is, the higher this deviation. When the frequency difference is too large and the presented control algorithm (which uses the radial forces) is used, the adapted TRD might be in-efficient.

Direction of major axis

The TAPs and consequently the target angular velocities of the rotors consist of $\dot{\vartheta}$ and $\dot{\varphi}_t$, see (4.55) and (4.56). If the DOMA does not change in time, the target angular velocities of the rotors are approximately ω_n, see figure 4.10. However, if the DOMA changes in time (due to an excitation or if an elliptical motion path becomes circular) and the device is active, see figure 4.11, the bandwidth of the filter of subsection 4.6.3 determines the rate in which the DOMA changes in time and consequently the target angular velocities induced by the change of the DOMA. Because of this, the design of the low-pass filter determining the dynamics of the major axis is a trade-off between a quick alignment of the direction of the control force towards the current DOMA and the preference of having small variations in the TAV of the rotors.

Adapted TRD for stochastically forced vibrations

Even though the device is tuned to a single frequency, see (4.55), it is also effective if the oscillator is affected by a stochastic excitation force (see section 4.8) and consequently responds with different frequencies. However, it must be mentioned that the TDOF oscillator considered in section 4.8 has small inherent damping; thus, it mainly responds with frequencies in the vicinity of the damped natural frequency. (See also second to last discussion point of section 3.4.) If the TDOF oscillator responds with a frequency different from the damped frequency, the algorithm still ensures that the radial forces projected on the DOMA oppose the velocity along the DOMA, thus producing the damping effect. However, additional and disrupting rotor accelerations are required, increasing the power and energy demands on the actuators.

4.9.2 Comparison of adapted TRD with CAMD

A trade-off between both the adapted TRD and the CAMD is not easily assessed as the adapted TRD is to be tuned for each system and load case scenario individually. However, one can highlight some pros and cons of the adapted TRD and the CAMD and make some distinctions.

Control force generation method

The greatest advantage of the adapted TRD over the CAMD is the lower power demand on the actuators up to a certain vibration reduction. This is due to the manner in which the control force is generated. By using the centrifugal forces (radial forces), the rotor velocity can be held constant while the control action is continuously being produced, see figure 4.10. Only small accelerations must be induced by the actuators in the continuous rotation mode. This is in contrast to the CAMD which must continuously accelerate and decelerate the control masses to produce the desired control action, see figure 4.15.

Effective damping range

The CAMD is effective over all vibration amplitudes, whereas the adapted TRD is only effective if a certain vibration-amplitude threshold is exceeded. These thresholds cannot be set to arbitrary small values. The smaller the vibrations, the more non-harmonic the responses of the TDOF oscillator become. Consequently, the target angular velocities of the rotors vary more. When the tangential force to radial force ratio becomes too large, a further reduction of the vibration-amplitude thresholds is ineffective. However, in case of small vibration amplitudes, an alternative mode of operation can be used in which the tangential forces instead of the radial forces are used for vibration control. The adapted TRD then operates like a conventional active mass damper, resulting in a larger power demand. The fact that the vibration-amplitude thresholds cannot be set to arbitrarily small values results in an additional disadvantage. The adapted TRD cannot reach arbitrarily large vibration reductions as the CAMD if the TDOF oscillator is under a stochastic excitation force. However, if the controller of the CAMD is tuned such that large vibration reductions are possible, the power demand on the actuators increases extremely, see figure 4.16.

*

5

Conclusions

The twin rotor damper (TRD), an active mass damper, uses the centrifugal forces of two eccentrically rotating control masses. In the continuous rotation mode, the preferred mode of operation, the two eccentric control masses are driven by individual actuators in opposite directions about two parallel axes with a mostly constant angular velocity. Under further operational constraints, a harmonic control force in a single direction is produced. A continuous feedback control is developed, guaranteeing the anti-phasing between the harmonic control force of the TRD and the velocity of the single degree of freedom (SDOF) oscillator performing mono-frequent vibrations.

It is shown for mono-frequent vibrations that the TRD has a power advantage compared to conventional active mass dampers which create their damping action by continuously accelerating and decelerating control masses. This power advantage is due to the fact that the control action fed to the actuators of the TRD is not directly related to the damping action. Rather, with a constant angular velocity, the TRD produces its damping action.

When the vibrations of the SDOF oscillator become small, the control algorithm for the continuous rotation mode no longer results in the desired constant angular velocity. The TRD can even re-excite the vibrations. One method to prevent this undesired outcome, the on/off method, is to turn the device off when the vibration amplitude falls below a certain threshold value and back on again when the vibration amplitude exceeds another (higher) threshold. To reach and leave the continuous rotation mode, ramp-up and ramp-down trajectories are developed. The trajectories are optimized with the help of cost functions, penalizing the work done by the actuators and the power demand on the actuators during the ramp-up and ramp-down processes.

To illustrate the on/off method, a complete closed-loop control damping sequence for a SDOF oscillator controlled with the TRD is presented and validated on a test setup for the damping of mono-frequent vibrations. The results show that the TRD effectively damps mono-frequent vibrations in a power-efficient manner.

An analytic solution describing the steady-state damping performance of the TRD is then derived. The experiments show that the TRD can reach the analytically derived steady-state damping performance with an appropriate control algorithm. The analytic derivations prove that the TRD adds damping to the SDOF oscillator. The damping the TRD provides does not only depend on the design parameters of the TRD, but also on the steady-state vibration amplitude. The provided damping increases with the design parameters of the TRD and with lower steady-state vibration amplitudes. Above a certain frequency ratio (border frequency ratio), the control force amplitude of the TRD is larger than the harmonic excitation force. Thus, a steady-state is not reached.

The analytically derived steady-state response solution is applicable to other active mass dampers which generate their control action by harmonically accelerating and decelerating a control mass between two end positions. Setting the control force of such an active mass damper in anti-phase to the velocity of a SDOF oscillator, the same steady-state damping performance as derived analytically here is reached. The analytic solution allows for a comparison of the TRD with a tuned mass damper (TMD) of comparable size (stroke) and control mass. It is shown that the TRD achieves greater damping performance than such a TMD.

Control algorithms for two further re-excitation prevention methods are discussed using a SDOF oscillator disturbed by a stochastic excitation force. One of the methods uses two TRD units. For large vibration amplitudes, both TRD units jointly damp the motion of the SDOF oscillator. For small vibration amplitudes, the phasing between the control forces of the TRD units is adjusted such that they cancel each other out. The other method de-tunes the anti-phasing between the velocity of the SDOF oscillator and the control force of a single TRD unit such that the resultant damping effect can be varied. Both methods prevent the re-excitation for small vibrations. However, the vibration control of small vibration amplitudes is still not possible.

Subsequently, the application of the TRD for the vibration control of stochastically forced vibrations is investigated. To ensure the anti-phasing between the velocity of the SDOF oscillator and the control force of the TRD, the TRD must deviate from the continuous rotation mode by varying the angular velocity of the rotors. If the required variation of the angular velocity is too high, it is no longer beneficial to operate the TRD in the continuous rotation mode. For an example loading scenario, it is shown that below a specific vibration-amplitude threshold, an operation in the continuous rotation mode is no longer beneficial. It is then discussed that this statement applies to any loading scenario. If the vibrations fail to exceed the specific vibration-amplitude threshold, an operation in the continuous rotation mode, for the considered loading scenario, is not beneficial.

A phase-locked loop (PLL) filter is proposed to simplify the tuning of the continuous rotation mode for stochastically forced vibrations. With help of the PLL filter, a filtered target angular position (TAP) can be produced. The filtered TAP allows the designer to set the balance between ensuring the anti-phasing between the control force of the TRD and the velocity of the SDOF oscillator and the preference of having a constant filtered target angular velocity (resulting from the filtered TAP) of the TRD. With the proposed PLL filter, a single parameter is derived to enable this trade-off. A procedure to tune the PLL filter and to determine an appropriate mass-radius control product for the TRD is then proposed. In this step, the power demand on the actuators of the TRD is defined by the designer for the operation in the continuous rotation mode.

To additionally control vibrations below the specified vibration-amplitude threshold, the TRD is required to operate in an alternative mode of operation, the so-called swinging mode. For this purpose, a control algorithm to operate the TRD in the swinging mode is developed. The previously determined power demand defined by the designer for the operation in the continuous rotation mode serves as an upper bound for the power demand in the swinging mode. Although a greater damping performance is achieved with the continuous rotation mode, the swinging mode is required for the damping of small vibrations. Based on numerical simulations and experiments, the effectiveness of the control-loop and the tuning procedure for the damping of stochastically forced vibrations is validated.

In the final chapter, the layout of the TRD is adapted, allowing for the vibration control of an oscillator with two translational degrees of freedom. The two degree of freedom oscillator performs planar motion and has an elliptic motion path when a free vibration is considered. To control this elliptic motion, the layout of the TRD is adapted. The control masses now rotate about a single axis. By imposing small variations in the angular velocity, the direction of the control force can be changed in the plane of motion of the two degree of freedom (TDOF) oscillator. This allows for the vibration control of the two degree of freedom oscillator in the continuous rotation mode with small variations in the angular velocities. Two control algorithms are derived for this purpose.

The first control algorithm is derived analytically by minimizing the work done by the harmonic control force on the TDOF oscillator under several assumptions. It results in a target angular position (TAP) for each rotor. Tracking these TAPs, the desired continuous motion of the rotors is obtained and the TDOF oscillator is effectively damped in an arbitrary direction in the plane of motion. However, once the motion of the TDOF oscillator forms a circular motion path, discontinuities occur in the target angular positions and the control algorithm is no longer effective. For this purpose, a second control algorithm is developed.

The second control algorithm is no longer derived analytically, but works as follows. The direction of the major axis of the elliptic motion path is detected. To achieve maximum damping action, the directed harmonic control force is set such that it is in anti-phase with the velocity of the TDOF oscillator along the major axis. The algorithm was validated experimentally for free vibrations and numerically for stochastically forced vibrations. For a TDOF oscillator with small inherent damping, it is shown that the power demand and the energy consumption of the adapted TRD are smaller than those of a conventional active mass damper.

*

A

Energy balances

A.1 Single degree of freedom oscillator with twin rotor damper

To verify the numerical simulations or post-computations, the energy balance can be checked. Therefore, some energy terms defined in subsection 2.6.6 must be refined. The energy balance is given by

$$E_T(t) + E_{rot,0} + E_{kin,0} + E_F(t) = E_d(t) + E_{rot}(t) + E_v(t) \tag{A.1}$$

in which $E_T(t)$ refers to the work done by the actuators given in (2.158) with $t_l = 0$ and $t_u = t$ and $E_d(t)$ to the dissipated energy given in (2.157) with $t_l = 0$ and $t_u = t$. The other terms are introduced now. Assuming that both rotors perform the same motion, the kinetic energy $E_{rot}(t)$ of both rotors is given by

$$E_{rot}(t) = \frac{1}{2} m_c \left[\left(\dot{x}(t) - r\dot{\varphi}(t) \sin \varphi(t) \right)^2 + \left(r\dot{\varphi}(t) \cos \varphi(t) \right)^2 \right] \tag{A.2}$$

and the vibratory energy $E_v(t)$ of the main mass m is, for this energy balance, defined as

$$E_v(t) = \frac{1}{2} m \dot{x}(t)^2 + \frac{1}{2} k x(t)^2 \tag{A.3}$$

The energy terms, $E_{kin,0}$ and $E_{rot,0}$, are the respective energy terms at the time-point $t = 0$. $E_f(t)$ refers to the work done by the excitation force on the SDOF oscillator given by:

$$E_f(t) = \int_0^t f_e(t) \dot{x}(t) \mathrm{d}t \tag{A.4}$$

The energy balance discussed here was not used in subsection 2.6.6, which considers the kinetic energy of the main mass m and the control mass m_c combined. This can be done as for the energy analysis done in chapter 2, the rotors are, at the considered time-points, not in motion or at the particular angular positions $\varphi(t) = n\pi$ where n is an integer number. Note at the particular angular position $\varphi(t) = n\pi$, the term, $r\dot{\varphi}(t) \sin \varphi(t)$ in (A.2), cancels out. Consequently, the energy term $0.5 m_c \dot{x}(t)$ can be added to (A.3), which was done in subsection (2.6.6). The remaining term of (A.2), $0.5 m_c \left(r\dot{\varphi}(t) \cos \varphi(t) \right)^2$, simplifies to $0.5 m_c r^2 \dot{\varphi}(t)^2$ with $\varphi(t) = n\pi$, which is the rotational energy stored in both rotors of (2.99) with the rotational inertia of a single rotor of $J = 0.5 m_c r^2$ (point mass).

The energy terms introduced in chapter 2 are, in the opinion of the author, more appropriate, in particular for the derivation of the ramp-up trajectories. However, the energy balance of this chapter was used for the evaluation of the numerical simulations of chapter 3.

A.2 Two degree of freedom oscillator with adapted twin rotor damper

For the energy balance of the two degree of freedom (TDOF) oscillator with the adapted TRD, the energy balance is given by

$$E_1(t) + E_2(t) + E_{rot,1,0} + E_{rot,2,0} + E_{kin,0} + E_{f,X}(t) + E_{f,Y}(t) = \tag{A.5}$$
$$E_{d,x}(t) + E_{d,x}(t) + E_{rot,1}(t) + E_{rot,2}(t) + E_v(t) \tag{A.6}$$

whose energy terms are derived in the following. The works done by the actuators $E_1(t)$ and $E_2(t)$ are given by (4.64) with $P_1(t)$, $P_2(t)$, $M_1(t)$ and $M_2(t)$ of (4.61) to (4.63). The works done by the excitation forces are:

$$E_{f,X}(t) = \int_0^t f_{e,X}(t)\dot{x}(t)\mathrm{d}t \qquad E_{f,Y}(t) = \int_0^t f_{e,Y}(t)\dot{y}(t)\mathrm{d}t \tag{A.7}$$

$$E_{d,X}(t) = 2\xi_x\omega_n(m+m_c)\int_0^t \dot{x}(t)^2\mathrm{d}t \qquad E_{d,Y}(t) = 2\xi_y\omega_n(m+m_c)\int_0^t \dot{y}(t)^2\mathrm{d}t \tag{A.8}$$

The kinetic energies of the rotors (assuming the control masses as point masses) is:

$$E_{rot,1}(t) = \frac{1}{4}m_c\sqrt{[\dot{x}(t) - r\dot{\varphi}_1(t)\cos\varphi_1(t)]^4 + [\dot{y}(t) - r\dot{\varphi}_1(t)\sin\varphi_1(t)]^4} \tag{A.9}$$
$$E_{rot,2}(t) = \frac{1}{4}m_c\sqrt{[\dot{x}(t) + r\dot{\varphi}_2(t)\cos\varphi_2(t)]^4 + [\dot{y}(t) - r\dot{\varphi}_2(t)\sin\varphi_2(t)]^4} \tag{A.10}$$

Assuming that the $k = k_x = k_y$, the vibratory energy E_v of the main mass for the TDOF oscillator is:

$$E_v = \frac{1}{2}m\left(\dot{x}(t)^2 + \dot{y}(t)^2\right) + \frac{1}{2}k\left(x(t)^2 + y(t)^2\right) \tag{A.11}$$

The energies $E_{rot,1,0}$, $E_{rot,2,0}$ and $E_{kin,0}$ of (A.6) refer to the respective energy terms of (A.9) to (A.11) at the time-point $t = 0$.

B

Further tables and diagrams

Table B.1: Test results of uncontrolled steady-state response

w_e [(rad)/s]	η	d_0 [m]	$A_{0,m}$ [m]	D	D_m	ΔD
5.00	0.93	0.10	0.036	7.51	7.24	0.035
5.05	0.94	0.10	0.043	8.64	8.35	0.033
5.10	0.95	0.10	0.052	10.18	9.88	0.030
5.15	0.96	0.10	0.065	12.43	12.26	0.013
5.20	0.97	0.10	0.083	15.98	15.29	0.043
5.25	0.98	0.04	0.049	22.42	22.31	0.005
5.30	0.99	0.04	0.081	37.61	36.10	0.040
5.35	1.00	0.02	0.101	104.14	88.02	0.155
5.40	1.01	0.02	0.092	78.29	78.70	−0.005
5.45	1.01	0.04	0.073	32.63	30.53	0.064
5.50	1.02	0.04	0.045	20.24	18.68	0.077
5.55	1.03	0.07	0.059	14.61	13.65	0.066
5.60	1.04	0.07	0.047	11.40	10.70	0.061
5.65	1.05	0.09	0.050	9.33	8.70	0.067
5.70	1.06	0.09	0.043	7.88	7.40	0.061
5.75	1.07	0.10	0.042	6.82	6.35	0.068
5.80	1.08	0.10	0.038	6.00	5.68	0.053

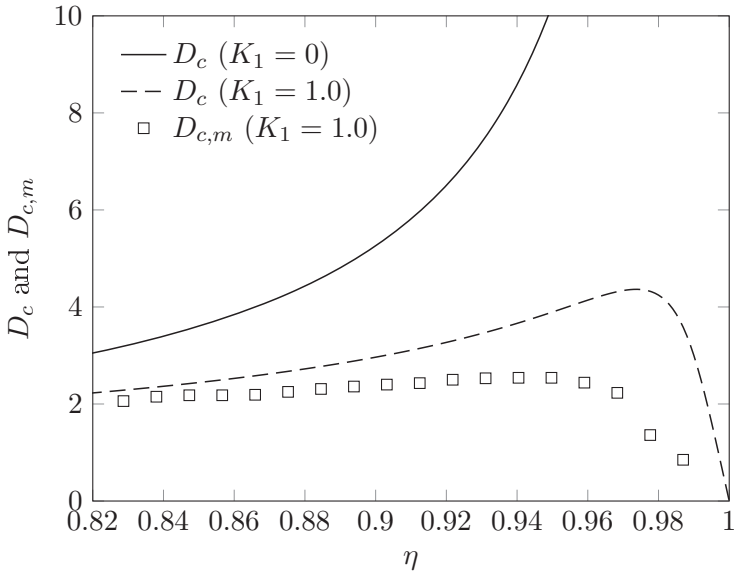

Figure B.1: Controlled dynamic amplification D_c and $D_{c,m}$ plotted against frequency ratio η for $\xi = 0.00305$ for $K_1 = 1.0$

Table B.2: Test results of controlled steady-state response for $K_1 = 0.7$

active TRD units	w_e [(rad)/s]	d_0 [m]	D_c	$A_{0,c}$ [m]	$A_{0,c,m}$ [m]	$D_{c,m}$	ΔD_c
both	4.45	0.0832	2.77	0.0092	0.00897	2.72	0.021
both	4.50	0.0814	2.90	0.0096	0.00865	2.62	0.096
both	4.55	0.0796	3.03	0.0100	0.00943	2.85	0.058
both	4.60	0.0779	3.18	0.0105	0.0099	3.00	0.059
both	4.65	0.0762	3.36	0.0111	0.0103	3.12	0.071
both	4.70	0.0746	3.55	0.0117	0.0109	3.30	0.072
both	4.75	0.0730	3.78	0.0125	0.0115	3.48	0.079
both	4.80	0.0715	4.05	0.0134	0.0123	3.72	0.080
both	4.85	0.0701	4.36	0.0144	0.0132	4.00	0.084
both	4.90	0.0686	4.74	0.0156	0.0144	4.36	0.080
both	4.95	0.0673	5.20	0.0172	0.0156	4.72	0.092
both	5.00	0.0659	5.78	0.0191	0.0172	5.21	0.099
both	5.05	0.0646	6.52	0.0215	0.0194	5.87	0.100
both	5.10	0.0634	7.53	0.0249	0.0226	6.84	0.091
both	5.15	0.0621	8.94	0.0295	0.0264	7.99	0.106
both	5.20	0.0609	11.10	0.0367	0.0329	9.96	0.103
both	5.25	0.0598	14.78	0.0488	0.0448	13.56	0.082
both	5.30	0.0587	22.31	0.0737	0.0668	20.22	0.093
one	5.35	0.0283	41.99	0.0681	0.0646	39.81	0.052
one	5.40	0.0278	34.76	0.0564	0.0509	31.37	0.098
both	5.45	0.0555	18.35	0.0606	0.0581	17.59	0.041
both	5.50	0.0545	11.99	0.0396	0.0397	12.02	−0.002
both	5.55	0.0535	8.75	0.0289	0.0295	8.93	−0.021
both	5.60	0.0525	6.79	0.0224	0.0233	7.05	−0.039
both	5.65	0.0516	5.48	0.0181	0.019	5.75	−0.050
both	5.70	0.0507	4.54	0.0150	0.016	4.84	−0.067
both	5.75	0.0498	3.83	0.0127	0.0137	4.15	−0.083
both	5.80	0.0490	3.27	0.0108	0.0123	3.72	−0.137
both	5.85	0.0482	2.82	0.0093	0.0107	3.24	−0.147
both	5.90	0.0473	2.45	0.0081	0.00932	2.82	−0.151
both	5.95	0.0465	2.14	0.0071	0.00825	2.50	−0.169
both	6.00	0.0458	1.86	0.0062	0.00725	2.19	−0.179

Table B.3: Test results of controlled steady-state response for $K_1 = 1.1$

active units	w_e [(rad)/s]	d_0 [m]	D_c	$A_{0,c}$ [m]	$A_{0,c,m}$ [m]	$D_{c,m}$	ΔD_c
both	4.45	0.0530	2.05	0.0043	0.0039	1.83	0.107
both	4.50	0.0518	2.09	0.0044	0.0038	1.82	0.129
both	4.55	0.0507	2.12	0.0045	0.0038	1.83	0.139
both	4.60	0.0496	2.16	0.0045	0.0038	1.80	0.164
both	4.65	0.0485	2.19	0.0046	0.0038	1.81	0.172
both	4.70	0.0475	2.22	0.0047	0.0038	1.81	0.186
both	4.75	0.0465	2.24	0.0047	0.0037	1.77	0.211
both	4.80	0.0455	2.26	0.0047	0.0035	1.64	0.272
both	4.85	0.0446	2.25	0.0047	0.0033	1.56	0.307
both	4.90	0.0437	2.22	0.0047	0.0029	1.39	0.375
both	4.95	0.0428	2.14	0.0045	0.0025	1.19	0.446
both	5.00	0.0419	1.97	0.0042	0.0020	0.97	0.508

Table B.4: Test results of controlled steady-state response for $K_1 = 1.0$

active units	w_e [(rad)/s]	d_0 [m]	D_c	$A_{0,c}$ [m]	$A_{0,c,m}$ [m]	$D_{c,m}$	ΔD_c
both	4.45	0.0582	2.28	0.0053	0.0048	2.06	0.099
both	4.50	0.0570	2.35	0.0054	0.0050	2.15	0.085
both	4.55	0.0557	2.42	0.0056	0.0050	2.18	0.100
both	4.60	0.0545	2.50	0.0058	0.0050	2.18	0.129
both	4.65	0.0533	2.58	0.0060	0.0051	2.19	0.152
both	4.70	0.0522	2.67	0.0062	0.0052	2.25	0.159
both	4.75	0.0511	2.77	0.0064	0.0054	2.31	0.166
both	4.80	0.0501	2.88	0.0067	0.0055	2.36	0.181
both	4.85	0.0490	3.01	0.0070	0.0056	2.40	0.202
both	4.90	0.0480	3.15	0.0073	0.0056	2.43	0.226
both	4.95	0.0471	3.30	0.0076	0.0058	2.50	0.243
both	5.00	0.0461	3.48	0.0080	0.0059	2.53	0.271
both	5.05	0.0452	3.67	0.0085	0.0059	2.54	0.307
both	5.10	0.0443	3.89	0.0090	0.0059	2.54	0.346
both	5.15	0.0435	4.12	0.0095	0.0057	2.44	0.406
both	5.20	0.0427	4.31	0.0100	0.0052	2.23	0.484
both	5.25	0.0418	4.32	0.0100	0.0032	1.36	0.685
both	5.30	0.0411	3.58	0.0083	0.0020	0.85	0.764

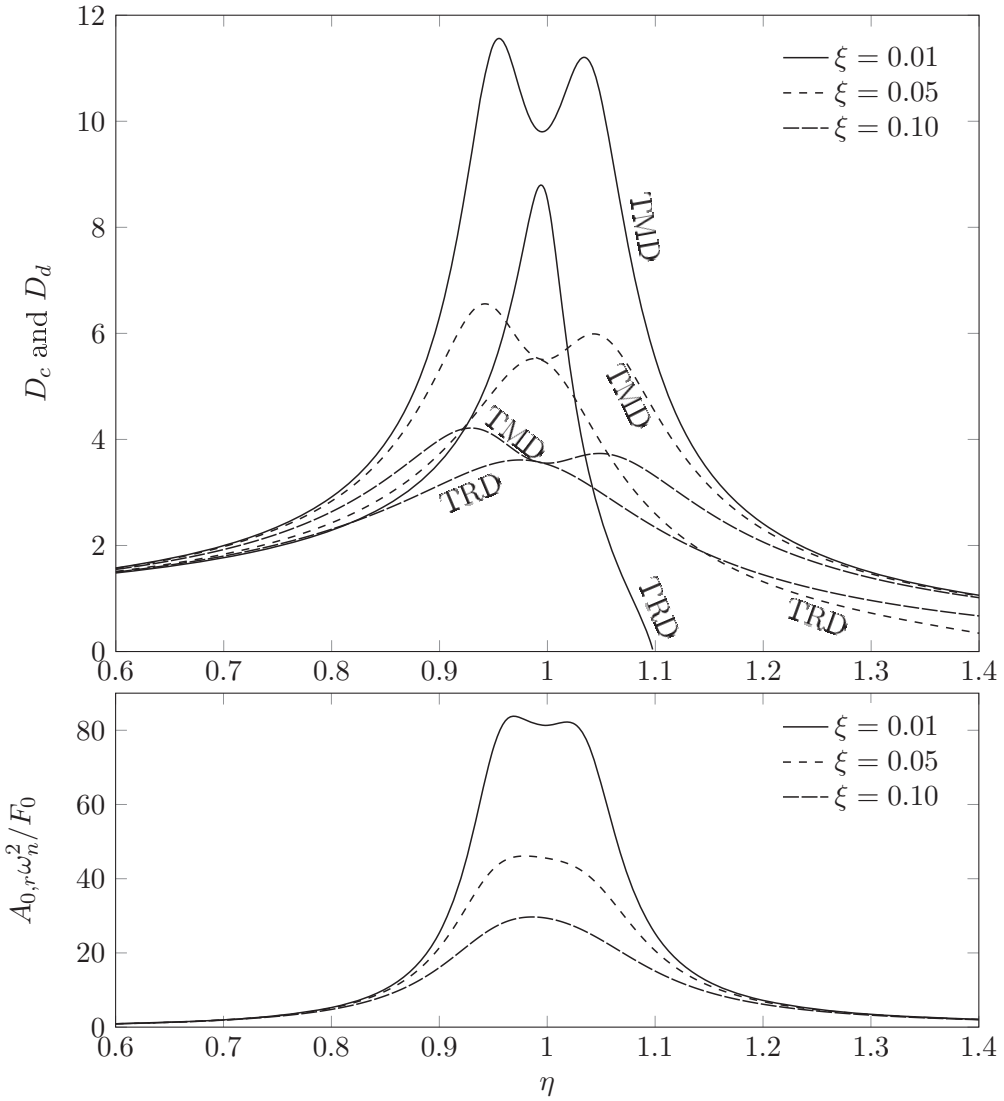

Figure B.2: Dynamic amplifications D_d (TMD), D_c (TRD) and normalized relative displacement amplitude $A_{0,r}\omega_n^2/F_0$ of the control mass in steady-state for $\mu_2 = 0.01$ for different values of ξ

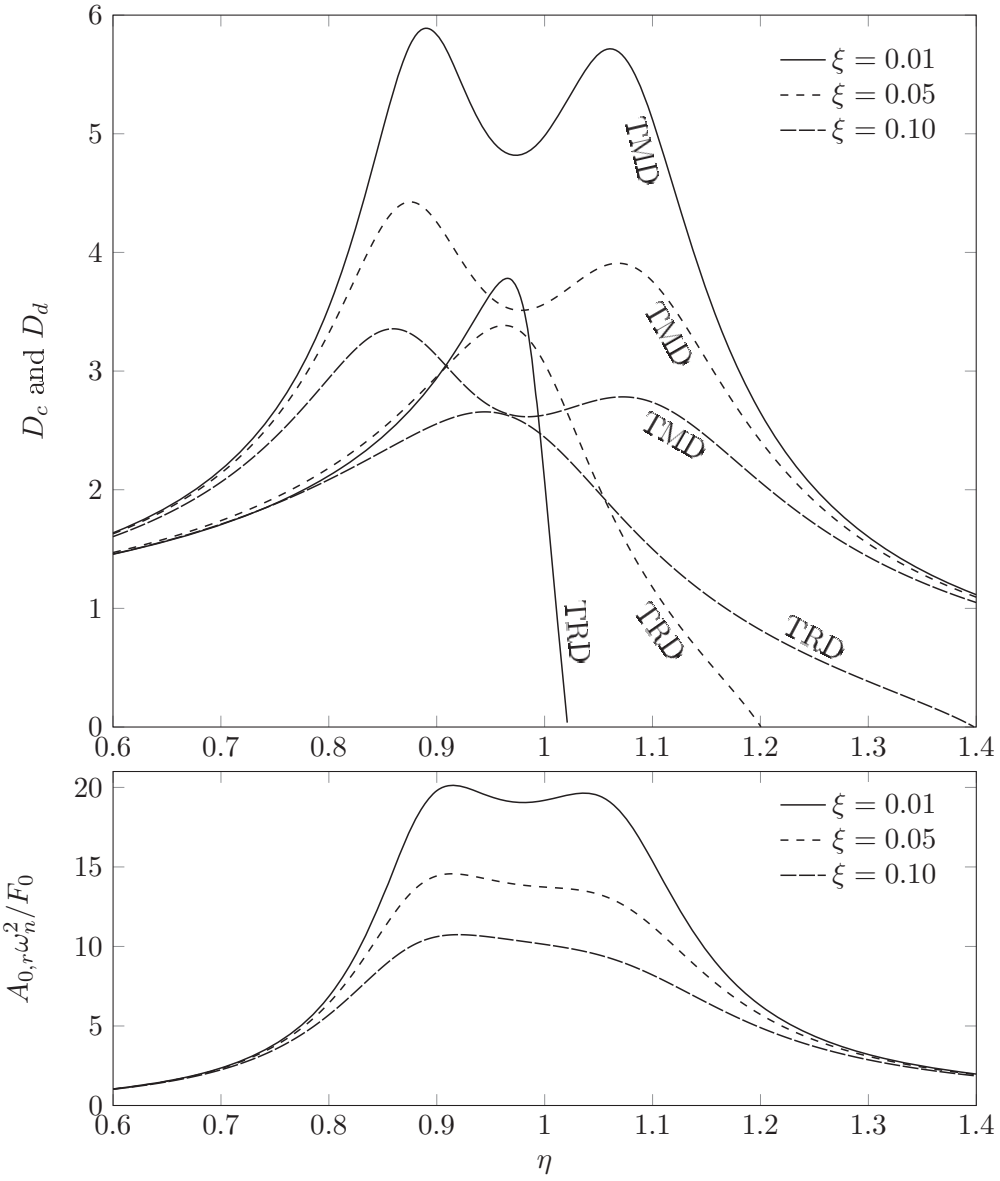

Figure B.3: Dynamic amplifications D_d (TMD), D_c (TRD) and normalized relative displacement amplitude $A_{0,r}\omega_n^2/F_0$ of the control mass in steady-state for $\mu_2 = 0.05$ for different values of ξ

Bibliography

[1] D. J. Inman. *Engineering vibration.* Prentice Hall, Englewood Cliffs, New Jersey, 1994.

[2] K. Y. Billah and R. H. Scanlan. Resonance, tacoma narrows bridge failure, and undergraduate physics textbooks. *American Journal of Physics*, 59(2):118–124, 1991.

[3] J. Q. Sun, M. R. Jolly and M. A. Norris. Passive, adaptive and active tuned vibration absorbers—a survey. *Journal of Mechanical Design*, 117(B):234–242, 1995.

[4] W. Fiebig. Reduction of vibrations of pedestrian bridges using tuned mass dampers. *Archives of Acoustics*, 35(2):165–174, 2010.

[5] C. Petersen. *Dynamik der Baukonstruktionen.* Friedrich Vieweg & Sohn, Braunschweig, 2000.

[6] J. P. Den Hartog. *Mechanical vibrations.* McGraw-Hill, New York, 1956.

[7] H. H. Lee, S.-H. Wong and R.-S. Lee. Response mitigation on the offshore floating platform system with tuned liquid column damper. *Ocean Engineering*, 33(8-9):1118–1142, 2006.

[8] K. A. Al-Saif, K. A. Aldakkan and M. A. Foda. Modified liquid column damper for vibration control of structures. *International Journal of Mechanical Sciences*, 53(7):505–512, 2011.

[9] S. Colwell and B. Basu. Tuned liquid column dampers in offshore wind turbines for structural control. *Engineering Structures*, 31(2):358–368, 2009.

[10] J. Hino, Y. Futabatake and T. Yoshimura. Semi-active dynamic absorber using the fuzzy theory for a beam subjected to moving loads. *Transactions of the Japan Society of Mechanical Engineers Series C*, 60(571):842–849, 1994.

[11] Y. Fujino, P. Warnitchai and B. M. Pacheco. Active stiffness control of cable vibration. *Journal of Applied Mechanics*, 60(4):948, 1993.

[12] N. Jalili. A comparative study and analysis of semi-active vibration-control systems. *Journal of Vibration and Acoustics*, 124(4):593, 2002.

[13] J. S. Lai and K. W. Wang. Parametric control of structural vibrations via adaptable stiffness dynamic absorbers. *Journal of Vibration and Acoustics*, 118(1):41, 1996.

[14] N. Alujević, I. Tomac and P. Gardonio. Tuneable vibration absorber using acceleration and displacement feedback. *Journal of Sound and Vibration*, 331(12):2713–2728, 2012.

[15] R. Yang, X. Zhou and X. Liu. Seismic structural control using semi-active tuned mass dampers. *Earthquake Engineering and Engineering Vibration*, 1(1):111–118, 2002.

[16] T. T. Soong and W. F. Chen. *Active structural control: Theory and practice.* Longman Scientific & Technical and Wiley, Harlow, Essex and New York, 1990.

[17] A. Preumont and K. Seto. *Active control of structures*. John Wiley, Chichester, United Kingdom, 2008.

[18] T. Kobori, N. Koshika, K. Yamada and Y. Ikeda. Seismic-response-controlled structure with active mass driver system. part 1: Design. *Earthquake Engineering & Structural Dynamics*, 20(2):133–149, 1991.

[19] T. Kobori, N. Koshika, K. Yamada and Y. Ikeda. Seismic-response-controlled structure with active mass driver system. part 2: Verification. *Earthquake Engineering & Structural Dynamics*, 20(2):151–166, 1991.

[20] C. Paulitsch, P. Gardonio and S. J. Elliott. Active vibration control using an inertial actuator with internal damping. *The Journal of the Acoustical Society of America*, 119(4):2131–2140, 2006.

[21] I. Nagashima. Optimal displacement feedback control law for active tuned mass damper. *Earthquake Engineering & Structural Dynamics*, 30(8):1221–1242, 2001.

[22] S.-T. Wu, Y.-R. Chen and S.-S. Wang. Two-degree-of-freedom rotational-pendulum vibration absorbers. *Journal of Sound and Vibration*, 330(6):1052–1064, 2011.

[23] J. Scheller. *Power-efficient active structural vibration control by twin rotor dampers*. Structural Analysis and Steel Structures Institute, Hamburg University of Technology, Ph.D. thesis. Mensch und Buch, Berlin, 2014.

[24] R. Bäumer and U. Starossek. Active vibration control using centrifugal forces created by eccentrically rotating masses. *Journal of Vibration and Acoustics*, 21(20), 2016.

[25] R. W. Clough and J. Penzien. *Dynamics of structures*. McGraw-Hill, New York, 2004.

[26] W. Burger and M. J. Burge. *Principles of digital image processing: Fundamental techniques*. Undergraduate topics in computer science. Springer, London, 2009.

[27] T. H. Glisson. *Introduction to Circuit Analysis and Design*. Springer Science+Business Media B.V, Dordrecht, 2011.

[28] R. Bäumer, U. Starossek and J. Scheller. *Continuous state feedback control for twin rotor damper*. Proceedings of the 9th International Conference on Structural Dynamics, Porto, Portugal, 30 June - 2 July, 2014.

[29] P. Knabner and W. Barth. *Lineare Algebra*. Springer, Berlin, Heidelberg, 2013.

[30] Gene F. Franklin, J. David Powell and Abbas Emami-Naeini. *Feedback control of dynamic systems*. Prentice Hall, Upper Saddle River, New Jersey, 2002.

[31] H. Ziems. *Erstellung eines Nichtlinearen Modells für einen Einläufigen Schwinger an einem Versuchsstand*. Structural Analysis and Steel Structures Institute, Hamburg University of Technology, Project Work. Hamburg, 2015.

[32] L. Ljung. *System identification: Theory for the user*. Prentice Hall, Upper Saddle River, New Jersey, 2012.

[33] G. F. Franklin, J. D. Powell and M. L. Workman. *Digital control of dynamic systems*. Addison-Wesley, Menlo Park, California, 2002.

[34] D. H. Wolaver. *Phase-locked loop circuit design.* Prentice Hall, Englewood Cliffs, New Jersey, 1991.

[35] J. B. Encinas. *Phase locked loops.* Chapman & Hall, London, 1994.

[36] R. Bäumer, S. Wollnack, J. Scheller, U. Starossek and H. Werner. *Twin rotor damper applied to the damping of non-harmonic vibrations.* Proceedings of the 9th International Conference on Structural Dynamics, Porto, Portugal, 30 June - 2 July, 2014.

[37] R. Bäumer and U. Starossek. Closed-form steady-state response solution of the twin rotor damper and experimental validation. *Journal of Vibration and Acoustics*, 139(2), 2017.

[38] R. Bäumer, R. Terrill and U. Starossek. *An analytic comparison regarding steady-state damping performance between the twin rotor damper and a dynamic vibration absorber.* EVACES'2017, Conference Proceedings, San Diego, California, 12 - 14 July, 2017.

[39] H. Frahm. *Device for damping vibrations of bodies.* U.S. Patents No. 989958 A, 1909.

[40] R. Bäumer and U. Starossek. *Control strategies for Active Vibration Control via Twin Rotor Damper.* IABSE Symposium Report, Volume 105, Issue 17, page 1-8, Geneva, Switzerland, 23-25 September, 2015.

[41] R. Bäumer, S. Wollnack and U. Starossek. *Vibration damping via twin rotor damper.* Conference Proceedings, EVACES'2013, Experimental Vibration Analysis for Civil Engineering Structures, Ouro Preto, Brazil, 28-30 October, 2013.

[42] R. Bäumer, R. Terrill, S. Wollnack, H. Werner and U. Starossek. Twin rotor damper for the damping of stochastically forced vibrations using a power-efficient control algorithm. *Journal of Sound and Vibration*, 413:308–331, 2018.

[43] H. Dehling, A. C. Hoffmann and T. Gottschalk. *Stochastic modelling in process technology.* Elsevier, Amsterdam and Boston and London, 2007.

[44] F. Beichelt. *Stochastische Prozesse für Ingenieure.* Teubner Verlag, Stuttgart, 1997.

[45] Yarlagadda and R. K. Rao. *Analog and Digital Signals and Systems.* Springer-Verlag US, Boston, Massachusetts, 2010.

[46] S. Haykin and B. van Veen. *Signals and systems.* Wiley, Hoboken, New Jersey, 2005.

[47] A. Klenke. *Wahrscheinlichkeitstheorie.* Springer, Berlin, 2013.

[48] H. R. Schwarz and N. Köckler. *Numerische Mathematik.* Vieweg+Teubner Verlag, Wiesbaden, 2011.

[49] W. S. Levine. *The control handbook.* CRC Press, Boca Raton, Florida, 1996.

[50] J. Yi, D. Zhao, W. Wang and D. Liu. Design of a stable sliding-mode controller for a class of second-order underactuated systems. *IEE Proceedings - Control Theory and Applications*, 151(6):683–690, 2004.

[51] Y. Zhang, L. Li, B. Cheng and X. Zhang. An active mass damper using rotating actuator for structural vibration control. *Advances in Mechanical Engineering*, 8(7), 2016.

[52] I. Venanzi, F. Ubertini, G. Comanducci and A. L. Materazzi. *Adaptive control strategies for active mass driver system with physical limitations.* Proceedings of the 9th International Conference on Structural Dynamics, Porto, Portugal, 30 June - 2 July, 2014.

[53] C.-J. Wan, D. S. Bernstein and V. T. Coppola. Global stabilization of the oscillating eccentric rotor. *Nonlinear Dynamics*, 10(1):49–62, 1996.

[54] X. Xin and Y. Liu. *Control design and analysis for underactuated robotic systems.* Springer, London, 2014.

[55] H. Werner. *Optimal and robust control.* Lecture Notes, Hamburg University of Technology, 2005.

[56] K. Zhou and J. C. Doyle. *Essentials of robust control.* Prentice Hall, Upper Saddle River, New Jersey, 1998.

[57] M.-Y. Liu, W.-L. Chiang, C.-R. Chu and S.-S. Lin. Analytical and experimental research on wind-induced vibration in high-rise buildings with tuned liquid column dampers. *Wind and Structures*, 6(1):71–90, 2003.

[58] T. Ekelund. Yaw control for reduction of structural dynamic loads in wind turbines. *Journal of Wind Engineering and Industrial Aerodynamics*, 85(3):241–262, 2000.

[59] R. Bäumer and U. Starossek. Active vibration control of an oscillator with two translational degrees of freedom using centrifugal forces created by two eccentrically rotating masses. *International Journal of Dynamics and Control*, online: 25 November 2016, doi: 10.1007/s40435-016-0280-8, 2016.

[60] I. N. Bronshtein and K. A. Semendyayev. *Handbook of mathematics: Bronshtein.* Verlag Harri Deutsch, 1985.

[61] R. Bäumer, R. Terrill and U. Starossek. *An energy approach for the active vibration control of an oscillator with two translational degrees of freedom using two auxiliary rotating masses.* Journal of Physics Conference Series 744(1), Southampton, England, 03-06 July, 2016.